Towards detecting redshifted HI with the Ooty Wide Field Array

A thesis

submitted to the
Tata Institute of Fundamental Research, Mumbai
for the degree of
Doctor of Philosophy
in Physics

by

Visweshwar Ram Marthi

National Centre for Radio Astrophysics
Tata Institute of Fundamental Research
Pune – 411 007, India.

October 2016

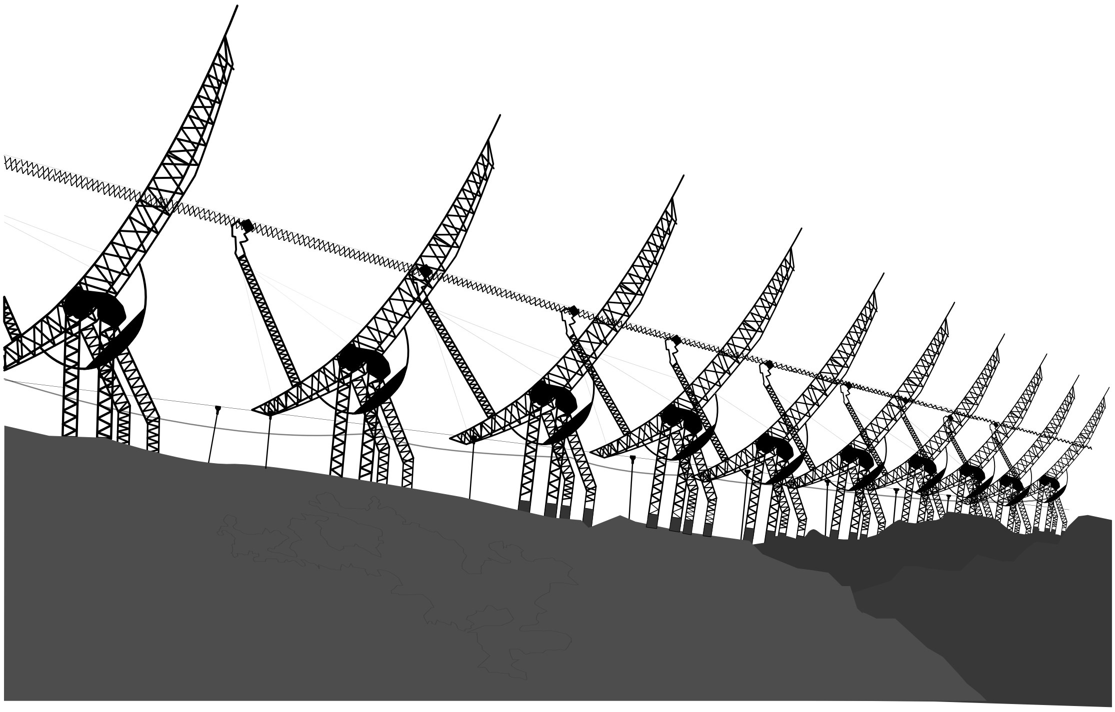

The Ooty Radio Telescope

To the memory of
my beloved grandpa

Marthi Ramaswamy

Acknowledgements

As one who has navigated the hazards of writing a Ph.D. thesis, I'm pleasantly surprised that I've survived the rigours. This is indeed a watershed moment in one's career, as several years of toil come to fruition. No Ph.D. occurs in splendid isolation, and mine is no exception. I have many people to thank personally and professionally. Jayaram Chengalur has greatly influenced my thinking, and has shown by example how to keep the feet firmly on the ground and never lose sight of the larger picture. He has set for me very high standards to aspire after for the remainder of my career. I'm grateful to him for setting me up to work on aspects of the ORT upgrade, and entrusting me with a role in the redshifted HI project that I couldn't have relished any less. Throughout, he has given me abundant freedom to work at my own pace. Often have I barged into his office to express a seemingly clever point or explain a trivially implicit concept on the whiteboard, and he has always received me with a great measure of zen-like calm. Jayaram has helped me in matters beyond the ambit of academics, at times of apparent crises, for which I'm forever indebted to him. To me, he has been a guide, philosopher and friend.

Somnath Bharadwaj, Jasjeet Bagla and Tirthankar Roychoudhury, together with Jayaram, have played major roles in shaping my understanding of 21-cm cosmology. I fondly recollect the extremely fruitful bi-annual meetings we held in Ooty, and the memorable team dinners every time. I must thank the other members of the team: C. R. Subrahmanya, P. K. Manoharan, Abhik Ghosh, Saiyad Ali, Suman Chatterjee, Anjan Sarkar, Debanjan Sarkar, Samir Choudhuri, Ramu Yadav, Bharat Gehlot and Peeyush Prasad. Special thanks to Somnath Bharadwaj, his family and his graduate students for making a three-week trip to IIT Kharagpur so much a memorable one. To my colleagues in NCRA, I owe a debt of gratitude: Nissim Kanekar especially, for help and sage advice on many occasions, Divya Oberoi, Poonam Chandra, Dharam Vir Lal, Subhashis Roy, Yogesh Wadadekar, Ruta Kale - it's been a pleasure working and conversing with you all. Thanks to the administrative staff at NCRA and RAC for enabling my multiple up-down

trips and making my stay at RAC always pleasant. I thank K. Kalyanasundaram, D. Nandagopal, Magesh, Praveen, Jude, R. Venkatasubramani, K. Aravindakrishnan, D. Ravikumar, R. Chandrasekharan, E. Elamathi, Amit Mittal and Arun Varghese at RAC for their help and support during installation, system tests and observations.

I have benefited from discussions with many people, both rigorous and casual, but always useful: for that, I must acknowledge Mihir Arjunwadkar, Avinash Deshpande, Shiv Sethi and Dinesh Raut. I'm grateful to Rajaram Nityananda for his insightful lectures and allowing me many contact hours during the Galactic Dynamics course. I believe I have learnt some amount of radio astronomy in these years, mostly through an osmotic process. Pramesh Rao's mentorship in the early days was possibly the best start one could have hoped for. Yashwant Gupta helped me find my feet in NCRA. Thanks to V. Venkatasubramani and his SysAdmin team for patiently listening to my tirades against Linux quirks, hard disk anomalies and network issues between NCRA and RAC Ooty, and resolving them with alacrity.

Many friends over the long years, some from school and college, have enriched my life in many ways. To my friends Neeraj Gupta, Sambit Roychwdhury, Maryam Arabsalmani, Nirupam Roy, Susmita Chakravorty, Chandreyee Sengupta, Aritra Basu and Vishal Gajjar, thanks for making life in the hostel so much enjoyable. My family has been extremely supportive of my endeavours: I thank my parents who have never questioned my choices, and my parents-in-law for their support and encouragement. Thank you Anu, Balaji, Jayasree, Teju and Vijay for being such a wonderful bunch. My grandparents retain their special place in my life, even if they've departed to meet their Maker. They would've been extremely happy to see me completing the Ph.D., but I should perhaps realize that they indeed are.

No words can sufficiently express my gratitude for my wife Nandini. She has been a selfless companion, enduring my long hours away when writing. My little daughter Hiranmayee has brought us much joy. Without them, I would be alone and bitter. Thanks Nandini and Hiranmayee, for keeping me a largely sane and balanced individual.

Declaration

This thesis is a presentation of my original research work. Wherever contributions of others are involved, every effort is made to indicate this clearly, with due reference to the literature, and acknowledgement of collaborative research and discussions.

The work was done under the guidance of Prof. Jayaram Chengalur, at the National Centre for Radio Astrophysics, Tata Institute of Fundamental Research, Pune.

Visweshwar Ram Marthi

In my capacity as supervisor of the candidate's thesis titled "**Towards detecting redshifted HI with the Ooty Wide Field Array**", I certify that the above statements are true to the best of my knowledge.

Prof. Jayaram Chengalur
(Thesis Supervisor)

Pune
October 25, 2016

Synopsis

The 21-cm radiation from the hyperfine transition of neutral hydrogen is an important cosmological probe over a wide range of redshifts. It has been suggested as a tracer of the large scale structure before the formation of the first stars (or the so called "cosmic dark ages", $z \sim 200 - 40$) through 21-cm absorption against the Cosmic Microwave Background (Bharadwaj & Srikant, 2004). 21-cm observations of the "cosmic dawn" and the epoch of reionisation ($z \sim 15 - 6$) probe the era starting from the formation of the first ionising sources through the time when the bulk of the hydrogen is reionised (see e.g. Pritchard & Loeb, 2012). Finally, 21-cm tomography of the "post-reionisation" era ($z < 6$), where the bulk of the neutral gas is in collapsed objects can constrain a variety of cosmological parameters (see e.g. Bharadwaj *et al.*, 2009). The promise of 21-cm cosmology has led to a renewed interest in low frequency radio astronomy, and several experiments to probe these different regimes are being planned or even carried out. Planned and ongoing experiments to probe the post-reionisation era include CHIME (Bandura *et al.*, 2014), BAOBAB (Pober *et al.*, 2013b) and the Tianlai CRT (Chen, 2011). In this thesis, I discuss experiments being planned with the upgraded Ooty Radio Telescope, dubbed the Ooty Wide Field Array (OWFA).

OWFA represents a comparatively modest upgrade (in terms of expense) to an existing telescope (Prasad & Subrahmanya, 2011; Subrahmanya *et al.*, 2016a), which allows one to build a wide field of view interferometer well suited to probing HI during the post-reionisation era. The telescope works at a frequency of ~ 327 MHz or a redshift of ~ 3.35 for the HI 21-cm line. The sensitivity is sufficient to allow detection of the HI signal in integration times of ~ 150 hrs (Bharadwaj *et al.*, 2015), allowing one to determine the HI bias at these redshifts. Longer integrations would allow for measurements of the HI power spectrum and hence constraints on cosmological parameters (Ali & Bharadwaj, 2014; Bharadwaj *et al.*, 2009).

Even though the telescope has the thermal sensitivity to fairly easily detect the HI 21-cm signal, in common with other such experiments, a major challenge is to understand and overcome systematics. Two major issues that all such experiments need to address are regarding accurate calibration of the data and accurate subtraction of the foreground signals, which are many orders of magnitude larger than the HI signal itself. Since the details of both of these depend critically on the telescope parameters, it is important to fully understand and characterise the telescope in order to be able to make progress. This thesis represents the first detailed effort to characterise OWFA with sufficient depth to allow evaluation of different strategies for calibration, as well as to understand the foregrounds as seen by the telescope. This is done primarily by building a detailed model of the telescope and the expected signals (both foregrounds and the HI signal). These would in turn allow us to run realistic simulations of the observations themselves as well as study in depth the estimators constructed from the observations.

The first chapter of the thesis is a broad introduction to the field of cosmology using the HI 21-cm line. It sets the context for the study of the post-reionisation HI signal by defining the key questions we want to address. We are specifically interested in measuring the power spectrum of HI at $z \sim 3.35$, and in the first instance, measuring the bias factor "b", and whether bias shows a dependence on the angular scale. The nature of b has important consequences for the growth of large scale structure. Chapter 2 describes the legacy Ooty Radio Telescope (ORT) and the ongoing upgrade to the ORT to operate as the Ooty Wide Field Array (OWFA). The ORT is a cylindrical paraboloid with a line feed composed of 1056 dipoles, each followed by an LNA and phase shift module. The telescope is $530\ \text{m} \times 30\ \text{m}$ in size, and is located on a N-S hillside whose slope is equal to the latitude at that point. This makes the telescope effectively equatorially mounted. The sky can hence be tracked by a rotation of the telescope along the long axis of the cylinder. The telescope can also be steered electronically in the N-S direction. In the legacy system the signals from these dipoles are added together using an analog beamforming network. The beamforming network is hierarchical; the second smallest unit in this hierarchy corresponds to the combined output of 4 dipoles. The OWFA system digitises the output of each of these 4-dipole units resulting in an array with 264 equi-spaced elements. These 264 signals are cross-correlated using a software correlator to produce a 264 element interferometer with a field of view $\sim 27^\circ \times 2^\circ$. The entire OWFA system is described in this chapter, and the suitability of OWFA for observations of the post-reionisation HI signal is also highlighted. In particular, since the telescope is equatorially mounted, each baseline measures the same Fourier component as the sky is tracked unlike in the case of earth rotation aperture synthesis arrays. Chapter 3 describes the software model that has been built in order to be able to fully characterise the instrument. This model has been implemented in a software package which allows end-to-end simulation of the observations, and can also serve as a data analysis package once sky data is available.

Chapter 4 examines the issue of calibration, in the specific context of OWFA. OWFA is a highly redundant array, and so redundancy calibration algorithms are a natural choice. Moreover, this class of algorithms is model independent, as one simultaneously solves for the sky and the antenna visibilities. I first review existing algorithms for redundancy calibration (e.g. Wieringa, 1992; Liu *et al.*, 2010; Noorishad *et al.*, 2012). The parameters that we examine particularly are bias (if any) of the solutions as well as the computational expense. I show that most of the existing algorithms are either biased or computationally expensive. I then describe a new fast non-linear solver (Marthi & Chengalur, 2014). The solutions - both the complex antenna gains as well as the complex sky visibilities - are obtained iteratively as those that minimize an objective function. This algorithm is both unbiased and also significantly faster than earlier algorithms that gave unbiased solutions. I also show that the solutions achieve the Cramér-Rao bound of minimum variance. The errors on the calibration solutions can be obtained on the fly during the calibration process itself, by computing the Hessian matrix of the objective function. The calibration algorithm is demonstrated on both simulated data as well as real data from an earlier prototype system for OWFA. We also discuss post-correlation beam formation in this chapter. While not of direct interest for the HI experiment, such beam formation is expected to be useful for other experiments being planned with OWFA, especially studies of transient sources.

Chapter 5 discusses the dominant foregrounds as seen by OWFA. The foreground emission at the OWFA frequency of ~ 327 MHz is dominated by the diffuse Galactic synchrotron emission and the emission from extragalactic radio sources. The diffuse Galactic synchrotron foreground has been studied extensively both within the context of redshifted HI 21-cm cosmology (see e.g. Jelić *et al.*, 2014; Ghosh *et al.*, 2012) and as a tracer of the ionised component of the Galactic ISM (see e.g. Iacobelli *et al.*, 2013b). We use the results of these studies to parametrize the synchrotron emission. This parametrization is then used to generate random realisations of the synchrotron foreground. The extragalactic radio source distribution has also been extensively studied. In the context of OWFA, Ali & Bharadwaj (2014) have made predictions for the expected extragalactic point source foreground based on these earlier studies. Broadly, the extragalactic radio source component of the foregrounds is expected to have both a clustered part as well as a part with a Poisson distribution. I use the parametrization for both the clustered and the Poisson distributions as given by Ali & Bharadwaj (2014) to generate random realisations of the extragalactic radio sky. The simulation uses both these (i.e. diffuse synchrotron as well as extragalactic radio source) foregrounds along with the instrument parameters to generate simulated visibilities. Various sanity checks are performed to show that the simulated data is as would be expected from the parametrization of the foregrounds. A very brief description of an N-body simulation to obtain the HI signal is included. In the remaining chapters, the simulated visibilities are used for further analysis.

The primary estimator that we use for both the foreground and the cosmological signal is the two visibility correlation, viz. $\langle \mathcal{V}(\mathbf{U}_n, \nu_i)\, \mathcal{V}^*(\mathbf{U}_m, \nu_j) \rangle$. This is a useful estimator in situations like the current one, where the bulk of the observed astrophysical signal, viz. the foregrounds, is not stationary, i.e. is a function of (ν_i, ν_j) and not $|\nu_i - \nu_j|$ alone. The properties of this estimator have been explored in detail in Choudhuri *et al.* (2014). For a given baseline pair, the two visibility correlation $\langle \mathcal{V}(\mathbf{U}_n, \nu_i) \mathcal{V}^*(\mathbf{U}_m, \nu_j) \rangle$ can be described by the covariance matrix $\mathbf{S}_2(\nu_i, \nu_j)$ with the number of rows and columns equal to the number of spectral channels. I find that the estimator completely recovers the input power spectrum. The matrix representation of the estimator allows us to recover the angular power spectrum at any pair of frequencies. I find that even after putting in all the chromatic effects, such as the chromaticity of the source, the primary beam, and the length of the baseline vector, the dominant foreground contribution is still very smooth. The properties of the smooth galactic synchrotron emission probe the magneto-ionic Galactic ISM and are of interest in themselves. I show that at the OWFA baselines one can achieve quite high signal-to-noise ratio measurements of the power spectrum of the diffuse Galactic emission in extremely short integration times. This would allow for a rapid characterisation of the galactic ISM over wide fields of view.

I also apply the two visibility estimator to the foreground-free HI signal, obtained by assigning HI to dark matter halos according to a scale-independent bias prescription (Bagla *et al.*, 2010). The dark-matter distribution itself is obtained through an N-body simulation (Chatterjee *et al.*, 2016). I find from simulations that the HI signal is confined to $\Delta\nu < 1$ MHz in almost all the baselines, in line with our understanding of the properties of the HI signal. The $\mathbf{S}_2(\nu_i, \nu_j)$ matrix corresponding to the wanted HI signal is hence diagonally dominant, with the diagonal dominance increasing with baseline length. We can use this fact to try and separate the foreground from the signal. I show that fitting and subtracting smooth functions to the foreground allows one to suppress its contribution by ~ 7 orders of magnitude. The residual foreground however is still stronger than the HI signal, and is dominated by chromatic effects. I show that, as expected, these chromatic effects come primarily from the chromaticity of the primary beam and the chromatic baseline length, and that the instrinsic sky chromaticity itself has very little role to play (Marthi *et al.*, 2016). Sources further from the phase centre arrive at the two antennas of the baseline with a larger time delay, that translates into higher frequencies for the oscillatory patterns in the $\mathbf{S}_2(\Delta\nu)$ space. This corresponds to the so-called "foreground wedge" in the 3D cylindrical power spectrum (see e.g. Seo & Hirata, 2016, and references therein). I show that, although the chromatic effects can indeed be seen, the large number of short baselines of OWFA means that there is a significant portion of the $\mathbf{k}$-space that could be used for foreground isolation based HI signal estimation.

The visibility covariance matrix $\mathbf{S}_2(\mathbf{U}, \nu_i, \nu_j)$ can be expanded in an eigen basis. For the foreground signal, this results in a very small rank (two to be precise) for the covariance matrix. The diagonalised representation can be used to estimate the band-averaged angular power spectrum. In contrast the expected HI signal is stationary in ν, which results in a full-rank expansion of its covariance matrix. This has led to an interesting application: simulated HI visibilities can be obtained from random realisations of the diagonalised covariance matrix (Sarkar *et al.*, 2016b). These discussions comprise Chapter 6.

This thesis is organized as follows. Chapter 1 introduces 21-cm cosmology and sets the context for the thesis. Chapter 2 describes the Ooty Radio Telescope and the Ooty Wide Field Array. It also motivates the suitability of OWFA to doing this particular redshifted HI 21-cm experiment. Chapter 3 describes the software model I have developed, outlining the broad philosophy of the programming style and the elements that go on to make it suitable as an observatory data reduction pipeline. Chapter 4 discusses one of the two main topics this thesis is concerned with: calibration. It describes two earlier calibration schemes and their implementation and results for OWFA. A third algorithm we have developed for OWFA, the fast solver, is described in detail and its performance is studied. In Chapter 5, I discuss simulating the two main foreground components based on their parametrization. Simulated maps thus obtained are used to provide a realistic sky model for computing model visibilities and for power spectrum estimation. I briefly describe the HI signal and the simulated HI map. Chapter 6 deals with the topic of power spectrum estimation, the algorithm tuned for OWFA and the various systematics we expect to see in the estimator. The power spectrum of the simulated HI signal is also discussed. It also discusses the important results of the power spectrum estimation exercise. Chapter 7 summarises the work presented in the thesis, and proposes possible extensions to them in the near future.

List of Publications

List of publications linked to the thesis

Published

1. Marthi, V. R. & Chengalur, J. N., **Non-linear Redundancy Calibration**, 2014, **MNRAS, 437, 524**.

Submitted

1. Marthi, V. R., **A software model for OWFA**, 2016, **JApA** special issue on OWFA.
2. Chatterjee, S., Bharadwaj, S. & Marthi, V. R., **Simulating the $z \sim 3.35$ HI 21-cm visibility signal for OWFA**, 2016, **JApA** special issue on OWFA.

In preparation

1. Marthi V. R., Chatterjee, S., Chengalur, J. N. & Bharadwaj, S., **Simulated foreground predictions for the Ooty Wide-Field Array**, 2016, **MNRAS**.
2. Sarkar, A. K., Bharadwaj, S. & Marthi, V. R., **An eigen-decomposition method for realizing post-reionisation HI visibilities**, 2016, **MNRAS**.

Other refereed publications

1. Marthi, V.R. & Chengalur, J. N., **A search for the 55-MHz OH line**, 2010, **MNRAS, 407, 258**.
2. Marthi, V. R., Chengalur, J. N., Gupta, Y., Dewangan, G. C. & Bhattacharya, D., **The central point source in G76.9+1.0**, 2010, **MNRAS, 416, 2560**.

In conference proceedings

1. Marthi, V. R., Chengalur, J. N., Gupta, Y., Dewangan, G. C. & Bhattacharya, D., "**The central point source in G76.9+1.0**", **JApA, 32, 451** in **Diffuse Relativistic Plasmas**, March 2011, Raman Research Institute, Bangalore, India.
2. Marthi, V. R. & Chengalur, J. N., "**Non-linear Redundancy Calibration**" in **The Metre Wavelength Sky**, Dec. 2013, National Centre for Radio Astrophysics, Pune, India.

Contents

List of Figures

List of Tables

Chapter 1

Introduction

1.1 Overview of Cosmic Evolution

Observations of the Cosmic Microwave Background (Smoot *et al.*, 1992; Bennett *et al.*, 2013) in combination with observations of high redshift Type Ia supernovae (Riess *et al.*, 1998; Schmidt *et al.*, 1998) have shaped our current understanding of the constituents and evolution of the universe. In the so called concordance model, or ΛCDM model, the major constituents of the universe are believed to be dark energy, dark matter, baryonic matter, photons and neutrinos. In the local universe the most easily observed component are galaxies, which themselves are assembled in groups, clusters, filaments and other elements of the large scale structure (LSS). According to the Big Bang model, the universe evolved to the current state from an initial extremely dense and hot state called the Big Bang. It is further believed that shortly after the Big Bang the universe went through a short period of exponential expansion, called inflation. Inflation is believed to have been driven by the energy density in some (as of yet unidentified) field called the “inflaton”, whose energy density remains constant as the universe expands. However, the energy density in all other fields, including the standard model particles, curvature, inhomogeneities, etc. falls during inflation, leaving the current observable universe flat and isotropic on large scales. The quantum fluctuations in the inflaton also provide the primordial inhomogeneities from which the observed structure in the current universe evolved.

The plasma that filled the early universe was opaque to electromagnetic radiation due to Thomson scattering by free electrons. As the universe expands this plasma cools, finally sufficiently enough for the electrons and protons to combine to form hydrogen atoms. At this point - which occurs at a redshift ~ 1100, and which is called the recombination era - the photon scattering cross-section decreases dramatically, and the photons are effectively able to free stream through the universe. It is this relic radiation from the so called "last scattering surface" that is observed today as the Cosmic Microwave Background Radiation (CMB). The CMB, as detailed below, is an important probe of the early universe, and its study has significantly enhanced our understanding of cosmology. Existing studies of the CMB observe the continuum emission from the last scattering surface. However, as the electrons combine with the protons to form hydrogen atoms, they cascade down the energy levels of the hydrogen atom, producing spectral features (Chluba & Sunyaev, 2006; Rubiño-Martín *et al.*, 2006; Chluba *et al.*, 2007; Chluba & Sunyaev, 2007). These spectral features are in principle accessible at the current epoch as spectral ripples riding on the redshifted signal from the last scattering surface and form a potentially important probe of the Universe near the last scattering surface.

Following recombination, the universe continues to expand and cool. During this era there are no sources of electromagnetic radiation, and it has hence been dubbed the "dark ages". The inhomogeneities seeded during the inflation era are however growing via the process of gravitational instability (discussed in the next section). Eventually this leads to the formation of the first generation of stars, the so called Population-III stars. Pop-III stars have extremely low metallicity and are very massive (Rees, 1978; White & Rees, 1978; Puget & Heyvaerts, 1980; Abel *et al.*, 2002). The formation of the first luminous objects in the Universe is referred to as the cosmic dawn. The ultraviolet photons from these stars and the X-ray from environs of the first black holes formed either from these stars, or by some other process such as direct collapse (Eisenstein & Loeb, 1995), begin to heat and reionise the medium. Eventually the energy released from these first stars and galaxies causes the universe to go through the so called "Epoch of Reionisation" (EoR) after which the intergalactic medium (IGM) is essentially completely ionised.

The ionisation state of the IGM can be probed by spectral observations of distant quasars. Since the cross-section for Lyα absorption by hydrogen is extremely large, even trace amounts of atomic hydrogen in the IGM lead to an observable spectral signature. Distributed atomic hydrogen in the IGM would lead to an absorption trough bluewards of the Lyα emission of the quasar itself, the "Gunn-Peterson" trough (Gunn & Peterson, 1965). At low redshift, one observes only discrete absorption lines - the so called Lyα forest lines, as well as lines from higher column density systems - consistent with the expectation that at these redshifts the bulk of the IGM is ionised (e.g. Weymann *et al.*, 1981). As one approaches $z \geq 6$ however, the density of the absorption lines increases rapidly, and they blend to produce a broad absorption trough (e.g. Becker *et al.*, 2001; Fan *et al.*, 2006; Mortlock *et al.*, 2011), such as those seen in the spectra shown in Figure 1.1. The presence of the absorption trough however does not imply that the

IGM has become neutral, since, as mentioned above, even trace amounts of atomic hydrogen can lead to a large optical depth in Lyα. It does however indicate that one is beginning to see the last phases of the EoR.

Observations of the anisotropy of the polarized CMB also provide an independent constraint on reionisation. Thomson scattering due to the free electrons produced during reionsation greatly enhance the CMB polarisation anisotropy at large angular scales. Observations of this anisotropy hence allows one to determine the total Thomson scattering optical depth τ_e, and via this the epoch of reionsation (Hu, 1995; Hu & Sugiyama, 1995; Zaldarriaga, 1997; Kaplinghat *et al.*, 2003). Current measurements based on the WMAP 9-year data (Bennett *et al.*, 2013) give an optical depth $\tau_e = 0.0851$ and the redshift of the EoR as $z = 10.36$, assuming the width of reionisation to be $\Delta z = 0.5$. Figure 1.2 shows a model for the evolution of the Thomson scattering optical depth (Page *et al.*, 2007), consistent with reionisation completing around $z \sim 6 - 7$ as indicated by the observations of high-z QSOs described above.

Following the EoR, the bulk of the neutral gas is confined to collapsed objects (Carilli & Walter, 2013). The total neutral hydrogen content of the Universe at these redshifts can be inferred via counts of the incidence rates of high HI column density absorbers - the so called "Damped Lyα" systems - seen in the spectra of quasars. Observations show a *nearly* constant neutral gas density $\Omega_{\rm HI} \sim 0.001$ at $2 \lesssim z \lesssim 5$ (see e.g. Noterdaeme *et al.*, 2012; Crighton *et al.*, 2015; Neeleman *et al.*, 2016). The details of the amount and distribution of the gas inside these objects depends on complex astrophysical processes. The large scale distribution of these objects is however largely dependent on cosmological parameters and the growth of large scale structure. Observations of the large scale distribution of the collapsed objects in the so called "post-reionisation" era can constrain both cosmological parameters as well as the evolution of structure in the universe. This thesis is largely concerned with making a detailed study of one such experiment, to be conducted with the Ooty Wide Field Array (OWFA; Subrahmanya *et al.* 2016a). In the next section we give a brief introduction to structure formation in the expanding universe.

1.2 Structure formation

As mentioned above, the small inhomogeneities seeded by the quantum fluctuations in the inflation era grow via gravitational instability to produce the rich range of structures seen in the local universe. Essentially, regions with higher density accrete the ambient matter via gravity, thus further enhancing the density contrast between this region and its surroundings. The background expansion of the universe, the coupling

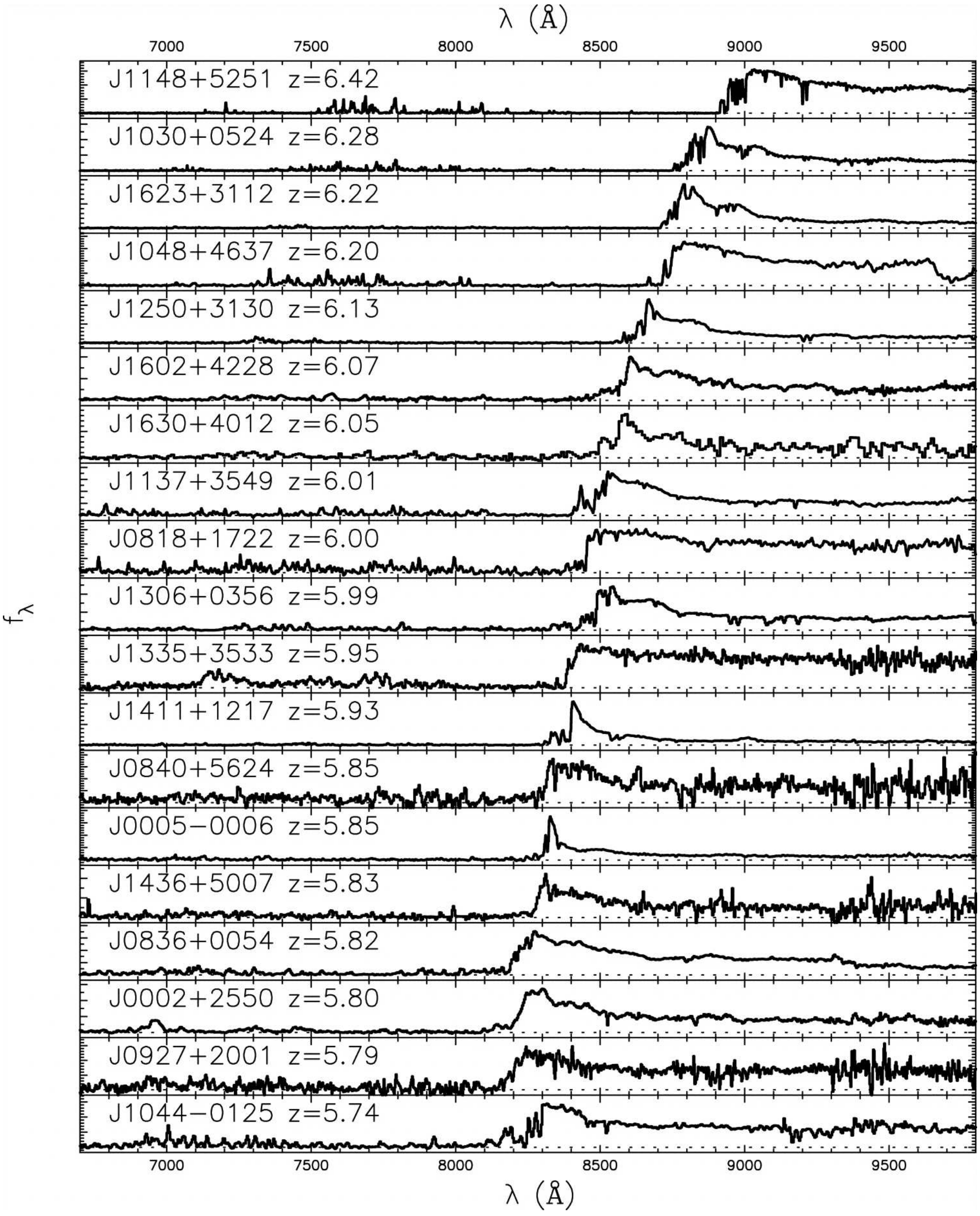

Figure 1.1: The spectra of a sample of quasars with redshifts $5.74 < z < 6.43$. The X-axis gives the observed wavelength while the Y-axis gives flux. As can be seen, there is a sharp cut off of the flux bluewards of the Lyα emission line of the quasar, arising due to absorption from the residual neutral gas in the IGM. Reproduced from Fan *et al.* 2006.

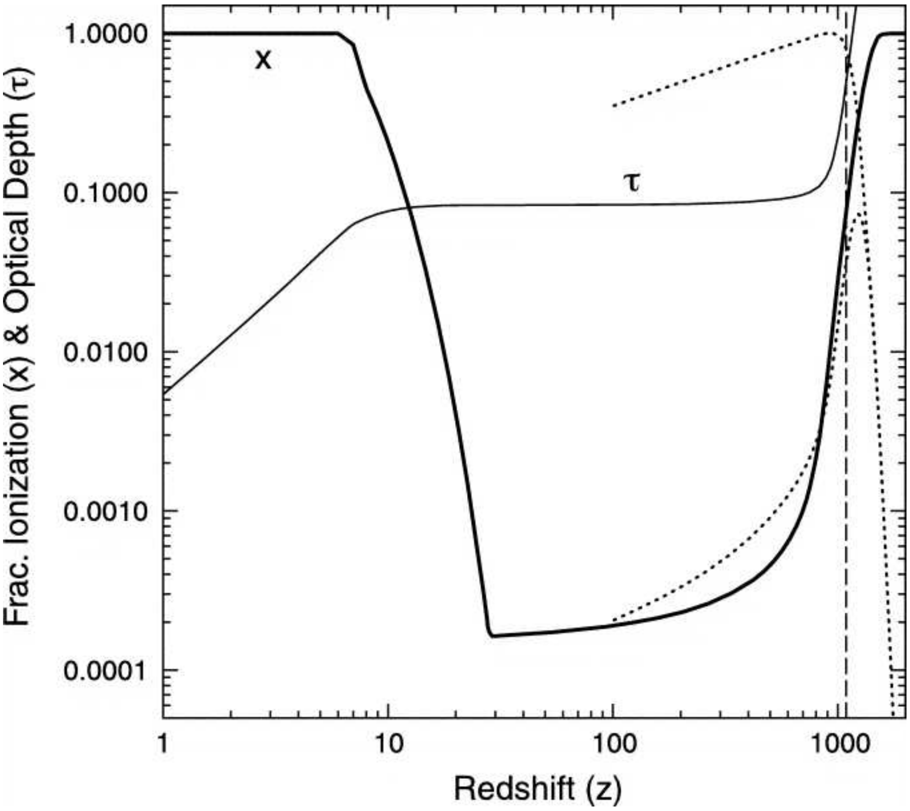

Figure 1.2: A model of net Thomson scattering optical depth τ_e and the fractional ionisation x (from Page *et al.* 2007). The model produces a net optical depth consistent with the WMAP observations, and also has the bulk of reionisation completed by $z \gtrsim 6$, as indicated by observations of high redshift quasars.

between the hot photon bath and the baryons, the nature of dark matter as well as the equation of state of dark energy are all factors that affect the growth of structure and the distribution of the collapsed objects at late times. Conversely, as described below, observations of large scale structure can hence help constrain these cosmological parameters.

The quantum fluctuations produced during inflation are expected to form a Gaussian random field with a scale invariant power spectrum. By the recombination era at $z \sim 1100$, these fluctuations are observed to have grown to the order of 10^{-5} with a power spectrum close to what is predicted by inflation (Smoot *et al.*, 1992; Bennett *et al.*, 2013). While on large scales the growth of perturbations is still in the linear regime, a number of processes cause the spectrum to deviate from the simple scale invariant initial spectrum at small scales. An important feature in the angular power spectrum in this context is the so called Baryon Acoustic Oscillations, or BAO. Prior to recombination, the baryons are tightly coupled to the photons: the protons couple to the electrons via Coulomb forces while the electrons couple to the photons via Thomson scattering. This baryon-photon fluid has significant pressure support. Gravitational collapse around dense regions hence leads to acoustic oscillations. At the time of recombination, the photons decouple, removing the pressure support, and these oscillations are then frozen in the baryon distribution leading to a distinct feature in the distribution of the baryons at a comoving scale of $150h^{-1}$ Mpc. This feature has been observed both in the CMB (Miller *et al.*, 1999; Bennett *et al.*, 2013) as well as in the galaxy distribution as measured using SDSS data (Eisenstein *et al.*, 2005). The BAO feature both confirms the growth of inhomogeneities via gravitational instability as well as the ΛCDM model.

Following the recombination era, structure continues to grow via gravitational collapse. The baryons collect in the centres of the potential wells formed by the overdense regions of dark matter. Since the baryons can cool, they collapse to high densities. The growth of these collapsed objects happens hierarchically, with small objects forming first and then merging to form larger and larger systems. Star formation in these systems marks the end of the dark ages and the start of the cosmic dawn. The detection of these objects is one of the key science goals of next generation telescopes like the James Webb Space Telescope (JWST; Gardner *et al.* 2006). Emission in the 21-cm line of neutral hydrogen is another promising probe, which has the potential to be useful from the dark ages through to the post-reionisation era. This probe is discussed in the next section.

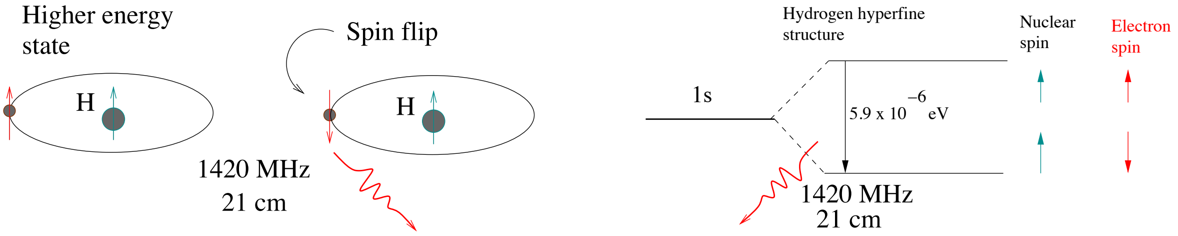

Figure 1.3: The two spin states in the ground state of the hydrogen atom. The transition from the parallel and anti-parallel spin states leads to the emission of a photon with $\lambda \sim 21$ cm.

1.3 21-cm cosmology

The hyperfine ("spin-flip") transition of hydrogen has emerged as an important probe of both cosmology as well as structure formation. The energy difference between the parallel and anti-parallel spin states of the proton and the electron in the ground state of the hydrogen atom is 5.9 μeV (Ewen & Purcell, 1951; Muller & Oort, 1951). A transition between these states hence gives rise to a photon with a wavelength of $\lambda = 21.1$ cm, as depicted in Figure 1.3. The Einstein A coefficient for this transition is extremely small: $A_{21} = 2.9 \times 10^{-15}$ s^{-1}. However the very high cosmic abundance of hydrogen makes the net signal quite easily measurable from the Inter Stellar Medium (ISM) of galaxies at low redshifts.

Because of the expansion of the universe, the HI 21-cm line from an emitter situated at a cosmological distance from the observer is stretched to longer wavelengths. This is quantified by the redshift z, given by

$$1 + z = \frac{\lambda_o}{\lambda_e} = \frac{\nu_e}{\nu_o} \tag{1.1}$$

where $\lambda_e = 21.1$ cm is the wavelength at the emitter and λ_o is the observed wavelength. The detectability of this emission at high redshifts depends on the contrast between the excitation temperature (the "spin temperature") of this transition and the temperature of the CMB.

The cosmic evolution of the spin temperature of neutral hydrogen has been the subject of several studies (see e.g. Pritchard & Loeb, 2012, for a review). Through the dark ages, the adiabatic cooling of the neutral hydrogen due to the expansion of the universe causes the gas kinetic temperature to decline as $(1 + z)^2$, whereas the CMB temperature declines only as $(1 + z)$. This results in the gas cooling faster than the CMB. However, the spin temperature is only weakly coupled to the kinetic temperature. Nonetheless in at least part of this era one could expect to see the hydrogen in absorption against the CMB. During the cosmic dawn, the scattering of Lyα photons produced by the first stars couples the spin temperature to the kinetic temperature, i.e. via the Wouthuysen-Field effect (Wouthuysen, 1952; Field, 1958, 1959; Madau *et al.*, 1997; Loeb & Barkana, 2001), resulting in the spin temperature falling below the CMB temperature. At these epochs, the spin temperature T_s has been predicted to be about 100 mK lower than the CMB temperature $T_{\rm CMB}$, giving rise to a 21-cm absorption signal against the CMB (e.g. Bharadwaj & Ali, 2004; Chen & Miralda-Escudé, 2004; Loeb & Zaldarriaga, 2004). As structure formation proceeds the gas also begins to get heated up, via X-ray and ionising emission from the early type stars and blackholes. The spin temperature eventually exceeds the CMB temperature, and the gas would be seen in emission. Finally the gas ionises. The ionising regions are at first confined to regions around the ionising sources, but gradually grow and merge until the entire IGM is ionised. The universe is now in the post-reionisation era where, as discussed above, neutral gas is confined to collapsed objects. The emission from the individual objects is too faint to be detected by the current generation of radio telescopes. However, low angular resolution observations are sensitive to the total emission from all the objects within the resolution element, which allows one to make measurements of the auto-correlation function of the hydrogen emission, or its cross-correlation with other tracers of the large scale structure (see e.g. Bharadwaj & Sethi, 2001; Chang *et al.*, 2008; Wyithe & Loeb, 2009). The angular two-point correlation function is given by

$$\zeta(\theta) = \langle I(x) I(x+\theta) \rangle \tag{1.2}$$

where $I(x)$ is the intensity of the 21-cm emission arising from the point x. This is related to the power spectrum $P(\mathbf{k})$ through a Fourier transform. We discuss next the expected power spectrum of the HI 21-cm brightness fluctuations. The global mean post-EoR HI brightness temperature $\bar{T}$ (see e.g. Bharadwaj & Ali, 2005; Ali & Bharadwaj, 2014) can be expressed as

$$\bar{T}(z) = 4.0\ (1+z)^2 \left(\frac{\Omega_b h^2}{0.024}\right) \left(\frac{0.7}{h}\right) \left(\frac{H_0}{H(z)}\right)\ \mathrm{mK} \tag{1.3}$$

where z is the redshift of observation, Ω_b is the baryon density. Most of the experiments discussed below aim at detecting not the global signal, but the fluctuations about the mean as characterised either by (a) the angular two-point correlation function $\zeta(\theta)$, or

(b) the power spectrum $P_{\rm HI}(\mathbf{k})$. The H I power spectrum $P_{\rm HI}(\mathbf{k})$ is given by

$$P_{\rm HI}(\mathbf{k},\mu) = b_{\rm HI}^2\ \bar{x}_{\rm HI}^2\ \bar{T}^2\ [1+\beta\mu^2]^2\ P(\mathbf{k}) \tag{1.4}$$

where $P(\mathbf{k})$ is the dark matter power spectrum at redshift z, $b_{\rm HI}$ is the bias, β is the linear redshift-space distortion parameter, and μ is the correction term to account for the line-of-sight contribution of the peculiar velocities and $\bar{x}_{\rm HI}$ is the fraction of neutral gas (see e.g. Bharadwaj & Srikant, 2004). If a linear, scale-independent bias $b_{\rm HI}$ is assumed, the shape of $P_{\rm HI}(\mathbf{k},\mu)$ is unaltered from the dark matter power spectrum $P(\mathbf{k})$. The evolution of the amplitude and the slope of the power spectrum with redshift can constrain the evolution of the bias $b_{\rm HI}$ with redshift, which is an important input to understanding galaxy evolution.

Observations of the redshifted large-scale H I 21-cm signal holds the potential of allowing us to study large scale structures (LSS) across the entire post-reionisation era at $z \lesssim 6$ (Bharadwaj & Pandey, 2003; Bharadwaj & Srikant, 2004; Bagla *et al.*, 2010). In turn these can also constrain cosmological parameters (see e.g. Loeb & Wyithe, 2008; Bharadwaj *et al.*, 2009; Villaescusa-Navarro *et al.*, 2015). For example, as discussed above, observations of the BAO signal at different redshifts constrain the dark energy content of the universe (see e.g. Eisenstein *et al.*, 2007; Chang *et al.*, 2008; Bharadwaj *et al.*, 2009; Visbal *et al.*, 2009; Masui *et al.*, 2010; Seo & Hirata, 2016). Not surprisingly, there are a large number of ongoing efforts to observe the redshifted 21-cm signal.

1.4 21-cm cosmology experiments

1.4.1 Epoch of reionisation

A significant fraction of the effort in 21-cm cosmology today is focused on detecting the redshifted H I 21-cm signal from the Epoch of Reionisation (EoR). The redshifted 21-cm radiation from the EoR probes the distribution of the first luminous sources at cosmic dawn (Madau *et al.*, 1997; Shaver *et al.*, 1999; Barkana & Loeb, 2001; Pritchard & Loeb, 2011; Zaroubi *et al.*, 2012). Although this thesis is focussed on the post-reionisation signal, there is considerable overlap in the techniques used to detect the signal from the EoR and the post-reionsation era. The nature of the signal, the challenges in its detection and the methods required for signal and parameter extraction are all very similar. The discussion of the ongoing EoR experiments below is brief and is mainly to give a fuller prespective of 21-cm cosmology. Dedicated experiments to detect H I from the EoR or post-EoR include the **E**xperiment to **D**etect the **G**lobal **E**oR **S**tep (EDGES;

Bowman & Rogers 2010b), Donald C. Backer **P**recision **A**rray for **P**robing the **E**poch of **R**eionisation (PAPER; Parsons *et al.* 2010), **M**urchison **W**idefield **A**rray (MWA; Bowman *et al.* 2013; Tingay *et al.* 2013) and the **Lo**w **F**requency **Ar**ray (LOFAR; van Haarlem *et al.* 2013, Yatawatta *et al.* 2013). EDGES (Bowman *et al.*, 2008; Bowman & Rogers, 2010a) has placed a lower limit of $\Delta z \gtrsim 0.06$ for the interval over which reionisation proceeded. The first generation interferometric experiments, such as with the GMRT (Paciga *et al.*, 2011, 2013) and PAPER (Parsons *et al.*, 2010, 2014) have yielded upper limits to the EoR power spectrum. A second generation of efforts to detect the global all sky signal (Sathyanarayana Rao *et al.*, 2015; Singh *et al.*, 2015) as well as the 21-cm power spectrum, e.g. the **H**ydrogen **E**poch of **R**eionization **A**rray (HERA; Pober *et al.* 2014), are also in progress. We next look at the ongoing efforts to observe the post-reionisation 21-cm signal.

1.4.2 Post-reionisation redshifted 21-cm

As discussed above, the post-EoR redshifted HI 21-cm signal can provide important constraints on cosmological parameters, as well as inputs to understanding galaxy evolution (Loeb & Wyithe, 2008; Wyithe *et al.*, 2008; Bharadwaj *et al.*, 2009; Visbal *et al.*, 2009; Villaescusa-Navarro *et al.*, 2015; Padmanabhan *et al.*, 2016).

Chang *et al.* (2010) have measured the neutral hydrogen content at redshifts $0.53 < z < 1.12$, and provide a lower limit to the gas density $\Omega_{\rm HI} = 5.5 \pm 1.5 \times 10^{-4} \times (1/rb)$ at a mean effective redshift of $z \sim 0.8$, where r is the stochasticity and b is the bias factor. Several efforts to detect the post-EoR redshifted HI 21-cm signal are also ongoing. The **C**anadian **H**ydrogen **I**ntensity **M**apping **E**xperiment (CHIME; Peterson *et al.* 2006; Bandura *et al.* 2014) is aimed at mapping the distribution of neutral hydrogen over a wide range of redshifts, viz. $z \sim 0.8 - 2.5$, corresponding to 400-800 MHz. The Tianlai **C**ylinder **R**adio **T**elescope (CRT; Chen 2011, 2012, 2015; Xu *et al.* 2015) pathfinder is expected to be identical to CHIME in its frequency coverage, but will eventually probe the full redshift range $z \sim 0 - 2.55$ in the frequencies 400-1420 MHz. The **B**aryon **A**coustic **O**scillation **B**roadband **A**nd **B**road-Beam Array (BAOBAB; Pober *et al.* 2013b) will probe the frequency range 600-900 MHz, or the redshift interval $z \sim 0.5 - 1.5$.

This thesis describes a large field-of-view experiment to detect the large-scale redshifted HI 21-cm using an upgrade to the Ooty Radio Telescope (ORT; Swarup *et al.* 1971). The upgraded telescope is dubbed the **O**oty **W**ide **F**ield **A**rray (OWFA, Prasad & Subrahmanya 2011; Subrahmanya *et al.* 2016a). The initial aim of the OWFA $z = 3.35$ post-EoR experiment (Subrahmanya *et al.*, 2016a), introduced in the next section, is to detect the post-EoR HI power spectrum. We note that the OWFA experiment does not overlap in redshift with the other post-reionisation experiments. These experiments are therefore complementary to each other.

1.5 The Ooty Wide Field Array redshifted 21-cm experiment

A statistical detection of the extremely faint cosmological HI signal entails the following requirements, that directly translate into desirable features of the radio telescope in question. Firstly, it is desirable to observe a very large volume of the universe to boost the contribution of the HI signal: this means a telescope with a large instantaneous field of view and a large instantaneous bandwidth is required. For a robust measurement of the power spectrum, a large number of Fourier modes on the sky have to be measured: this translates into observing with an interferomter with a large number of baselines. Accurate and sensitive measurements are called for so as to minimise the errors on the measured power spectrum: a telescope with a large collecting area is hence desirable which, in addition should be accurately calibratable. Given the faint nature of the signal, it is absolutely essential to build signal-to-noise ratio by integrating sufficiently long: this aspect would benefit significantly from being able to run a dedicated observing campaign with as little demands for time on the telescope for other observations. In the next few pages and particularly in Chapter 2, it will be shown that OWFA does indeed satisfy many of the above requirements.

Having motivated and set the context for observing the post-reionisation redshifted HI 21-cm emission at large scales, I now set out to introduce the OWFA redshifted HI 21-cm experiment. The ORT is being upgraded to operate as an interferometer, with two concurrent modes of operation: a large field-of-view 4.5° × 2° mode and a wide field-of-view 28° × 2° mode. I shall describe the upgrade itself in greater detail in Chapter 2. One of the key science drivers behind the upgrade is to detect the redshifted HI 21-cm emission from the large scale structure. The ORT is well-suited to such an experiment because its frequency of operation, 327 MHz, corresponds to a redshift $z \sim 3.35$ for the neutral atomic hydrogen 21-cm line, where, as described above, OWFA would complement other similar experiments. This redshift corresponds to an epoch in the history of the universe where a transition is taking place (at a scale which falls within the observable **k**-space of the OWFA) from the linear growth of structure to the non-linear. Figure 1.4 shows the departure of the dark matter power spectrum from the analytically computed linear dark matter power spectrum, obtained

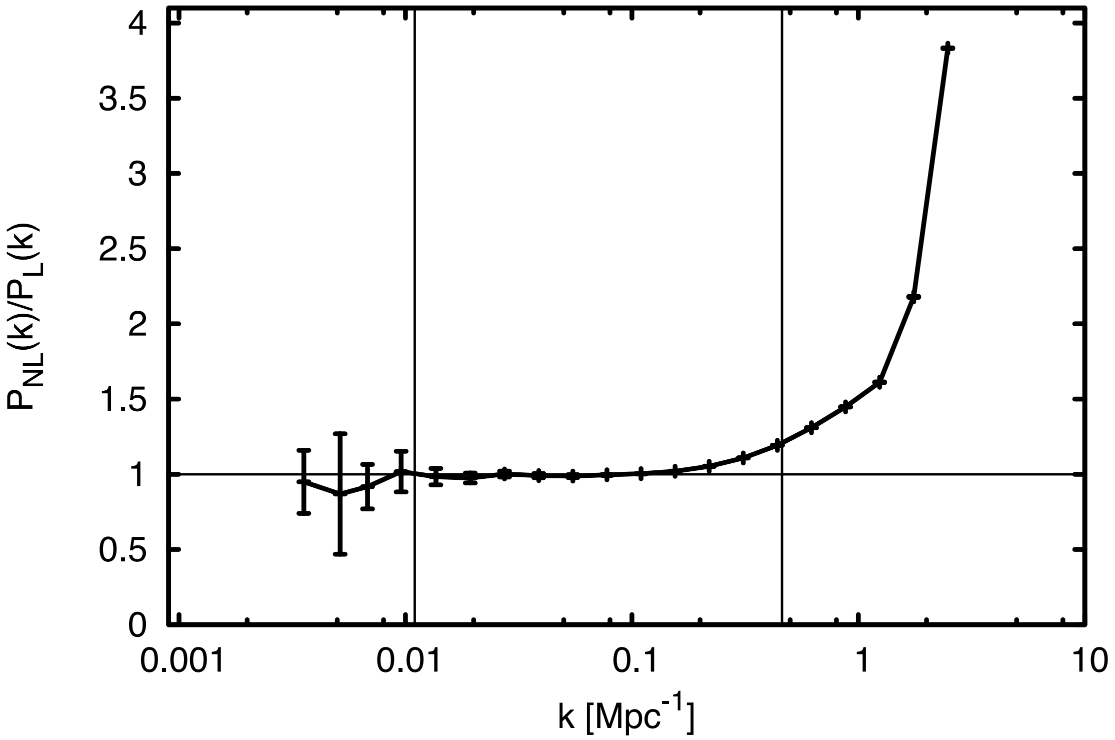

Figure 1.4: The excess power in the dark matter in a 10-realisation average from an N-body code, shown here with respect to the analytically computed DM linear power spectrum. We can see that non-linearity has manifested at $z = 3.35$ in the small scales $k > 0.1\text{Mpc}^{-1}$. The range of wavenumbers probed by OWFA is bounded by the solid vertical lines. Figure adapted from Chatterjee *et al.* 2016.

by averaging ten DM distribution realisations from an N-body code. $P_{\rm NL}(k)/P_{\rm L}(k)$, a dimensionless quantity, is shown for the range of k accessible to OWFA.

The legacy ORT is being converted into an interferometer by digitising the signals from the dipoles along the feed line and cross-correlating them. The signals from a group of dipoles are combined together using an analog beam former and then digitised to form the elements of OWFA. This produces a compact set of highly redundant baselines. At 327 MHz, the longest baseline thus obtained would be $\sim 500\ \lambda$, enabling access to angular scales $\sim 0.1^\circ$ on the sky. Two interferometric modes are envisaged for OWFA. In the first mode every 12.5 m section of the aperture would be digitised, giving a north-south field of view (FoV) of 4.5°, while in the second mode every or 2 m section would be digitised giving a north-south FoV of 27.5° respectively at 0° declination. The east-west FoV is set by the diameter of the ORT, and is 1.75° for both modes. The upgraded RF electronics would allow access to ~ 39 MHz instantaneous bandwidth.

As we would see in Chapter 2, these numbers translate into a very large volume of

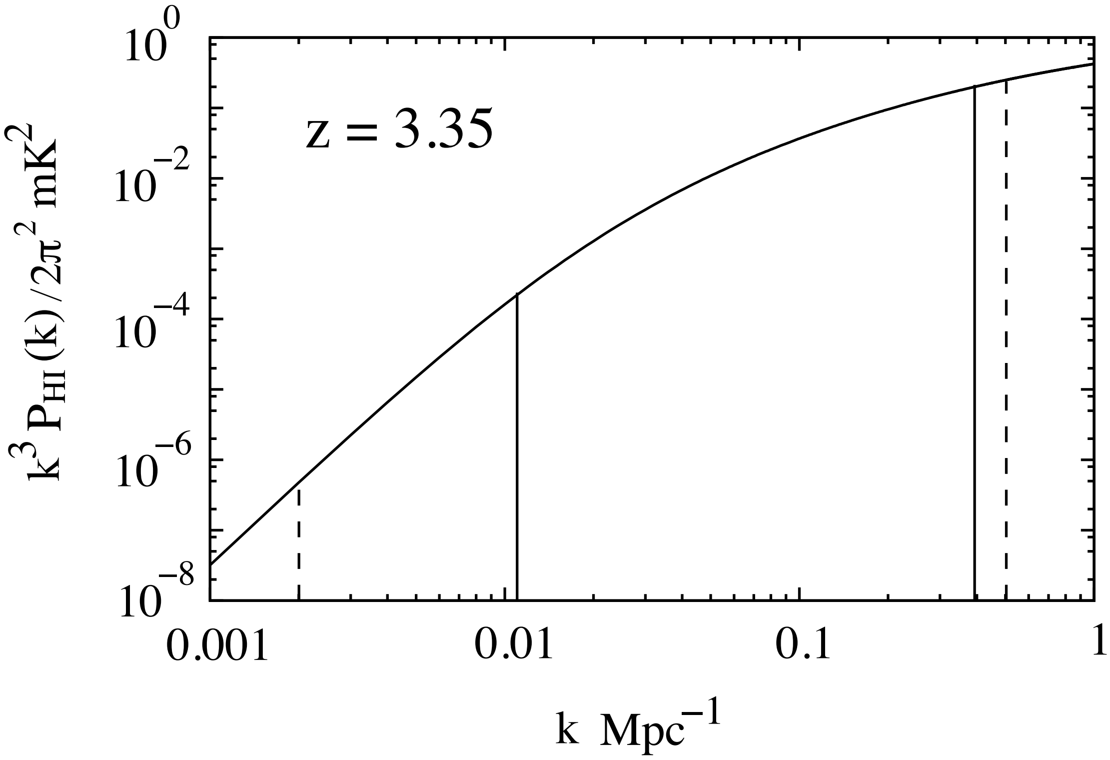

Figure 1.5: The expected HI power spectrum at $z \sim 3.35$ that ORT will have access to. The dashed and solid vertical lines indicate the range of k values for the two interferometer modes with 27° × 2° and 4.5° × 2° fields of view respectively. Only the $k_\perp$ range is shown in this figure. Figure reproduced from Ali & Bharadwaj 2014.

the universe that can be instantaneously sampled, a setup ideally suited to observing the large scale structure. At the conclusion of the upgrade, the two concurrent modes will provide an overlapping range of angular scales with different sampling densities. However, the Wide Field mode provides exclusive access to angular scales between 4.5° and 27.5°. Observations are proposed in campaign mode for measuring the power spectrum of the post-reionisation signal. Figure 1.5 shows the expected HI power spectrum at $z \sim 3.35$, the redshift of operation of OWFA. Estimates tuned to OWFA indicate that the telescope sensitivity is sufficient to make a $\sim 5\sigma$ measurement of the amplitude of the power spectrum (assuming that the shape is known) in integration times as short as $\sim 150hr$ (Ali & Bharadwaj, 2014) assuming that the foregrounds have been fully subtracted. Integration times of $\sim 2000hr$ would allow one to constrain the shape of the power spectrum (Bharadwaj *et al.*, 2015). Gehlot & Bagla (2016) have compared OWFA with other telescopes operating in the same frequency range, and show that OWFA has an edge compared to other existing telescopes.

This thesis takes a detailed look at several aspects of the proposed experiment. In particular, the fundamental requirement of robust calibration is addressed. Besides, simulations are used to study power spectrum estimation. A comprehensive software model is built for both the instrument and the sky signal to numerically simulate the observed interferometric visibilities. The cosmological HI signal is to be extracted in the presence of foregrounds and other systematics introduced by the foregrounds, as it interacts with the instrument in complex ways. One of the principal aims of this thesis is hence to develop an understanding of the systematics introduced by the interaction of the bright foregrounds with the instrument response. Since this thesis represents the efforts toward detecting the power spectrum, the discussion is restricted to aspects of calibration and power spectrum estimation. Interpretation of the detected power spectrum is largely out of scope of this work. Below is a brief overview of the issues involved in calibration and estimating the HI signal in the presence of foregrounds.

1.5.1 Calibration

Calibration is the process of converting the observed visibilities to the true visibilities corresponding to the total signal from the sky. Since the signal of interest is weak and is further buried in a much brighter foreground (see below), accurate calibration is critical. Almost all first-generation experiments and upcoming next generation experiments have designed interferometers with in-built redundancy, in order to allow for good calibration. By redundancy is meant that one makes multiple simultaneous measurements of the same visibility. These observed visibilities hence differ only by the instrumental gains, and if there is sufficient redundancy, one can simultaneously make model-independent measurements of both the instrumental gains as well as the true sky visibilities. The issue of redundancy calibration is discussed in Chapter 4 (based on Marthi & Chengalur 2014), where a new, efficient algorithm for redundancy calibration is proposed and characterized.

1.5.2 Foregrounds

Foregrounds are astrophysical signals apart from the one of interest that arise from the same region of the sky we observe. Tegmark *et al.* (1999) give an "operational definition" for foregrounds, but in the context of the CMB:

- *A foreground is an effect whose dependence on cosmological parameters we cannot compute accurately from first principles at the present time.*

For our purpose, any unwanted astrophysical signal that the telescope is sensitive to, but is chiefly of nuisance value, can be termed foregrounds. In the post-reionisation experiment, the principal foregrounds are the synchrotron emission from the diffuse warm ionised medium within the Milky Way and the extragalactic radio sources. These foregrounds are not only significantly brigher (typically 10^{4-5} times) than the HI signal, but they also interact with the instrument response in ways that cause the net observed foreground to contaminate the HI signal. This makes disentangling one from the other an extremely delicate exercise. In Chapter 5 I describe simulations of the expected foreground at OWFA.

1.5.3 Foreground removal and foreground isolation

Given that foregrounds are orders of magnitude brighter than the signal of interest, two classes of techniques have been suggested to deal with it, viz. foreground removal and foreground isolation. The foreground removal technique attempts to first characterise the foregrounds accurately, and then subtract it from the observed signal. Understandably, the extent to which this works depends on how accurately the foregrounds have been characterised. Proposed techniques for foreground subtraction include fitting and subtracting out spectral functions to the foregrounds in the image cube (Morales *et al.*, 2006; Jelić *et al.*, 2008; Bowman *et al.*, 2009; Chapman *et al.*, 2012; Liu *et al.*, 2009b) or the visibility data (McQuinn *et al.*, 2006; Gleser *et al.*, 2008; Petrovic & Oh, 2011; Liu *et al.*, 2009a). Ghosh *et al.* (2011a,b, 2012) have attempted a model-free characterisation of the foregrounds by fitting low-order polynomials as a function of frequency separation $\Delta\nu$ to the observed angular power spectrum $C_\ell(\Delta\nu)$ at different multipole moments ℓ.

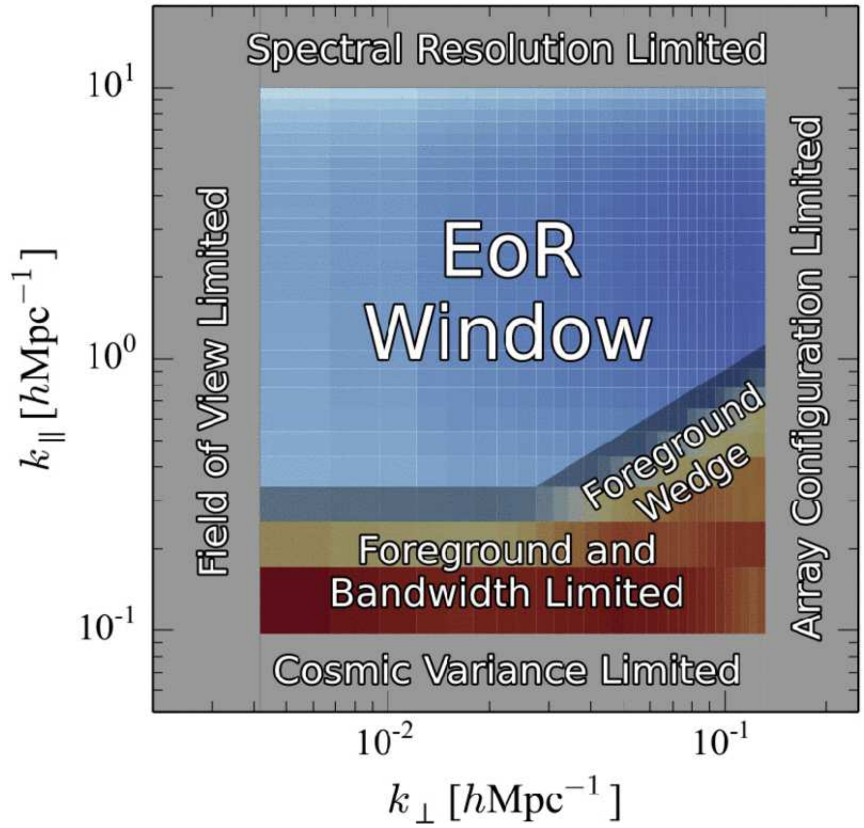

Figure 1.6: This schematic of the cylindrical power spectrum shows the foreground wedge and the EoR window. Reproduced from Liu *et al.* 2014.

The alternative approach is foreground isolation. One of the principal difficulties in foreground subtraction is that the instrument response is chromatic. As a result, even smooth featureless foreground spectra interact with the instrument in very complex ways to produce spectral features. One of the well-understood manifestations of instrument chromaticity is the "foreground wedge" (Datta *et al.*, 2010; Thyagarajan *et al.*, 2013; Vedantham *et al.*, 2012; Liu *et al.*, 2014) in the instrumental **k**-space. This is shown schematically in Figure 1.6. The wedge indicates the region where spectral features from the foreground are confined. This leaves a complementary foreground-free region in the **k**-space, which can be used to estimate the HI signal. Although I don't discuss foreground subtraction in detail in this thesis, I shall touch upon polynomial fitting as well as the foreground wedge in the cylindrical power spectrum while discussing foreground estimation.

1.6 Outline of the thesis

This thesis is chiefly a work that aims to develop an understanding of the OWFA instrument and the systematics we would confront in the redshifted HI 21-cm experiment. However, many elements of research have come together to provide a comprehensive and coherent body of work: mathematical modelling and simulation, measurement of instrument responses, numerical simulations and computing algorithms, astronomical test observations and cosmology. This chapter has motivated the OWFA redshifted HI 21-cm experiment, especially in the context of post-reionisation cosmology. The rest of the thesis is organised as follows.

In Chapter 2, I introduce the Ooty Wide Field Array (OWFA) as a programmable interferometer, which is the foundation for the 21-cm experiment. In particular, I shall list out and briefly describe the geographical and geometrical advantage of upgrading the ORT to operate as an interferometer. I shall then discuss the antenna and interferometric sensitivity, antenna and system temperature, and the two interferometric modes and report the sensitivity measurements carried out in the field to measure the antenna temperature and electromagnetic coupling between the dipoles.. I will also calculate the relevant cosmological numbers for the two modes.

Chapter 3 details the software model I have developed for end-to-end simulations of the 21-cm experiment, starting with the geometric description of the instrument, simulating a realistic sky, and finally obtaining the visibilities. I also introduce a co-ordinate system that allows a simplified form for the van Cittert-Zernike theorem for computing the visibilities. I then detail the emulator software pipeline and walk the reader through the steps going from the instrument through the sky to the observed visibilities. The systematics are built in naturally through a frequency-dependent description of the instrument and the sky signal. This is useful at a later stage to understand the interaction between the sky and the instrument.

Chapter 4 exclusively discusses calibration for the OWFA. The highly redundant geometry of the two interferometric modes is a great advantage for cosmological experiments. I will describe “redundancy calibration” and show examples of implementation of two such algorithms based on linear least-squares (LLS) fitting. I will then present a fast and efficient calibration algorithm based on non-linear least-squares (NLS) fitting and justify its implementation as the algorithm of choice for the OWFA experiment. Specifically, the NLS algorithm gives an edge over the earlier LLS algorithms in terms of unbiasedness and computational complexity. I shall show results from simulated data as well as real data recorded with OWFA on astronomical sources. Other planned experiments at OWFA require the formation of phased array beams, and I discuss this briefly as well.

In Chapter 5, I detail the methods used to simulate the two dominant foreground components: (a) the Galactic synchrotron emission which is diffuse in nature, and (b) the extragalactic radio source population which is discrete. These two components have very different statistical descriptions. The diffuse component is simulated as a Gaussian realisation of an input power spectrum. Simulating a population of extragalactic radio sources is more involved, although at its heart it follows a power spectrum prescription. However, it is not as straightforward as the diffuse foreground. I will explain how the discrete source population is simulated. I will validate the two simulated foreground components against the input power spectrum. Very briefly, I will also describe how the HI signal can be obtained from N-body simulations, and compare the signal of interest with the foregrounds.

Once the foregrounds have been successfully simulated and the model visibilities have been obtained, we have the simulated astrophysical signal in hand. Our final aim however is to measure the power spectrum of the HI fluctuations. I present a formalism to estimate the power spectrum directly from the visibilities. A differentiating feature of the estimator, called the Multi-frequency Angular Power Spectrum (MAPS) estimator, is that its statistics are well understood, and in the manner in which it has been cast for OWFA, it is a full representation in $d - \nu - \nu$ space. Various other estimators, like the cylindrical power spectrum, or the correlation coefficient as a function of frequency separation can be easily derived from it. I apply the estimator to the simulated foregrounds and draw important conclusions about the systematics resulting from the sky-instrument interaction and its implications for foreground separation. I also apply the estimator separately to the simulated HI signal to bring out the distinguishing spectral features in contrast with the foregrounds. These discussions comprise Chapter 6.

I summarise the work in all the earlier chapters, conclude with the results and indicate possible avenues where more work is called for in the near future, in Chapter 7.

Chapter 2

The Ooty Wide Field Array

This chapter introduces the pre-upgrade Ooty Radio Telescope (ORT) as well as its upgrade to the Ooty Wide Field Array (OWFA). The system architecture is described for the two interferometer modes - Mode-I and Mode-II. A historically relevant Phase-I in an early prototype system is briefly described, drawing largely on previous work by Prasad & Subrahmanya (2011). Certain advantages accrue when the telescope is operated as an interferometer. Some system measurements that are relevant to the particular HI experiment, but also useful in general, are described. For the system parameters of the two modes, numbers for the parameter space that they correspond to for the redshifted HI observations are provided.

2.1 The Ooty Radio Telescope

The Ooty Radio Telescope was built in the late 1960s and commissioned in 1970 (Swarup *et al.*, 1971). It is situated in the hill station of Udhagamandalam (Ooty, colloquially) in the Nilgiris in the Indian peninsula. Its geographical coordinates are: latitude $11^\circ\ 22'\ 50''$ N, longitude $76^\circ\ 40'$ E and altitude 2,154 m. The ORT is a steerable telescope with an offset parabolic cylindrical reflector. It is 529 m long and 30 m wide, having an effective collecting area of 8700 m^2. This is equivalent to a parabolic dish of diameter 138 m with an aperture efficiency of $\eta = 0.6$. The axis of rotation of the 529 m long parabolic cylinder has been made parallel to that of Earth by locating the telescope on a hill whose slope equals the local latitude. This makes the telescope equatorially mounted. In the tracking mode, the telescope can track a radio source in hour angle for $9\frac{1}{2}$ hours by mechanical rotation of the reflector. In its earliest configuration, the beam could be steered electronically from declination $+36^\circ$ to -36° using phase shifters and delay lines. Subsequently, this declination range has been improved to $\pm 55^\circ$ (Selvanayagam *et al.*, 1993).

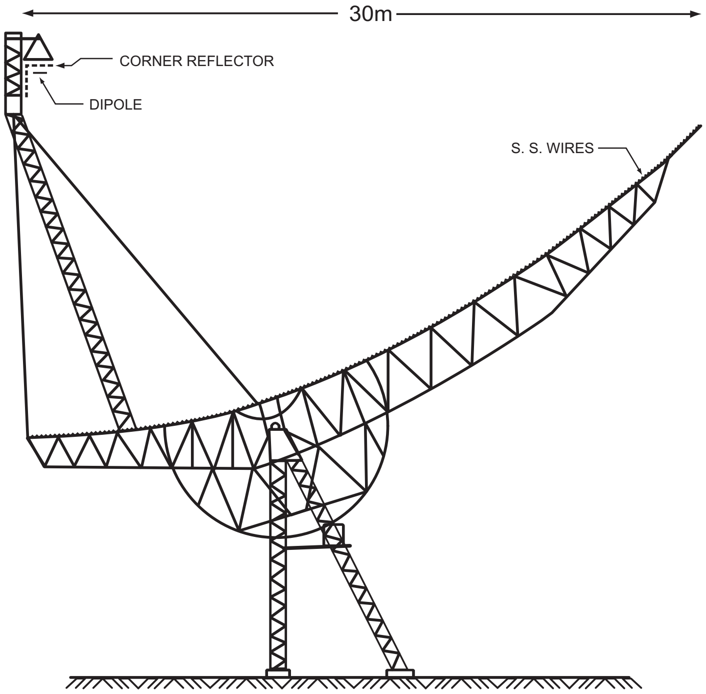

Figure 2.1: A section of one of the 24 frames of the Ooty Radio Telescope. Courtesy: S. G. Meshram.

The ORT consists of 24 parabolic frames, each 30 m wide, supported on 12 to 18 m high towers to account for the local terrain about the mean slope of the hill. Figure 2.1 shows a frame in section. It must be appreciated that, without the hill the same design would entail progressively taller towers northwards: the northernmost tower would be $\sim$ 96 m taller than the southernmost tower. The telescope is logically divided into two halves - the North array and the South array. Each half has 11 frames that are numbered outward from the mid-point. The northern half has frames numbered N01, N02, ... N11, and similarly the southern half S01, S02, ... S11. Each frame supports 48 dipoles, divided logically into two half-modules. Each half-module has 24 dipoles. Besides, there are two extremal half-frames, N12 and S12. They have been provided to avoid vignetting when steering the beam to the extreme declinations. The parabolic surface has a focal length of 16.5 m. The frames are spaced 23 m in the north-south direction. The reflecting surface is formed by 1100 stretched stainless steel wires, each 0.38 mm in diameter. The 24 frames are rotated in unison through a common driveshaft with a gear reduction of 4320:1. In hour angle, the telescope can track from $4h\,05m$ east to $5h\,30m$ west. The asymmetric design of the parabolic frame allows for easy access to the focal line feed when it is brought down to the west limit for servicing and maintenance. The other advantage of the offset reflector is that it avoids aperture blockage and the associated loss in efficiency and increase in sidelobe levels.

2.1.1 Antenna system

The feed system consists of 1056 dipoles, each spaced 0.57λ apart. The dipoles have a centre frequency of 326.5 MHz and are $\lambda/2$ long each. The feed line is placed within a 90° corner reflector in order to reduce the illumination spillover. The dipoles are combined in a passive, christmas-tree combiner network (Joshi *et al.*, 1988; Subrahmanya *et al.*, 2016a) shown in Figure 2.2. Every set of four adjacent dipoles is combined in a four-way combiner. The outputs from two such neighbouring four-way combiners are added in a two-way combiner. Three two-way combiner outputs are again combined in a three-way combiner to give one half-module consisting of a total of 24 dipoles. The other half-module, which is obtained identically, is added again in a two-way combiner to produce the output from a full 48-dipole module. The entire passive combiner network and the low noise amplifiers are all placed in a weather-proof aluminum channel that runs through the length of the telescope. Figure 2.3(a) shows a photograph of the aluminium channel and the dipoles supported by the channel. We shall see in Section 2.2 that this christmas-tree arrangement of the combiner network enables early digitisation of the signals.

2.1.2 Electronic receiver

The signal at the dipole is very weak - its power is -110 dBm. It goes through a Low Noise Amplifier (LNA) which boosts the power by 15 dB. The broadband phase shifter that immediately follows the LNA is called the LNA phase shifter. This phase shifter is used to steer the directional response of the dipole array. The observing declination is set by the effective phase shift imparted by this phase shifter to the signal from the dipole. The signals from four dipoles are combined in the passive four-way combiner, that also introduces a 6 dB loss to the signal. The next two-way combiner introduces an additional 3 dB loss, followed by the three-way combiner that introduces a loss of 5dB to the signal. At the output of the three-way combiner, the strength of the signal is -109 dBm, with a bandwidth of 50 MHz (Selvanayagam *et al.*, 1993). This signal goes into the RF analog box, one for each module, that is located in the aluminium channel. The arrangement upto this point is shown in Figure 2.4

The analog box has a two-way combiner: it takes one input from each of the two half-modules, that corresponds to the signal from 24 dipoles. The two-way combiner introduces a 3 dB loss to the signal. The -112 dBm signal is amplified by the first high-gain, 30 dB amplifier, to -82 dBm. A bandpass filter with a bandwidth of 16 MHz centered on 327 MHz introduces a 2 dB loss to the signal before it is passed on to the mixer. The local oscillator (LO) signal, with a frequency of 297 MHz, is amplified and

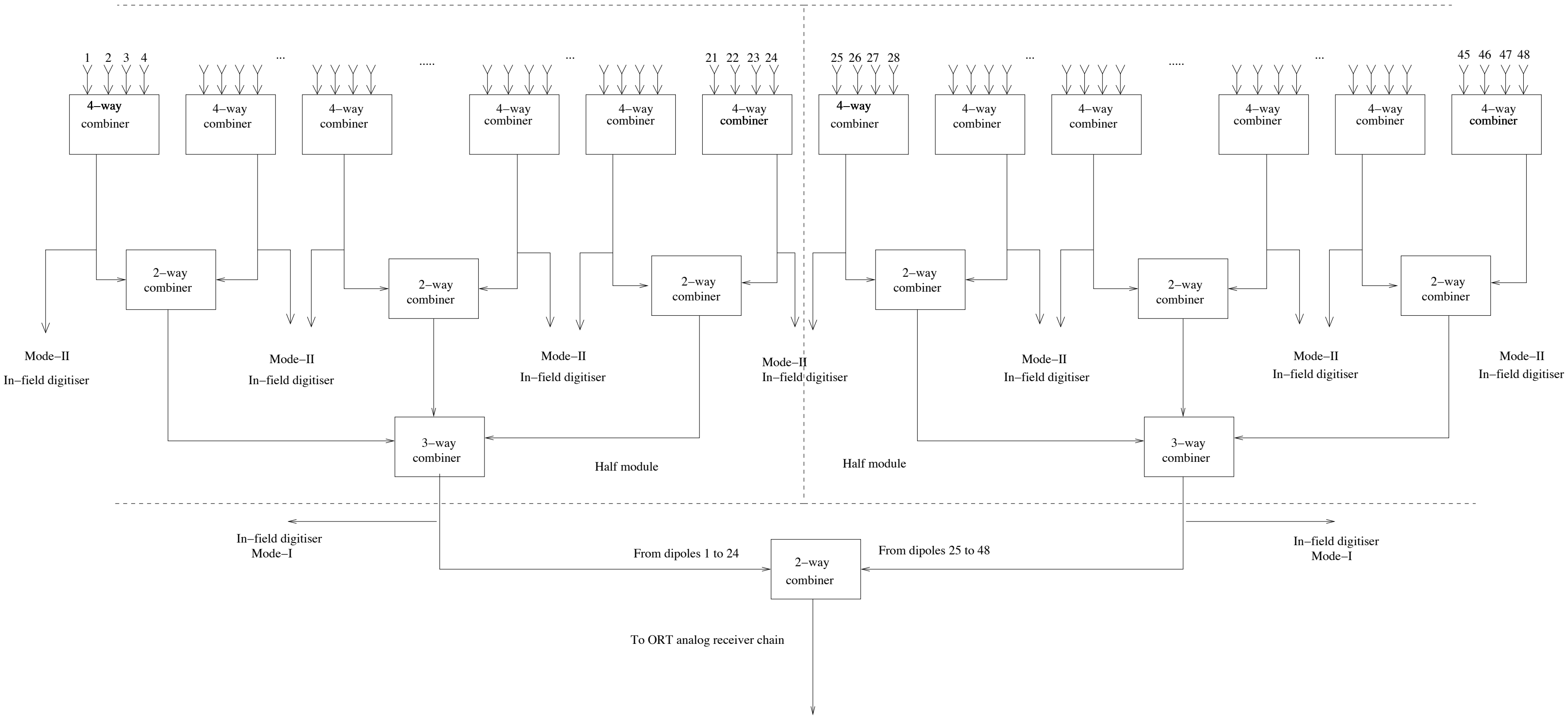

Figure 2.2: The passive christmas-tree combiner network of the ORT.

(a) Aluminium channel and dipoles

(b) Analog box

Figure 2.3: (a) The aluminium channel houses the passive combiner network and supports the dipoles. (b) The analog box that houses some active electronics and the mixer stage.

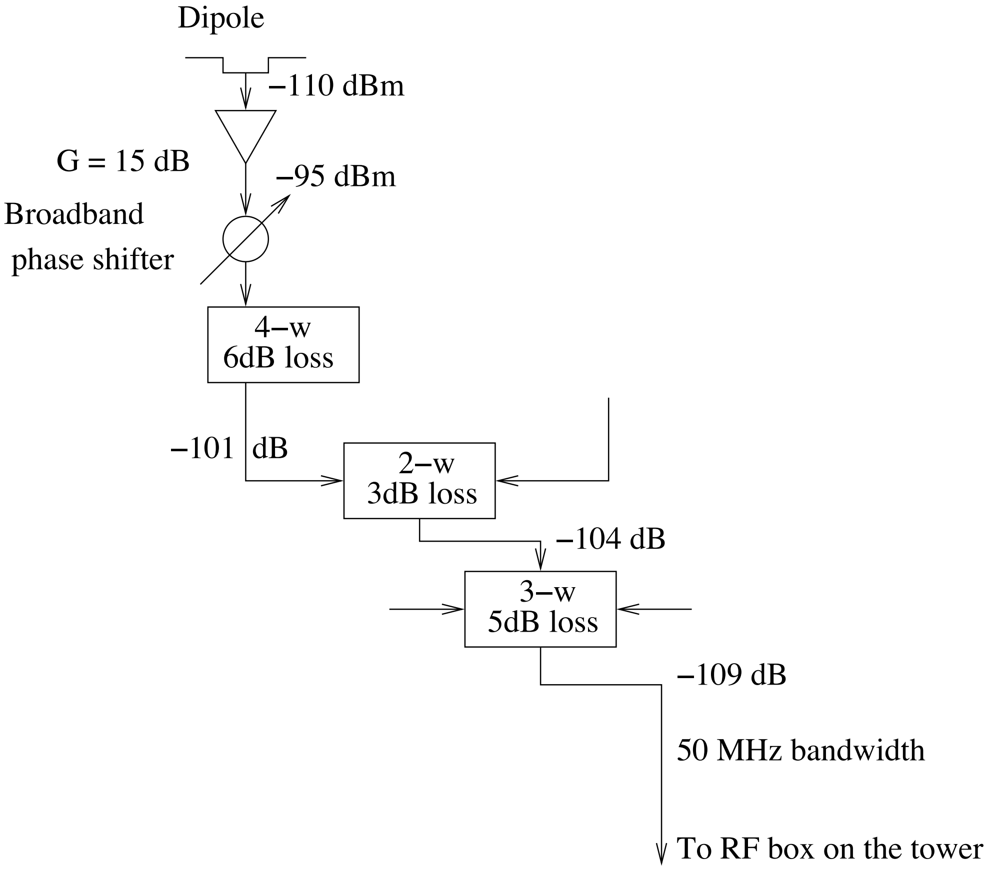

Figure 2.4: The passive combiner network with the associated losses and the typical signal strength at each point.

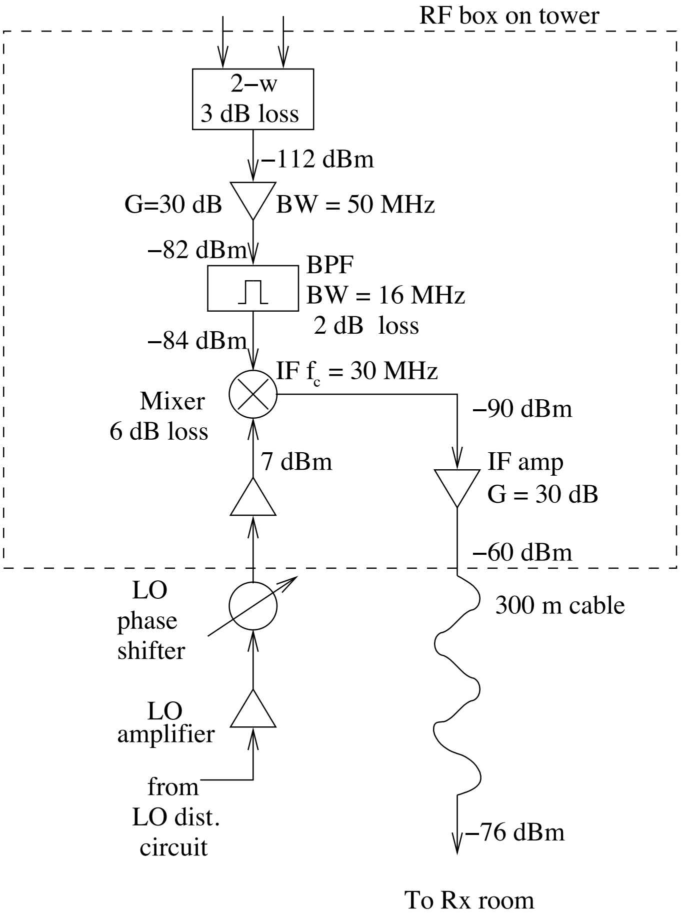

Figure 2.5: The analog box adjacent to the aluminium channel and the active electronics housed in it.

passed through a phase-shifter before the mixer. The mixer takes the RF signal from the bandpass filter, and the local oscillator, to produce an intermediate frequency (IF) of 30 MHz: at this point the signal power is -90 dBm, since the mixer introduces a 6 dB loss. The IF signal undergoes a 30 dB amplification through the second high-gain amplifier. The output -60 dBm signal from the analog box is transported to the receiver room on a 300 m co-axial cable that introduces ∼16 dB of loss. Figure 2.3(b) shows a photograph of the analog box adjacent to the aluminium channel in the telescope. The schematic is shown in Figure 2.5.

2.1.3 Beamformer

The output from the analog box corresponds to a full module of the ORT. In the receiver room, the outputs from all the modules are collated. The phased outputs from the analog boxes are added to produce twelve beams on the sky. This beamforming operation happens independently for the outputs from the northern half and the southern half of the telescope. Historically, these twelve beams were used to track the moon, by covering the full disc during lunar occulation observations (Swarup *et al.*, 1971). One of the beams is obtained by adding the outputs from the eleven modules. The other eleven beams are obtained by adding the outputs through a phase-switched network (Swarup *et al.*, 1971). The two sets of twelve beams are then correlated with each other, thereby greatly reducing any systematics. Each beam has a half-power beamwidth (FWHM) of $\sim 2^\circ$ in hour angle. In declination, the phase-switched beam FWHM is $3.6\sec(\delta)$ and the total power beam is $5.6\sec(\delta)$ minutes of arc.

2.2 From a beamformer to a wide field interferometer

The upgrade to the ORT exploits the christmas-tree passive combiner network to tap the RF signal at the four-way combiner output while allowing the working of the legacy system to be unaffected. Since each dipole is $\lambda/2$ long, the four-way combiner output is equivalent to a 2λ aperture. Its field-of-view is therefore $1/2$ radian. Since there are a total of 1056 dipoles, tapping the four-way combiner output produces 264 RF signals, or equivalently 264 "antennas". The christmas-tree network in principle enables the signal to be tapped at any of the combiner outputs, according to the required field-of-view. However, the real limitation is imposed by the practicality of the downstream digital electronics required to handle the volume of the signal. Eventually, it is a trade-off between the field of view and data volume that sets the limit to where in the christmas-tree the signals can be comfortably tapped from. This is the advantage that was suggested in Section 2.1.1. The architecture of OWFA is now described briefly.

2.2.1 Architecture of the programmable receiver

The complete architecture of OWFA is described in Subrahmanya *et al.* (2016a), where they also spell out the chief scientific goals of the upgrade. The details of the OWFA Receiver System can be found in Subrahmanya *et al.* (2016b). A brief summary of the architecture of OWFA now follows. The RF signal from the four-way combiner goes through a primary stage of amplification within the Dual Stage-I signal conditioner unit, placed within the aluminium channel. This first stage of amplification gives the signal a boost of 26 dB. Figure 2.6 shows the Dual Stage-I amplifier housed in the aluminium channel. A surface acoustic wave (SAW) filter, followed by an RF amplifier, conditions the signal fed to a directional coupler. The coupled port output of the

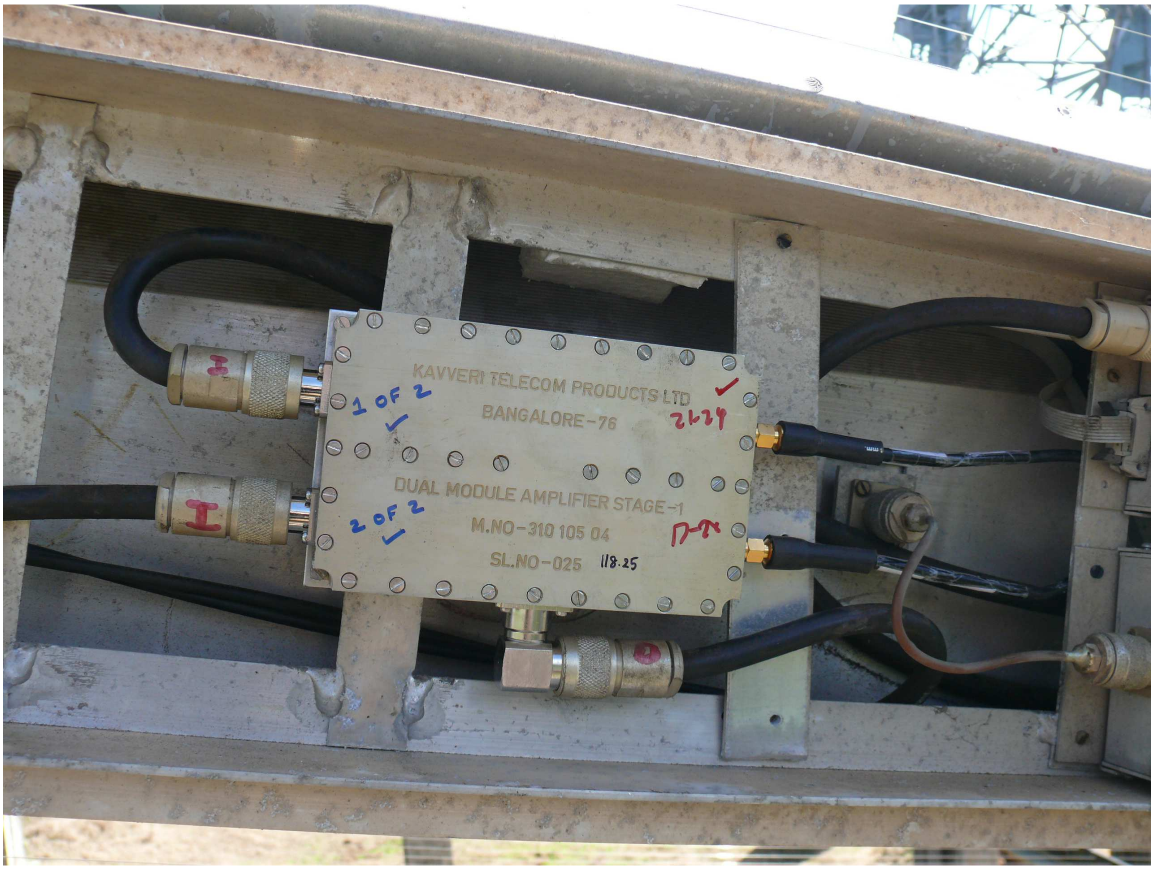

Figure 2.6: The Dual Stage-I signal conditioner is housed in the aluminium channel. The through port outputs proceed to the next Stage-II amplifier before digitisation. The coupled port outputs are internally combined and the output is given to a three-way combiner, effectively replacing the legacy two-way combiner.

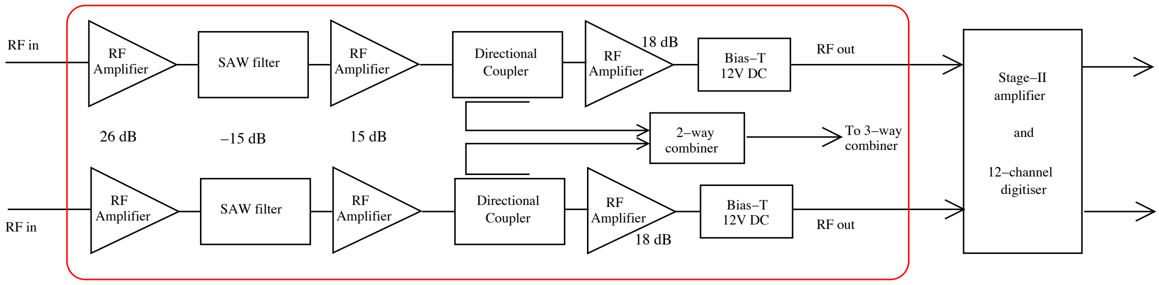

Figure 2.7: A schematic of the Dual Stage-I signal conditioner, adapted from Subrahmanya *et al.* 2016b.

directional coupler is fed to a two-way combiner within the Dual Stage-I conditioner, that effectively replaces the legacy two-way combiner. The output power of the coupled port is commensurate with the input of the first two-way combiner in the christmas tree of the ORT legacy system, so that the power level of the signal in the legacy system is unchanged. This output from the Dual Stage-I signal conditioner is then passed on to the three-way combiner of the legacy system. Figure 2.7, reproduced from Subrahmanya *et al.* (2016b), shows the details of the signal flow described above. The through port output of the directional coupler is passed on to an 18 dB RF amplifier before being fed to the Stage-II signal conditioner.

The Dual Stage-II conditioner and the digitiser are situated in the shielded structure near the tower at each frame, called a "pillar". The pillar is a weather-proof, steel enclosure to house the in-field electronics and provides controlled access and ventilation at the same time. The Stage-II conditioner is similar to the Stage-I conditioner, but the amplifier has a slightly higher gain and includes a SAW filter identical to that in Stage-I. It can take two RF inputs and gives two RF outputs. Since a frame caters to a total of 48 dipoles, there are twelve four-dipole RF signals that reach the pillar on equal length (60 m) coaxial cables. The conditioned RF signals from the output of the Stage-II are then fed into a 12-channel analog-to-digital converter (ADC). The net gain imparted to the signal by the Stage-I and Stage-II amplifiers before digitisation is ~ 70 dB (Subrahmanya *et al.*, 2016b).

The sampled signals are multiplexed and sent on two optical fiber links using the Xilinx Aurora protocol. Each fiber carries a 2.5 Gbps Aurora link all the way to the receiver room, where it is terminated in a data pooler card. The data pooler cards take all such Aurora links from all the other frames. The data pooler is at the heart of this architecture, and it is critical for downstream processing. The pooler and the bridge cards together collate all the data in a time synchronised fashion but apportion them in time-sliced chunks. Each such chunk has data from all the antennas. The pooler and the bridge cards essentially share the load of data pooling in two stages.

In addition, the bridge card converts the time-sliced data in the native Aurora format to the standard Internet Protocol (IP). The IP packets are shipped onward on copper CAT6 cables to an eight-node high-performance cluster. The bridge produces a total of 88 individual IP outputs. A group of eleven cables terminates in each node of the cluster. Figure 2.8 shows the block-level architecture of OWFA. Together, these eleven cables carry a one-eighth time-slice of all the data. All the 264 antennas are available at each node, but for one-eighth of the time. Therefore, cross-correlations between all antenna pairs can happen within a single compute-node of the cluster. These independent time-sliced cross-correlations are then written into disks with their sam-

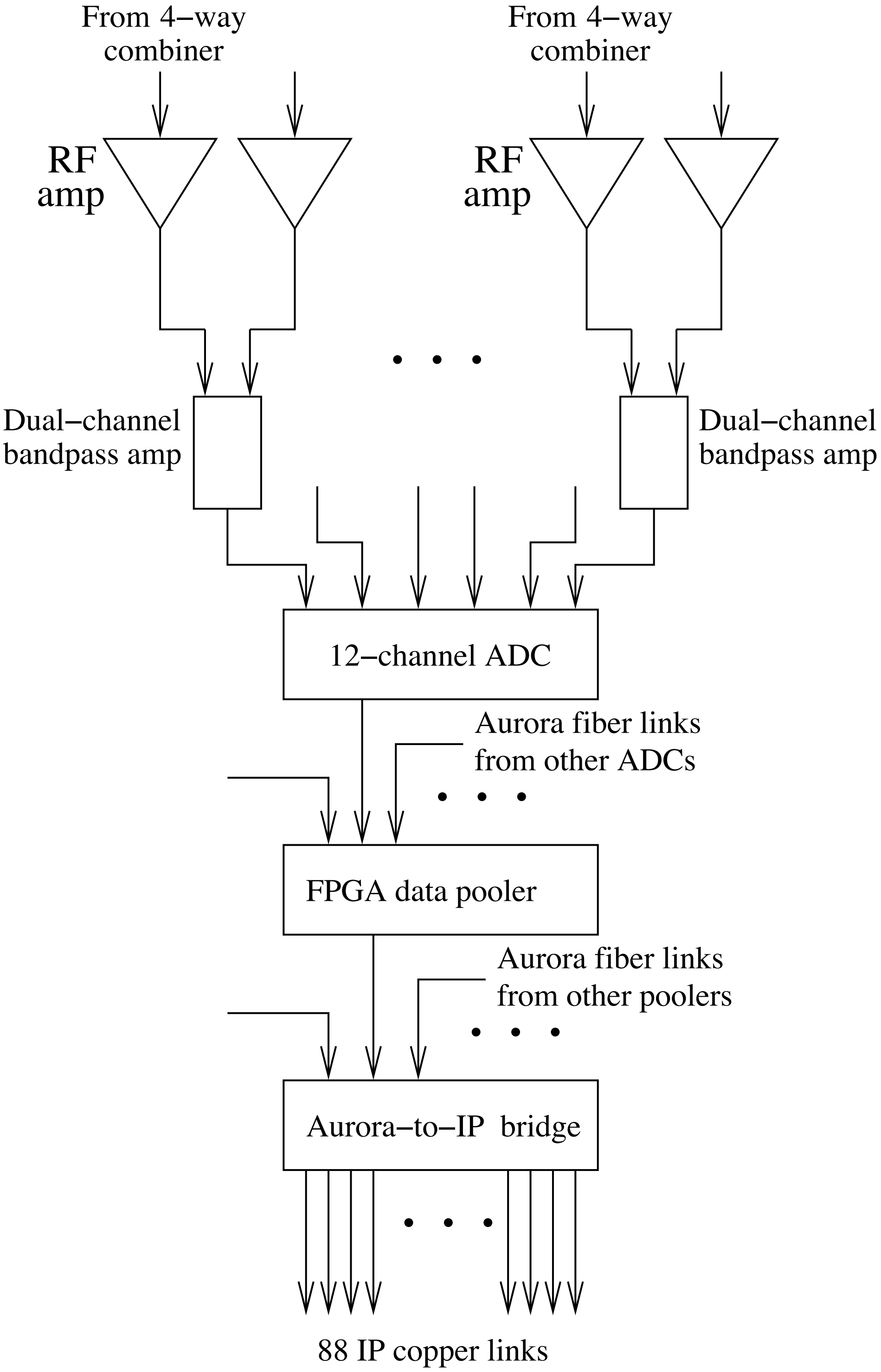

Figure 2.8: The block-level architecture of the OWFA system.

pling timestamps so that they can be sorted before final processing. Equivalently, they can be held in a buffer large enough to enable writing time-ordered cross-correlation data into the disks.

Historically, the upgraded ORT was envisaged to function as two independent interferometers with different fields of view and bandwidhts. These were to be called Phase-I and Phase-II, with a north-south FoV of 4.5° and $\sim 28°$ respectively. Being independent systems, they were to have a bandwidth of 16 MHz and 39 MHz respectively. The Phase-I system is currently not in use; however it is described here briefly for historical completeness and for setting the context for certain measurements presented in the following pages. In Phase-I, the signal from each half-module was digitised and correlated with other half-module signals. The anti-aliasing filter before sampling had a 16 MHz bandwidth. The measurements presented here were made for the Phase-I system. However, various improvements to the design have made the Phase-I system obsolete now. In a setup that we now call Mode-II, the signal from the four-way combiner is digitised. The pooler and bridge cards then collate the data as described above, and ship the IP packets to a high-performance cluster. But the functionality of Phase-I is not lost, as the data from Mode-II can be pooled once again to imitate a Phase-I-like system, which we now call Mode-I. A group of six contiguous Mode-II antenna (each of which is four dipoles) outputs can be summed coherently to imitate a Phase-I antenna, which we may recollect is the signal from 24 dipoles. This operation can happen entirely in software, thereby completely dispensing with the erstwhile Phase-I hardware. The advantage of the new arrangement is that, unlike Phase-I which gave a 16 MHz bandwidth, Mode-I retains the full 39 MHz bandwidth of the Mode-II system.

The Mode-I system, by virtue of having fewer "equivalent" antennas than the 264-antenna Mode-II system, produces ~ 50 times fewer correlations in the same time. Besides, it gives a smaller field of view (FoV): about one-sixth of that of the Mode-II system. The Mode-I system can hence be used as a pilot system to explore data handling methods, calibration, interference excision algorithms, foreground estimation and data characterisation. Experience with these aspects on the smaller-scale Mode-I will hopefully prepare us for the much larger data volumes expected from the Mode-II system.

2.2.2 Motivation for the upgrade

2.2.2.1 Large instantaneous field of view

Having briefly described the architecture of the programmable receiver, it is important to justify the effort. The scientific and technical motivation for the upgrade will now be set out. The ORT operates at 327 MHz, which corresponds to $z \sim 3.35$ for the 21-cm HI line. At such large redshifts, it is impossible to detect the 21-cm HI emission from individual galaxies. The only recourse is hence to observe HI emission from a very large volume. Statistical detection therefore works through techniques like intensity mapping (Chang *et al.*, 2008, 2010), wide field imaging (Zaroubi *et al.*, 2012) or power spectrum estimation (see e.g. Bharadwaj & Sethi, 2001; Zaldarriaga *et al.*, 2004; Bharadwaj & Ali, 2005). One of the fundamental requirements for statistical detection is a large field of view. This leads us to exploit the christmas-tree structure of the passive combiner network at the ORT: it is possible to obtain a large FoV - $\sim 28°$ - by tapping the RF signal higher up in the tree. We will return to the rationale of tapping at the output of the four-way combiner shortly, but after a brief digression.

2.2.2.2 Instantaneously redundant baselines

We saw in Section 2.2 that 264 RF signals would be available in the Mode-II system. These antennas are regularly spaced at 1.92 m. If the antennas are counted pairwise, it results in $\sim 34,000$ baselines. But most of these measurements are highly redundant, because there arise multiple instances of the same antenna pair separation that identically sample the same Fourier mode in the plane of the sky. Infact, only 263 unique measurements of the sky are possible. This enormous redundancy allows us to coherently sum the visibilities from all the instances of a baseline, leading to increased signal-to-noise ratio (SNR). Besides, redundancy is a great advantage for precision calibration, a topic that will be detailed in Chapter 4.

Now, to return to the rationale of tapping the output of the four-way combiner: if we were to correlate the signals from every dipole pair, it would result in half a million baselines. Although the higher degree of redundancy is tempting, processing the humongous amounts of data is a computational nightmare: it is both time- and power-consuming, to say the least about the requisite computing infrastructure. Being sensitive to all the radiation from horizon to horizon is indeed an incentive, but practical considerations must necessarily outweigh these attractions. The four-way combiner provides a 0.5 radian FoV, and still keeps the data volumes sufficiently tractable. Tapping the signals further downstream of course takes a huge stress off the computing system, but results in a smaller redundancy and a smaller FoV. Current high-performance computing technology allows the data volumes expected from the 264-antenna configuration to be handled within a reasonable cost. A future upgrade could perhaps consider tapping the signals at each dipole. The flexibility required to obtain smaller FoVs and data rates could then be part of an intelligent programmable receiver that allows collating the signals at a later stage to a comfortable level. This is now indeed the case, and the architecture is described in much greater detail in Prasad & Subrahmanya (2011). Therefore, the 264-antenna system is a trade-off between feasibility and scientific returns.

2.2.2.3 Instantaneously coherent visibilities

An aperture synthesis interferometer simulates a large telescope as the earth rotates, tracing loci on the uv plane. It is easy to see that to achieve better uv coverage through earth rotation synthesis, east-west antenna separations are needed. In addition north-south baselines allow imaging of sources near $\delta = 0^\circ$. Since OWFA is a north-south array and equatorially mounted, it samples the Fourier modes on the sky at fixed "points" on the uv plane. The visibilities can therefore be summed coherently. This is not possible in an earth rotation synthesis telescope, where each baseline's (u, v) co-ordinates change with time. Normally, the data are gridded on the uv plane, and the visibilities from within annuli of width $\mathbf{\Delta u} = \sqrt{\Delta u^2 + \Delta v^2}$ are summed incoherently. Coherent summation is an advantage as it results in higher SNR for the same quantity of data. Since the gradual changes in the visibility amplitude associated with earth rotation are absent, it is easier to identify time-variable radio frequency intereference (RFI), for example. A similar argument can be applied to radio transients in the sky. However, the price paid is the highly diminished number of Fourier modes otherwise possible through earth rotation aperture synthesis.

2.3 Sensitivity measurements

In this section, some important terms that are useful in a general radio astronomical context, like antenna and system temperature, sensitivity and gain shall be introduced. An exercise that allowed us to measure the bandshapes and sensitivity of the system is described and the results are presented.

2.3.1 Antenna and system temperature

Radio signals from celestial sources are extremely weak. To collect as much power as possible from these sources in a short time, a radio telescope must have a large collecting area and bandwidth. The electromagnetic field at the focus of the telescope excites electrical voltage fluctuations in the dipoles placed there. This input power to the telescope can be replaced by an equivalent resistor at the terminals kept at a particular temperature T_a. This temperature T_a, called the *antenna temperature*, is the physical temperature of the resistor that would feed the same amount of power at the input terminals of the antenna as the celestial radio source. Mathematically, we would write it as

$$\frac{1}{2}\; S\; A_{\mathrm{eff}}\; \Delta\nu = k_{\mathrm{B}}\; T_{\mathrm{a}}\; \Delta\nu \tag{2.1}$$

per polarisation, where S is the flux density of the source, A_{eff} is the effective collecting area of the radio telescope, T_{a} is the antenna temperature, k_{B} is the Boltzmann constant and $\Delta\nu$ is any frequency interval over which the measurement is made. The factor $\frac{1}{2}$ accounts for the single polarisation being considered here. A higher value for T_{a} means larger input power at the terminals of the telescope. This is the reason why radio telescopes are designed and built with ever increasing collecting areas. Even in the absence of radiation from a celestial source reaching the radio telescope, some power is available from the telescope. This is due to the thermal noise produced by the active and passive electronics, including the dipoles, cables, amplifiers and filters. This power can also be represented as an equivalent temperature called the *system temperature*, denoted by T_{sys}. The true equivalent temperature when looking at a celestial radio source is therefore $T_{\mathrm{a}} + T_{\mathrm{sys}}$.

The physical dimensions of ORT are 529 m in the north-south direction and 30 m east-west. The physical area is therefore 529m × 30 m. However, only a fraction η of the incident power is available at the focus. This is equivalent to having a smaller reflecting surface of area ηA in which all the incident power is available at the focus. This quantity ηA is called the effective area, denoted by A_{eff}, where η is the aperture efficiency. The ORT has an effective area of 8700 m^2 (Swarup *et al.*, 1971), giving an aperture efficiency of 55%. We can now compute the expected antenna temperature when looking at a radio source of known flux density, and hence the system gain. Consider a radio source in the beam of the telescope with a flux density of 1.0 Jy. Recalling equation 2.1, we have

$$\frac{1}{2}\;\times\;1.0\;\times\;10^{-26}\times\;8700\;=\;1.38\;\times\;10^{-23}\;\times\;T_{\mathrm{a}} \tag{2.2}$$

which gives $T_{\mathrm{a}} = 3.15$ K. The gain of the system is therefore 3.15 K/Jy. We must bear in mind that ORT is single polarised. Since this is the output of all 1056 dipoles phased together, the gain per dipole is $T_{\mathrm{a}} \sim 3$ mK/Jy. The signal-to-noise ratio determines the quality of a radio telescope. Therefore, certainly a more meaningful metric for radio telescopes is the quantity g/T_{sys}.

2.3.2 Measurements of the antenna parameters

Observations were made on 16th and 17th October 2011 to measure the sensitivity of a group 24 dipoles and to measure their usable 3-dB bandwidth. The specifics of the observations are outlined in this section. Details of the observations are given in Table 2.1.

Table 2.1: Details of the observations

S. No.	Date of observation	Target	Off-target	System
1	16-10-2011	Cygnus A	-2 h away in RA	Phase I - 24 dipoles - S03
2	17-10-2011	Sun	-2 h away in RA	Phase I - 24 dipoles - S03

The Phase-I system (now not is use) of the ORT programmable receiver employs direct bandpass sampling of the RF signal. A group of 24 phased dipoles comprises one input channel to the Phase-I digitiser (Prasad & Subrahmanya, 2011). Therefore, each RF channel corresponds to one half-module. Each Phase-I pillar takes 10 half-modules. There are four pillars for the Phase-I system, spaced five modules apart. These pillars are located under S08, S03, N03 and N08. The measurements of 16th and 17th Oct 2011 were made at the pillar under module S03. For each measurement shown in Table 2.1, the telescope was pointed at the target CygnusA and allowed to track. The power levels on the target and off-target ($2h$ away in hour angle) were recorded for each RF channel by disconnecting the input to the digitiser and connecting the same to the RF input of the spectrum analyser.

2.3.3 Results from the measurements

The ratio of on-source to off-source RF power is

$$a = \frac{T_{\mathrm{a}} + T_{\mathrm{sys}}}{T_{\mathrm{sys}}} \tag{2.3}$$

This ratio can be obtained from the deflection measurements by inverting

$$D = 10\ log_{10}(a). \tag{2.4}$$

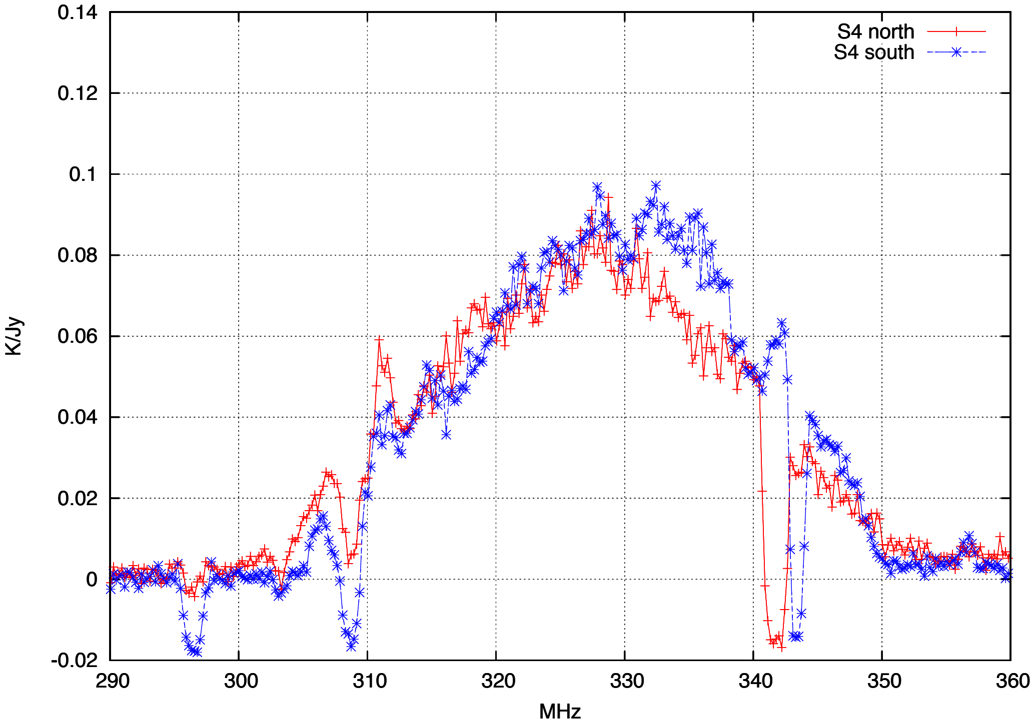

Figure 2.9: An example plot of the sensitivity of the two half-modules of the Phase-I S04 antennas

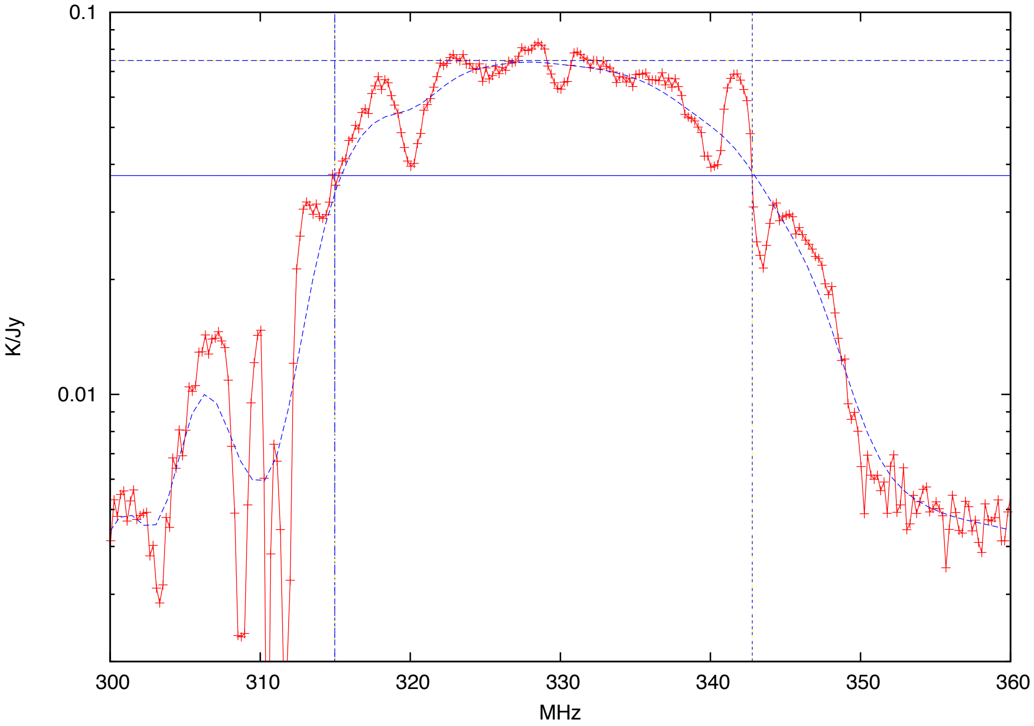

Figure 2.10: Mean sensitivity across the band for the Phase-I RF system for all the half-modules from S01 to S05 measured in the pillar S03.

where

$$D = P_{\text{on}} - P_{\text{off}} \tag{2.5}$$

If the flux of the source is known, the sensitivity of the system per polarisation is

$$g = \frac{(a-1)T_{\text{sys}}}{\frac{1}{2}S} \quad \text{K/Jy} \tag{2.6}$$

where $T_{\text{sys}} = 150$ K, measured independently (Joshi *et al.*, 1988). As an example, the sensitivity as a function of bandwidth is shown for the two half-modules of S04 is in Figure 2.9.

Table 2.2: Peak sensitivity of the Phase-I half-modules in S03

S. No.	Dipole group	Peak sensitivity - K/Jy
1	S1 North	4.83×10^{-2}
2	S1 South	1.07×10^{-2}
3	S2 North	6.77×10^{-2}
4	S2 South	9.42×10^{-2}
5	S3 North	4.32×10^{-2}
6	S3 South	2.53×10^{-2}
7	S4 North	8.21×10^{-2}
8	S4 South	8.54×10^{-2}
9	S5 North	9.82×10^{-2}
10	S5 South	8.30×10^{-2}

The Phase-I mean peak sensitivity of 75 mK/Jy is close to the expected sensitivity of 72 mK/Jy (24 dipoles of 3 mK/Jy each). The mean sensitivity of the Phase-I system measured at the pillar under S03 is shown in Figure 2.10. Their 3-dB bandwidths are also shown in the figure: for the Phase-I system it is approximately 314 MHz to 343 MHz.

The deflection measurements for the Phase-I system were subsequently repeated for the Sun. Since the flux density of the Sun is not known reasonably well at any given time, these observations were not used for measuring the sensitivities. However, by using arbitrary flux units, the shape of the sensitive RF band can be ascertained. The observing procedure is identical to that followed earlier for Cygnus A. The recorded spectra were analysed to obtain the deflection band shapes. The deflection and the bandshapes recorded on the observations on Sun are shown in Figures 2.11 and 2.12.

2.3.4 Television Interference Lines

Television transmission lines appear in the RF band of Phase I because of the increased bandwidth. These lines appear at 311 MHz and 343.25 MHz. The strength of these lines varies with the time of the day and telescope pointing. Shown below in Figure 2.13 are plots of these lines. These lines are often pronounced during evening hours and persistent throughout the day. However, we expect to be able to negotiate with the district officials for moving the TV carrier frequencies to some other sub-band.

2.4 Electromagnetic coupling between the dipoles

This section describes an experiment to measure the coupling between dipoles.

Consider a linear array of dipoles, without regard to their polarisation alignment. Consider two dipoles p and q, separated by a distance d. The array is observing the sky. Coupling could manifest in two ways:

- A fraction of the response of dipole p to the radiation from the sky is re-radiated to the surroundings, which dipole q picks up.
- A fraction of the self-generated noise from the front-end electronics (such as the low-noise amplifier) of dipole p is radiated, which is picked up by dipole q.

2.4.1 Coupling measurements

All measurements were done at the Phase-I pillar at S03. The Phase-I RF setup at the four pillars is as follows: each half-module RF output is tapped just before the last two-way combiner. Each pillar has ten RF inputs to the analog-to-digital converter, one from each half module and five on each side of the pillar. For S03, the half-modules are labelled S01N, S01S, S02N, S02S and so on upto S05S. Each half-module combines 24 dipoles through a combiner network.

The most direct method of measuring coupling is by measuring the output power at dipole q when dipole p is supplied with a known input power. Dipole-30 was disconnected from the downstream RF electronics and injected with a CW signal. Output power was measured at succesively further dipoles. Table 2.3 gives the numbers. Coupling as a function of distance is also given as a plot in Figure 2.15.

Dipole distance	Power - dBm
0	0
1	-19
2	-21
3	-24.7
4	-33.7

Table 2.3: Raw isolation between dipoles as a function of distance between the dipoles, also shown in Figure 2.15.

2.4.2 Results

The numbers in Table 2.3 reflect the low level of coupling between the dipoles in the ORT. The coupling between the nearest neighbours, which is of interest to us, is about -20 dB, or at the level of about 1%. At the fourth dipole away from the transmitter, it is already down to 0.05 %.

2.5 OWFA parameters for the HI experiment

Some numbers relevant to the OWFA HI experiment will be derived in this section and these will be used in several instances throughout the thesis. These numbers are derived for the ΛCDM model of cosmology, using the cosmological parameters from Planck results (Planck Collaboration *et al.*, 2014). OWFA will operate in two modes - as a 40-element interferometer in Mode-I and as a 264-element interferometer in Mode-II. The bandwidth of operation in both modes is 39 MHz. As the first step, let us compute the transverse and line-of-sight comoving scales. The redshift of access for OWFA, at 326.5 MHz, is

$$z = \frac{\lambda_{\rm e}}{\lambda_{\rm obs}} - 1 = \frac{1420.405}{326.5} - 1 = 3.35 \tag{2.7}$$

$\lambda_{\rm e}$ and $\lambda_{\rm obs}$ are respectively the rest frame and observed wavelength of the HI 21-cm emission. The transverse comoving scale at this redshift can be computed as

$$D(z) = \frac{c}{H_0}\int_0^z \frac{1}{\sqrt{\Omega_\Lambda + \Omega_0(1+z)^3}} \quad \simeq \; 6700 \text{ Mpc} \tag{2.8}$$

where the curvature term Ω_k has been omitted by setting it to zero. Ω_0 is the matter fraction, set here by taking $\Omega_0 = 1 - \Omega_\Lambda$. H_0 is the Hubble parameter given by

$$H_0 = \sqrt{\frac{8\pi\rho_c G}{3}} \tag{2.9}$$

whose value from Planck Collaboration *et al.* (2014) is 67.9 $\mathrm{km\,s^{-1}\,Mpc^{-1}}$. The dark energy fraction $\Omega_\Lambda = 0.7$ and therefore the matter fraction $\Omega_0 = 0.3$. The redshift space scale r'_ν can be easily derived by computing the line of sight comoving scale corresponding to a unit bandwidth:

$$r'_\nu = 11.34\ \mathrm{Mpc\,MHz^{-1}} \tag{2.10}$$

The wavenumber interval $\mathbf{k}$ can be computed separately for the transverse and the line-of-sight components. The transverse wavenumber $\mathbf{k}_\perp$ is given by

$$\mathbf{k}_\perp = \frac{2\pi\mathbf{U}}{D(z)} \tag{2.11}$$

and the line-of-sight wavenumber $k_\parallel$ is given by

$$k_\parallel = \frac{2\pi\eta H(z)}{(1+z)\lambda_{\mathrm{obs}}} \tag{2.12}$$

where η is the lag between two frequencies ν_i and ν_j separated by $\Delta\nu$, given by

$$\eta = \frac{1}{\Delta\nu} = \frac{1}{|\nu_i - \nu_j|} \tag{2.13}$$

For Mode-I, the shortest baseline is $\mathbf{U}_{\mathrm{min}} = 12.5\lambda$ and the longest is $\mathbf{U}_{\mathrm{max}} = 487.5\lambda$. For Mode-II, these numbers are $\mathbf{U}_{\mathrm{min}} = 2.1\lambda$ and $\mathbf{U}_{\mathrm{max}} = 548.9\lambda$ respectively. The wavenumber range for the two modes can be computed by plugging in these numbers, and a bandwidth of 39 MHz, which produces the smallest lag and consequently the smallest wavenumber $k_\parallel$. The largest $k_\parallel$ that represents the highest frequency mode is set by the largest lag produced by the smallest separation of two frequencies between two adjacent channels. Therefore, there is some choice in the maximum LOS wavenumber $k_\parallel$ through the number of channels within the band. The interferometric sensitivity can be computed for OWFA for the 39-MHz bandwidth split into N channels. The measured system temperature $T_{\mathrm{sys}} = 150$ K. The real (or imaginary) part of the rms noise fluctuation is

$$\sigma_{ab} = \frac{\sqrt{2}k_B T_{\mathrm{sys}}}{\eta A\sqrt{\Delta\nu\Delta t}} \tag{2.14}$$

per channel, where k_B is the Boltzmann constant, η is the aperture efficiency, $A = b \times d$ is the aperture area, $\Delta\nu = B/N$ the channel width and Δt the integration time. The numbers are summarised in Table 2.4.

Parameter	Notation	Mode-I	Mode-II
Antennas	$N_{\rm A}$	40	264
Transverse comoving dimension	D(z)	6.67 Gpc	6.67 Gpc
Shortest baseline	$\mathbf{U}_{\rm min}$	12.5λ	2.1λ
Longest baseline	$\mathbf{U}_{\rm max}$	487.5λ	548.9λ
Minimum transverse wavenumber	$k_{\perp}^{\rm min}$	1.1×10^{-2} Mpc^{-1}	2.0×10^{-3} Mpc^{-1}
Maximum transverse wavenumber	$k_{\perp}^{\rm max}$	4.6×10^{-1} Mpc^{-1}	5.2×10^{-1} Mpc^{-1}
Minimum LOS wavenumber	$k_{\parallel}^{\rm min}$	1.4×10^{-2} Mpc^{-1}	1.4×10^{-2} Mpc^{-1}
Maximum LOS wavenumber (768-channel)	$k_{\parallel}^{\rm max}$	11.2 Mpc^{-1}	11.2 Mpc^{-1}
Maximum LOS wavenumber (312-channel)	$k_{\parallel}^{\rm max}$	4.6 Mpc^{-1}	4.6 Mpc^{-1}
Single visibility noise rms	$\sigma_{\rm ab}$	6.3 Jy	37.6 Jy

Table 2.4: OWFA parameters pertinent to the cosmology experiment. The maximum value for $k_{\parallel}$ depends on the number of channels.

2.6 Summary

The ORT is being upgraded to operate as an interferometer. Being an equatorial mounted, north-south telescope, it gives no east-west baselines. An earlier 16-MHz, 40-antenna version of the interferometer, called Phase-I, is currently not in use. Instead, the 39-MHz 264-antenna Mode-II interferometer can provide the same functionality of the 40-antenna Phase-I system but with an improved bandwidth. This functionality is to be achieved in software, and it is called Mode-I. The Mode-I system will serve as a proof-of-concept design of the larger and more demanding Mode-II. The enormous number of redundant baselines is advantageous for the cosmology experiment as it enables coherent summation of visibilities and robust redundancy calibration. The wide FoV offers a crucial advantage for studying the large-scale structure, but brings with it its own challenges, which will be addressed in Chapter 6. This thesis restricts its study entirely to the 40-antenna Mode-I system.

2.7 Acknowledgements

I gratefully acknowledge the help received from D. Nandagopal, E. Elamathi, P .K. Manoharan and Jayaram Chengalur for the measurements made on 16 and 17 October 2011. The coupling measurements were made on 13 and 14 October 2014. Help from Amit Mittal, Kalyanasundaram, Arun Varghese and Magesh is acknowledged. I thank the telescope operators who helped with all of these observations.

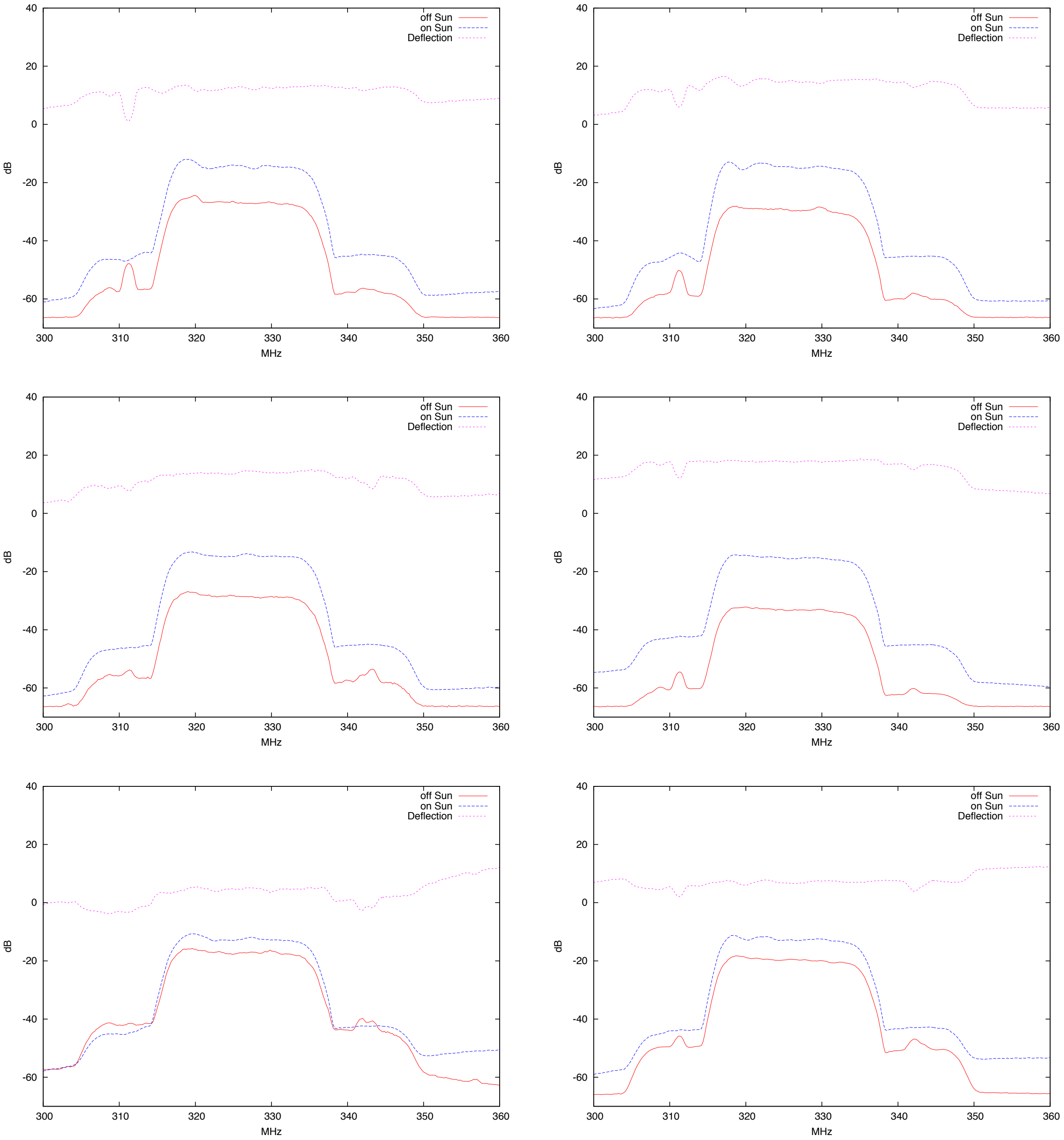

Figure 2.11: Deflections of Phase-I half-modules at S03 pillar measured on Sun: half modules in S1, S2 and S3.

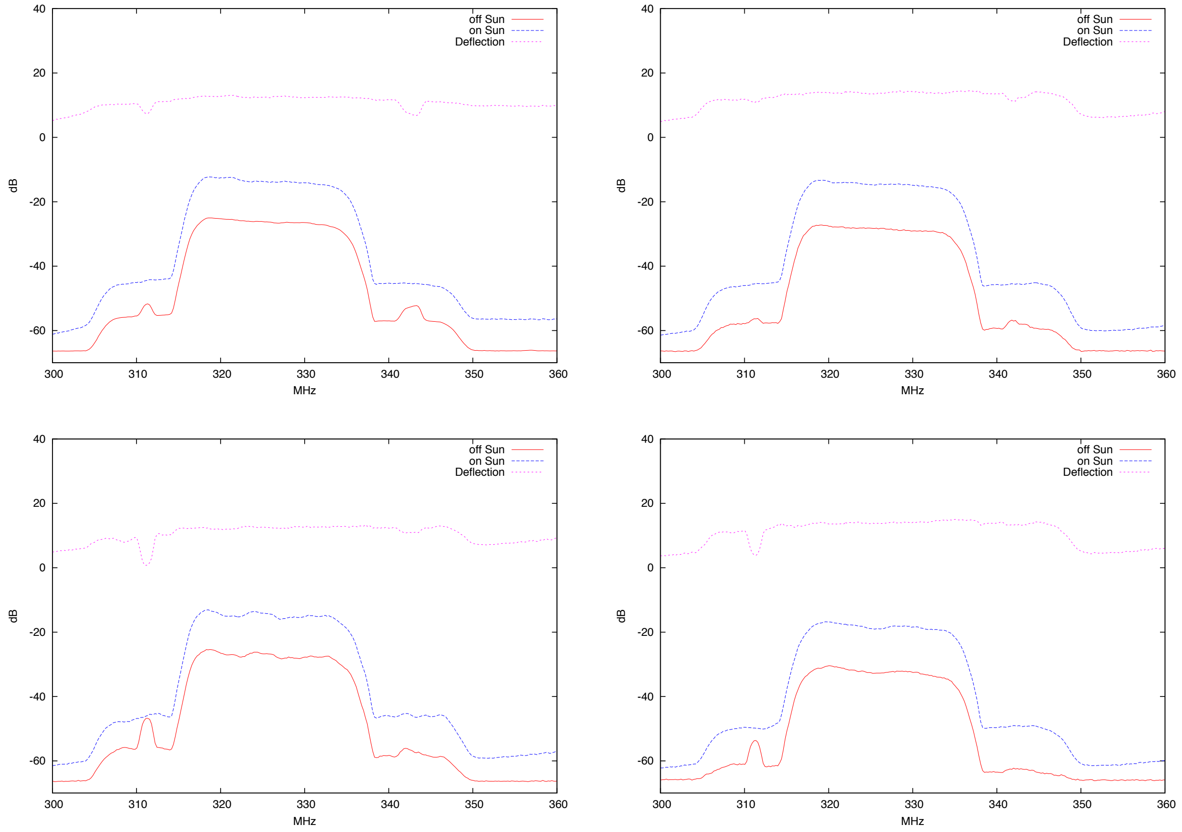

Figure 2.12: Deflections of Phase-I half-modules at S03 pillar measured on Sun: half modules in S4 and S5.

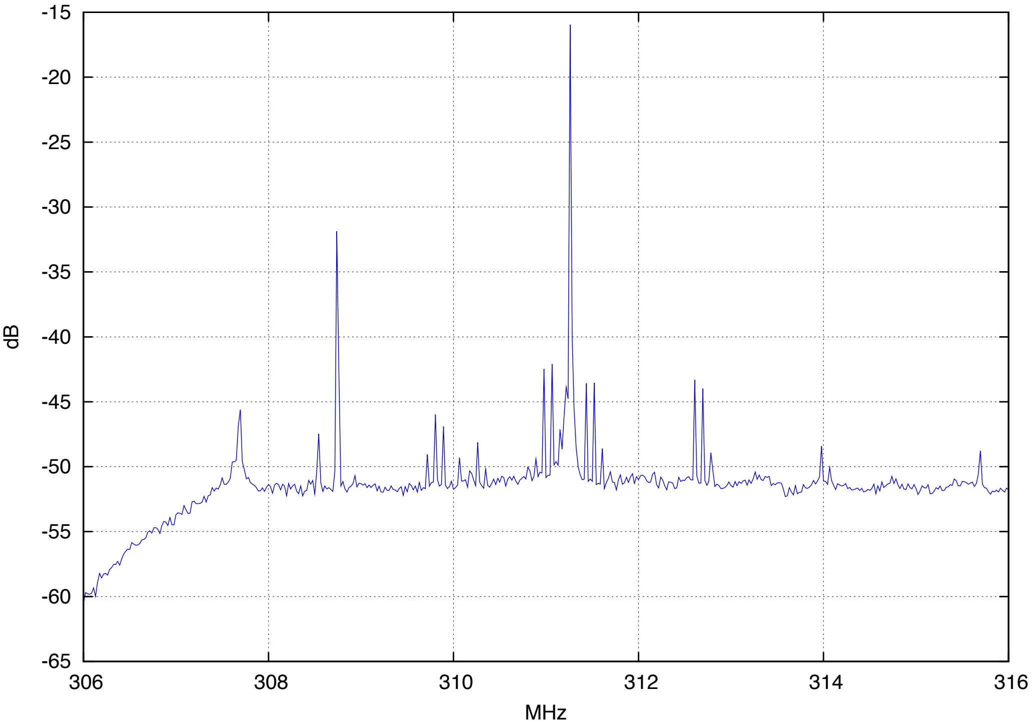

(a) TV line at 311 MHz

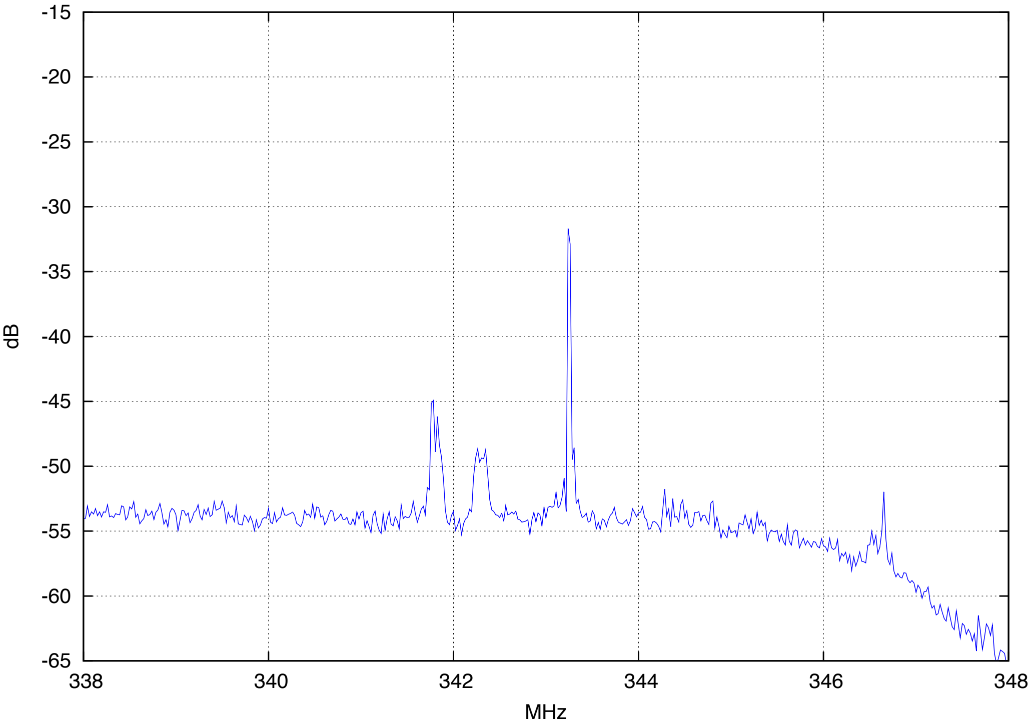

(b) TV line at 343.25 MHz

Figure 2.13: Magnified views of the television interference lines at 311 MHz and 343.25 MHz

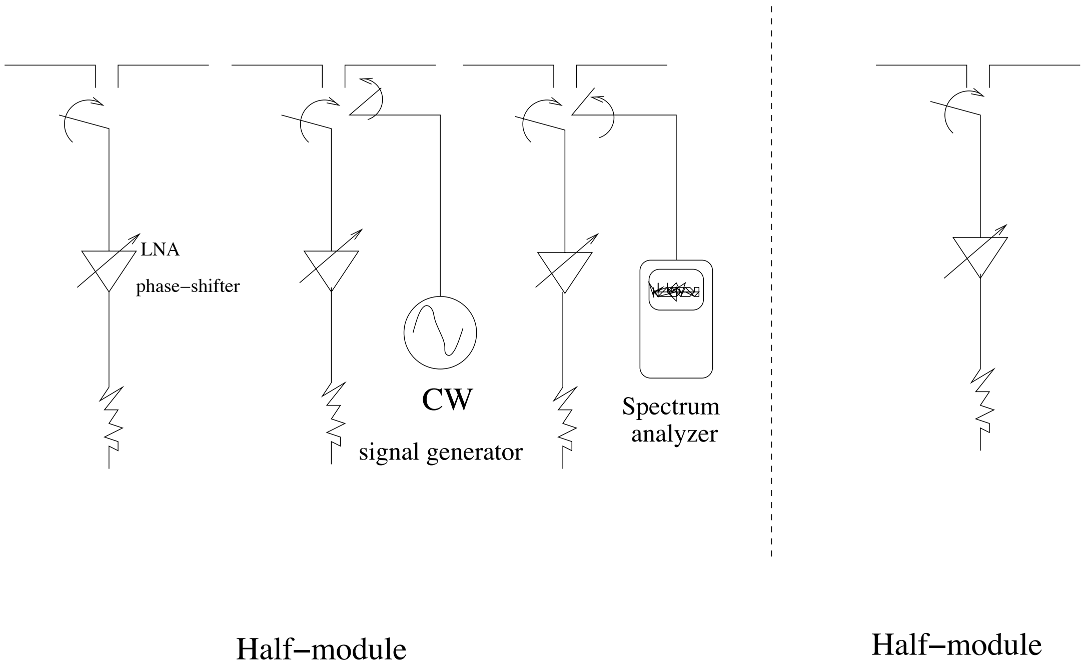

Figure 2.14: A schematic of the experimental setup for measuring the electromagnetic coupling.

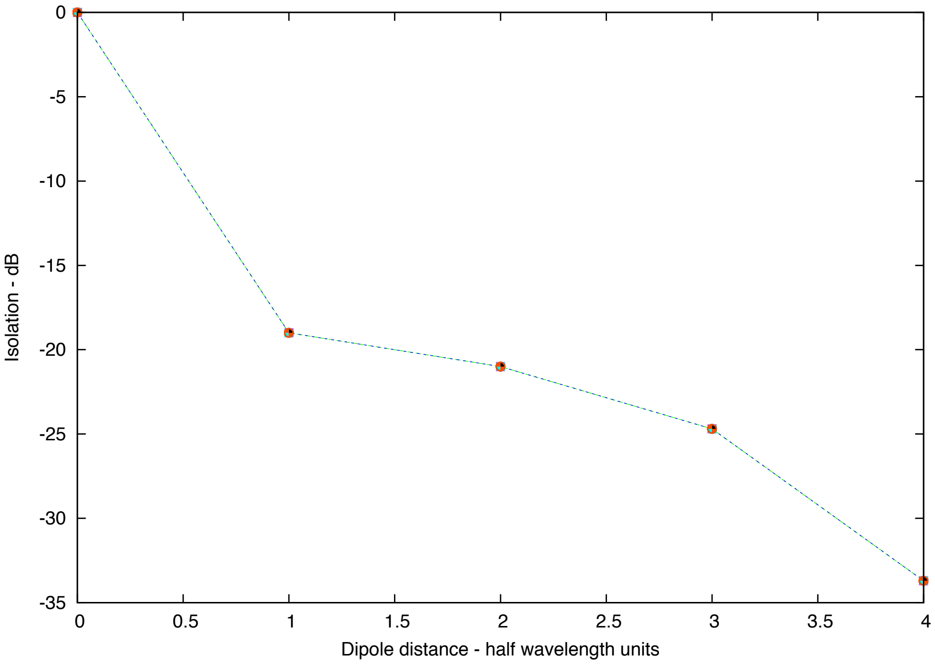

Figure 2.15: Electromagnetic isolation as a function of distance from a dipole shown as a plot of the Table 2.3.

Chapter 3

A software model for OWFA

One of the principal aims of the upgrade of the ORT to OWFA (Prasad & Subrahmanya, 2011; Subrahmanya *et al.*, 2016a,b) is to enable the detection of HI emission from large scale structures in the early universe, i.e. at redshifts ~ 3. Theoretical calculations of the expected emission tuned to the projected parameters of OWFA indicate that the telescope should have sufficient sensitivity to detect the power spectrum of the redshifted HI 21-cm emission, in integration times of a few hundred hours (Ali & Bharadwaj, 2014; Bharadwaj *et al.*, 2015; Sarkar *et al.*, 2016a). Currently, a number of experiments are in various stages of progress that aim to directly detect the brightness temperature fluctuations δT_b of the 21-cm post-reionisation cosmological signal, like CHIME (Bandura *et al.*, 2014), BAOBAB (Pober *et al.*, 2013b) and the Tianlai CRT (Chen, 2011; Xu *et al.*, 2015). These experiments would each operate at different frequency ranges; BAOBAB has been proposed to specifically detect the BAO feature in the redshifted HI 21-cm line in the 600-900 MHz band. The Tianlai CRT also is gearing up to detect the BAO features and constrain dark energy through redshifted HI 21-cm observations in the 700-1400 MHz band (Chen, 2011; Xu *et al.*, 2015). CHIME would overlap with both these experiments in the range $\sim 400-800$ MHz. The OWFA cosmology experiment is expected to fill a significant gap in understanding the evolution of post-reionisation neutral hydrogen at large scales in an important redshift interval of $z \sim 3.35$.

While the raw sensitivity of the telescope would be sufficient to detect the HI emission from redshifts $z \sim 3.35$ (Ali & Bharadwaj, 2014; Bharadwaj *et al.*, 2015), the expected signal is many orders of magnitude fainter than the other astrophysical signals, i.e. the "foregrounds" (see e.g. Di Matteo *et al.*, 2002; Santos *et al.*, 2005; Ali *et al.*, 2008). These include emission from the diffuse ionised galactic interstellar medium ("diffuse Galactic synchrotron emission" and "galactic free-free emission") and emission from the extragalactic radio sources (called "the extragalactic foreground") that the telescope is sensitive to. Many instrumental effects come into play when the signal of interest is buried in several orders of magnitude brighter foregrounds: systematics introduced by uncalibrated antenna gains, interference from terrestrial sources and effects of the complex intrinsic interaction between the instrument and the foregrounds, due to the chromatic response of the telescope, are thought to be the dominant contributors. A good understanding of all of these issues is required to enable a robust prediction of the cosmological signal that could be detected through observations with OWFA.

The first step to understanding the instrumental systematics is to develop a thorough understanding of the instrument itself, and capture it in a software model that would include all the expected instrumental effects. All of the astrophysical signals (e.g. the diffuse Galactic and the extragalactic point source foregrounds) can then be suitably parametrized and included in the model. One of the expected by-products of the exercise to detect the cosmological HI signal is a better understanding of some of the foregrounds, particularly of the diffuse Galactic foreground, which is the dominant foreground from within the Galaxy. The diffuse Galactic foreground emission is of interest in itself (see e.g. Iacobelli *et al.*, 2013a,b, 2014). The ability to characterise the foregrounds and the fundamental limitations set by the instrument are both crucial to enable realistic predictions for the redshifted HI 21-cm detection. The software model described in this chapter was developed in order to help better understand the systematics, as well as devise methods to devise foreground characterisation and subtraction methods.

3.1 The rationale for a software model

The OWFA HI experiment is a challenging one in terms of both the special hardware requirements as well as the methods and algorithms that would eventually enable us to measure the HI power spectrum. A significant component of the design of an experiment, especially in modern low frequency radio cosmology, has been the investment in simulating the instrument and the experiment itself based purely on a software model. The results from simulations can often influence the course of the experiment through valuable insight. This has been the driving philosophy for a simulator based on a software model for the OWFA HI experiment.

For OWFA, traditional interferometric data analysis software packages are not useful as they do not provide sufficient functionality for redundancy calibration, or for the final processing which, in this case, is not imaging. A complete software suite has been developed consisting of several standalone programs that serve two simultaneous purposes:

- to simulate visibilities as obtained from OWFA, based on the instrument and sky description. The instrument description should naturally lead to all the effects and systematics that are expected to be present in an actual interferometric observation. Simulated data can provide a test bed for devising and refining RFI mitigation algorithms, calibration algorithms and statistical estimators for signal characterisation, etc.

- to function as the observatory software pipeline that is used to process real data from the telescope, so that the simulations above inform us to refine and adopt optimal strategies for working with real data.

Given that a software model for the telescope and the sky would serve as a very useful guide to the experiment, the preliminaries needed for describing the emulator in some detail are set out, and its various features listed with examples.

3.2 The programming philosophy

The software suite that has been developed for OWFA simulations is a C-based collection of utilities and algorithm implementations. Visualisation of data is almost the first step in data handling and a standard format definition should therefore be the first choice. The suite was conceived from the early days as one that would grow organically to accommodate observatory needs. Therefore, the choice was to adhere to an international standard for the visibility data, so that a team of astronomers stationed in widely separated geographical locations can handle these data using this software suite. The following considerations were kept in mind during the development of the emulator.

- The Flexible Image Transport System (FITS; Wells *et al.* 1981) or the Measurement Set (MS; Kemball & Wieringa 2000) format definition were the obvious formats to choose from. A FITS file can be converted to MS using readily available tools. Given the popularity that FITS enjoys and the number of FITS tools available, like cfitsio, ds9 and fv (to name a few), it was but natural to choose it. Therefore the programs were developed around the FITS format for easy data portability. Besides, the fact that it is the data format at the GMRT and hence is familiar to astronomers both within NCRA and users of the GMRT played a significant role in the decision to adopt FITS.

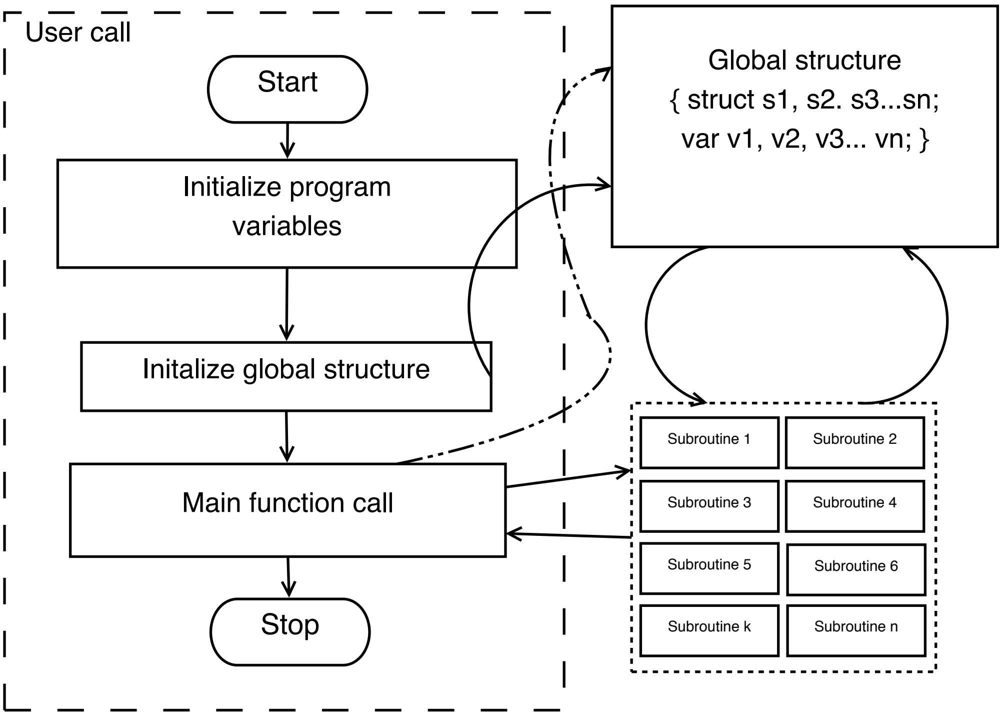

Figure 3.1: The general model for each program in the OWFA simulator suite

- The second major factor was the ability to add new utilities to the suite by anyone familiar with the FITS definition. Therefore, the suite comes with a very rich set of subroutine functions that do standard operations in a transparent manner. A new utility that has to operate on the FITS data at the level of individual records can hence draw on this library of subroutines.

- Finally, a high level of ease with which utilities can be added to the suite is achieved by making the chore of passing arguments to function calls a trivial operation. Instead of passing specific arguments to functions, the pointer to a global superstructure is passed uniformly to all function calls. The superstructure itself is a structure of many structures, which are defined in different header files depending on their functionality. Therefore, a new user would be able to add his or her own function definition to the existing subroutines without fussing too much about passing the right argument.

Figure 3.1 captures the spirit of the programming philosophy. The main call merely initialises a few variables specific to the program. Subroutines, variables and structures are segregated according to their functionality and defined in appropriate header files. Similarly, subroutine functions are defined in functionally separable C program files. For example, all function definitions related to the instrument are available in the

inc/sysdefs.h and **src/syssubs.c** files. FITS-related definitions and structures are to be found in **inc/fitsdefs.h** and **src/fitssubs.c** files. Sky simulations are grouped under **inc/skydefs.h** and **src/skysubs.c**. Mathematical function definitions and structures are grouped under **inc/matdefs.h** and **src/matsubs.c**. The global superstructure, which holds all the variables and structures, is defined to be of type **ProjParType** in **inc/sysdefs.h**.

3.3 Prowess - a Programmable OWFA Emulator System

The software suite is given the name "Programmable OWFA Emulator System" (**Prowess**), and it is self-explanatory. Programmable, because adding new utilities or functionality is made easy as described in the previous section, and the emulator is specific to OWFA. The preliminaries required to capture the instrument in a software model are now described.

3.3.1 Antennas and baselines

OWFA (Subrahmanya *et al.*, 2016a,b) would operate in two concurrent modes - Mode-I and Mode-II. Mode-I is a 40-antenna interferometer and Mode-II is a 264-antenna interferometer. The aperture is a $\sim$ 530 m long cylinder that is 30 m wide. Given the christmas-tree network, this long aperture would function as a multi-element system. The signal at the output of every four dipoles is digitised. The two interferometer modes provide two different aperture settings:

- Every group of 4 dipoles, or a sixth of a half-module, would operate as a single element in Mode-II. This corresponds to 1.92 m of the 530 m long cylinder, equivalent to 2λ. This results in 264 apertures throughout the length of the telescope.

- A software system coherently sums the signal from every group of six Mode-II elements to provide a second 40-antenna interferometer mode. This is equivalent to digitising every group of 24 dipoles, or a half-module, which constitutes a single element in Mode-I. This corresponds to 11.5 m of the 530 m long cylinder, equivalent to 12.5λ. This results in 44 apertures throughout the length of the telescope, but the peripheral 2 elements on each end of the telescope are ignored, giving a total of 40 elements.

```
#AntId    Ant     bx     by      bz     ddly    fdly
#------------------------------------------------------------
ANT00    N10N    0.0    0.0    10.0      0.0     0.0
ANT01    N10S    0.0    0.0    21.5      0.0     0.0
ANT02    N09N    0.0    0.0    33.0      0.0     0.0
ANT03    N09S    0.0    0.0    44.5      0.0     0.0
ANT04    N08N    0.0    0.0    56.0      0.0     0.0
ANT05    N08S    0.0    0.0    67.5      0.0     0.0
ANT06    N07N    0.0    0.0    79.0      0.0     0.0
ANT07    N07S    0.0    0.0    90.5      0.0     0.0
ANT08    N06N    0.0    0.0   102.0      0.0     0.0
ANT09    N06S    0.0    0.0   113.5      0.0     0.0
ANT10    N05N    0.0    0.0   125.0      0.0     0.0
ANT11    N05S    0.0    0.0   136.5      0.0     0.0
ANT12    N04N    0.0    0.0   148.0      0.0     0.0
ANT13    N04S    0.0    0.0   159.5      0.0     0.0
ANT14    N03N    0.0    0.0   171.0      0.0     0.0
ANT15    N03S    0.0    0.0   182.5      0.0     0.0
ANT16    N02N    0.0    0.0   194.0      0.0     0.0
ANT17    N02S    0.0    0.0   205.5      0.0     0.0
ANT18    N01N    0.0    0.0   217.0      0.0     0.0
ANT19    N01S    0.0    0.0   228.5      0.0     0.0
ANT20    S01N    0.0    0.0   240.0      0.0     0.0
ANT21    S01S    0.0    0.0   251.5      0.0     0.0
ANT22    S02N    0.0    0.0   263.0      0.0     0.0
ANT23    S02S    0.0    0.0   274.5      0.0     0.0
ANT24    S03N    0.0    0.0   286.0      0.0     0.0
ANT25    S03S    0.0    0.0   297.5      0.0     0.0
ANT26    S04N    0.0    0.0   309.0      0.0     0.0
ANT27    S04S    0.0    0.0   320.5      0.0     0.0
ANT28    S05N    0.0    0.0   332.0      0.0     0.0
ANT29    S05S    0.0    0.0   343.5      0.0     0.0
ANT30    S06N    0.0    0.0   355.0      0.0     0.0
ANT31    S06S    0.0    0.0   366.5      0.0     0.0
ANT32    S07N    0.0    0.0   380.0      0.0     0.0
ANT33    S07S    0.0    0.0   389.5      0.0     0.0
ANT34    S08N    0.0    0.0   401.0      0.0     0.0
ANT35    S08S    0.0    0.0   412.5      0.0     0.0
ANT36    S09N    0.0    0.0   424.0      0.0     0.0
ANT37    S09S    0.0    0.0   435.5      0.0     0.0
ANT38    S10N    0.0    0.0   447.0      0.0     0.0
ANT39    S10S    0.0    0.0   458.5      0.0     0.0
#END
```

Figure 3.2: The antenna definition file Antenna.Def.40 for Mode-I of the OWFA interferometer.

To begin with, the emulator has to be initialised with the antenna positions. This is done through an input Antenna Definition file, “Antenna.Def.40” for Mode-I and “Antenna.Def.264” for Mode-II. The parsing section of the code then figures out which of the two modes the telescope is being operated in. Accordingly, it sets the aperture dimensions. The user has the option to switch off certain antennas in the “Antenna.Def” file to simulate a situation when some antennas are not available. These are then omitted from the simulations as well as the output visibility data. This not only obviates the need to maintain a running log of the invalid antennas, but also eases memory and storage requirements. Figure 3.2 shows the antenna definition for Mode-I. The file has seven columns:

1. Column 1 shows the antenna identifier used by the FITS standard.
2. Column 2 is the antenna name; the name of each antenna is tied to its identifier. This helps in unambiguous bookkeeping even when switching off certain antennas.
3. Columns 3, 4 and 5 respectively give the antenna x, y and z co-ordinates in a right-handed co-ordinate system, which shall be described shortly.
4. Columns 6 and 7 respectively denote the delay in seconds, corresponding to the number of integer and fractional clock cycles offset with respect to a reference antenna. At the moment, these fields are not being used, hence their values are all set to zero. In practice, these would represent the fixed delays arising from differences in cable and optical path lengths. Therefore they can be measured reasonably accurately.

Since the dipoles are regularly spaced, the equivalent apertures in Mode-I and Mode-II are also regularly spaced. This results in an interferometer in which the separation between any pair of apertures is an integral multiple of the shortest separation between adjacent apertures,

$$d_{\mathrm{n}} = nd \tag{3.1}$$

where d is the both the size of the aperture as well as the shortest spacing. The 40-antenna Mode-I has twenty half-modules in the northern half and twenty in the southern half. The northern modules are named N01 to N10 outwards from the mid-point of the telescope, and similarly the southern modules. The two half-modules within each module are given a “N” or “S” identifier. The antenna definition file is parsed and the values are stored in the antenna structure within the superstructure (**ProjParType**).

In the co-ordinate system chosen for OWFA, the antennas are placed along the z-axis. Each antenna i is assigned a complex, frequency-dependent, electronic gain g_i, obtained as a random complex number distributed around a mean gain $|g|$, referred to the central frequency ν_0. The observing band is split into N channels. The antenna structure initialization information is written out in a log called "ant-init.info". The real and imaginary parts of the complex gains, as well as its amplitude and phase (in degrees) at ν_0 are written out in the file. An example is shown in Figure 3.3.

Baselines are then obtained as antenna pairs, and each baseline is written into a structure that holds the baseline number, the participating antenna pair, the projected lengths of the baseline in three dimensions and its length in wavelength units at the reference frequency. A log of the baselines is written out to "baseline.info", part of which is shown in Figure 3.4. An N_A antenna interferometer results in ${}^{N_A}C_2$ baselines, giving 780 for Mode-I and 34716 for Mode-II. The baseline vectors are obtained from the physical antenna separations, defined at the central frequency ν_0 but at each channel it is appropriately scaled when computing the visibilities.

$$\mathbf{d}_{|a-b|} = \mathbf{x}_a - \mathbf{x}_b \tag{3.2}$$

$$\mathbf{U}_{|a-b|} = \mathbf{d}_{|a-b|}\,\frac{\nu}{c} \tag{3.3}$$

Equation 3.2 shows the physical separation between antenna pairs, whereas equation 3.3 shows the baseline in wavelength units at any given frequency ν. The regular spacing of the antennas results in baselines with redundant spacings. As a result, we obtain $N_A - n$ copies of the baseline with a separation of n units. In this case of an N_A-antenna linear array, only $N_A - 1$ baselines out of ${}^{N_A}C_2$ are unique and non-redundant. All of these $N_A - 1$ baselines have redundant copies, except the longest one.

3.3.2 A co-ordinate system suitable for OWFA

A generalised framework for computing the visibilities is presented here. Consider a right-handed Cartesian coordinate system, shown in Figure 3.5, tied to the telescope, in which the z-axis is along the N-S direction, parallel to the axis of the parabolic cylinder, the x-axis is aligned with the normal to the telescope aperture which is directed towards $(\alpha_0, 0)$ on the celestial equator, and the y axis is in the plane of the telescope's aperture, perpendicular to both the x and z axes. $\hat{\mathbf{i}}, \hat{\mathbf{j}}$ and $\hat{\mathbf{k}}$ denote the unit vectors along x, y

```
###  Antenna   Re(gain)    Im(gain)    abs(gain)    arg(gain)
###
 0    N10N     2.111527   -1.651020    2.680375    -38.022146
 1    N10S    -0.769040    2.448255    2.566198    107.438412
 2    N09N    -0.913652   -2.671373    2.823295   -108.881507
 3    N09S    -0.190915    1.659500    1.670446     96.562654
 4    N08N     1.466966    0.517440    1.555549     19.429184
 5    N08S     1.348224    1.415455    1.954794     46.393533
 6    N07N     1.723441    0.145458    1.729569      4.824328
 7    N07S    -2.511021    1.459677    2.904459    149.830224
 8    N06N     0.463453    2.223640    2.271423     78.226895
 9    N06S     1.004124    0.798968    1.283205     38.508795
10    N05N    -0.046135   -1.031570    1.032601    -92.560763
11    N05S    -0.425501    1.201335    1.274463    109.503632
12    N04N     1.067091   -0.765654    1.313358    -35.660018
13    N04S    -0.976506   -0.795601    1.259581   -140.828831
14    N03N    -0.593958   -2.938420    2.997849   -101.427514
15    N03S    -1.075955    1.716523    2.025865    122.080404
16    N02N     0.634671   -2.132853    2.225280    -73.428618
17    N02S     2.248666    0.345837    2.275105      8.743388
18    N01N    -1.958163    0.338268    1.987166    170.199009
19    N01S    -0.212065    1.570783    1.585034     97.688771
20    S01N    -0.256268    2.037437    2.053490     97.168981
21    S01S    -1.398241    1.134270    1.800457    140.950603
22    S02N     0.940308   -1.253056    1.566629    -53.114995
23    S02S    -2.284185    1.273998    2.615449    150.849531
24    S03N    -1.082240    0.356707    1.139511    161.757747
25    S03S    -1.759266   -1.056243    2.051991   -149.019895
26    S04N     0.717962    1.183710    1.384428     58.761694
27    S04S     1.618630   -2.260757    2.780465    -54.398543
28    S05N    -1.119425   -0.141581    1.128343   -172.791702
29    S05S    -1.766846   -0.739613    1.915403   -157.285498
30    S06N    -1.451497    0.270899    1.476560    169.428287
31    S06S    -1.661479    2.259256    2.804416    126.331123
32    S07N     1.485732    0.379087    1.533331     14.313723
33    S07S    -0.112640    1.746786    1.750414     93.689545
34    S08N     1.000865    1.760449    2.025071     60.380554
35    S08S    -2.000693   -0.504059    2.063213   -165.859076
36    S09N    -1.705893    0.778837    1.875275    155.460620
37    S09S     0.519385    2.814091    2.861620     79.542844
38    S10N     0.112905    1.564518    1.568587     85.872353
39    S10S     1.386609   -1.809840    2.279958    -52.542475
```

Figure 3.3: The antenna initialiser log, with the complex gain assigned to each antenna.

```
###    Ant1  Ant2    FITSbl  Ant1    Ant2
###
  1     0     1       257    N10N    N10S
  2     0     2       258    N10N    N09N
  3     0     3       259    N10N    N09S
  4     0     4       260    N10N    N08N
  5     0     5       261    N10N    N08S
  6     0     6       262    N10N    N07N
  7     0     7       263    N10N    N07S
  8     0     8       264    N10N    N06N
  9     0     9       265    N10N    N06S
 10     0    10       266    N10N    N05N
 11     0    11       267    N10N    N05S
 12     0    12       268    N10N    N04N
 13     0    13       269    N10N    N04S
 14     0    14       270    N10N    N03N
 15     0    15       271    N10N    N03S
 16     0    16       272    N10N    N02N
 17     0    17       273    N10N    N02S
 18     0    18       274    N10N    N01N
 19     0    19       275    N10N    N01S
 20     0    20       276    N10N    S01N
 21     0    21       277    N10N    S01S
 22     0    22       278    N10N    S02N
 23     0    23       279    N10N    S02S
 24     0    24       280    N10N    S03N
 25     0    25       281    N10N    S03S
 26     0    26       282    N10N    S04N
 27     0    27       283    N10N    S04S
 28     0    28       284    N10N    S05N
 29     0    29       285    N10N    S05S
 30     0    30       286    N10N    S06N
 31     0    31       287    N10N    S06S
 32     0    32       288    N10N    S07N
 33     0    33       289    N10N    S07S
 34     0    34       290    N10N    S08N
 35     0    35       291    N10N    S08S
 36     0    36       292    N10N    S09N
 37     0    37       293    N10N    S09S
 38     0    38       294    N10N    S10N
 39     0    39       295    N10N    S10S
```

Figure 3.4: The log “baselines.info” that lists the baselines counted as pairs of the available antennas. Only the first 39 baselines of Mode-I are shown as an example.

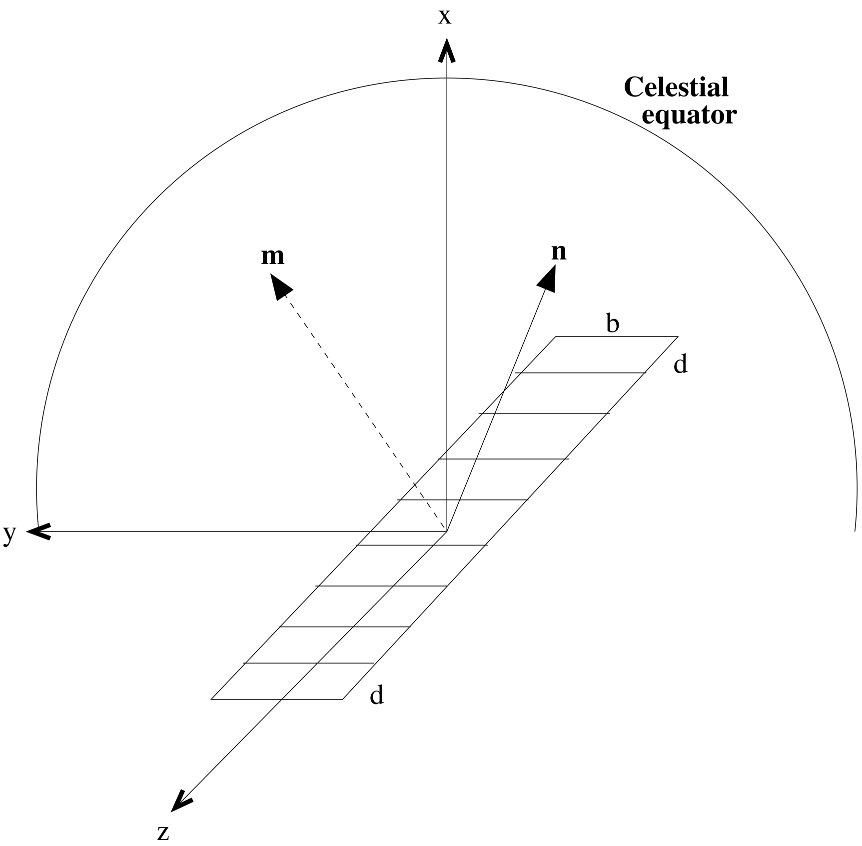

Figure 3.5: A schematic of the co-ordinate system for computing the visibilities, in which **n** is an arbitrary direction and **m** is the direction of pointing. The visibilities are computed over the entire solid angle of the celestial hemisphere.

and z respectively. In this coordinate system, we have

$$\mathbf{U} = v\hat{\mathbf{k}} \tag{3.4}$$

Observations are centered on a position (α_0, δ_0) on the celestial sphere: let the unit vector $\hat{\mathbf{m}}$ denote this position on the celestial sphere. $\hat{\mathbf{m}}$ always lives on the $x{-}z$ plane, and is given by

$$\hat{\mathbf{m}} = \sin(\delta_o)\,\hat{\mathbf{k}} + \cos(\delta_0)\,\hat{\mathbf{i}} \tag{3.5}$$

The measured visibility for a baseline $\mathbf{U}$ at a frequency ν can be written as

$$\mathbf{M}(\mathbf{U}, \nu) = \int d\Omega_{\hat{\mathbf{n}}}\, I(\mathbf{n}, \nu)\, A(\Delta\mathbf{n}, \nu)\, e^{2\pi i \mathbf{U}\cdot\Delta\mathbf{n}} \tag{3.6}$$

where $\hat{\mathbf{n}}$ refers to an arbitrary direction in the celestial sphere, given by

$$\hat{\mathbf{n}} = \sin(\delta)\,\hat{\mathbf{k}} + \cos(\delta)\,\Big[\cos(\alpha - \alpha_0)\,\hat{\mathbf{i}} + \sin(\alpha - \alpha_0)\hat{\mathbf{j}}\Big] \tag{3.7}$$

The solid angle integral here is over the entire celestial sphere, and

$$\Delta n = \hat{\mathbf{n}} - \hat{\mathbf{m}} \tag{3.8}$$

We finally have

$$\mathbf{M}(\mathbf{U}, \nu) = \int [d\sin(\delta)\, d\alpha]\, I(\alpha, \delta)\, e^{2\pi i v[\sin(\delta - \delta_0)]} A(\Delta n_y, \Delta n_z) \tag{3.9}$$

where $\Delta n_y = \cos(\delta)\,\sin(\alpha - \alpha_0)$ and $\Delta n_z = \sin(\delta - \delta_0)$. Note that in this co-ordinate system the argument of the exponent depends only on the baseline length and the declination, reflecting the 1D geometry of OWFA.

3.3.3 Aperture and the primary beam

We may write the general beam pattern for a rectangular aperture as $A(\Delta\mathbf{n}) \equiv A(\Delta n_y, \Delta n_z)$ where $(\Delta n_y, \Delta n_z)$ are respectively the y and z components of $\Delta\mathbf{n}$. The Mode-I aperture is 11.5m × 30m and the Mode-II aperture is 1.92m × 30m in $d \times b$. Figure 3.6 shows the aperture arrangement for OWFA. For the rectangular aperture we have in the case of OWFA, if we assume for the moment uniform illumination,

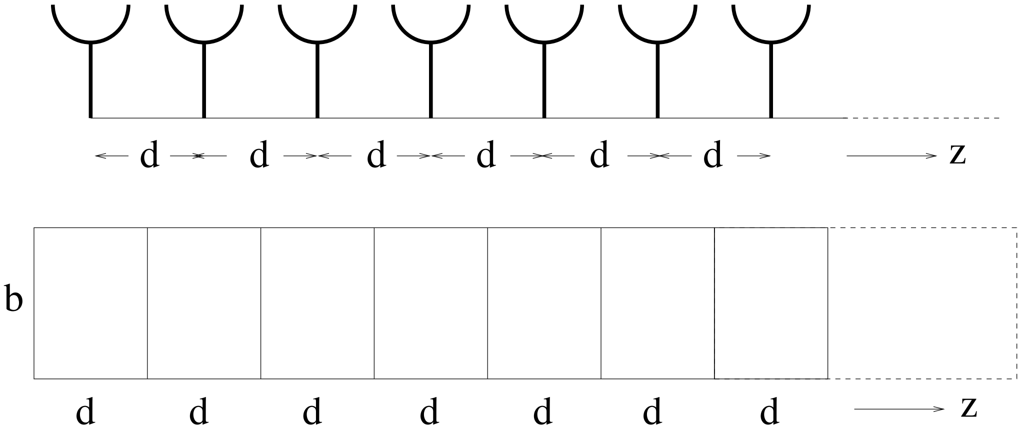

Figure 3.6: The aperture arrangement for OWFA.

$A(\Delta n_y, \Delta n_z)$ can be modelled as a product of sinc^2 functions:

$$A(\Delta n_y, \Delta n_z) = \mathrm{sinc}^2\left(\frac{\pi b\,\Delta n_y}{\lambda}\right)\mathrm{sinc}^2\left(\frac{\pi d\,\Delta n_z}{\lambda}\right) \tag{3.10}$$

However, the primary beam should infact be written as

$$\mathbf{A}(\boldsymbol{\theta}, \nu) = \left(\frac{\sin\left(\pi\,\frac{d\nu}{c}\,(\delta - \delta_0)\,\cos\,\delta_0\right)}{\pi\,\frac{d\nu}{c}\,(\delta - \delta_0)\,\cos\,\delta_0}\right)^2 \left(\frac{\sin\left(\left(\pi\,\frac{b\nu}{c}\right)\,(\alpha - \alpha_0)\right)}{\pi\,\frac{b\nu}{c}\,(\alpha - \alpha_0)}\right)^2 \tag{3.11}$$

The $\cos\delta_0$ factor in the primary beam function arises from the fact that the aperture is foreshortened in the d direction as seen from the source at δ_0. This effective reduction in the aperture size results in a broader primary beam as the declination increases, as well as reduced sensitivity. In **Prowess**, by default for Mode-I, the beam is computed out upto $\sim 18^\circ$ from the phase centre in each direction. This corresponds to three sidelobes north-south, and 10 sidelobes east-west at $\delta_0 = 0^\circ$. The beam is computed and stored as an array, with a pixel resolution $\sim 1.0' \times 1.0'$ and 2048×2048 pixels across. The simulated foreground maps, discussed in Chapter 5, are also computed and stored in an identical sized array. The sinc^2 beam used here is considered only as a worst-case scenario, i.e., as having the most pronounced sidelobes. In practice, the beam is a Gaussian in the east-west dimension as confirmed independently from slew-scan measurements. The full extent of the simulated primary beam power pattern is shown in Figure 3.7 at four different declinations. Having said that, **Prowess** can accommodate any definition for the primary beam power pattern, and it need not be constrained to the two-dimensional sinc^2 pattern.

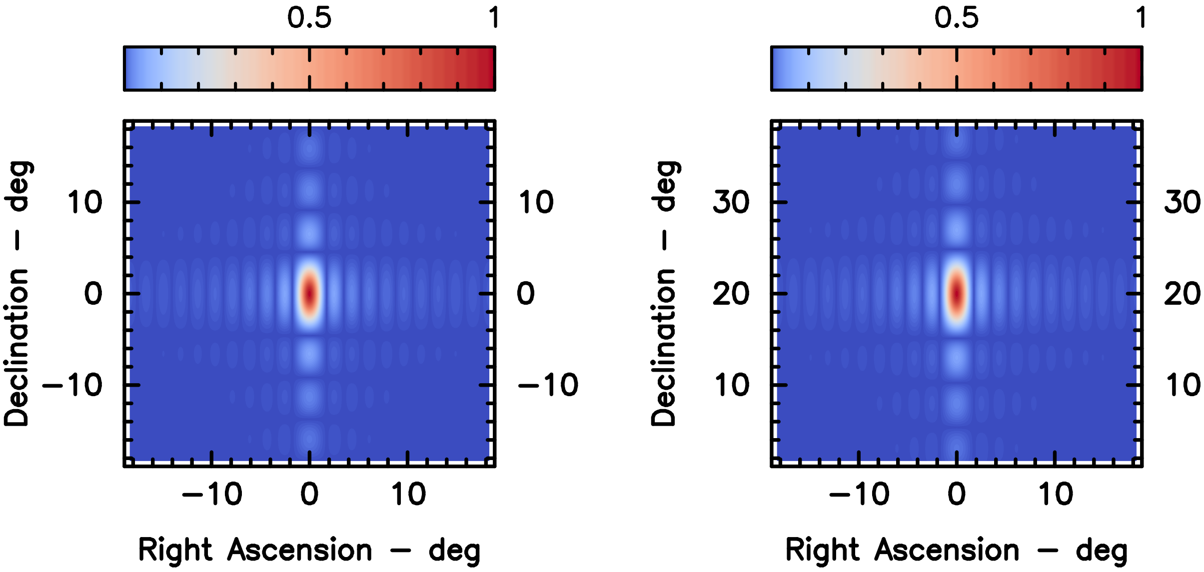

(a) $\delta_0 = 0°$ (b) $\delta_0 = 20°$

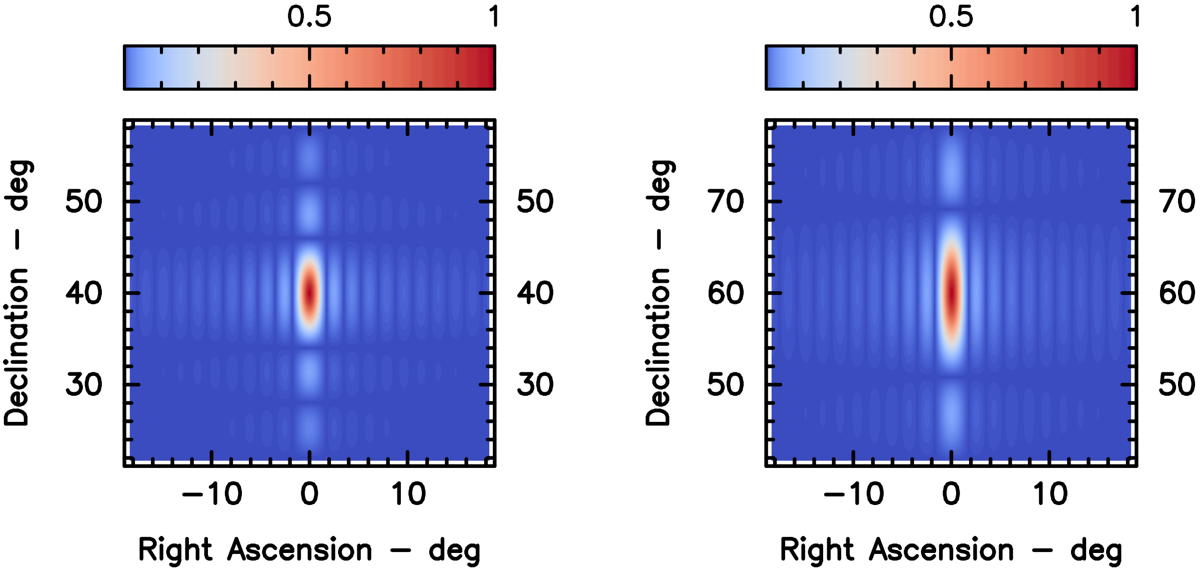

(c) $\delta_0 = 40°$ (d) $\delta_0 = 60°$

Figure 3.7: The primary beam power pattern at declinations (a) $\delta_0 = 0°$, (b) $20°$, (c) $40°$ and (d) $60°$. The beam widens noticeably in declination extent at higher declination as the projected aperture size shrinks as $\cos\,\delta_0$.

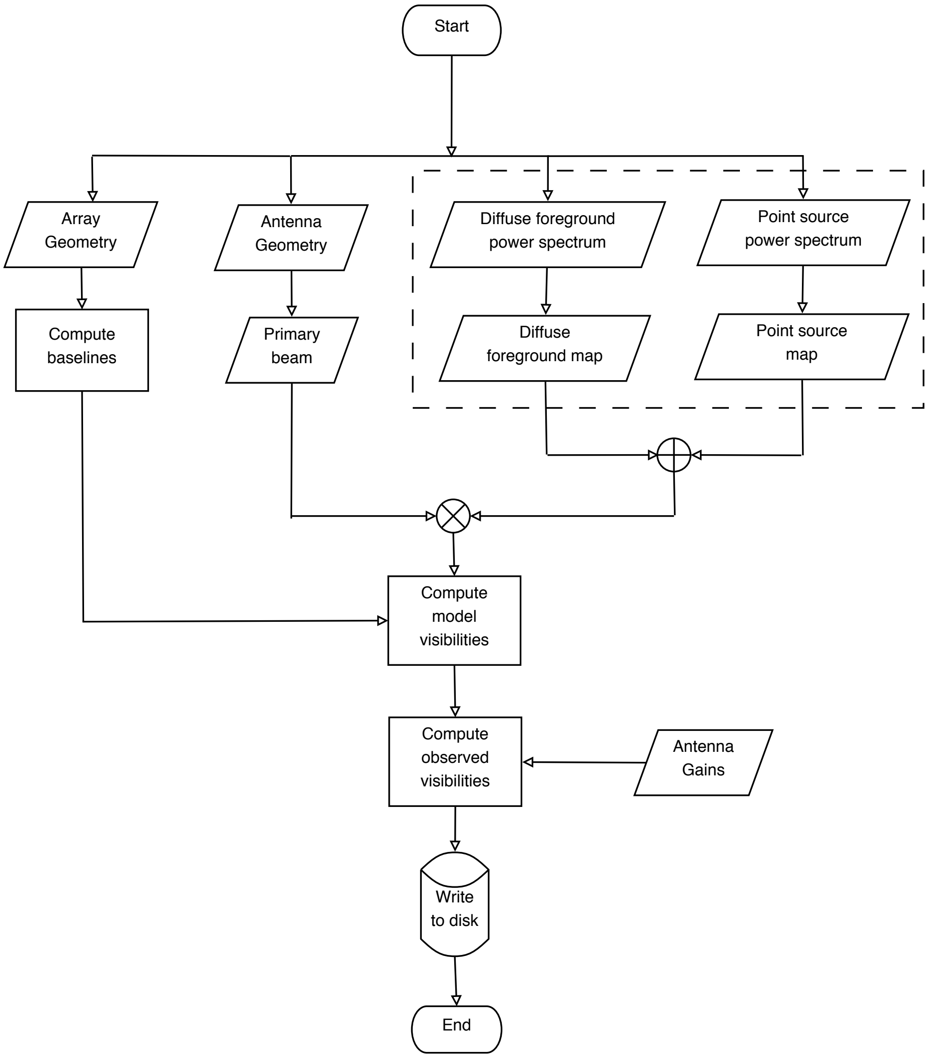

Figure 3.8: This flowchart gives an overall picture of the part of the simulator that produces the model and observed visibilities.

3.3.4 Sky and model visibilities

The computation of the model visibilities is now described below. In the model for the foregrounds, only two components are considered here as they are the most dominant at ~ 325 MHz. The diffuse Galactic synchrotron foreground dominates the emission from within the Galaxy at very large scales ($\gtrsim 2^{\circ}$), while the extragalactic sources dominate at scales typically smaller than a degree (Ali & Bharadwaj, 2014). Random realisations of the foreground emission are obtained from the assumed power spectrum of the emission: the details of how they are generated are explained in Chapter 5. Once the maps are available, their individual components are superimposed in sky-coordinates to obtain the total emission from the sky. The specific intensity function is then given by

$$I(\alpha,\delta,\nu) = \Delta I_D(\alpha,\delta,\nu) \ + \sum_{k=1}^{L} I_k(\alpha_k,\delta_k,\nu) \tag{3.12}$$

where $\Delta I_D(\alpha,\delta,\nu)$ is the fluctuation in the specific intensity of the diffuse foreground emission, and the L distinct extragalactic radio sources are identified by their co-ordinates (α_k,δ_k) and specific intensities I_k. The discrete sources are each confined to a pixel, so that the specific intensity of each source is equal to its flux density. For the diffuse foregrounds, the simulated maps are already pixelised, and the specific intensity in each pixel has already been scaled by the solid angle of the pixel. The flux density of the sky is

$$S(\alpha,\delta,\nu) = \Delta S_D(\alpha,\delta,\nu) + \sum_{k=1}^{L} S_k(\alpha_k,\delta_k,\nu) \tag{3.13}$$

Since the model visibilities $M(\mathbf{U},\nu)$ for the non-redundant set of baselines are obtained as a pixel-by-pixel Fourier sum of the primary-beam weighted specific intensity distribution, we finally have

$$\mathbf{M}(\mathbf{U},\nu) = \sum_{\alpha,\delta} \ S(\alpha,\delta,\nu) \ \mathbf{A}(\alpha,\delta,\nu) \ e^{-i2\pi\mathbf{U}.\hat{\mathbf{n}}} \tag{3.14}$$

which is the discretised version of equation 3.6.

The observing band is centered at 326.5 MHz with a bandwidth of ~ 39 MHz split into 312 channels in the simulations. The frequency resolution in this case is 125 kHz per channel. Based on our understanding of the distribution of the neutral gas around the redshift of $z \sim 3.35$, it is expected that the HI signal at two redshifted frequencies, separated by more than $\Delta\nu \sim 1$ MHz, decorrelates rapidly (Bharadwaj & Ali, 2005; Bharadwaj *et al.*, 2009). This means that with a channel resolution of 125 kHz, the HI signal correlation is adequately sampled over the 1-MHz correlation interval. In reality, the channel resolution is likely to be much finer (~ 50kHz), with about 800 channels across the 39-MHz band. This is useful for the identification and excision of narrow line radio frequency interference. Beyond the need to handle RFI, there is no real incentive to retain the visibility data at this resolution at the cost of downstream computing and storage requirements. Eventually, we may smooth the data to a resolution of 125 kHz, keeping in mind the decorrelation bandwidth of the HI signal. The emulator itself is indeed capable of running at any frequency resolution, including the actual final configuration of the Mode-I and Mode-II systems. But the

125-kHz resolution used in the simulations allows for rapid processing, especially if they are to be run repetitively for a wide range of different parameters.

The model visibilities $\mathbf{M}(\mathbf{U})$ need be obtained only for the set of distinct non-redundant baselines, denoted by $\mathbf{U}_{|i-j|}$. The observed visibility V_{ij} for a baseline with antennas i and j depends on the model visibility for that particular spacing $M_{|i-j|}$, as well the gains of the individual antennas:

$$V_{ij} = g_i \; g_j^* \; M_{|i-j|} + N_{ij}(\nu) \tag{3.15}$$

where M is the model visibility including the primary beam as described above, g_i and g_j are the complex antenna gains and N_{ij} is the complex Gaussian random noise equivalent to the system temperature $T_{\rm sys}$. The real and imaginary parts of the noise N_{ij} in equation 3.15 have a RMS fluctuation

$$\sigma_{ij} = \frac{\sqrt{2} k_B T_{\rm sys}}{\eta A \sqrt{\Delta\nu \Delta t}} \tag{3.16}$$

per channel, where k_B is the Boltzmann constant, η is the aperture efficiency, $A = b \times d$ is the aperture area, $\Delta\nu$ the channel width and Δt the integration time. The foreground maps give the flux in Jy units at every pixel, therefore the Fourier sum directly produces the model visibilities in Jy units as well. The flowchart in Figure 3.8 gives a bird's eye view of the part of the simulator pipeline used to obtain the visibilities, and summarises the emulator part of **Prowess**. The dashed box in the flowchart represents the functionality that simulates the foreground maps. The emulator also has the functionality to accept an external FITS image (e.g. via observations from some other telescope) of the foreground.

3.3.5 Data visualisation

The simulated visibilities are written into a FITS file in the UVFITS data format. This is a standard format for reading and writing the radio interferometric visibility data, and is the format being used at the GMRT. However, **Prowess** has its own interface that helps in visualising the visibility data, which is explained here. The data are available in time-baseline-frequency order. That is, the coarsest data identifier is the record number, which is tagged to the timestamp. At each timestamp, all the ${}^{N_A}C_2$ baselines are sorted in a specific order, indexed by the FITSbl number shown in Figure 3.4. Each baseline has N channels, and each channel has a real and imaginary number for the visibility, and an associated weight. The visibility data therefore reside in a gridded three-dimensional co-ordinate system where the three axes are time,

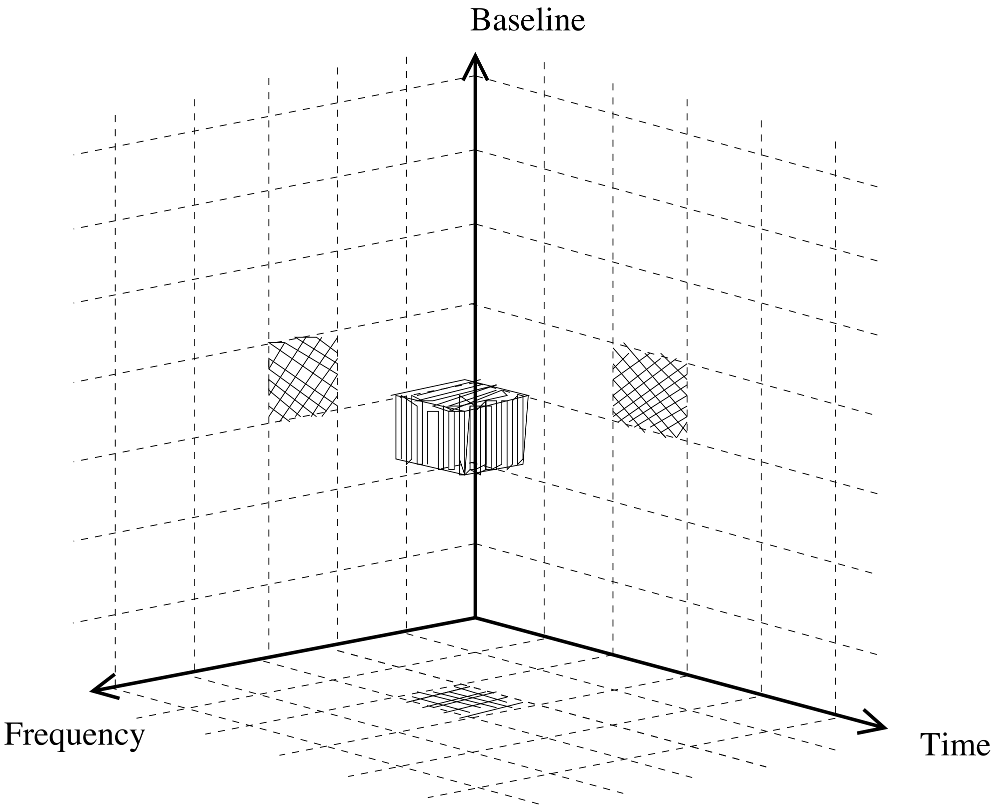

Figure 3.9: The display buffer with gridded Time, Frequency and Baseline axes, where the complex visibility resides.

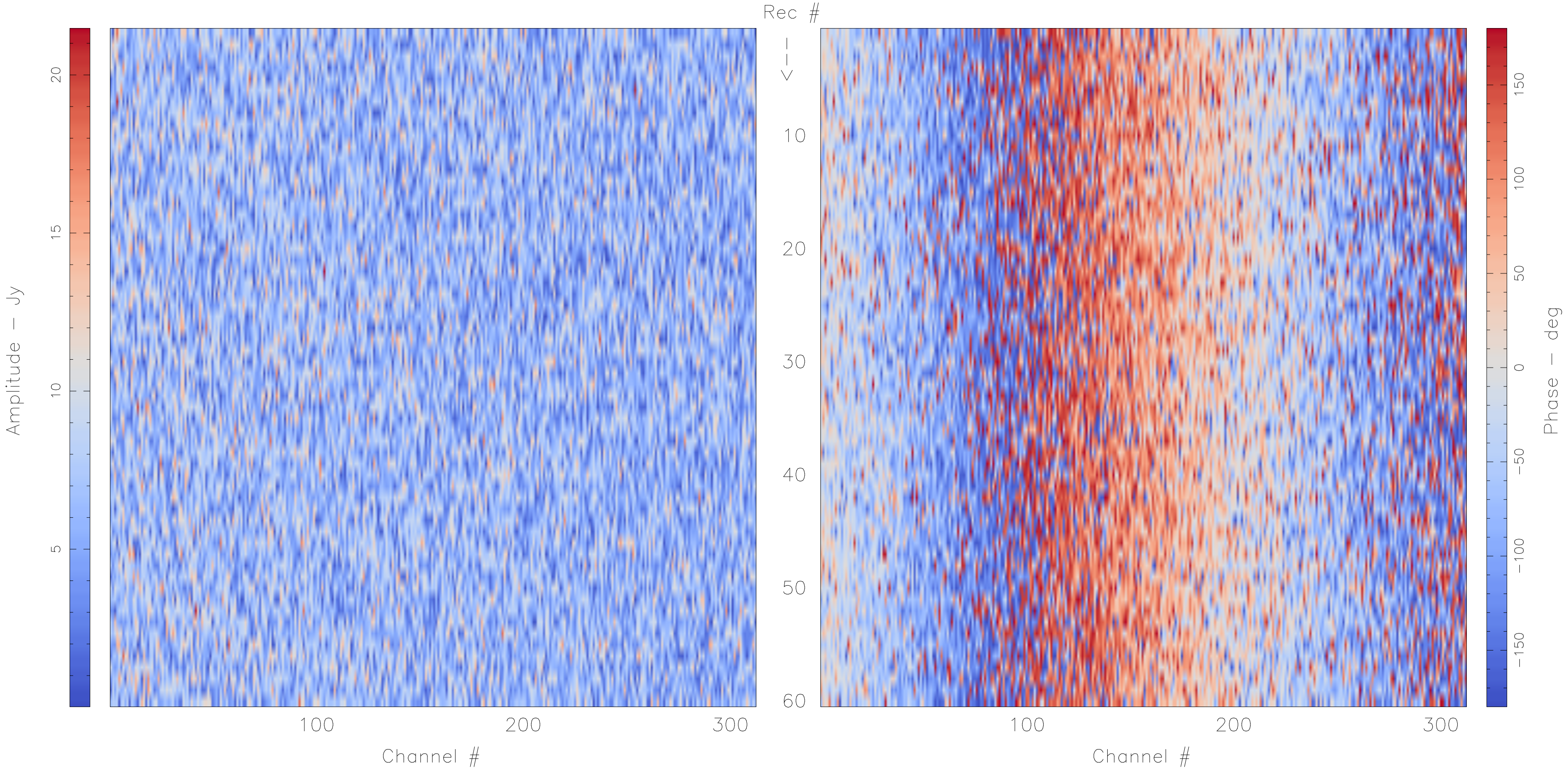

Figure 3.10: A time-frequency view of the visibility data on the $T-N$ plane for $B=1$.

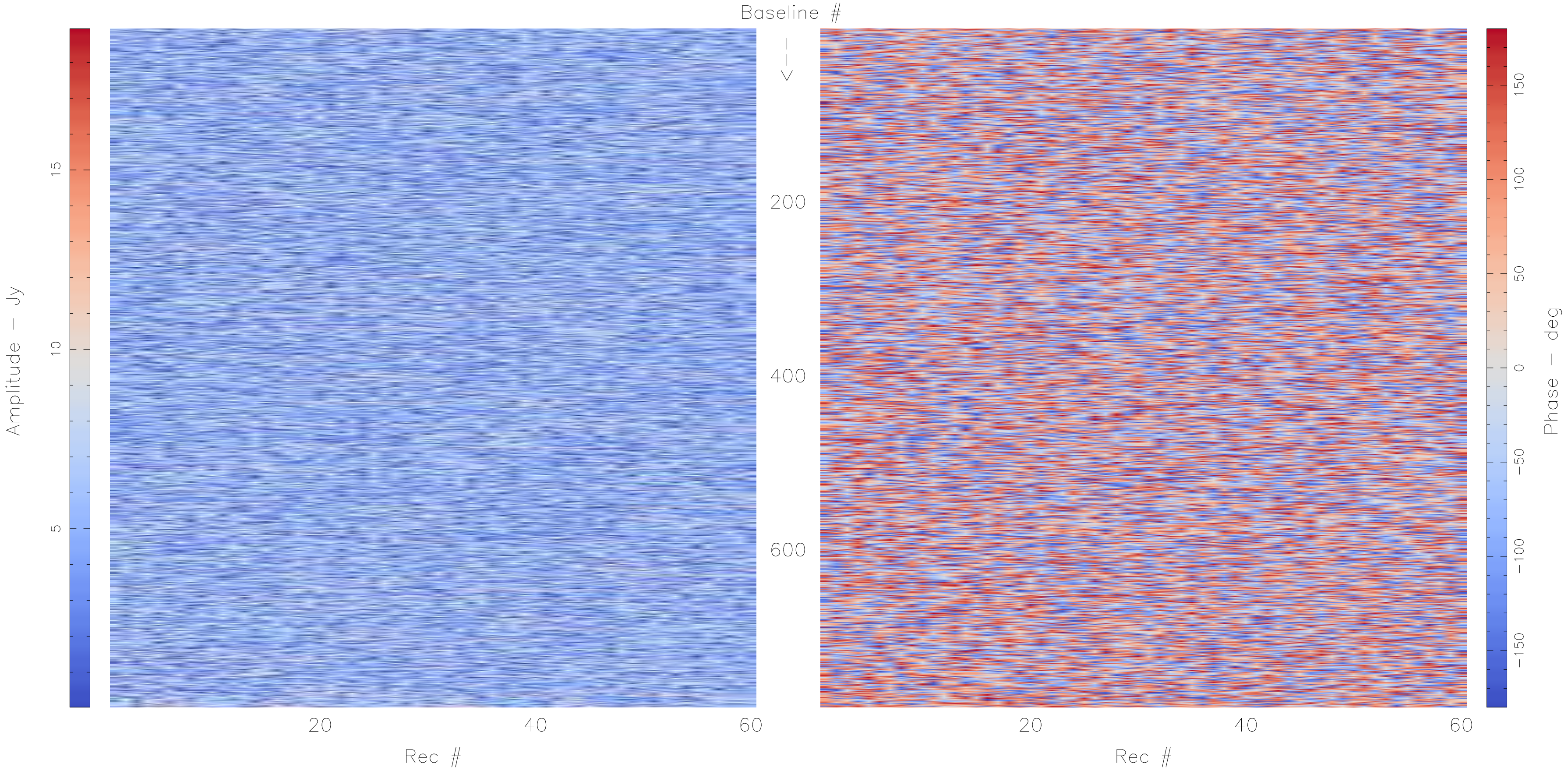

Figure 3.11: A time-baseline view of the visibility data on the $T - B$ plane for $N = 156$.

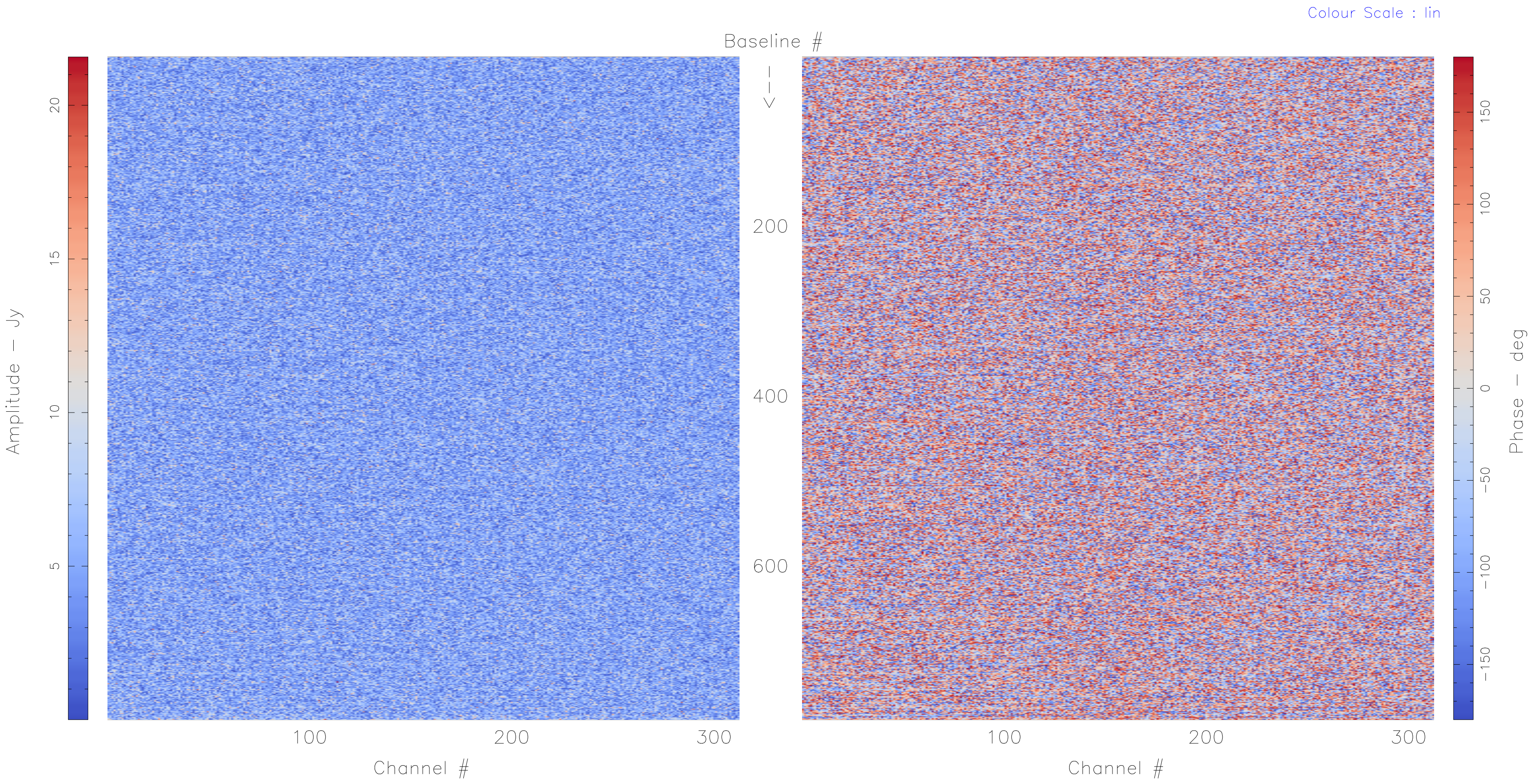

Figure 3.12: A frequency-baseline view of the visibility data on the $N - B$ plane for $T = 30$.

baseline and frequency. There are $T \times B \times N$ grid cells, where T is the number of records, B is the number of baselines and N is the number of channels, shown in Figure 3.9. This arrangement is very convenient; therefore the native structure that holds these visibility data in a display buffer is similarly defined. For visualising the data, they are therefore read from the FITS record into the display buffer. The visualisation programs hence access one of the planes parallel to the $T-B$, $B-N$ or $T-N$ planes. Figures 3.10, 3.11 and 3.12 show the simulated visibility accessed from the display buffer for an example run with a particular realisation for the diffuse Galactic foreground, with the 312-channel, 40-antenna, 780-baseline Mode-I configuration observed for 60 seconds with a record being written to disk every second. There is an option to dynamically switch between a real/imaginary or an amplitude/phase view, and dynamically switch between linear, square-root and logarithmic image transfer functions. A dynamic zooming feature is available in these interfaces as well. Besides the colour-coded plan view, these plane data from the display buffer can also be viewed in a conventional viewscope format, again, with the option to dynamically switch between real/imaginary and amplitude/phase view formats.

3.4 The observatory data processing pipeline

Prowess is not an emulator alone, as the name may suggest. It was described in Section 3.1 why the emulator was conceived: it serves the dual purpose of an emulator and would potentially become the standard post-correlation data processing pipeline at the observatory. It would be useful now to dwell a little on the data processing pipeline aspect of **Prowess** and state what functionality it is meant to provide.

The data pooled from the antennas would terminate in the eight high-performance compute nodes through eleven copper ethernet links each. These nodes correlate the signal from every pair of antennas and accumulate the products upto an interval of time, usually programmable. The typical integration time, called the Long Term Accumulation (LTA), is of the order of $1-10$ seconds. Once the data are available in FITS format, **Prowess** can completely take over downstream processing, which include calibration and power spectrum estimation. The uncalibrated FITS data can as well be stored in the disks for offline calibration. The enormous redundancy of the measurements and the structure of OWFA are best exploited by calibrating the visibilities using a non-linear least squares redundancy calibration algorithm (see Chapter 4). This is a fast N_A^2 algorithm that is capable of running in real time. The calibrated visibilities are later processed to obtain the power spectrum of the observed sky (see Chapter 6). A list of most useful programs that can be run standalone or be pipelined is given in Appendix A.

3.5 Summary

A software model that captures the instrumental and geometric details of OWFA has been described. This detailed model is an important aid to understanding the systematics introduced by the instrument and to make robust and meaningful predictions for the foregrounds and the HI signal. The programming philosophy allows for modular function definitions and easy addition of new functionality. The suite features a rich and interactive visual environment to play back the visibility data. These programs comprise not just an emulator for OWFA, but they are also designed to serve as observatory data analysis software. Prowess has greatly aided our understanding of the instrument and the systematics expected in the OWFA cosmology experiment; these will be described in the following chapters.

Chapter 4

Redundancy calibration

The visibilities obtained by a radio interferometer have to be corrected for the unknown gains of the antennas before they can be used for further processing. This is a well known problem (viz. "calibration") and calibration routines are available in several different interferometric data reduction packages. A special case of calibration arises when the array is such that a given antenna spacing is present multiple times. Each instance in such a "redundant" baseline set measures the same Fourier component of the sky brightness distribution. The only differences between the copies are due to the different multiplicative gains and additive noise along the different signal paths. For a sufficiently redundant array, this multiplicity of measurements of the same physical quantity allows simultaneous estimation of both the antenna gains as well as the true sky visibilities. Some of the earliest work on "redundancy calibration" was done at the Westerbork Synthesis Radio Telescope (WSRT; Noordam & de Bruyn 1982; Wieringa 1991, 1992). Interest in redundancy calibration has seen a revival in the recent past because a number of new instruments (e.g. LOFAR: Falcke 2006; van Haarlem *et al.* 2013, PAPER: Parsons *et al.* 2010 and MWA: Lonsdale *et al.* 2009; Tingay *et al.* 2013) have been designed with some degree of redundancy. The LOFAR stations, for instance, have a redundant $N_A \times N_A$ geometry that allows accurate calibration of each of the antennas within the station (Noorishad *et al.*, 2012). Further, certain astrophysics and cosmology experiments would benefit from redundant configurations for the telescope geometry: CHIME (Peterson *et al.*, 2006; Bandura *et al.*, 2014), the Tianlai CRT (Chen, 2011; Xu *et al.*, 2015) and BAOBAB (Pober *et al.*, 2013b) are specific examples, while Parsons *et al.* (2012) discuss redundant configurations for redshifted HI 21 cm studies such as the Epoch of Reionisation (EoR).

Many of the algorithms in previous work on redundancy calibration largely used linear least squares (LLS) methods to solve for the antenna gains and sky visibilities. A popular LLS redundancy calibration algorithm by Wieringa (1991, 1992), and its recent modification by Liu *et al.* (2010) are described briefly. A fast, non-linear least squares (NLS) algorithm is then derived and its performance is compared with the two earlier algorithms. In the course of doing so, results are presented for simulated data, comparing the error estimates with ensemble average errors from a Monte-Carlo simulation. It will also be established that this new NLS solver is statistically optimal. A large part of the work presented in this chapter is based on Marthi & Chengalur (2014).

4.1 Algorithms for redundancy calibration

At any instant of time, a two-element interferometer measures a single Fourier mode (called the visibility) of the incident radiation field. The complex gains along each of the signal paths and the additive thermal noise cause the measured visibility to differ from the true visibility. Mathematically:

$$V_{ij} = g_i g_j^* M_{ij} + N_{ij} \tag{4.1}$$

where g_i and g_j are the complex gains associated with the antennas i and j respectively, M_{ij} is the true visibility of the sky corresponding to the baseline between antennas i and j, and N_{ij} is the complex-valued additive noise.

The model visibility in equation 4.1 is assumed to already include the primary beam. We also assume that phase variations arising from the ionosphere can be lumped together with the complex gain of the receiver chain, and that the correlator does not introduce any baseline based gains or errors. We return to a discussion of these assumptions in Section 4.3. In order to recover the true visibility, the gains g_i would have to be known, i.e. the interferometer would have to be calibrated. For a multi-element interferometer with N_A elements, the number of instantaneous visibility measurements goes like $\sim N_A^2$, while the number of unknown gains is only N_A. In addition the measured visibilities must obey the amplitude and phase closure constraints,

$$\frac{|V_{ij}|\,|V_{kl}|}{|V_{ik}|\,|V_{jl}|} = \frac{|M_{ij}|\,|M_{kl}|}{|M_{ik}|\,|M_{jl}|} \tag{4.2}$$

$$\phi_{ij} + \phi_{jk} + \phi_{ki} = \theta_{ij} + \theta_{jk} + \theta_{ki} \tag{4.3}$$

which relate the measured visibilities to the true visibilities. Because of these constraints, fixed point methods can be used to iteratively refine both the gains and the visibilities, (viz. do *self* calibration) provided some reasonable initial guess for the gains and the structure of the source is available (see e.g. Thompson *et al.*, 2008). Conceptually, the simplest way to do this would be to observe a region of the sky where the true visibilities M_{ij} are known, to solve for the unknown gains g_i using the observed visibilities V_{ij}. Such regions are called calibrator fields, and one would need to know their visibilities over the entire range of Fourier scales that the interferometer probes. If the gain variation timescale is long compared to the time interval between observations of calibrator sources, the solutions can be interpolated in time to obtain the gains at some intermediate time, for example when the *target* source, whose true visibilities one would like to estimate, is being observed.

An interesting case arises when the array is redundant, i.e. there are multiple instances of the same antenna separation. The measurement equation is modified accordingly to reflect the fact that the set of distinct model visibilities repeat on the redundant baselines. We then have

$$V_{ij} = g_i g_j^* M_{|i-j|} + N_{ij} \tag{4.4}$$

The observed visibilities on these redundant baselines would differ only by the instrumental gains and the additive thermal noise. If there is sufficient redundancy this would allow solving for the unknown antenna gains, *as well as the true visibilities, essentially independent of any assumed model for the sky* (see e.g. Cornwell & Fomalont, 1999). This special class of calibration is called “redundancy calibration”. Redundancy calibration algorithms discussed in the literature are broadly based on linear least squares (LLS) methods. One such example is the LLS algorithm proposed by Noordam & de Bruyn (1982). A brief description is given below, and the interested reader is directed to the longer discussion in Noordam & de Bruyn (1982) and those of Wieringa (1991, 1992) and Liu *et al.* (2010). In recent times, a number of new arrays with redundant spacings are being or have been built for doing low frequency cosmology experiments. This has spawned a revival of interest in redundancy calibration (see e.g. Newburgh *et al.* 2014; Zheng *et al.* 2014; Ali *et al.* 2015; Dillon 2015).

4.1.1 Linear Least Squares algorithms

In the linear least squares (LLS) approach to redundancy calibration, the nonlinear equation 4.4 is linearised. The antenna gains and visibilities are estimated together as complex numbers with an amplitude and phase. Two different methods, viz. those proposed by Wieringa (1992) and by Liu *et al.* (2010) are reviewed here. Results from their implementation in **Prowess** (Marthi, 2016), in comparison with the NLS algorithm described in Section 4.1.2 willl be presented.

Ignoring the noise term N_{ij} and taking the logarithm of equation 4.4 we get:

$$\ln|V_{ij}| = \ln|g_i| + \ln|g_j| + \ln|M_{|i-j|}| \tag{4.5}$$

$$\angle V_{ij} = \angle g_i - \angle g_j + \angle M_{|i-j|} \tag{4.6}$$

which is now a system of linear equations. Therefore, they can be written in matrix form:

$$\mathbf{y} = \mathbf{A}\ \mathbf{x} \tag{4.7}$$

separately for the amplitude and the phase equations, where $\mathbf{y}$ is a column vector containing the amplitudes (or phases) of the observed visibilities on all the redundant baselines, $\mathbf{x}$ is a column vector containing the amplitudes (or phases) of the antenna gains and the true visibilities, with the dimension of $\mathbf{x}$ being significantly smaller than the dimension of $\mathbf{y}$. $\mathbf{A}$ is a matrix depending only on the array geometry. For example, in the case of a uniformly-spaced linear N_A-element array like OWFA, $\mathbf{y}$ is of length ${}^{N_A}C_2$ while the length of $\mathbf{x}$ is $N_A + (N_A - 1)$. Therefore $\mathbf{A}$ has dimensions $({}^{N_A}C_2) \times (2N_A - 1)$. For OWFA Mode-I, $\mathbf{A}$ is 780×39. Specifically, for the amplitude equation 4.5:

$$\mathbf{y} = \begin{bmatrix} \ln|V_{1,2}| \\ \ln|V_{1,3}| \\ \ln|V_{1,4}| \\ \vdots \\ \ln|V_{n-1,n}| \end{bmatrix}, \quad \mathbf{x} = \begin{bmatrix} \ln|g_1| \\ \ln|g_2| \\ \ln|g_3| \\ \vdots \\ \ln|g_n| \\ \ln M_{|1|} \\ \vdots \\ \ln M_{|n-1|} \end{bmatrix} \tag{4.8}$$

and

$$\mathbf{A} = \begin{bmatrix} 1 & 1 & 0 & \cdots & 1 & 0 & \cdots & 0 & 0 \\ 1 & 0 & 1 & \cdots & 0 & 1 & \cdots & 0 & 0 \\ 1 & 0 & 0 & 1 & \cdots & 0 & \cdots & 0 & 0 \\ \vdots & & & & \ddots & & & \vdots & \\ 0 & 0 & \cdots & 1 & 1 & 0 & 0 & 0 & 0 \\ 0 & 0 & \cdots & 1 & 0 & 1 & 0 & 0 & 0 \\ 0 & 0 & \cdots & 1 & 1 & 0 & 0 & 0 & 0 \end{bmatrix} \tag{4.9}$$

For the phase part of the solution, some elements of the matrix **A** undergo a sign change corresponding to the complex conjugation of one of the gains, without the structure of the matrix itself being altered.

$$\mathbf{A} = \begin{bmatrix} 1 & -1 & 0 & \cdots & 1 & 0 & \cdots & 0 & 0 \\ 1 & 0 & -1 & \cdots & 0 & 1 & \cdots & 0 & 0 \\ 1 & 0 & 0 & -1 & \cdots & 0 & \cdots & 0 & 0 \\ \vdots & & & & \ddots & & & \vdots & \\ 0 & 0 & \cdots & -1 & 1 & 0 & 0 & 0 & 0 \\ 0 & 0 & \cdots & -1 & 0 & 1 & 0 & 0 & 0 \\ 0 & 0 & \cdots & -1 & 1 & 0 & 0 & 0 & 0 \end{bmatrix} \tag{4.10}$$

It can be seen that the matrix **A** is highly sparse, leading to fast computation of the solution

$$\mathbf{x} = \mathbf{A}^{-1}\,\mathbf{y} \tag{4.11}$$

in a single step, separately for the amplitudes and the phases. It must be clarified that by $\mathbf{A}^{-1}$ is meant the generalised inverse $(\mathbf{A}^T\mathbf{A})^{-1}\mathbf{A}^T$. Further, since the matrix **A** is static, its inverse has to be computed only once, after which it can be used for all time instants at which the redundancy calibration needs to be done.

While this algorithm is fast and straightforward to implement, it ignores the additive noise, and hence is suitable only in high signal-to-noise ratio (SNR) situations. Ignoring the noise term in situations where the SNR is low leads to a significant bias in the solutions. This is a well-known limitation of this algorithm. Liu *et al.* (2010) discuss the problems that arise if the Wieringa (1992) algorithm is used in the low-SNR regime, and suggest an alternative algorithm. Their method is based on linearising the equations by considering a Taylor series expansion of the complex exponentials in equation 4.4, instead of the logarithm.

Following a Taylor series expansion and approximation to the linear term, the complex gains and visibilities can be rewritten as

$$g_i = g_i^0[1 + \Delta\eta_i + i\Delta\phi_i] \tag{4.12}$$

$$g_j = g_j^0[1 + \Delta\eta_j + i\Delta\phi_j] \tag{4.13}$$

$$M_{|i-j|} = M_{|i-j|}^0[1 + \Delta\zeta_{|i-j|} + i\Delta\theta_{|i-j|}] \tag{4.14}$$

$$V_{ij} = V_{ij}^0[1 + \Delta\rho_{ij} + i\Delta\psi_{ij}] \tag{4.15}$$

$$\delta_{ij} = V_{ij} - V_{ij}^0 \tag{4.16}$$

where

$$V_{ij}^0 = g_i^{0*} g_j^0 M_{|i-j|}^0 \tag{4.17}$$

The superscript denotes the initial guess for the various quantities that has to be provided at the start of the algorithm. Recognising that

$$V_{ij} = g_i g_j^* M_{|i-j|} \tag{4.18}$$

we can rewrite equation 4.16 in the expanded terms of V_{ij}^0 and V_{ij} as

$$\delta_{ij} = g_i^0 g_j^{0*} M_{|i-j|}^0 \left[(1 + \Delta\eta_i + i\Delta\phi_i)(1 + \Delta\eta_j - i\Delta\phi_j)(1 + \Delta\zeta_{|i-j|} + i\Delta\theta_{|i-j|}) \;-\; 1 \right] \tag{4.19}$$

Finally, the reduced expression for the correction term to the measured visibility, after dropping the terms of order greater than one, reads

$$\delta_{ij} = V_{ij}^0 \left[\Delta\eta_i + i\Delta\phi_i + \Delta\eta_j - i\Delta\phi_j + \Delta\zeta_{|i-j|} + i\Delta\theta_{|i-j|}\right] \tag{4.20}$$

If $\mathbf{x}$ is defined as

$$\mathbf{x} = \begin{bmatrix} \Delta\eta_1 \\ \Delta\eta_2 \\ \vdots \\ \Delta\phi_2 \\ \Delta\phi_2 \\ \vdots \\ \Delta\zeta_{|1|} \\ \Delta\theta_{|1|} \\ \vdots \end{bmatrix} \tag{4.21}$$

then equation 4.20 can be written in matrix form as

$$\mathbf{y} = \mathbf{B}\ \mathbf{x} \tag{4.22}$$

This equation can be inverted to obtain the corrections to the gains and the visibilities, contained in the vector $\mathbf{x}$: the negative signs and the complex number i of the phase correction terms are absorbed into the matrix $\mathbf{B}$ appropriately. Unlike the earlier case, here the amplitude and phase equations are coupled. Further, unlike the matrix $\mathbf{A}$, which depends only on the geometry of the array, the matrix $\mathbf{B}$ depends on both the geometry of the array and the current estimate of the gains and true visibilities. It hence has to be updated and a fresh pseudo-inverse computed for each iteration. Note also that one has to supply the fiducial solutions g_i^0 and $M^0_{|i-j|}$ at the start. Both the methods outlined above lend themselves to straightforward implementation using any one of the several available linear algebra libraries.

Another recent algorithm of interest is the Weighted Alternating Least Squares (WALS) algorithm proposed by Wijnholds (2010) and Noorishad *et al.* (2012). The antenna gains and phases are obtained as the solutions that minimise the covariance matched weighted differences between the measured and the estimated visibilities:

$$\left\{\widehat{\mathbf{g}}, \widehat{\mathbf{M}}_0, \widehat{\sigma}_n\right\} = \underset{\widehat{\mathbf{g}}, \widehat{\mathbf{M}}_0, \widehat{\sigma}_n}{\arg\min} \; \|\mathbf{W}_c\left(\widehat{\mathbf{V}} - \mathbf{G}\mathbf{M}_0\mathbf{G}^H - \mathbf{\Sigma}_n\right)\mathbf{W}_c\|^2 \tag{4.23}$$

where $\widehat{\mathbf{g}}$ is the vector of the antenna gains to be estimated and $\mathbf{G}$ is the diagonal matrix of the gains. $\widehat{\mathbf{M}}_0$ is the Toeplitz matrix of the true visibilities (to be estimated) of all baselines obtained from the compact set of visibilities $\mathbf{M}$ from the non-redundant baselines. $\widehat{\sigma}_n$ is the noise power vector to be estimated and $\mathbf{\Sigma}_n$ is the diagonal noise covariance matrix. The weighting factor is chosen as $\mathbf{W}_c = \mathbf{V}^{-1/2}$, where $\mathbf{V}$ is the matrix of the measured visibilities. A model is assumed initially to estimate the gains $\mathbf{g}$ from an eigenvalue decomposition. In the next step, these gains are used to estimate the visibilities $\mathbf{M}_0$. The procedure is repeated iteratively until a suitable convergence criterion is satisfied to obtain the estimates $\widehat{\mathbf{g}}$ and $\widehat{\mathbf{M}}_0$. Unlike the logarithmic least squares method which biases the solutions at low SNRs, the WALS method is statistically efficient in the sense that it provides minimum variance unbiased estimates (MVUEs).

The first two methods outlined above estimate the amplitudes and phases of the gains and the visibilities. Instead, the steepest descent algorithm based on non-linear least squares minimisation described below estimates the gains and the visibilities directly as complex numbers of the form $z = a + ib$ on the Argand plane, instead of $z = |z|e^{i\angle z}$. The phases estimated from the complex numbers in the Argand plane are free from the errors inherent in the logarithmic method or the linearised method of Liu *et al.* (2010), where they are found to be unreliable when large due to the $2\pi n$ phase wrap ambiguities. Nevertheless, alignment of the amplitudes and phases would still require external calibration as explained below. Besides, all the above three methods use matrix inversion, resulting in N^4 operations. As an exception, the WALS method is capable of exploiting the redundant structure of the problem thereby achieving N^2 complexity, putting it on par with the steepest descent method described below. A similar algorithm called Alternating Direction Implicit (ADI; Salvini & Wijnholds 2014) calibration is found to be of complexity N^2 and statistically efficient.

4.1.2 A Non-linear Least Squares steepest descent algorithm

In the general case of arrays with arbitrary geometry, equation 4.4 is routinely solved for the unknown antenna gains using non-linear least squares (NLS) minimisation algorithms. It seems reasonable hence to try a similar method in the redundancy calibration case, with the difference being that one would solve not only for the unknown antenna gains, but also for the unknown true visibilities. The algorithm described below, the results and the accompanying diagnostics are based on Marthi & Chengalur 2014.

We begin by defining a real-valued objective function

$$\Lambda = \sum_{i}\sum_{j>i} w_{ij} \left\| \left(V_{ij} - g_i g_j^* M_{|i-j|}\right)\left(V_{ij}^* - g_i^* g_j M_{|i-j|}^*\right)\right\| \tag{4.24}$$

summed over all baselines, where w_{ij} is a real-valued weight. We aim to minimise the objective function Λ with respect to the complex valued gains g *and* the true sky visibilities M. At this juncture, it is worth pointing out that the difference between equation 4.24 and formulation of the WALS method in equation 4.23 is the following: in the WALS method, the additive noise power is also a quantity to be estimated. In the non-linear minimisation, the mean squared error between the measured and the estimated visibilities is sought to be matched to the additive noise, similar to the chi-squared fitting of a model to a set of measurements. For brevity, henceforth let us call the vector $[\ \mathbf{g}\ \mathbf{M}\ ]$ the parameter vector $\mathbf{\Theta}$.

$$\mathbf{\Theta} = [\ \mathbf{g}\ \mathbf{M}\ ] = \big[\ g_1,\ g_2,\ \dots\ g_{N_A},\ \ M_{|1|},\ M_{|2|},\ \dots\ M_{|L|}\ \big] \tag{4.25}$$

corresponding to a redundant array consisting of N_A antennas and L redundant baselines. The solutions $\widehat{\mathbf{\Theta}}$, being the estimates of $\mathbf{\Theta}$ that minimise Λ, are those at which the derivatives of Λ with respect to the elements of $\mathbf{\Theta}$ vanish uniformly, i.e.

$$\frac{\partial \Lambda}{\partial g_k} = 0 \ \ \forall\ k \in \{\ 1, 2, \dots, N_A\ \} \tag{4.26}$$

and

$$\frac{\partial \Lambda}{\partial M_{|k-j|}} = 0 \ \ \forall\ k-j \in \{\ 1, 2, \dots, L\ \} \tag{4.27}$$

It is worth going through the full algebra. Equation 4.26 becomes

$$\frac{\partial \Lambda}{\partial g_k} = \frac{\partial}{\partial g_k} \sum_i \sum_{j>i} w_{ij} \left(g_i\, g_j^*\, M_{|i-j|} - V_{ij}\right) \left(g_i^*\, g_j\, M^*_{|i-j|} - V^*_{ij}\right) \tag{4.28}$$

$$\begin{aligned}
&= \sum_{j>k} w_{kj} \left(g_j^*\, M_{|k-j|}\right) \left(g_k^*\, g_j\, M^*_{|k-j|} - V^*_{kj}\right) + \sum_{j<k} w_{jk} \left(g_j\, g_k^*\, M_{|j-k|} - V_{jk}\right) \left(g_j^*\, M^*_{|j-k|}\right) \\
&= \sum_{j>k} w_{kj}\, |g_j|^2\, g_k^*\, |M_{|k-j|}|^2 - w_{kj}\, g_j^*\, M_{|k-j|}\, V^*_{kj}) + \\
&\qquad \sum_{j<k} \left(w_{jk}\, g_k^*\, |g_j|^2\, |M_{|j-k|}|^2 - w_{jk}\, g_j^*\, V_{jk}\, M^*_{|j-k|}\right) \\
&= \sum_{j\neq k} \left(w_{kj}\, g_k^*\, |g_j|^2\, |M_{|k-j|}|^2 - w_{kj}\, g_j^*\, M_{|k-j|}\, V^*_{kj}\right) \ = \ 0
\end{aligned}$$

Rearranging the last line yields

$$g_k^* = \frac{\sum\limits_{j\neq k} w_{kj}\, g_j^*\, M_{|k-j|}\, V^*_{kj}}{\sum\limits_{j\neq k} w_{kj}\, |g_j|^2\, |M_{|k-j|}|^2} \tag{4.29}$$

which, upon conjugating becomes

$$g_k = \frac{\sum\limits_{j\neq k} w_{kj}\, g_j\, M^*_{|k-j|}\, V_{kj}}{\sum\limits_{j\neq k} w_{kj}\, |g_j|^2\, |M_{|k-j|}|^2} \tag{4.30}$$

Likewise, equation 4.27 becomes

$$\frac{\partial \Lambda}{\partial M_{|i-j|}} = \frac{\partial}{\partial M_{|i-j|}} \sum_i \sum_{j>i} \left(g_i\, g_j^*\, M_{|i-j|} - V_{ij}\right) \left(g_i^*\, g_j\, M^*_{|i-j|} - V^*_{ij}\right) \tag{4.31}$$

$$= \sum_{j>i} w_{ij}\, g_i\, g_j^* \;\left(g_i^*\, g_j\, M^*_{|i-j|} - V^*_{ij}\right)$$

$$= \sum_{j>i} w_{ij}\, |g_i|^2\, |g_j|^2\, M^*_{|i-j|} - \sum_{j>i} w_{ij}\, g_i\, g_j^*\, V^*_{ij} \;\; = \;\; 0$$

which yields

$$M^*_{|i-j|} = \frac{\sum\limits_{j>i} w_{ij}\, g_i\, g_j^*\, V^*_{ij}}{\sum\limits_{j>i} w_{ij}\, |g_i|^2\, |g_j|^2} \tag{4.32}$$

which, upon conjugating, becomes

$$M_{|i-j|} = \frac{\sum\limits_{j>i} w_{ij}\, g_i^*\, g_j\, V_{ij}}{\sum\limits_{j>i} w_{ij}\, |g_i|^2\, |g_j|^2} \tag{4.33}$$

where the sum is taken over the appropriate redundant baseline sets.

Note that equations 4.30 and 4.33 involve the unknown true gains and visibilities. This circularity can be circumvented by taking an iterative approach to the solution: one takes small steps in the direction of the true solutions, starting from an arbitrary initial guess. The corrective steps have to be taken in the direction of the negative gradient for the most rapid convergence. We can redefine the quantities in equations 4.30 and 4.33 as $\mathbf{Q_k}$ and $\mathbf{R_{kj}}$ respectively:

$$\mathbf{Q_k} = \frac{\sum\limits_{j\neq k} w_{kj} g_j M^*_{|k-j|} V_{kj}}{\sum\limits_{j\neq k} w_{kj} |g_j|^2 \; |M_{|k-j|}|^2} \tag{4.34}$$

$$\mathbf{R_{kj}} = \frac{\sum\limits_{j>k} g_k^* g_j V_{kj}}{\sum\limits_{j>k} w_{kj}|g_k|^2|g_j|^2} \tag{4.35}$$

If we additionally define a step size $0 < \alpha < 1$, then the solutions can be obtained iteratively as

$$g_k^{n+1} = (1-\alpha)g_k^n + \alpha \mathbf{Q_k}^n \tag{4.36}$$

$$M_{|k-j|}^{n+1} = (1-\alpha)M_{|k-j|}^n + \alpha \mathbf{R_{kj}}^n \tag{4.37}$$

The instantaneous solution vector is a small correction to the solution vector obtained at the previous instant, the correction terms being given by $\mathbf{Q_k}$ and $\mathbf{R_{kj}}$, computed as equations 4.34 and 4.35. α can be interpreted to function as a "forgetting factor" that weights the past and the instantaneous measurements appropriately. Of course, the rate of convergence will depend upon the value chosen for α: if it is too small (i.e. $\alpha << 1$), convergence will be slow, on the other hand a large value (i.e. $\alpha \sim 1$), could lead to situations where the algorithm fails to converge. There are well known methods such as, for example, the Levenberg-Marquardt method (see e.g. Press *et al.*, 1992) for determining the optimal value for α; however these require computation of the Hessian matrix at each iteration, and are computationally more expensive. In our simulations below we use a fixed value of α (i.e. ~ 0.3). While a fixed value for α may not be optimal, it compensates adequately for the expense of computing the Hessian, even if consuming a few more iterations.

The steps involved in steepest descent method for estimating the antenna gains and the sky visibilities, using the non-linear least squares algorithm given above, are now enumerated:

1. If this is the first time step being solved for, initialise the gains and model visibilities to $\mathbf{\Theta} = [\ \mathbf{g}\ \mathbf{M}\ ] = [(1,0),\ (1,0),\ (1,0),\ \dots(1,0)]$. Otherwise set them to the solutions obtained for the last time step. Set the weights w appropriately based on the system temperature[1]. Choose an ϵ for the convergence criterion (set to $\epsilon = 0.005$ in our simulations).

2. Integrate the correlated signal from each antenna pair, i.e. the visibility from each baseline $V_{ij}\ \forall\ i,j \in 1,2,\dots N_A, j>i$, for the specified time interval.

---

[1] In the simulations described in this chapter, we set them all uniformly to unity.

3. Using the available $\mathbf{\Theta} = [\ \mathbf{g}\ \mathbf{M}\ ]$ and w, compute each $\mathbf{Q_k}$ and $\mathbf{R_{kj}}$ using expressions 4.34 and 4.35.
4. Update the gains $\mathbf{g}$ and the visibilities $\mathbf{M}$ using equations 4.36 and 4.37.
5. Compute the fractional change in each element of $\mathbf{g}$ and $\mathbf{M}$. If the largest fractional change is $> \epsilon$ go to step 3 else stop.

In the case of routine interferometric calibration, the visibilities $M_{|k-j|}$ are known, and hence there is only one equation to work with, viz. equation 4.36. We point out in passing a further similarity with the calibration of non-redundant arrays. Consider the fundamental equation 4.4 which we rewrite here for the redundant array, ignoring the additive noise term for the moment.

$$V_{ij} = g_i\, g_j^*\, M_{|i-j|} \tag{4.38}$$

Scaling $g_i g_j^*$ by some complex constant z_k while simultaneously scaling $M_{|i-j|}$ by $1/z_k$ leaves the equation unchanged. This is the well-known ambiguity problem of selfcal (see e.g. Hamaker, 2000a,b). Equivalently, in the redundant calibration solution, the gain amplitudes are determinable only up to an overall scale factor, and the visibility amplitudes to the inverse square of this scale factor. Similarly the gain phases are determinable only up to a linear gradient and the visibility phases to the negative of this gradient. In this respect, redundancy calibration is analogous to self-calibration. In the simulations described below, we use the known input source positions and the known input source fluxes to determine the scale factor and phase gradient. In practice these factors would have to be determined by some external calibration. In other words, external calibration takes the solutions from a local minimum in the objective function to its global minimum. One of the ways proposed to resolve these ambiguities (see discussion in Wieringa, 1991, 1992; Noorishad *et al.*, 2012, for example) is to apply the following constraints to the solutions

$$\sum_{i=1}^{N_A} |g_i| = N_A\, |g_c|\ ; \quad \sum_{i=1}^{N_A} \phi_i = 0\ ; \quad \sum_{i=1}^{N_A} \vec{\mathbf{r}_\mathbf{i}} \phi_i = 0 \tag{4.39}$$

where $|g_c|$ is some mean gain known apriori, $|g_i|$ and ϕ_i are the antenna gain and phase respectively, and $\vec{\mathbf{r}_\mathbf{i}}$ is the position vector of the i^{th} element in the array. In the case of OWFA, where the telescope is equatorially mounted, and the baseline lengths do not change with time, resolving these ambiguities by external calibration and the requirement that the gain solutions vary slowly but that the visibility solutions are constant with time may be a viable option.

4.1.3 The error covariance matrix

The error covariance matrix for the estimator just described above can be derived rigorously, but it may be useful to begin with a few preliminaries. Let $l(\mathbf{\Theta})$ be a log-likelihood function corresponding to an exponential family of distribution functions. The real and imaginary parts of the visibilities are distributed normally. The *Fisher Information* matrix $\mathbf{I}(\mathbf{\Theta})$ is a symmetrical $p \times p$ matrix containing the entries

$$\mathbf{I}(\mathbf{\Theta}) \;=\; -\frac{\partial^2}{\partial\theta_i\,\partial\theta_j}\, l(\mathbf{\Theta}), \quad 1 \leq i,j \leq p \tag{4.40}$$

The observed *Fisher Information* matrix is simply $\mathbf{I}(\widehat{\mathbf{\Theta}}_{\mathrm{ML}})$, the information matrix evaluated at the maximum likelihood estimate(MLE):

$$\mathbf{I}(\widehat{\mathbf{\Theta}}_{\mathrm{ML}}) \;=\; -\frac{\partial^2}{\partial\theta_i\,\partial\theta_j}\, l(\widehat{\mathbf{\Theta}}_{\mathrm{ML}}), \quad 1 \leq i,j \leq p \tag{4.41}$$

The Hessian is defined as

$$\mathbf{H}(\mathbf{\Theta}) \;=\; \frac{\partial^2}{\partial\theta_i\,\partial\theta_j}\, l(\mathbf{\Theta}), \quad 1 \leq i,j \leq p \tag{4.42}$$

which are merely the second derivatives of the log-likelihood function with respect to the parameters. Clearly,

$$\mathbf{H}(\widehat{\mathbf{\Theta}}_{\mathrm{ML}}) \;=\; -\,\mathbf{I}(\widehat{\mathbf{\Theta}}_{\mathrm{ML}}) \tag{4.43}$$

Further, the inverse of the *Fisher Information* matrix is an estimator of the asymptotic covariance matrix:

$$\Sigma_{\widehat{\mathbf{\Theta}}_{\mathrm{ML}}} \;\geq\; \left[\mathbf{I}(\widehat{\mathbf{\Theta}}_{\mathrm{ML}})\right]^{-1} \tag{4.44}$$

The standard errors are then the square roots of the diagonal elements of the covariance matrix $\Sigma_{\widehat{\mathbf{\Theta}}_{\mathrm{ML}}}$. For the asymptotic behaviour of a Maximum Likelihood Parameter (MLP) distributed normally, one can write

$$\widehat{\mathbf{\Theta}}_{\mathrm{ML}} \sim \mathcal{N}\left(\widehat{\mathbf{\Theta}}_0, \left[\mathbf{I}(\widehat{\mathbf{\Theta}}_{\mathrm{ML}})\right]^{-\frac{1}{2}}\right) \tag{4.45}$$

where $\widehat{\mathbf{\Theta}}_0$ is the true parameter value. Hence the estimated standard error of the MLE is given by

$$\sigma\left(\widehat{\mathbf{\Theta}}_{\mathrm{ML}}\right) \geq \frac{1}{\sqrt{\mathbf{I}(\widehat{\mathbf{\Theta}}_{\mathrm{ML}})}} \tag{4.46}$$

Equation 4.44 is called the "Information Inequality" or "Cramér-Rao Inequality" in statistical signal processing (see e.g. Poor, 1994). The lowest error that can be achieved in equation 4.44 is called the Cramér-Rao bound (CRB), defined as

$$\mathrm{CRB} = \left[\mathbf{I}(\widehat{\mathbf{\Theta}}_{\mathrm{ML}})\right]^{-1} \tag{4.47}$$

An estimator that achieves the CRB is called a **M**inimum **V**ariance **U**nbiased **E**stimate (MVUE) and the estimator is said to be efficient.

Consider a normally distributed complex measurement $\mathbf{y}$ whose model is $\mathbf{Y}$. The measurement equation is

$$\mathbf{y} = \mathbf{Y} + \mathbf{n} \tag{4.48}$$

where $\mathbf{n}$ is the complex measurement noise vector with a covariance matrix Σ. The multivariate probability density function for the measurement vector $\mathbf{y}$ can be written as

$$f_{\mathbf{y}}(y_1, y_2, \ldots, y_N) = \prod_{i=1}^{N} \frac{1}{\sqrt{2\pi\sigma_i^2}} \; e^{-\frac{(y_i - Y_i)(y_i - Y_i)^*}{2\sigma_i^2}} \tag{4.49}$$

The likelihood function is defined as

$$l(\mathbf{y}) = log\, f_{\mathbf{y}}(\mathbf{y}) \tag{4.50}$$

Ignoring the sum of constants resulting from taking the logarithm, we get a χ^2-like function

$$\chi^2 = \sum_{i=1}^{N} \frac{1}{\sigma_i^2}(y_i - Y_i)(y_i^* - Y_i^*) \tag{4.51}$$

For the moment, let us consider general variables a and b, with respect which to differentiate equation 4.51. Then,

$$\frac{\partial \chi^2}{\partial a} \;=\; \sum_{i=1}^{N} \frac{1}{\sigma_i^2} \left[(y_i^* - Y_i^*) \frac{\partial y_i}{\partial a} \;+\; (y_i - Y_i) \frac{\partial y_i^*}{\partial a} \right] \tag{4.52}$$

Differentiating again with respect to b, we get

$$\frac{\partial \chi^2}{\partial a \partial b} \;=\; \sum_{i=1}^{N} \frac{1}{\sigma_i^2} \left[(y_i - Y_i) \frac{\partial^2 y_i^*}{\partial a \partial b} \;+\; \frac{\partial y_i^*}{\partial a} \frac{\partial y_i}{\partial b} \;+\; (y_I^* - Y_i^*) \frac{\partial^2 y_i}{\partial a \partial b} \;+\; \frac{\partial y_i}{\partial a} \frac{\partial y_i^*}{\partial b} \right] \tag{4.53}$$

The terms on the right-hand side of the general second-order partial derivative in equation 4.53 can be computed for the specific case we are interested in, namely for a parameter vector $\mathbf{\Theta} = [\;\mathbf{g} \quad \mathbf{M}\;]$ where $\mathbf{g}$ is the vector of antenna-wise complex electronic gains and $\mathbf{M}$ is the vector of the model visibilities. The general index i can be substituted by a more intuitive one like ij to indicate the baseline. We then have

$$\frac{\partial V_{ij}}{\partial g_k} \;=\; \begin{array}{ll} g_j^* M_{|k-j|} & \text{when } k = i \\ 0 & \text{when } k \neq i \end{array} \tag{4.54}$$

$$\frac{\partial V_{ij}^*}{\partial g_k} \;=\; \begin{array}{ll} g_i^* M_{|k-j|}^* & \text{when } k = j \\ 0 & \text{when } k \neq j \end{array} \tag{4.55}$$

$$\frac{\partial V_{ij}}{\partial M_{|i-j|}} \;=\; \begin{array}{ll} g_i g_j^* & \text{when } ij \in \{i, j\} \\ 0 & \text{when } ij \notin \{i, j\} \end{array} \tag{4.56}$$

$$\frac{\partial V_{ij}^*}{\partial M_{|i-j|}} \;=\; 0 \qquad \text{always} \tag{4.57}$$

$$\frac{\partial^2 V_{ij}}{\partial g_i \partial g_j} \;=\; \frac{\partial^2 \left[g_i g_j^* M_{|i-j|} \right]}{\partial g_i \partial g_j^*} \;=\; 0 \tag{4.58}$$

$$\frac{\partial^2 V_{ij}}{\partial M_{|k|} \partial M_{|l|}} \;=\; \frac{\partial^2 \left[g_i g_j^* M_{|k|} \right]}{\partial M_{|k|} \partial M_{|l|}} \;=\; 0 \tag{4.59}$$

$$\frac{\partial^2 V_{ij}^*}{\partial g_i \partial g_j} \;=\; \frac{\partial^2 V_{ij}^*}{\partial M_{|k|} \partial M_{|l|}} \;=\; 0 \qquad \text{similarly} \tag{4.60}$$

$$\frac{\partial^2 V_{ij}}{\partial g_k \partial M_{|l|}} \;=\; \frac{\partial^2 \left[g_k g_m^* M_{|l|} \right]}{\partial g_k \partial M_{|l|}} \;=\; g_m^* \tag{4.61}$$

$$\frac{\partial^2 V_{ij}^*}{\partial g_k \partial M_{|l|}} \;=\; \frac{\partial^2 \left[g_k^* g_m M_{|l|}^* \right]}{\partial g_k \partial M_{|l|}} \;=\; 0 \tag{4.62}$$

These terms comprise the elements of the Hessian matrix $\frac{\partial\chi^2}{\partial a \partial b}$. The error covariance matrix can then be obtained as

$$\Sigma_{\widehat{\boldsymbol{\Theta}}_{\mathrm{ML}}} = -[\mathbf{H}(\widehat{\boldsymbol{\Theta}}_{\mathrm{ML}})]^{-1} \tag{4.63}$$

4.2 Simulations

The redundancy calibration algorithms were checked against simulated data, as well as with pilot data from one quarter of the early prototype Phase-I system. For the purpose of establishing the performance of the solver algorithm and to obtain diagnostics, we find it useful to apply it to simulated data, where it can be compared against input data.

The visibilities were simulated as described in Section 3.3.4. Thermal noise equivalent to $T_{\mathrm{sys}} = 150$ K was added to the model visibilities. It is to be noted that although the simulations have been done in the specific context of OWFA, the NLS steepest descent algorithm is generic and applicable to any redundant array. The figures and results presented below are for a redundant configuration with upto 40 stations, as appropriate for Phase I of OWFA. However, the NLS algorithm is found to work well even for arrays with as few as 5 stations.

The matrices A and B in the Wieringa (1992) and Liu *et al.* (2010) algorithms are sparse and often singular: techniques like QR decomposition or singular value decomposition (SVD) would hence have to be employed to solve the corresponding matrix equations. In our implementation we have used matrix calls from the GNU Scientific Library (GSL). In the NLS steepest descent method, as described above, equations (4.36) and (4.37) are directly coded and iterated.

4.3 Results

Figure 4.1(a) shows the trajectory of the complex gain vector for a simulation of Mode-I of OWFA. The initial estimate for the gains has come from a run of the linearised Gauss-Newton algorithm of Liu *et al.* (2010) described in Section 4.1.1. This ensures rapid convergence and locking of the solutions to the desired solutions. Figure 4.1(b) shows the estimated gains against the true input gains on the Argand plane. The offset between the true and the estimated gains is not random as it might appear; there is a linear phase gradient as a function of antenna. Figure 4.2 similarly shows the convergence trajectory of the estimated complex visibility vector and the true and estimated visibilities on the Argand plane.

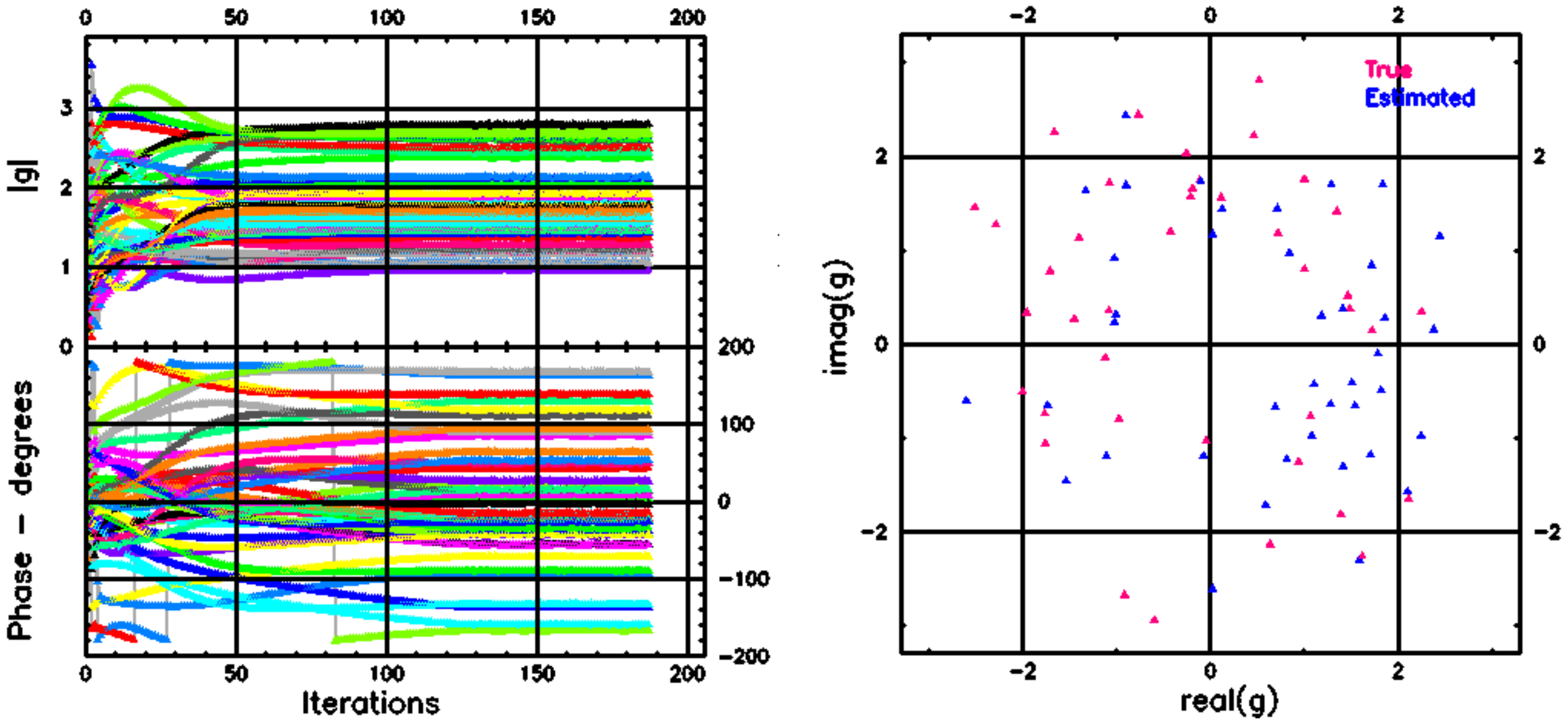

(a) Trajectory of the gain vector

(b) True and estimated gains

Figure 4.1: (a) The trajectory of the complex gain vector is shown from an initial value to its final converged value. (b) The estimated complex gains are shown against the true gains.

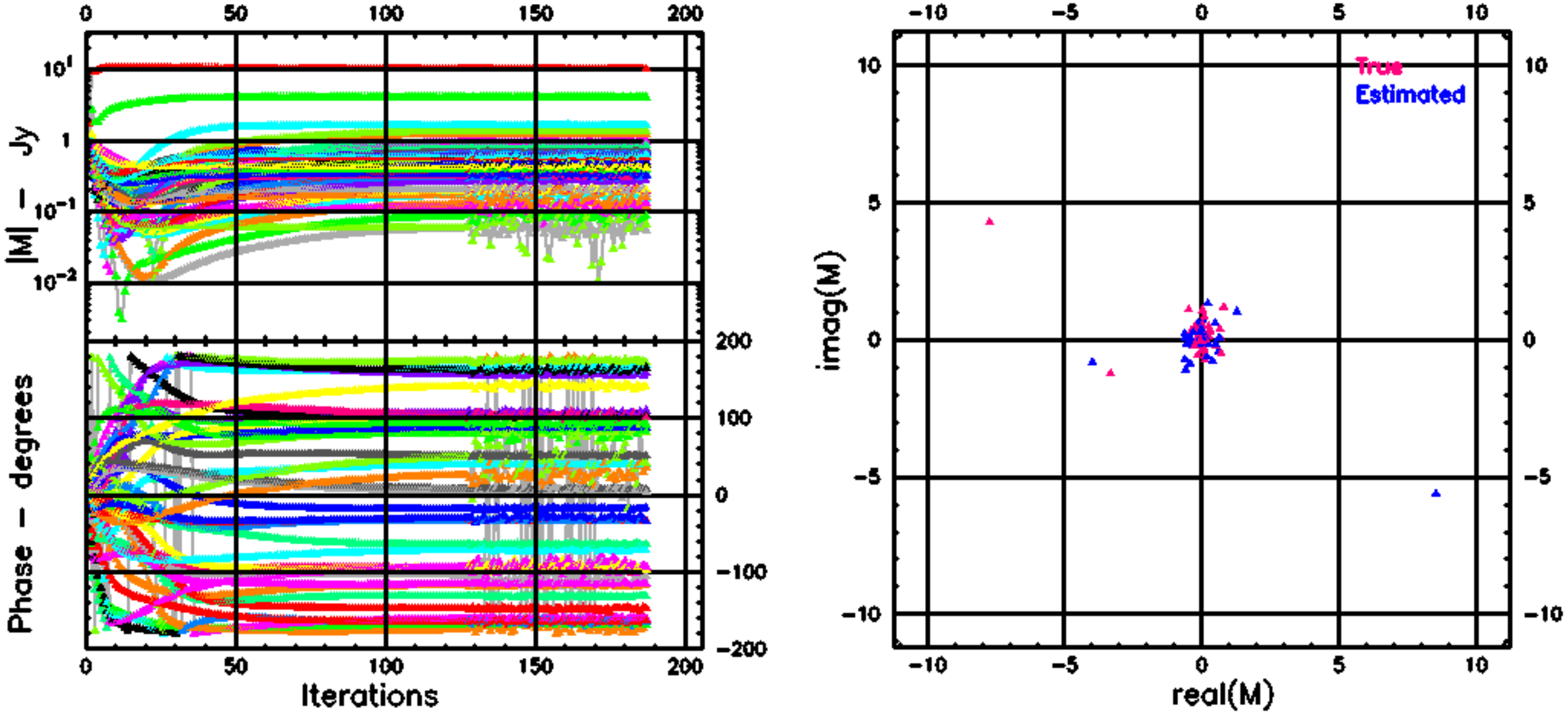

(a) Trajectory of the visibility vector

(b) True and estimated visibilities

Figure 4.2: (a) The trajectory of the complex visibility vector is shown from an initial value to its final converged value. (b) The estimated complex visibilities are shown against the true visibilities.

Figure 4.3 shows the antenna gains and phases estimated from a run of the logarithmic redundancy calibration algorithm of Wieringa (1992), compared against the same numbers estimated from a run of the NLS algorithm. Here, the model used is a single point source at the phase centre of the primary beam. The signal-to-noise ratio per visibility is 10. Although the NLS algorithm works well and provides unbiased solutions for a realistic sky model, this figure is shown here for the simplest input model, i.e. a point source at the phase centre, so as to illustrate the bias on the gains and phases at uniform SNR on all baselines. It can be seen that despite a reasonable signal-to-noise ratio and a simple sky model, the logarithmic method still gives biased estimates. The principal aim of the Liu *et al.* (2010) method was to eliminate this bias and, in their paper, they show results to establish the efficacy of their method. In our implementation of the same, we find that the Liu *et al.* (2010) method does indeed give unbiased results; however for clarity only results from the NLS method and the Wieringa (1992) method in Figure 4.3 have been shown, since the intention here is to establish that the NLS estimator is unbiased.

To further illustrate the quality of the NLS solutions we show in Figure 4.4 the results from a different simulation in which the antenna gains and sky visibilities were kept fixed from run to run, but each run had independent noise added to the simulated visibilities. The visibilities themselves correspond to a model sky with a source population that matches that expected from the source counts (Wieringa, 1991; Sirothia *et al.*, 2009) at 325 MHz, but ignoring the clustering behaviour of radio sources. Essentially, this strictly corresponds to a Poisson-only power spectrum since the sources are distributed with a uniform 2D distribution. The objective is to establish the efficacy of the NLS algorithm, since redundancy calibration is essentially “model-free”, inasmuch as it neither needs nor makes any assumption for the model of the sky. The figure shows the known input parameters to the simulation as well as the mean and 1σ error bars (computed over the different runs, i.e. the ensemble rms) of the estimated parameters. The input gains and visibilities are connected by the straight line segments, whereas the recovered gains and visibilities (in both cases, amplitudes only) are shown by the triangles with the error bars. The error bars have been scaled by a factor of 10 for the gains and 5 for the visibilities so that they can be seen clearly in the plot. The error bars on the gains are also seen to scale with the degree of redundancy. Recently, Patil *et al.* (2016) have found that calibration based on an incomplete sky model leads to a suppression of the diffuse foregrounds as well as excess noise. Model-free redundancy calibration poses no risk of loss to any component of the sky visibilities, since the gains and the visibilities are simultaneously solved for.

Although the linearised method described in Liu *et al.* (2010) avoids the bias inher-

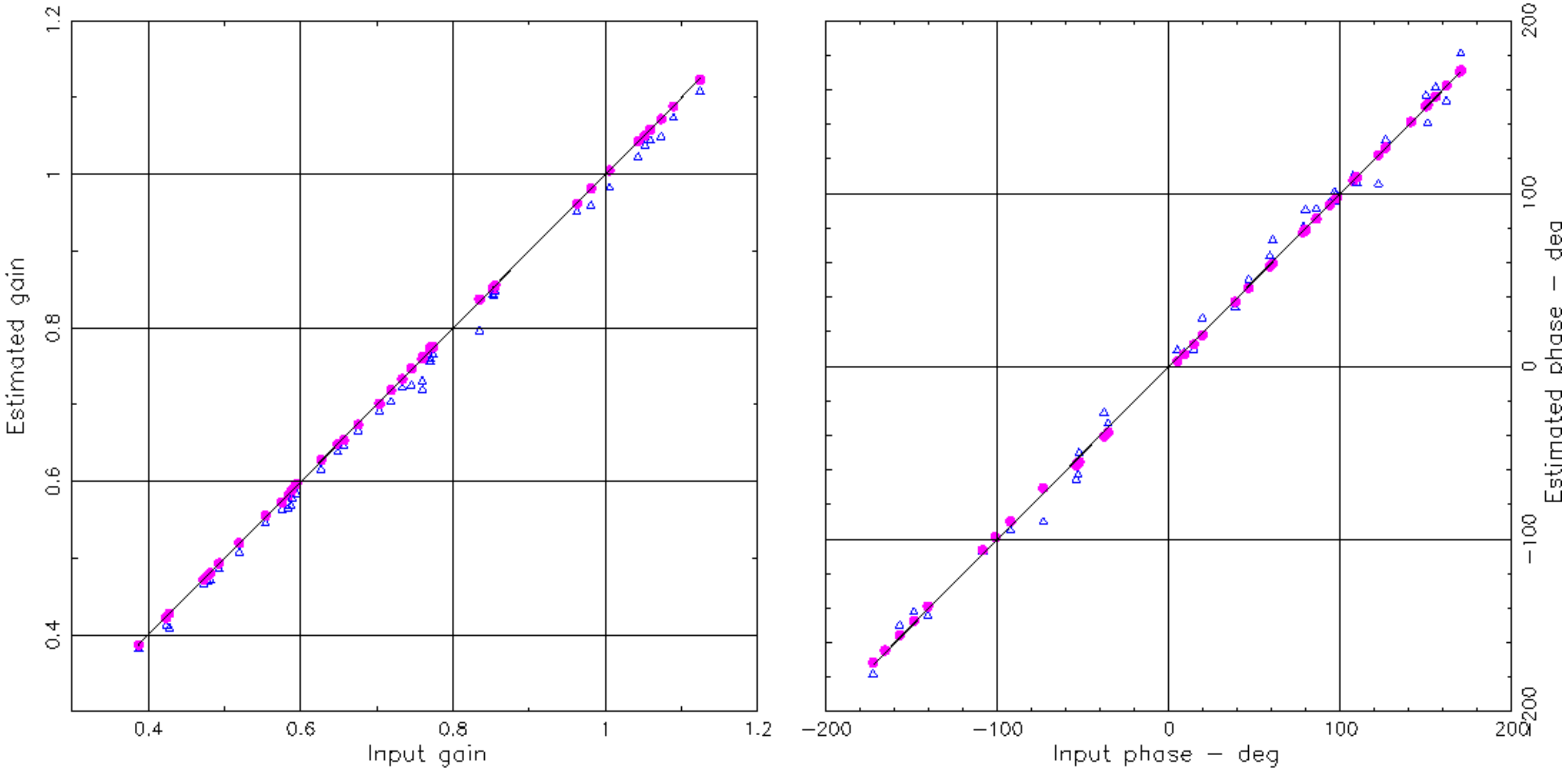

Figure 4.3: The comparison between the antenna gain amplitudes and phases as estimated by the logarithmic method of Wieringa (1992) and the NLS method is described here. The SNR per visibility is 10, and the input model is the simplest possible, viz. a single source at the phase centre. The solid line represents the ideal situation where the estimated values are equal to the input values. As can be seen, even for this simple model and at this relatively good SNR, the logarithmic method gives biased estimates, shown here as the open circles. In contrast, the NLS estimates, shown by the filled triangles, are not biased. Liu *et al.* (2010) discuss a linearised logarithmic method which removes this bias, but which is computationally significantly more expensive.

ent in the logarithmic methods, it is computationally significantly more expensive than the Wieringa (1992) method. Figure 4.5 shows the time taken by the Liu *et al.* (2010) and NLS algorithms as a function of the total number of antennas. The run times exclude the time taken for data I/O from the disk. The linearised algorithm of Liu *et al.* (2010) clearly shows a N_A^4 dependence, whereas the NLS[1] algorithm behaves as N_A^2: this means that the time taken by the algorithm to converge to the best solution scales as the number of baselines. We note that there was no explicit multi-threading in our implementation, nor was compiler optimisation turned on. The NLS algorithm is significantly faster, and is therefore potentially very attractive for real-time calibration.

Since calibration is essentially an estimation problem, it is natural to ask what the errors on the estimated parameters (i.e. the gains and visibilities in this case) are, and how the errors obtained via the NLS algorithm compare with fundamental bounds on the error, viz. the CRB. It has already been shown rigorously (see equation 4.63) that the error covariance matrix and the Hessian are related. In Figure 4.6 are shown the “kite plots”: the Hessian and covariance matrices. Further, if the measurement errors are independent and identically distributed (i.i.d) Gaussian noise, then the Hessian matrix, except for the sign, is equal to the Fisher information matrix. This is true for any exponential family of distribution and therefore holds for Gaussian. The variances estimated from the Fisher Information matrix equal the CRB. The parameter errors estimated in this way would hence be a lower bound to the true error. Figure 4.7 shows a comparison between the mean ensemble error obtained from the simulations for runs with different system temperatures i.e. with different signal-to-noise ratios. The ensemble errors attain the CRB when the SNR $\gtrsim$ 10.

4.4 Discussion

Let us return to a discussion on the Hessian and covariance matrices shown in Figure 4.6. These matrices are clearly diagonally dominant. A good approximation to the variance can hence be obtained quickly by approximating the Hessian matrix to be diagonal. In the simulation described above, this approximation leads to a difference of only $\sim$ 1% in the values of the estimated standard deviation. Since the diagonal approximation simplifies the inversion of the Hessian, we could adopt this approximation in the Levenberg-Marquardt algorithm to refine the step size dynamically after each

---

[1] Jan Noordam, while reviewing our work in Marthi & Chengalur (2014), communicated to us that the NEWSTAR package used for WSRT data analysis also uses a steepest descent method which leads to N_A^2 performance, but when the redundant structure of the calibration problem is properly exploited.

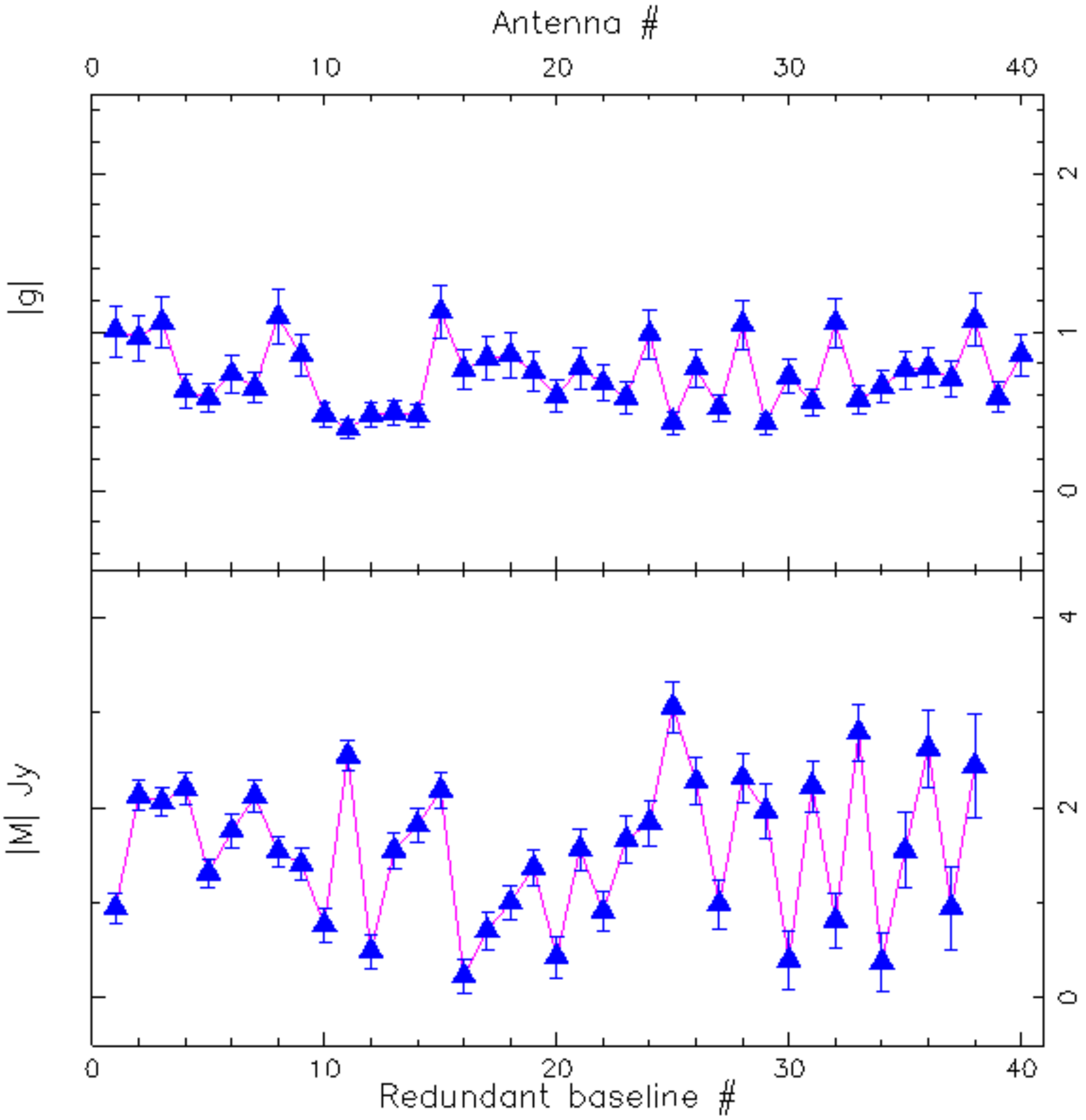

Figure 4.4: The solutions, with their error bars obtained from a sky model with sources following the radio source counts relation (Wieringa, 1991; Sirothia *et al.*, 2009) but without the clustering properties, are shown here. The signal-to-noise ratio for a 2 Jy radio source is 4, which can be considered to be the mean SNR over all baselines. The upper panel shows the amplitudes of the gains and the lower panel shows the visibilities. The solid line connects the true solutions and the filled triangles are the estimated solutions. The error bars on the estimated gains have been magnified by a factor of 10 and those on the estimated visibilities by a factor of 5 to enable them to be seen clearly.

iteration to attain the most rapid convergence. However, we do find that a constant step-size is indeed adequate.

As stated in Section 4.1 we have been assuming that the beamshapes of the individual antenna elements are identical, and that the ionospheric phases can be lumped together with the electronic gains of the elements. In general these assumptions are only approximately true. Further, we have been only dealing with a scalar equation, whereas, in the presence of phenomena which mix the two polarisations (e.g. differential Faraday rotation) across the array, receptors whose response is not perfectly orthogonal, (i.e. suffer from "leakage", "ellipticity", which themselves could in general vary across the field of view) it is not possible to decouple the calibration of the nominally orthogonal polarisations. High dynamic-range imaging would require one to address all of these issues, and there have been a number of algorithms proposed (dubbed "3GC" calibration algorithms; see e.g. Bhatnagar *et al.* 2008; Noordam & Smirnov 2010; Smirnov 2011) to address these issues. A further issue that is relevant in dealing with dipole arrays (as is the case for OWFA) is that there could be mutual coupling between the elements. However, here are some considerations which suggest that the approximations made above are reasonable to first order for the problem at hand.

- Firstly, ORT measures only the polarisation along the length of the telescope, i.e. north-south. The dipoles are hence arranged end-to-end, a configuration that one would intuitively expect to minimise mutual coupling. Our measurements have determined that the coupling between the dipoles is indeed negligible (see Section 2.4.1). Infact, independent measurements of the sensitivity indicate that the sensitivity of the ORT increases linearly with the number of dipole signals added, again suggesting that mutual coupling can be ignored to first order.

- Further, since the ORT is equatorially mounted, the beams do not rotate in the sky as it tracks the source, and hence to the extent that the different sections have identical beams, the calibration issues are greatly simplified. Interestingly, this means that the baseline lengths will also be fixed as it tracks the source, meaning that each element pair measures the same sky visibility at all times (see Sections 2.2.2.2 and 2.2.2.3).

- Finally since the "array" is small (530m), Mode-I of the upgrade (which breaks the array up into 40 elements) falls within Lonsdale's regime 1 (Lonsdale, 2005), where the traditional solution to the ionospheric phase suffices. Mode-II, where every ∼2m segment of the telescope is digitised (i.e. a compact array, wide field of view, although note that even in this case, the E-W field of view is limited to

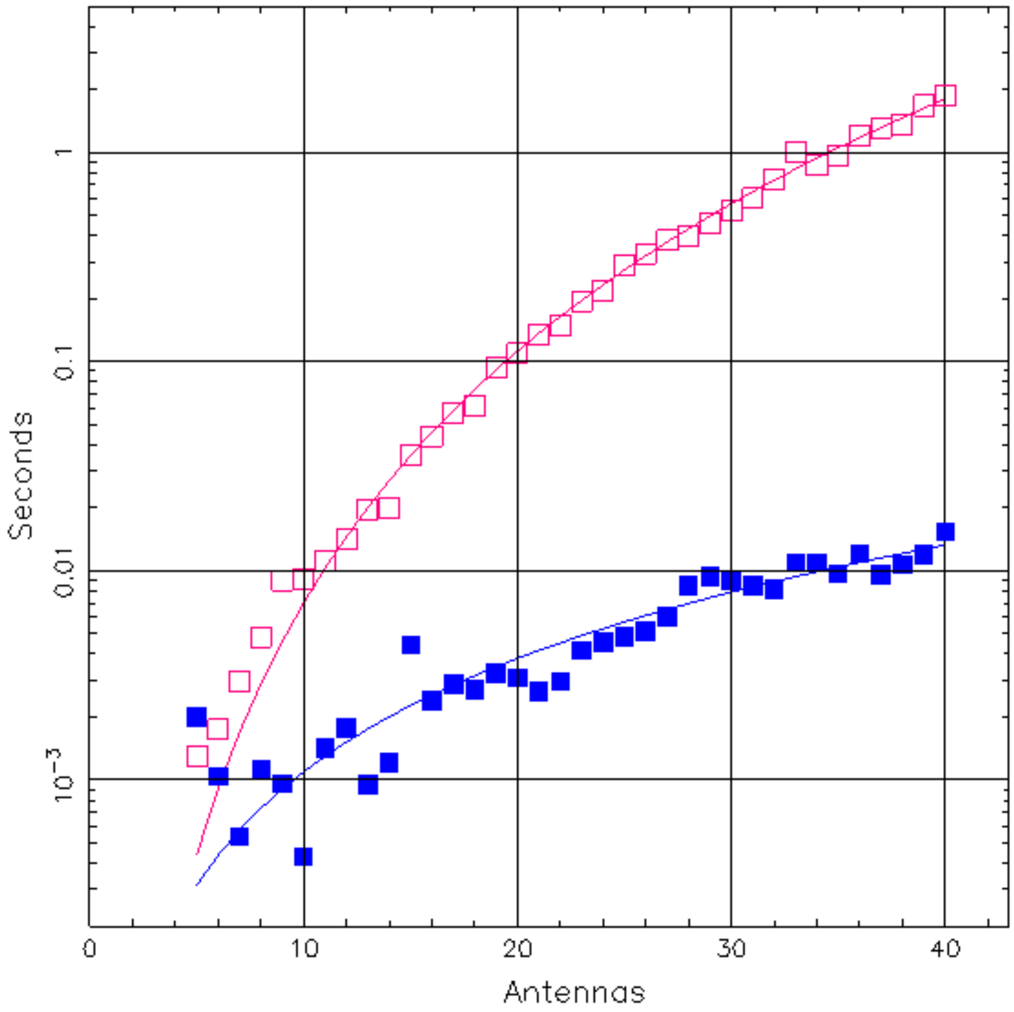

Figure 4.5: Plot showing the comparison between the time taken for the two algorithms: the linearised method by Liu *et al.* (2010) and the NLS method described in this chapter. The plot shows the time taken by the algorithms (excluding the time taken for disk I/O) as a function of the number of antennas in the array. The sky model is generated from the known source counts at 325 MHz, and the average SNR per visibility is ≈ 4. The filled squares show the time taken by the NLS algorithm for different number of antennas, and the open squares show the corresponding time taken by linearised method of Liu *et al.* (2010). The corresponding solid lines show the empirical curves of the form $a.x^n$ with $a = 7.0{\times}10^{-7}, n = 4.0$ and $a = 8.2{\times}10^{-6}, n = 2.0$ for the Liu *et al.* (2010) and NLS methods respectively, clearly reflecting the structure of the algorithm.

> 2° because of the reflector) would fall into Lonsdale's case 3 where each source in the field of view could be shifted by a time variable offset, that would need to be calibrated for.

It is to be noted that the NLS algorithm suggested above would also be useful to quantify the importance of such effects. Residuals obtained after calibration between the visibilities measured on nominally redundant baselines would be indicative of the importance of the direction dependent effects.

The observing band is usually split into N channels, and the complex response of the telescope is a function of frequency as well. Therefore, any calibration has to account for the spectral behaviour as much as the temporal. There could be a channel-to-channel variation of the gain itself, and a fixed delay in the electronics would also translate into different phases at different frequencies, causing a phase-ramp across the band. For OWFA, we achieve bandpass calibration by applying the NLS redundancy calibration algorithm independently to every channel. Since the gain is expected to vary smoothly across frequency channels, one could use the solution in one channel to seed the solutions for the next channel. However, this will not be ideal in algorithms which parallelise across channels. In that case, each channel will have to be independently calibrated and the final bandpass calibration can be done by scaling the channels individually through external calibration.

4.5 Results from real data - an example

The NLS steepest descent calibration algorithm was demonstrated on simulated data, and it was also established through Figure 4.7 that it is efficient and statistically optimal. We shall now see the results of redundancy calibration on real data. These data were obtained on 28 January 2014 during a test run. The telescope was pointed at the Crab nebula and the data were recorded for two minutes. These data were recorded with an early prototype, i.e. the Phase-I system described in Prasad & Subrahmanya (2011), of which only one quarter was used here. Specifically, the ten antennas from S01N to S05S were used, resulting in 45 baselines. The data were taken on the Crab nebula. The model visibilities recovered from "channel zero", in this case the central channel (channel 32) are shown in Figure 4.10. The recovered flux has an amplitude of ~ 2.45 Jy. The data shown here were recorded on the target for the entire 2-minute observation and no other source was observed to serve as a calibrator. The bandpass responses of the baselines are shown in Figure 4.8 for the S03 data from Phase-I, before bandpass calibration. Figure 4.9 shows the bandpass response of the same baselines after bandpass calibration. Figure 4.11 shows a part of the pre-calibrated visibility

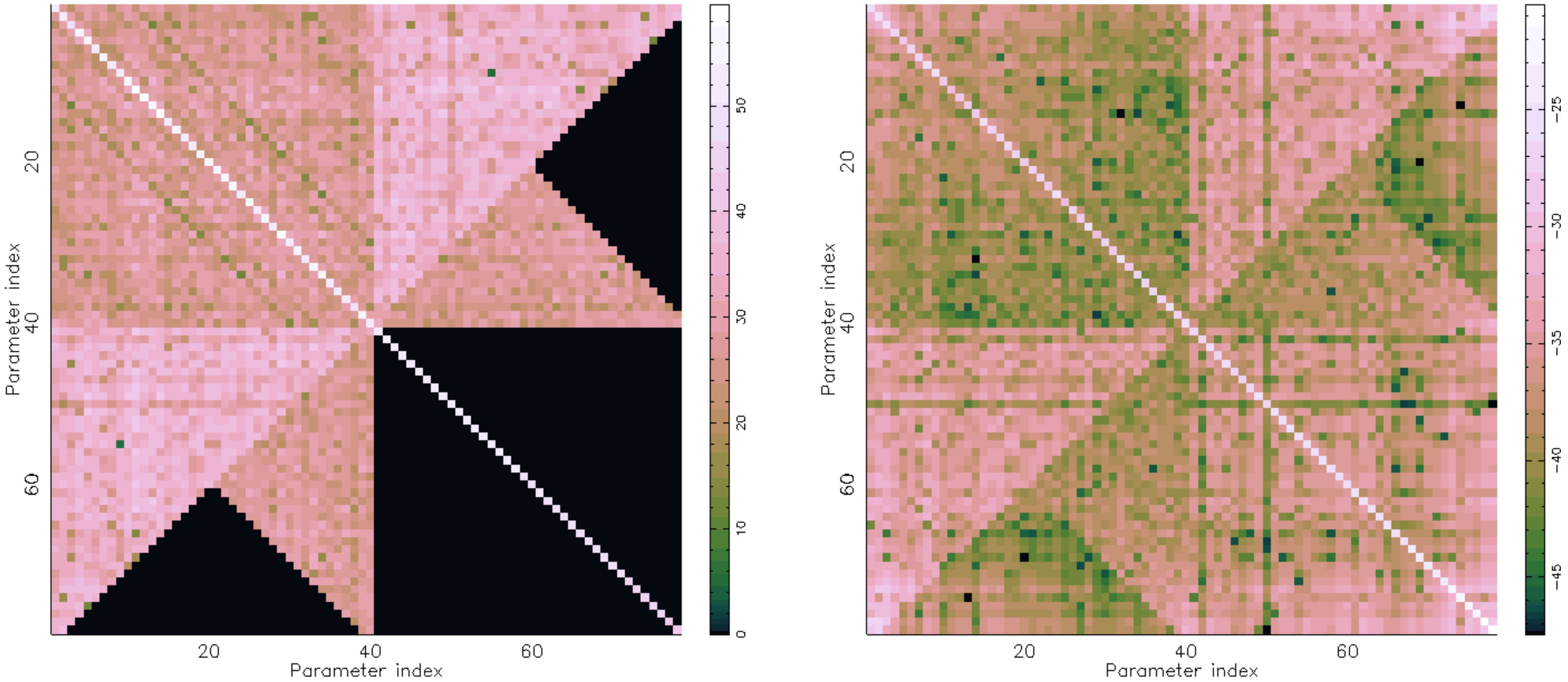

(a) Hessian matrix of the estimated parameters

(b) Covariance matrix of the estimated parameters

Figure 4.6: The kite plots: (a) shows the magnitude of the complex elements of the Hermitian-symmetric Hessian matrix, and (b) shows the magnitude of the complex elements of the Hermitian-symmetric covariance matrix, both given in decibel ($10\ log_{10}(.)$) scale to accommodate the large contrast. The matrices are both 78×78 elements across, with the first 40 elements on each side corresponding to the errors on estimated complex antenna gains $\widehat{g}_i$, and the next 38 elements, the errors on the estimated model visibilities $\widehat{M}_{|i-j|}$. The diagonal elements of the matrices are, of course, real. The full range of grayscale intensity is exploited here using the "cubehelix" mapping scheme (Green, 2011).

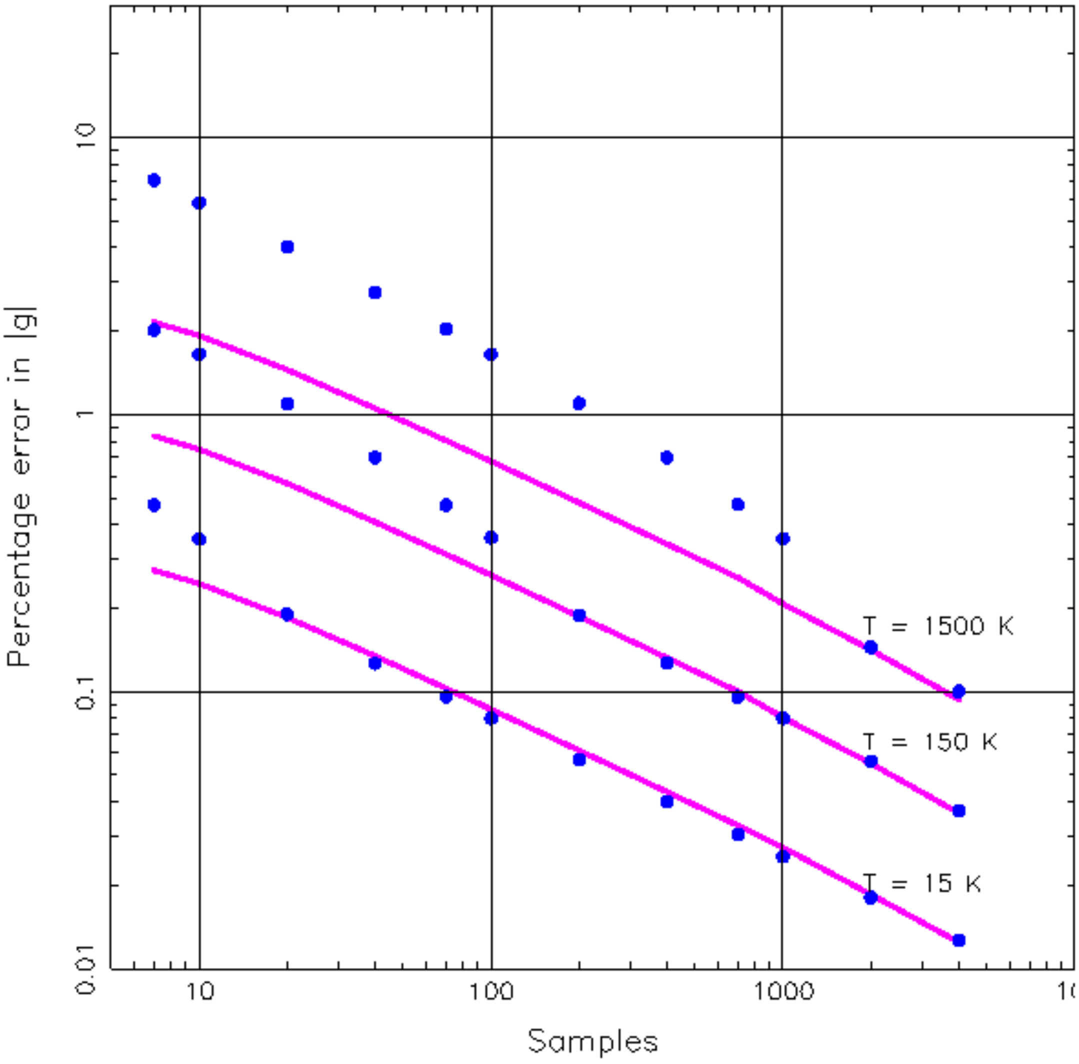

Figure 4.7: This figure shows the behaviour of the error on the antenna-averaged gains for three different system temperatures. The filled circles represent ensemble errors obtained from the Monte Carlo run, whereas the solid line is the Cramér-Rao bound. At lower system temperatures, the errors reach the CRB upon integration of fewer samples. At $T_{sys} = 1500$ K, for example, many more samples would have to integrated than at $T_{sys} = 150$ K to attain the CRB.

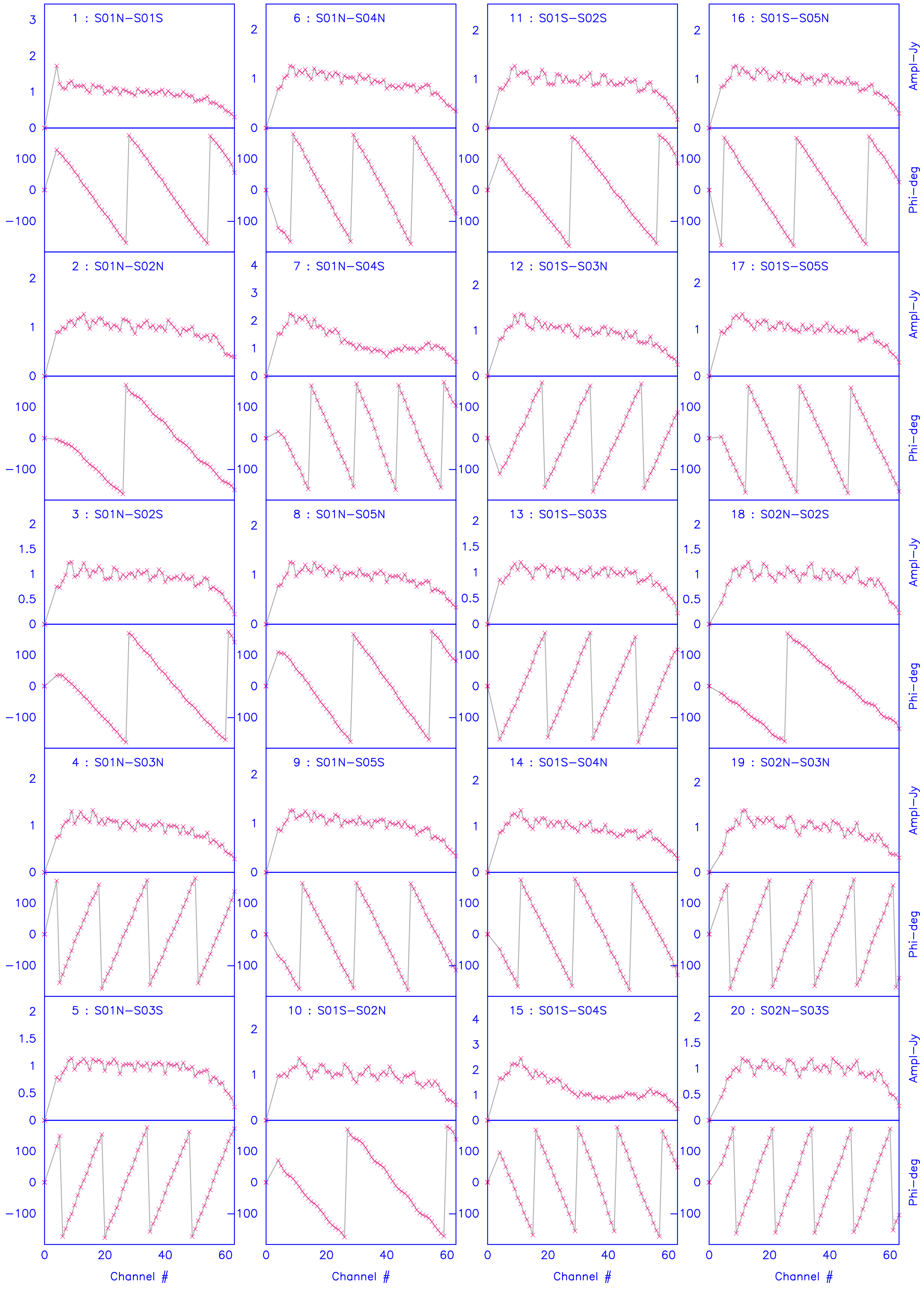

Figure 4.8: The bandpass response of some of the baselines of the earlier Phase-I system, of which only a quarter was operational, is shown here before bandpass calibration. The bandpass plots are derived over a 19-MHz band split into 64 channels on an observation centered on the Crab nebula.

Figure 4.9: The bandpass response of the baselines of Figure 4.8 is shown here after bandpass calibration.

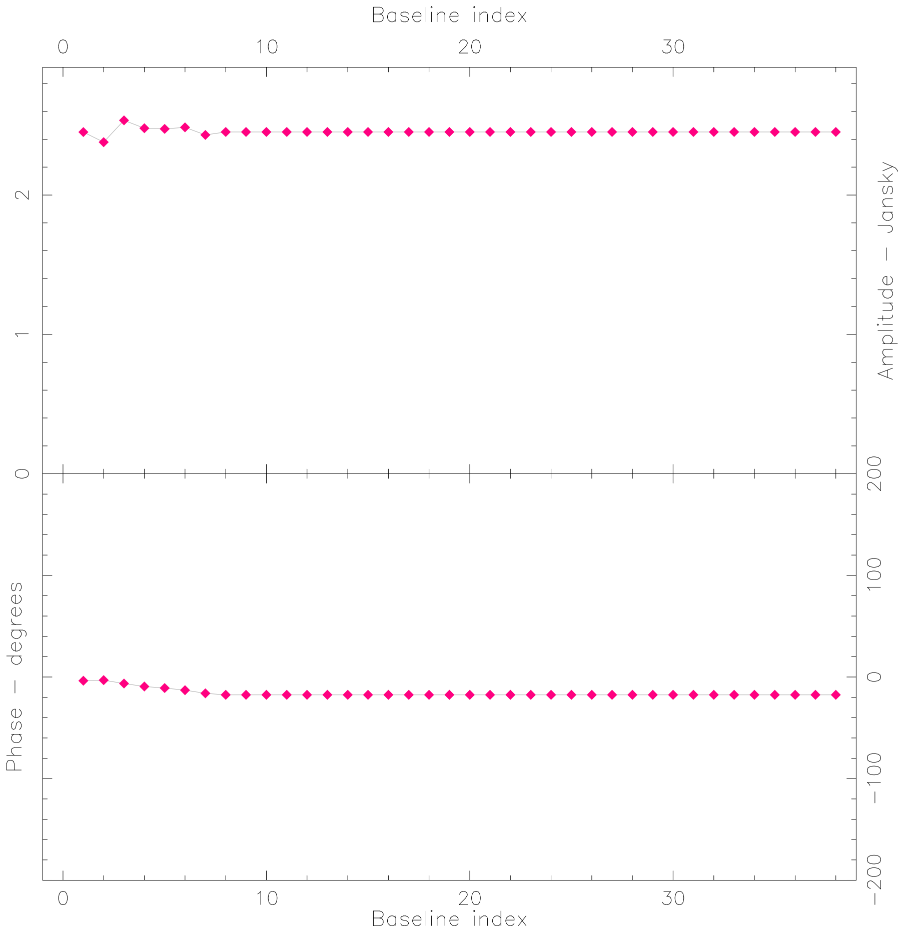

Figure 4.10: The model visibilities recovered from channel-32 for the Crab nebula, from the 10-antenna Mode-I prototype system. Here, the absolute scale has not been set. Since Crab is a very bright source, he error bars on the recovered visibilities and phases, obtained from the Hessian, are so small that they are not visible in this plot.

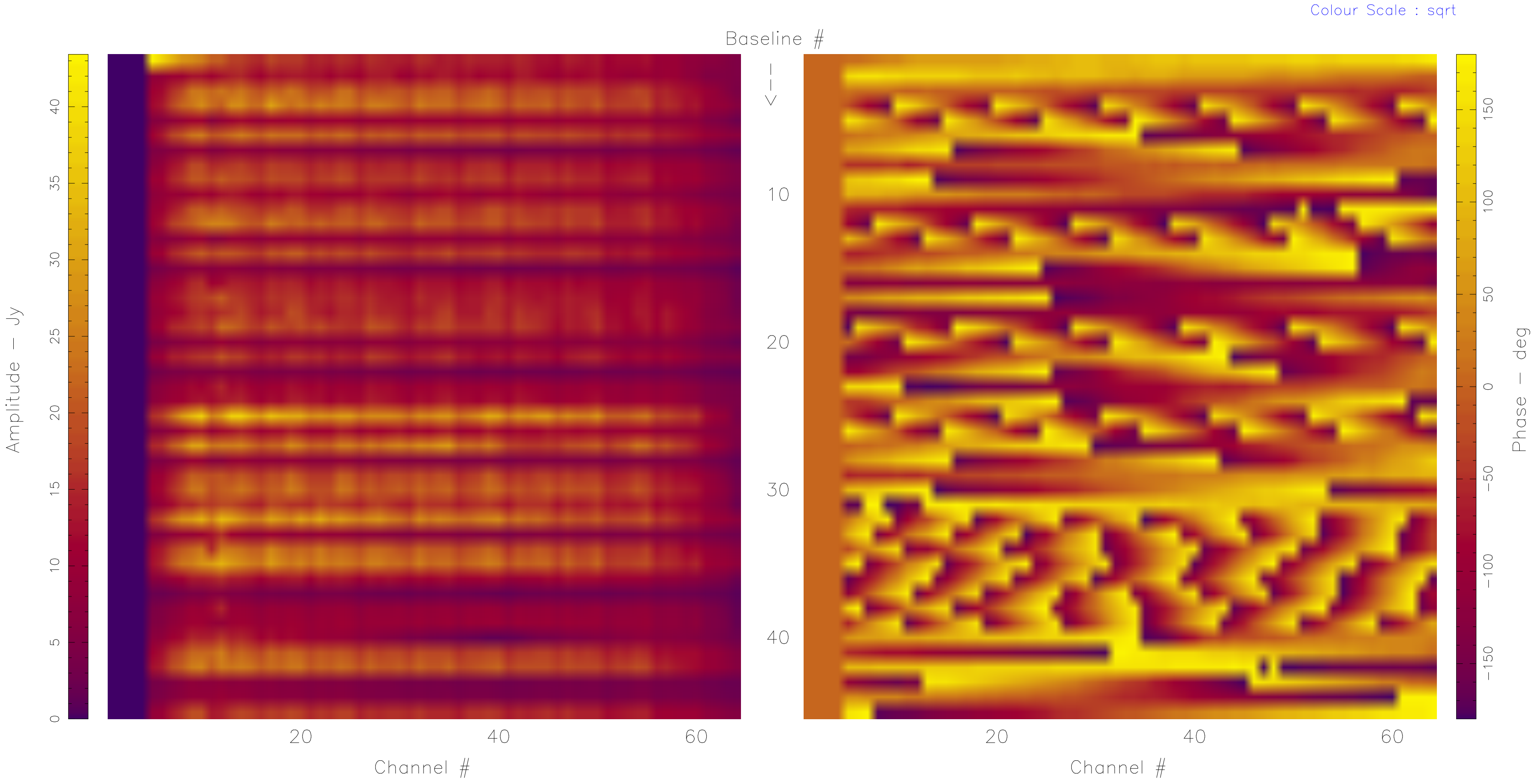

Figure 4.11: The 19-MHz band split into 64 channels, observing the Crab nebula. One record (one second) is shown from the 2-minute observation. The uncalibrated data show different baseline-wise fluxes and the phases ramping across the band.

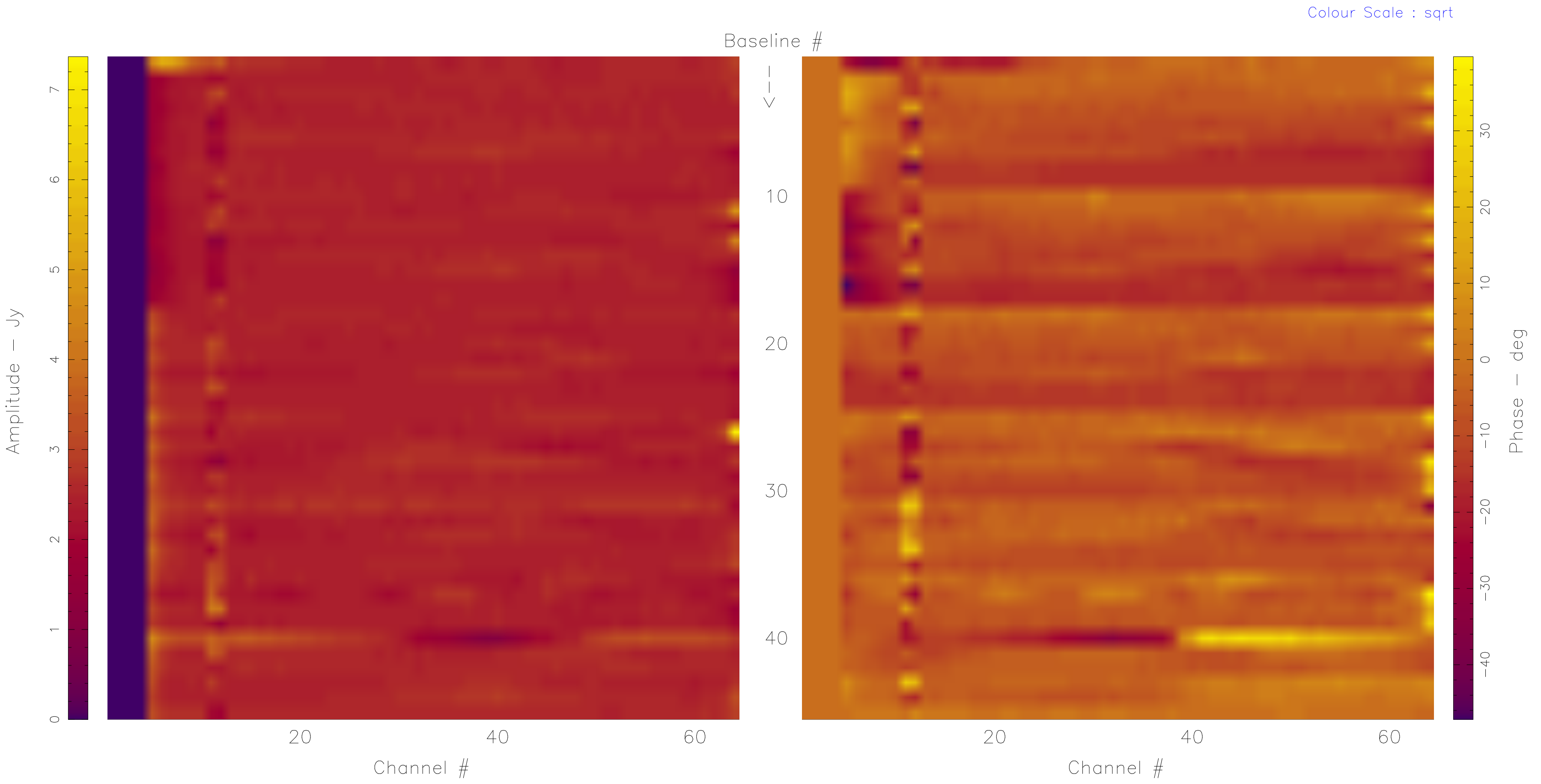

Figure 4.12: The 19-MHz band split into 64 channels, observing the Crab nebula. One record (one second) is shown from the 2-minute observation. The calibrated data show almost equal baseline-wise fluxes and the phases aligned across the band.

data and Figure 4.12 shows the calibrated data. In these three figures, the first two channels (0 and 1) have been blanked as they are corrupted. Channels 11 and 12 appear to be corrupted by RFI, and calibration appears to have been ineffective on baseline 40, which is indicative of bad data: the phase across the band still remains wound. It is clear that the first round of calibration has revealed bad channels and baselines. Similarly, bad time instants stand out after calibration as well. It appears then that the first round of calibration has aided identifying pathological data, suggesting its exclusion and re-calibration of the remainder of the good data. Absolute calibration has not been applied to this observation.

4.6 Post-correlation beamforming

Having dwelt on calibration at length, we could perhaps turn our attention to an application. Beamforming is a spatial filtering technique, often employed to improve the signal-to-noise ratio of time-series data. This technique is particularly useful for studying time-variable phenomena. In cases where the time variation of the signal is slow because it is either intrinsic or the dispersion within a channel is too large to be corrected for, post-correlation beamforming could be effective. The difference between pre- and post-correlation beamforming is only the missing auto-correlations in the latter. However, of course the visibilities have to be calibrated and rotated to the location of the desired beam.

For OWFA, the projected length U_n of the baseline between a pair of antennas separated by a distance nd is

$$U_n = nd\ cos\,\delta \tag{4.64}$$

when observing a source at delination δ_0. The path length difference l between an adjacent antenna pair as looked at from the direction (α, δ) towards which the beam is to be formed, is given by

$$l = u\ sin(\delta - \delta_0) \tag{4.65}$$

where $u = d\cos\delta_0$. The phase difference corresponding to this path length difference at a given wavelength λ is

$$\phi\ = 2\pi\frac{l}{\lambda}\quad = 2\pi\frac{d\ cos\delta_0\ sin(\delta - \delta_0)}{\lambda} \tag{4.66}$$

Therefore the phase difference between a pair of antennas separated by distance nu is

$n\phi$. The beam is formed towards the source at (α, δ) by taking the sum over all the ${}^{N_A}C_2$ baselines:

$$V_b(t, \nu) = \frac{2}{N_A(N_A - 1)} \sum_{i=1}^{N_A} \sum_{j \neq i}^{N_A} V_{ij} \; e^{-i|\phi_j - \phi_i|} \tag{4.67}$$

where N_A is the number of antennas, and V_{ij} is the visibility from the baseline consisting of antennas i and j, and the phase argument of the complex exponential adjusts for the extra phase accrued to the visibility from δ with respect to δ_0. The phases across the array form a linear gradient; the sign and slope of the gradient determine the direction of the beam. Figure 4.13 and Figure 4.14 show the amplitude and phase response for the beam obtained off and on Crab respectively with data from the S03 antenna of the prototype Phase-I. In this particular case, the beam is formed towards the center of the pointing direction: therefore the phase corrections are all identically zero. However there is no loss of generality here, as this can be treated as a particular case of the general direction of the beam δ_b being equal to δ_0. These data were taken at a date later than 28 January 2014, on which day the data for which the calibration results are shown in Section 4.5 were taken. The amplitude of the visibility after calibration is $\sim$ 1.3 Jy, where again, an external calibration scale has not been applied to these data. In the absence of external calibration, identical flux values cannot be guaranteed for the calibrated visibilities from different observations on the same target.

4.7 Conclusions

Calibration is the process of estimating the true signal and the instrument gains; it is a fundamental step in radio interferometric data analysis. In this chapter, two different classes of redundancy calibration have been described: (1) the linear least squares method which estimates the gain and visibility phasors, and (2) the non-linear least squares method which directly estimates them as complex numbers on the Argand plane. The logarithm-based LLS algorithm due to Wieringa (1991) is a simple one-step process for OWFA, as the measurement matrix A depends only on the geometry. It never changes and its inverse has to be computed just once. However, it suffers poor performance when the SNR is not sufficiently high: the solutions are biased. The linearised Gauss-Newton algorithm of solving for the gains and visibilities due to Liu *et al.* (2010) avoids the bias whereas its measurement matrix B depends on the array geometry as well as the data. Therefore it has to be computed at regular intervals. Moreover, it is compute-intensive as the typical complexity of operation goes as N_A^4

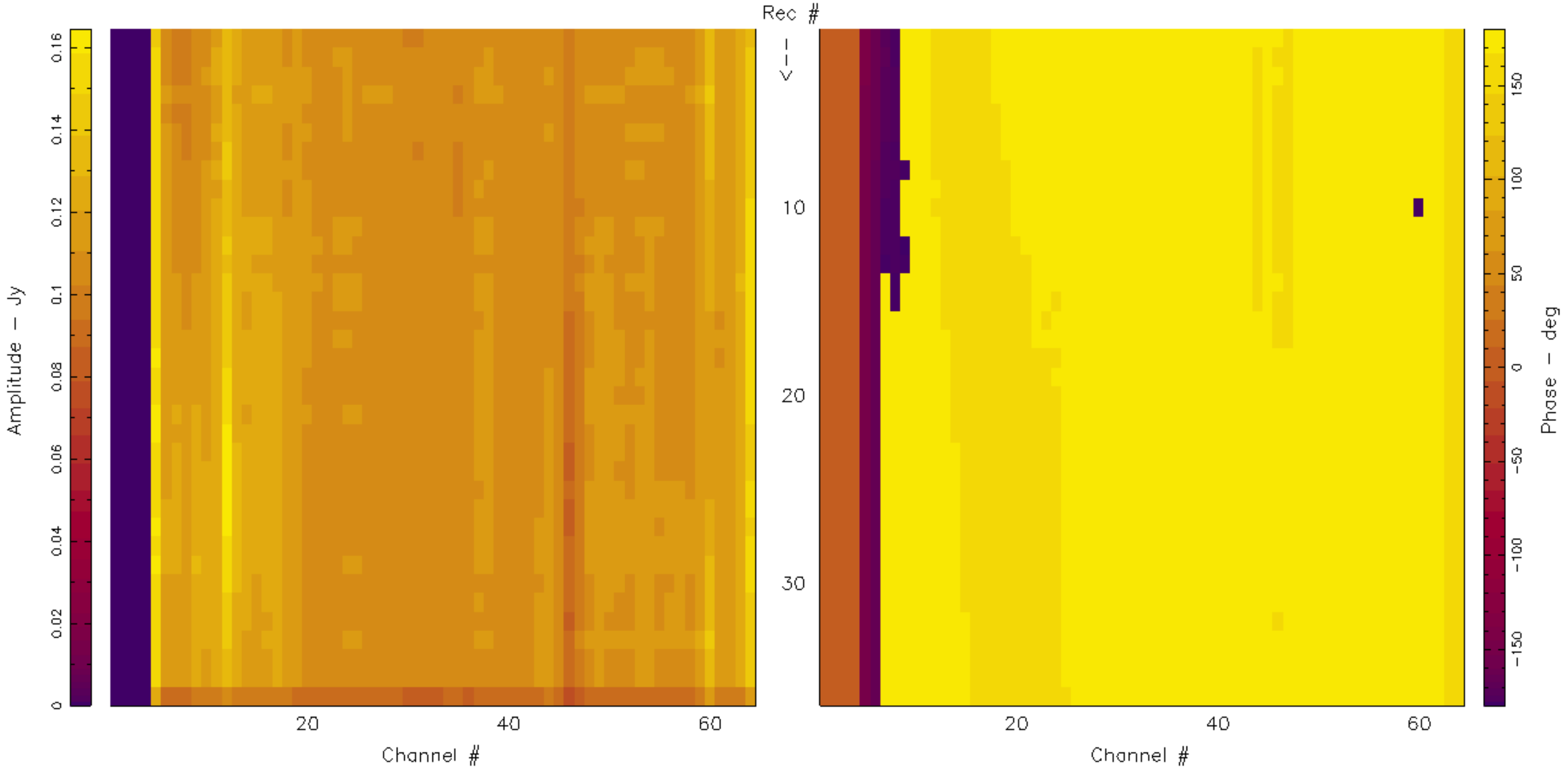

Figure 4.13: This plot shows the actual amplitude and phase response across the band for a beam off the source. The per-channel RMS error in amplitude is 1.0×10^{-3} Jy and in phase is 0.32°. The phase is not centered at 0°, since there is little signal off the source. The first four channels have been blanked and set to zero.

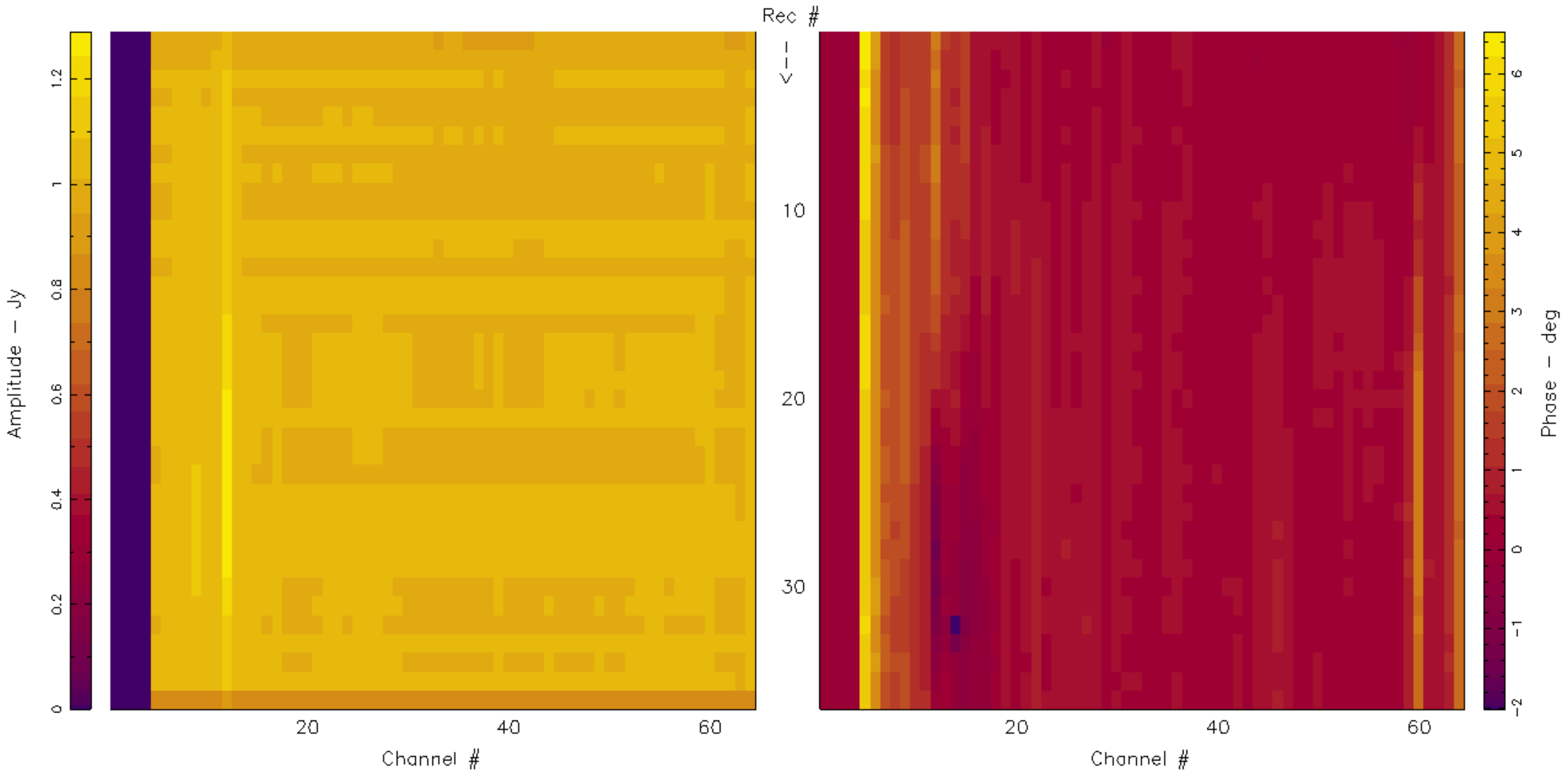

Figure 4.14: This plot shows the actual amplitude and phase response across the band for a beam on the source. The per-channel RMS error in amplitude is 1.5×10^{-2} Jy and in phase is 0.25°. The phase is centered at 0°, except in the few bad channels. The first four channels have been blanked and set to zero.

(see Figure 4.5).

The non-linear least-squares iterative algorithm, based on a steepest descent implementation avoids the bias (see Figure 4.3) inherent in the logarithmic LLS algorithm, as well as runs much faster than the Taylor expansion-based linearisation algorithm. It is shown to be an efficient and a minimum variance unbiased estimator by achieving the CRB. It is used in an implementation of bandpass cailbration. Results from simulated data establish the statistical optimality of the estimator and its efficacy. Besides, results from real data appear to indicate that the calibration algorithm is indeed very effective. It is also amenable to straightforward real-time implementation as it avoids matrix inversions. Besides, very fast convergence is achieved as the vector $\widehat{\mathbf{\Theta}} = [\,\widehat{\mathbf{g}} \;\; \widehat{\mathbf{M}}\,]$ needs only to be updated from the previous instant: the estimator tracks the gain and visibility vectors efficiently. Redundancy calibration nevertheless is very similar to self-cal inasmuch as it results in the measurement plane or image plane ambiguity. It is immune to either plane being rotated, equivalent to a phase gradient along the array or a systematic image shift in the celestial sphere. This ambiguity would necessarily have to be resolved through external calibration. Coherent post-correlation beamforming is a useful application for studying slow transients with high SNR. An example was shown with a coherent beam on the target radio source at the pointing direction, without loss of generality.

Chapter 5

The dominant foregrounds and the HI signal

5.1 Introduction

The Ooty Wide Field Array is designed to operate at 326.5 MHz, with a bandwidth of $\sim$ 39 MHz. At the centre frequency, the HI 21-cm wave is stretched to a wavelength of $\sim$ 91 cm andthe telescope is sensitive to the HI 21-cm emission from a redshift of $z \sim 3.35$. However, that is not the only astrophysical signal the telescope is expected to be sensitive to. Besides the HI signal we are interested in, the telescope is invariably sensitive to astrophysical foregrounds. Foregrounds can be broadly defined as all the emission from astrophysical sources other than the cosmological HI signal. In this thesis, two distinct foreground emission components are considered:

- the diffuse Galactic synchrotron foreground arising from the tenuous, ionised component of the interstellar medium of the Milky Way
- the extragalactic foreground comtribution from discrete extragalactic radio sources beyond the Milky Way

The origin and nature of this foreground emission is reasonably well understood. The diffuse Galactic synchrotron foreground component arises from relativisitic cosmic ray electrons (CRe) spiralling in the interstellar magnetic fields. The distribution of their energies is a well known power law (Ginzburg & Syrovatskii, 1965, 1969). It follows from the electron energy distribution that the radio synchrotron brightness temperature follows the same spectral power law. Many different studies over a wide range of radio frequencies have attempted to understand and characterise the Galactic diffuse emission, such as Turtle & Baldwin (1962) and Turtle *et al.* (1962) at 26 MHz, 178 MHz and 400 MHz, Alexander & Novaco (1974) at ∼ 4 MHz, Haslam *et al.* (1982) at 408 MHz, etc. de Oliveira-Costa *et al.* (2008) summarise all such previous studies (references therein) and propose a global model that encompasses over four decades of radio wavelengths from 10 MHz to 100 GHz. The extragalactic point source foreground component has been studied in detail through many surveys (e.g. Condon, 1989; Hopkins *et al.*, 1998; Richards, 2000; Hopkins *et al.*, 2003; Seymour *et al.*, 2004; Huynh *et al.*, 2005; Simpson *et al.*, 2006; Owen & Morrison, 2008) These seem to fit the observed SEDs very well (see e.g. Toffolatti *et al.*, 1998; González-Nuevo *et al.*, 2005). There have been numerous attempts at measuring the foregrounds for use in 21-cm cosmlology experiments, e.g. by Ali *et al.* (2008), followed by Ghosh *et al.* (2011a,b, 2012), Yatawatta *et al.* (2013), Jelić *et al.* (2014, 2015), Vedantham *et al.* (2015), Franzen *et al.* (2016) and Offringa *et al.* (2016). In this chapter, the two foreground components shall be introduced individually. They are simulated using parameters based on the measurements cited above. Using the realistic foreground model, we can obtain model visibilities for OWFA. The rationale for simulating the foreground components is hence two-fold:

- Ali & Bharadwaj (2014) have made detailed predictions for the HI signal with OWFA, as well as the foregrounds. Their foreground predictions are based on simple analytical models, and they have not considered any instrumental systematics. The instrumental effects are a crucial ingredient in foreground or signal predictions. In this thesis, the effects of the instrument response on foreground predictions for OWFA are studied.
- Foreground removal is possibly the most important step in realising a detection of the HI signal. Unless the foregrounds are characterised well and estimated robustly, its removal would remain a distant reality. Power spectrum estimation of foregrounds affected by the instrument response is a realistic scenario, and we may do well to understand and quantify such effects for OWFA. Simulations can definitely serve to enlighten us with the limitations posed by the instrument, and allow us to find avenues of mitigating such effects through new techniques, or devising alternative foreground removal schemes.

5.2 The diffuse Galactic synchrotron foreground

5.2.1 Statistical parameters from observations

The diffuse Galactic synchrotron emission has been studied extensively. The Haslam map (Haslam *et al.*, 1981, 1982) gives a consistently calibrated all-sky map of the brightness temperature at 408 MHz. La Porta *et al.* (2008) have determined the mean angular power spectrum (APS) from the Haslam total-intensity all-sky map at scales larger than 0.5°. The power law index γ determined from the mean APS is found to take values in the range $[2.6, 3.0]$. Inorder to measure the spectral index α, they compare the 408-MHz maps with 1420-MHz maps (Reich, 1982; Reich & Reich, 1986; Reich *et al.*, 2001; Testori *et al.*, 2001). They derive a spectral index α in the interval [2.9, 3.2] from the mean APS of the two frequencies at $\ell \in [20, 40]$. γ is found to vary systematically with latitude: the angular power spectrum is found to be steeper at higher galactic latitudes. At scales smaller than 0.5°, the index γ has been inferred from a variety measurements at 150 MHz: (a) Bernardi *et al.* (2009) have determined $\gamma = 2.2$ and $A_0 = 253$ mK^2 with the Westorbork Synthesis Radio Telescope (WSRT) observations in a field around Galactic latitude $b = 8°$, (b) Ghosh *et al.* (2012) find $\gamma = 2.34$ and $A_0 = 513$ mK^2 in a field around $b = 14°$ using GMRT, and (c) Iacobelli *et al.* (2013b) determine $\gamma = 1.84 \pm 0.19$ and $A_0 = 100$ mK^2 with LOFAR for the same field observed with WSRT. All the measurements cited above were made at $\ell_0 = 1000$. We can hence conveniently define the angular power spectrum, accounting for frequency scaling, as

$$C_\ell(\nu) = A_0 \left(\frac{\nu_0}{\nu}\right)^{2\alpha} \left(\frac{\ell_0}{\ell}\right)^{\gamma} \tag{5.1}$$

Rogers & Bowman (2008) have determined a mean spectral index $\alpha = 2.52$ in the frequency range 150-408 MHz at high Galactic latitudes. In this thesis, the values $A_{150} = 513$ mK^2 from the GMRT observations of Ghosh *et al.* (2012) at 150 MHz are used. Consequently, following Ali & Bharadwaj (2014), this temperature scale is extrapolated to 326.5 MHz using the mean spectral index $\alpha = 2.52$ from Rogers & Bowman (2008), and $\gamma = 2.34$ again from the GMRT observations of Ghosh *et al.* (2012). Substituting these values, the angular power spectrum at 326.5 MHz, relevant for OWFA, is

$$C_\ell = 513\ \text{mK}^2 \times \left(\frac{150}{326.5}\right)^{2\times2.54} \left(\frac{1000}{\ell}\right)^{2.34} = 10.2\ \text{mK}^2 \times \left(\frac{1000}{\ell}\right)^{2.34} \tag{5.2}$$

5.2.2 Simulating the diffuse foreground

The diffuse Galactic foreground has been simulated in many previous studies. For example, Tegmark *et al.* (2000) adopt a simple power-law prescription to describe the diffuse foregrounds in the CMB context, and Santos *et al.* (2005) for EoR studies. Giardino *et al.* (2002) find from 2.4 GHz Parkes data that the diffuse Galactic foregrounds are well described by a single-index power law. More recently Jelić *et al.* (2008) have simulated the most important foreground components, including the diffuse foregrounds, for LOFAR Eor studies: however, they simulate a 4-D foreground model - three dimensions in space and one in frequency. This method does come at the cost increased computing power and time, but its advantages are attractive. The 4-D model can naturally account for line-of-sight variation of the temperature scale A_0 as well as the index of the power law γ. In this thesis, a prescription based on a single power law for the entire field, similar to Ali & Bharadwaj (2014), is used. Let us assume that the fluctuations in the diffuse Galactic synchrotron brightness temperature are statistically homogeneous and isotropic, described by a Gaussian random field whose statistical properties are completely specified by the angular power spectrum. In addition, assume that the angular power spectrum is well described by a single power law in the entire range of angular scales of our interest, given by equation 5.2. The steps to simulate the diffuse Galactic synchrotron radiation from the angular power spectrum are now described. A concise description can also be found in Choudhuri *et al.* (2014) and Marthi *et al.* (2016).

Consider the model angular power spectrum given in equation 5.2. The Fourier components of the brightness temperature fluctuations are generated on a grid through

$$\Delta\tilde{T}(u,\nu) = \sqrt{\frac{\Omega\, C_\ell(\nu)}{2}}\,(x+iy)\,, \tag{5.3}$$

where Ω is the total solid angle of the simulated field, and x and y are independent Gaussian random variables with zero mean and unit variance. The map of the brightness temperature fluctuations $\delta T(\vec{\theta},\nu)$ is obtained through a Fourier inversion. Alternatively, one can work with the Fourier components of the flux density by scaling equation 5.3 with the conversion factor

$$\frac{\partial B}{\partial T} = \frac{2k_{\mathrm{B}}}{\lambda^2} \tag{5.4}$$

so that

$$\Delta\tilde{S}(u,\nu) = \left(\frac{\partial B}{\partial T}\right)\sqrt{\frac{\Omega\, C_\ell(\nu)}{2}}\,(x+iy) \tag{5.5}$$

The grid is chosen to be $2^n \times 2^n$ in size so that a Fast Fourier Transform can be performed. The brightness temperature distribution on the sky is a real quantity; therefore the two half-planes of the Fourier grid are complex conjugates. This Hermitian symmetry of the Fourier transform has been exploited while populating the 2-D Fourier grid.

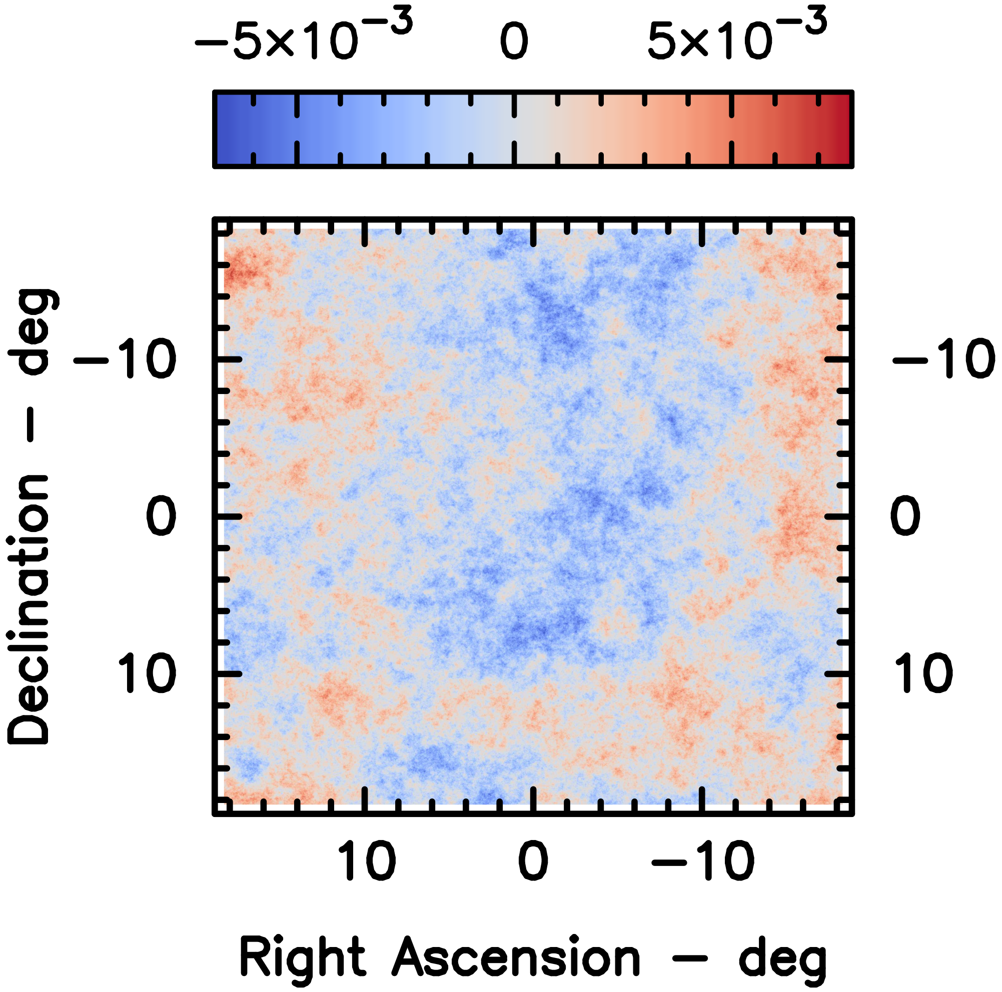

Figure 5.1: The brightness distribution obtained from a temperature distribution of a single random realisation of the diffuse Galactic foreground. This map shows only the fluctuations about the mean, set here to zero, in Jy units. The pixel resolution of the map is $1' \times 1'$ and the map is 2048×2048 pixels across. This map has been simulated at the central channel of the 39-MHz band, at which the frequency is 326.5 MHz.

The inverse FFT results in a 2-D brightness temperature distribution as a function of sky co-ordinates. The map is 2048×2048 pixels across, with a pixel resolution of $1' \times 1'$. The angular extent of each side is $\sim 38°$. The zero-frequency value, which corresponds to the mean temperature about which these fluctuations occur, can be set to zero since an interferometer does not measure the zero spacing visibility. An example distribution produced in this way is shown in Figure 5.1.

How does the spectral index α of the diffuse emission fold into the simulated map? The scaling from 150 MHz to 326.5 MHz is already in place; this means that the specific intensity map at the channel at which the frequency is 326.5 MHz is correctly represented. The specific intensity in other channels has to be scaled appropriately to give the diffuse foreground an "in-band" spectral shape. This can be done in the following manner: we scale the specific intensity in the central channel by the ratio of the frequencies of the two channels, raised to the spectral index $\alpha - 2$, bearing in mind that we are scaling flux, not temperature.

$$S(\theta, \nu) = S(\theta, \nu_0) \times \left(\frac{\nu_0}{\nu}\right)^{\alpha - 2} \tag{5.6}$$

This step completes our simulation of the diffuse Galactic foreground. In **Prowess**, the map is available as a FITS cube with the sky co-ordinates in each plane of the cube, and channel frequency for the third axis of the cube.

5.2.3 Validating the diffuse foreground simulation

The simulation can be quickly validated as follows: The simulated foreground flux density fluctuation map $\Delta S(\theta, \nu)$ is inverse-Fourier transformed to $\Delta\tilde{T}_B(\mathbf{U}, \nu)$. To recover the power spectrum without applying an estimator, the whole $\mathbf{U}$ range is then divided into 20 equally spaced logarithmic bins. The angular power spectrum is estimated using $\Delta\tilde{T}_B(\mathbf{U}, \nu)$ of all the grid points in a particular bin, corresponding to an annulus in the Fourier plane. Since there is no weighting of the simulated foreground map, there is no scaling after the Fourier transform: the recovered power spectrum matches the input power spectrum. Figure 5.2 shows the result of this validation exercise.

In reality, the sky brightness distribution is weighted by the primary beam power pattern. Therefore, we multiply the simulated flux density map $\Delta S(\theta, \nu)$ by the primary beam $A(\theta, \nu)$. This is inverse Fourier transformed after scaling by equation 5.4 to give $\Delta\tilde{T}_B(\mathbf{U}, \nu)$ on the same grid we originally started with. If the FT on the grid now is the original temperature fluctuation power spectrum convolved with the FT of the primary beam pattern, we must recover a convolved version of the original power spectrum $C_\ell(\nu)$. The Fourier pair given below makes the above statement valid:

$$\delta T(\theta, \nu) \times A(\theta, \nu) \overset{F}{\rightleftharpoons} C_\ell(\nu) * \tilde{A}\left(\frac{\ell}{2\pi}, \nu\right) \tag{5.7}$$

where $\ell = 2\pi\mathbf{U}$. Under the assumption that the value of $C_\ell(\nu)$ does not change much within the width of the function $|\tilde{A}(\mathbf{U} - \mathbf{U}')|^2$, the convolution of C_ℓ by $\tilde{A}(\mathbf{U})$ can be approximated as a product (Ali & Bharadwaj, 2014):

$$\langle \Delta\tilde{T}_B(\mathbf{U}, \nu) \Delta\tilde{T}_{B*}(\mathbf{U}, \nu) \rangle = \left[\int d^2\mathbf{U}' |\tilde{A}(\mathbf{U} - \mathbf{U}')|^2\right] C_\ell(\nu) \tag{5.8}$$

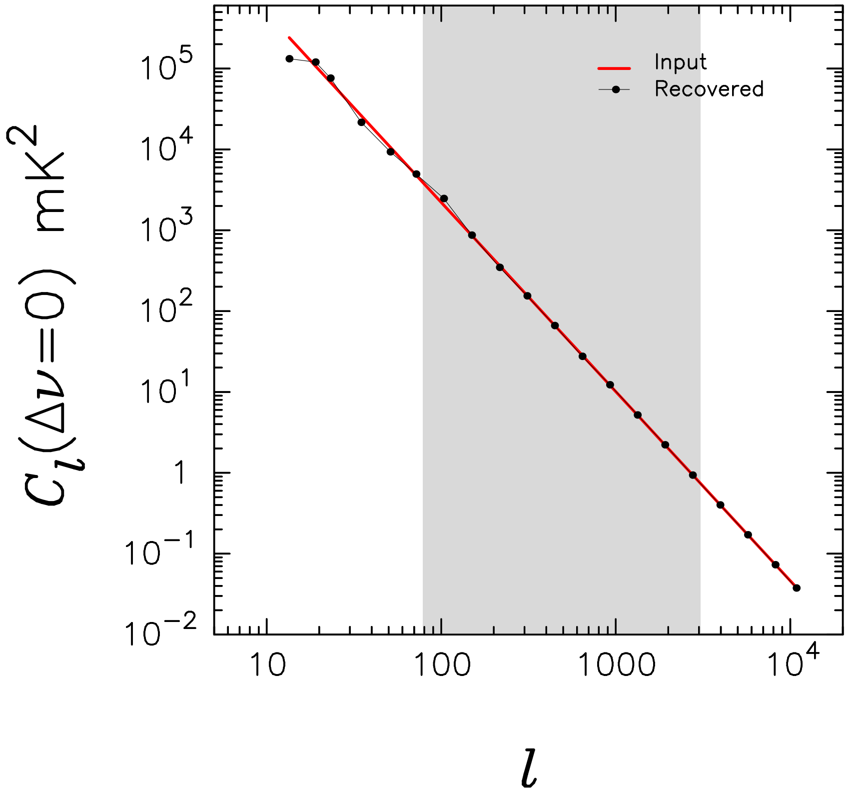

Figure 5.2: The input model angular power spectrum $C_\ell^M(\Delta\nu)$ at $\nu = 326.5$ MHz, shown by the curve in red. The angular power spectrum obtained from a random realisation of the input angular power is shown by the black points, obtained over 20 logarithmically spaced bins. The shaded region shows the multipole range accessible to OWFA.

where, $\tilde{A}(\mathbf{U})$ is the Fourier transform of the primary beam $A(\boldsymbol{\theta}, \nu)$. This is valid since $\tilde{A}$ has compact support in $\mathbf{U}$ due to the finite aperture size. Therefore, the factor by which the input and output power spectra differ is $\int d^2\mathbf{U}' |\tilde{A}(\mathbf{U} - \mathbf{U}')|^2$. The recovered power spectrum is scaled down by this factor: if now the input and the output power spectra match, our simulation has been successfully validated.

Figure 5.3 shows the comparison between the bin-averaged angular power spectrum $C_\ell(\nu)$ (given by equation 5.8), scaled down by the FT of the primary beam power pattern and the model $C_\ell^M(\nu)$ which has been used as the input to simulate the diffuse signal. The bin-averaged angular power spectrum is convolved with the beam but divided by the same number, and it can be seen that at large ℓ the convolution matches the approximation to a product given by equation 5.8. We independently confirm that the simulated foreground reproduces the input power spectrum by averaging many independent realisations of the diffuse foreground, in Section 6.3; it is found to be in excellent agreement with the input power spectrum.

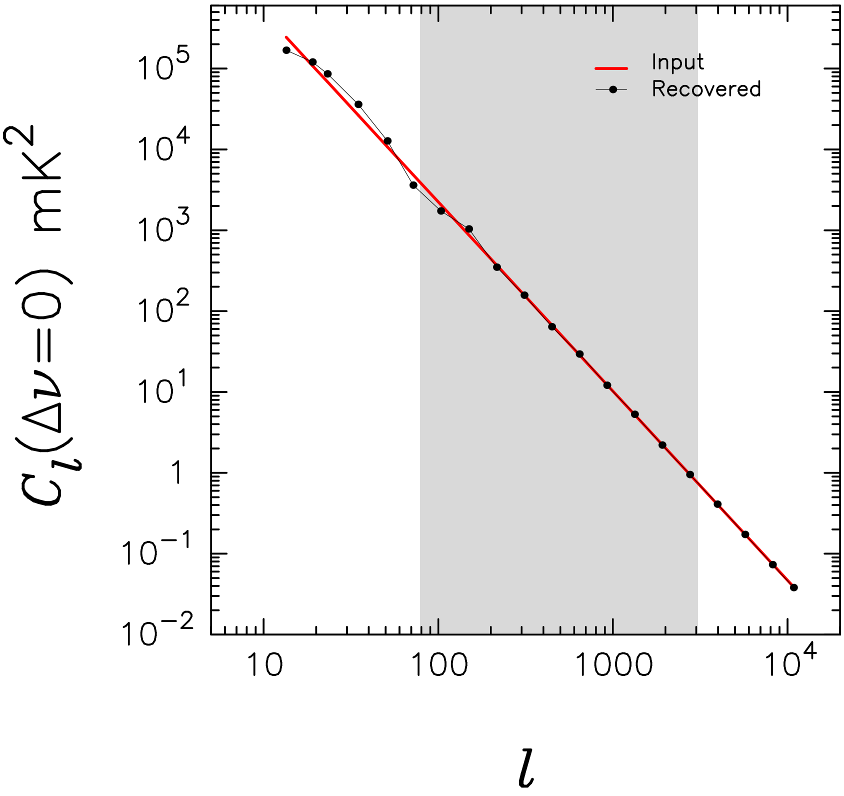

Figure 5.3: The input model angular power spectrum $C_\ell^M(\Delta\nu)$ at $\nu = 326.5$ MHz, shown by the curve in red. The input angular power spectrum is convolved with the Fourier transform of the primary beam $\tilde{A}(\mathbf{U})$ and scaled back by the integral in equation 5.8 in the black curve. The approximation is valid throughout the entire ℓ range, except at the smallest multipoles where the primary beam dominates the fluctuations in those scales. The shaded region shows the multipole range $\ell_{\min} - \ell_{\max}$ accessible to OWFA.

5.3 The extragalactic radio foreground

5.3.1 Statistical parameters from observations

Extragalactic point sources are expected to dominate the emission from the 325-MHz sky at most of the angular scales of our interest (Ali & Bharadwaj, 2014). The contribution to this emission comes from active galactic nuclei and star-forming galaxies (Santos *et al.*, 2005). Different radio surveys have been conducted at various frequencies from 150 MHz to 8.5 GHz, with a wide range of angular resolutions from $1''$ to $5'$. Singal *et al.* (2010) provide a comprehensive list of references for a large number of surveys in this frequency range. The two vital pieces of information that can statistically describe the extragalactic point source population completely are (a) the binned differential radio source counts and (b) the power spectrum of spatial distribution.

5.3.1.1 Differential source counts

Singal *et al.* (2010) have shown that the differential radio source counts, measured at widely different frequencies, are roughly consistent. At ~ 325 MHz, relevant for OWFA, the source counts between Wieringa (1991), Rengelink *et al.* (1997) and Sirothia *et al.* (2009) follow nearly the same behaviour except at the lowest flux bins. WENSS (Rengelink *et al.*, 1997) reaches a 5σ sensitivity of 18 mJy, and is therefore unable to constrain the source counts at smaller fluxes. Wieringa (1991) achieves a sensitivity of $\sim$ 4 mJy, which is very close to the confusion limit for the resolution of WSRT at 325 MHz, $1' \times 1'$. Sirothia *et al.* (2009) use the GMRT to observe the ELAIS-N1 field, attaining a sensitivity of 40 μJy, well above the confusion limit at the resolution of $\sim 9'' \times 9''$. This is the deepest 325-MHz radio source count study at the moment. However, for deriving the source counts, they consider sources brighter than 315 μJy, which is 8σ. Although there is a hint of evidence for the radio source counts flattening near 3-4 mJy limit of Wieringa (1991) with the WSRT, Sirothia *et al.* (2009) find clear evidence for flattening at 3 mJy. However, the 1 mJy flattening of the differential source counts was first reported at 1.4 GHz by Oort & van Langevelde (1987), Oort (1987) and Condon (1989). Subsequently, Rowan-Robinson *et al.* (1993), Hopkins *et al.* (1998), Richards (2000), Hopkins *et al.* (2003), Jarvis & Rawlings (2004), Seymour *et al.* (2004), Huynh *et al.* (2005), Simpson *et al.* (2006) and Owen & Morrison (2008) have re-restablished the same behaviour at 1.4 GHz. Weistrop *et al.* (1987) have reported source count flattening for fluxes < 1 mJy at 5 GHz with the VLA. It is attributed to the emergence of a population of radio sources with very low flux levels, typically $\sim$1 mJy, understood to be star forming galaxies and low luminosity AGN, as gleaned from their spectra (see e.g. Windhorst *et al.*, 1985; Windhorst, 1986; Windhorst *et al.*, 1993). This ∼1 mJy turnover flux at 1.4 GHz is consistent with 3 mJy at 325 MHz and 1.9 mJy at 610 MHz (with the GMRT; Bondi *et al.* 2007; Garn *et al.* 2007, 2008) from the spectral index argument, assuming $\alpha = 0.7$.

5.3.1.2 Angular power spectrum

The extragalactic point sources make two distinct contributions to the angular power spectrum: a part that has a Poisson distribution and a part that is clustered (see e.g. Cress *et al.*, 1996; Condon, 2007; Owen & Morrison, 2008; Vernstrom, 2015). The angular power spectrum can hence be written as

$$C_\ell = C_\ell^{\mathrm{P}} + C_\ell^{\mathrm{cl}} \tag{5.9}$$

In the case of the discrete point sources, the amplitude of the angular power spectrum is set by the total flux provided by all the sources within the field of view. The Poisson angular power spectrum is independent of the multipole moment ℓ, and it takes the general form (see Condon *et al.*, 2012)

$$C_\ell^{\mathrm{P}} = \left(\frac{\partial B}{\partial T}\right)^{-2} \left[\int_0^{S_c} S^2 \frac{dN}{dS}\, dS\right] \tag{5.10}$$

where S_c is the upper cut-off limit for the flux upto which we want to integrate (Ali & Bharadwaj, 2014). It is implicitly assumed that all sources brighter than S_c have been identified and subtracted. Cress *et al.* (1996) have determined the angular two point correlation function at 1.4 GHz for the FIRST radio sources (Becker *et al.*, 1995) in the range $1.2'$ to 2°. This translates into a $\mathbf{U}$ range of $14 < \mathbf{U} < 1430$ at OWFA wavelengths (Ali & Bharadwaj, 2014). The two point angular correlation function takes the form of a single power law

$$\omega(\theta) = \left(\frac{\theta}{\theta_0}\right)^{-\beta} \tag{5.11}$$

for which the measured clustering scale is $\theta_0 = 17.4'$ and $\beta = 1.1$Cress *et al.* (1996). Consequently, the angular power spectrum of the clustered part can be written as

$$C_\ell^{\mathrm{cl}} = 0.88 \times \frac{2\pi}{\theta_0^{-\beta}} \left(\frac{\partial B}{\partial T}\right)^{-2} \left[\int_0^{S_c} S^2 \frac{dN}{dS}\, dS\right] \ell^{\beta-2} \tag{5.12}$$

after a Legendre transform of the angular two point correlation function. This can be further simplified by plugging in the numbers, and written in the familiar form

$$C_\ell^{\rm cl} = 3.3 \times 10^{-5} \cdot \left(\frac{\partial B}{\partial T}\right)^{-2} \left[\int_0^{S_c} S^2 \frac{dN}{dS}\, dS\right] \left(\frac{1000}{\ell}\right)^{\gamma} \tag{5.13}$$

where $\gamma = 2 - \beta$, and $\gamma = 0.9$ here specifically.

The sum of these two parts, given by equation 5.9 produces a double power law fit.

With the source counts and the form of the expected power spectrum, we can now make predictions for the extragalctic point source foreground. The source counts from Wieringa (1991) has the advantage that it is confusion limited (~ 4 mJy) at the resolution of $1' \times 1'$. The OWFA resolution is $6' \times 1.8^\circ$, and the smaller dimension of the beam - $6'$ - can be comfortably Nyquist sampled at the resolution of $1' \times 1'$. This is guaranteed to give us confusion limited maps for OWFA. For OWFA at 326.5 MHz, we can use the source counts relation at 325 MHz from either of Wieringa (1991), Rengelink *et al.* (1997) or Sirothia *et al.* (2009). In practice, however, we use the 325-MHz polynomial fit provided by Wieringa (1991), which also agrees with the measurements provided by the other 325-MHz studies for fluxes > 3 mJy:

$$log_{10}\left(\frac{dN}{dS} S^{5/2}\right) = 0.976 + 0.613\, x + 0.3028\, x^2 - 0.083\, x^3 \tag{5.14}$$

where $x = log_{10}\,(S)$. Here, the flux S is in mJy. We can rewrite this equation as

$$log_{10}\left(\frac{dN}{dS}\right) = 0.976 + 0.613\, x + 0.3028\, x^2 - 0.083\, x^3 - 2.5\, x \tag{5.15}$$

which becomes

$$log_{10}\left(\frac{dN}{dS}\right) = 0.976 - 1.887\, x + 0.3028\, x^2 - 0.083\, x^3 \tag{5.16}$$

We now have

$$\frac{dN}{dS} = 10^{\left(a + bx + cx^2 + dx^3\right)} \tag{5.17}$$

where a = 0.976, b = -1.887, c = 0.3028 and d = -0.083. Equation 5.17 can then be directly plugged into equations 5.10 and 5.13, and the integral in each can be computed numerically.

5.3.2 Simulating the extragalactic foreground

Simulating extragalactic radio sources, the vast majority of which are unresolved at the resolution of the OWFA, is more involved than the straightforward Fourier inversion of the power spectrum of the diffuse foreground. The difficulty arises from the fact that the extragalactic sources do not constitute a Gaussian random field in the sky. This must also be obvious from the fact that unlike in the diffuse foreground where the fluctuations are excursions about a mean specific intensity which can be set to zero, the point sources only have positive flux density values.

The method used here has been adapted from González-Nuevo *et al.* (2005) but it is elaborated here for completeness. Let $\tilde{n} = n/N$ be the mean number density of sources per pixel in a map which has n sources in N pixels. For a confusion limited map, $\tilde{n} \sim 1$. We begin with a random Poisson field of source density with $\tilde{n}$, for which the density contrast is defined as $\delta(x) = [n(x) - \tilde{n}]/\tilde{n}$. Then, its Fourier transform is given by

$$\Delta(\mathbf{k}) = \frac{1}{\Omega^2} \int \delta(x) e^{-i\mathbf{k}.\mathbf{x}} dx \tag{5.18}$$

where Ω is the angular size of the map in solid angle. Let its angular power spectrum be denoted by C_ℓ^{P}, which can be calculated from $\Delta(\mathbf{k})$, and is given by equation 5.10. We can modify C_ℓ^{P} by the clustering angular power spectrum C_ℓ^{cl}; accordingly the Fourier transform of the density contrast is modified as

$$\Delta'(\mathbf{k}) = \Delta(\mathbf{k}) \sqrt{\frac{C_\ell^{\mathrm{P}} + C_\ell^{\mathrm{cl}}}{C_\ell^{\mathrm{P}}}} \tag{5.19}$$

The modified density contrast spectrum $\Delta'(\mathbf{k})$ is now reverse transformed to give the modified density contrast function $\delta'(x)$. Finally, the modified pixel source density is given by $n'(x) = \tilde{n}[1 + \delta'(x)]$.

The integrals have been computed from a polynomial fit to the source counts from Wieringa (1991). The simulated map hence represents the true source distribution in the sky as no bright sources are assumed to have been subtracted, equivalent to an infinite cutoff flux. However, we impose a cutoff of 30 Jy in the numerical integration: this is a reasonably good approximation to an infinite cutoff flux, as the number of sources beyond ~ 3 Jy falls very sharply, and this behaviour is well captured by the polynomial approximation to the differential source counts. Although, Wieringa (1991) gives a range of 4 mJy $<$ 1 Jy for the polynomial fit to the normalised differential source counts. The integral is not very sensitive to the lower limit to the flux, here 4 mJy, because the flattening at 3 mJy is not observed at the limit of 4 mJy by Wieringa (1991). The polynomial falls sharper than the expected flattening, and hence is unlikely to affect the integral in any significant way. We are therefore quite justified in setting the lower limit of the integral to zero.

The solid angular extent of the simulated map is Ω. So the number of sources we expect in the map is

$$N(S) = \Omega \times \int_0^{S_c} \frac{dN}{dS}\, dS \tag{5.20}$$

since the number counts are defined for a steradian of the sky. For a confusion limited map, we want the mean source density per pixel $n \sim 1$, which means $N(S) \sim N$, the number of pixels in the map. For an angular extent much less than a steradian, this is likely to result in fractional numbers less than unity for the source counts in the higher flux bins. This leads to difficulties in sampling the distribution to reach the total number of sources given by $N(S)$. This difficulty can be circumvented by resorting to a sparse sampling technique, introduced by Kaiser (1986). Instead of simulating a single map of extragalactic point sources, we simulate a large number of maps M simultaneously. The angular extent of the sky we are trying to populate with sources now is $\Omega \times M$ such that the product is atleast the of order of a steradian. For this simulation, $M = 100$ has been considered. In doing so, our objective is to get assured numbers greater than unity for the radio source counts in the largest flux bins. Therefore, the number of sources to generate effectively becomes a slightly modifed version of the previous equation:

$$N_M(S) = M \times \Omega \times \int_0^{S_c} \frac{dN}{dS}\, dS \tag{5.21}$$

Having generated the population of the sources (let us call it the source bank), we employ sparse sampling to obtain the M individual maps. We randomly choose N sources from the source bank to populate the N pixels from among the approximately $N_M(S)$ sources.

The clustered part has a power law index of $\gamma = 0.9$ (Cress *et al.*, 1996). The mean values are $C_\ell^{\mathrm{P}} = 1580$ mK^2 and $C_{1000}^{\mathrm{cl}} = 444$ mK^2. The input angular power spectrum for the extragalactic point sources in shown in Figures 5.5 and 5.6. The spectral indices for the point source fluxes have been assigned randomly, drawing from a Gaussian fit to the distribution centered at $\alpha = 0.7$ with a dispersion of $\sigma_\alpha = 0.25$, inferred from Sirothia *et al.* (2009), and their channel-wise fluxes scaled accordingly. The central zoom-in of one of the simulated point source maps is shown in Figure 5.4.

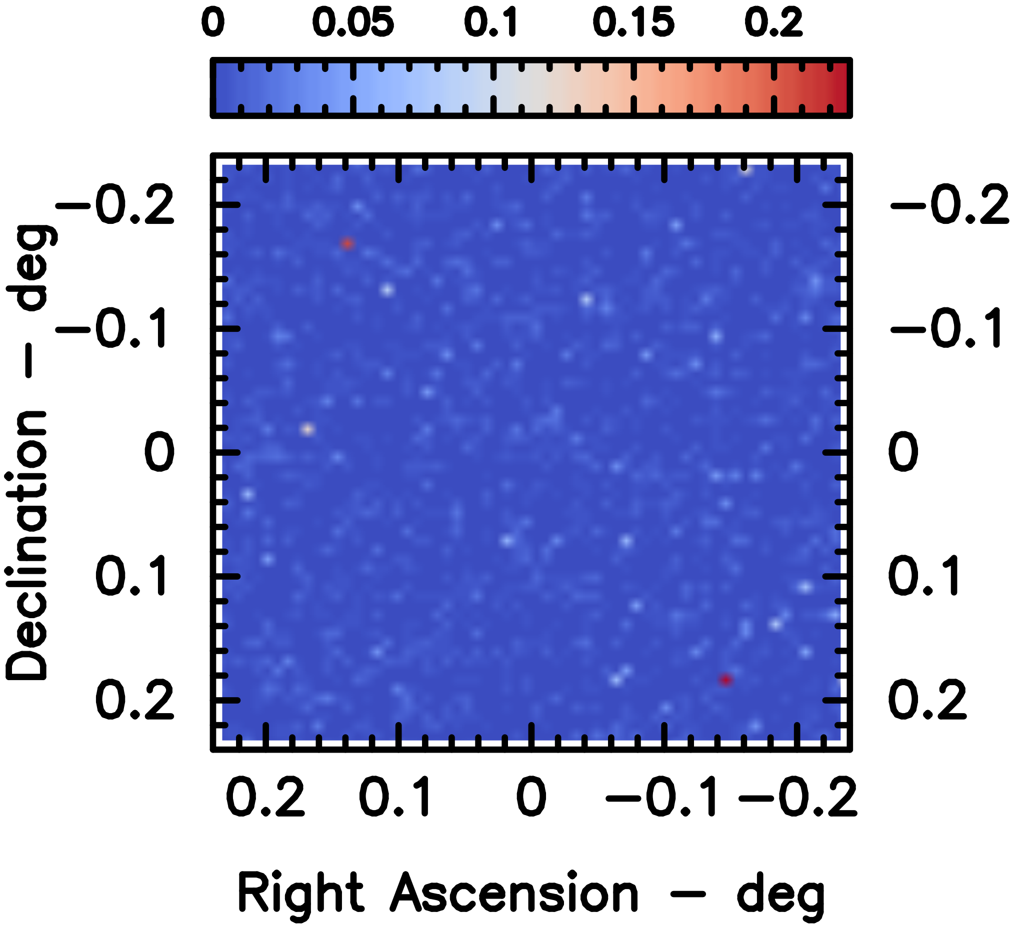

Figure 5.4: The central 0.5°×0.5° portion of the simulated extragactic point source map is shown here. The sources have been drawn from the differential source counts relation given by Wieringa (1991), and the spectral indeices of the sources have been randomly drawn from a Gaussian fit to the distribution of indices from Sirothia *et al.* (2009), centered at $\alpha = 0.7$. The flux scale is in Jy and the central channel at the frequency of 326.5 MHz is shown. The map has been simulated for a 39-MHz bandwidth with 312 channels.

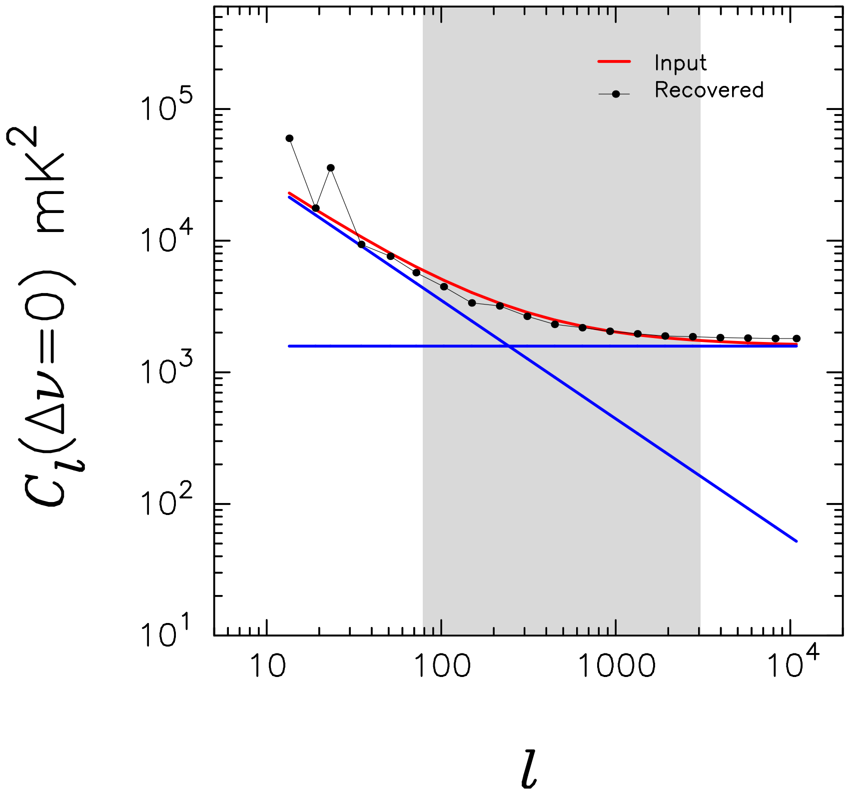

Figure 5.5: The input model angular power spectrum $C_\ell^M(\Delta\nu)$ at $\nu = 326.5$ MHz, shown by the curve in red, which is the sum of the Poisson and the clustered parts shown in blue. The angular power spectrum obtained from a random realisation of the input angular power is shown by the black points, obtained over 20 logarithmically spaced bins. The shaded region shows the multipole range accessible to OWFA.

The extragactic foreground simulation can be validated as well, following the same method used for the diffuse foreground component. The result for the angular power spectrum recovered after weighting without the primary beam is shown in Figure 5.5 and with the primary beam is shown in Figure 5.6. Unlike the diffuse foreground simulation where the differences between the recovered power spectra, with and without primary beam weighting, are more readily perceptible, the differences between the two cases for the extragalactic foreground are too small to be noticeable in these plots.

The confusion limit for OWFA is 175 mJy (Ali & Bharadwaj, 2014). However, we do not propose to identify and subtract sources from the one-dimensional images made using OWFA. Instead, a model for the sky obtained from deep GMRT imaging could, for example, be used to subtract the contribution to the visibility from the extragalactic radio sources. Alternatively, the model visibilties upto 18 mJy (the 5σ lmit) could just as well be obtained from the shallower Westerbork Northern Sky Survey (WENSS; Rengelink *et al.* 1997).

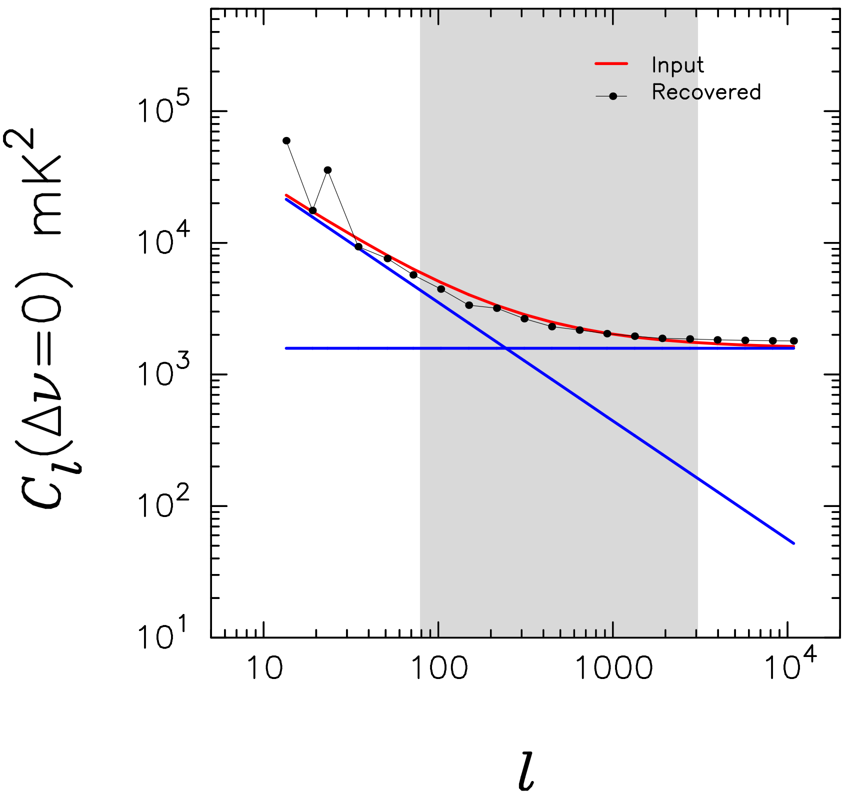

Figure 5.6: The input model angular power spectrum $C_\ell^M(\Delta\nu)$ at $\nu = 326.5$ MHz, shown by the curve in red, which is the sum of the Poisson and the clustered parts shown in blue. The input angular power spectrum is convolved with the Fourier transform of the primary beam $\tilde{A}(\mathbf{U})$ and scaled back by the integral in equation 5.8 in the black curve. The approximation is valid throughout the entire ℓ range, except at the smallest multipoles where the primary beam dominates the fluctuations in those scales. The shaded region shows the multipole range $\ell_{\rm min} - \ell_{\rm max}$ accessible to OWFA.

5.4 Visibilities of the realistic sky model

Having obtained both the diffuse foregrounds as well as the extragalctic point source contribution, the viisbilities for OWFA can be computed for a realistic model of the sky that consists of the sum of these two foreground contributions. The flux density function is then given by

$$S(\alpha, \delta, \nu) = \Delta S_D(\alpha, \delta, \nu) \; + \; \sum_{k=1}^{L} S_k(\alpha_k, \delta_k, \nu) \tag{5.22}$$

where $\Delta S_D(\alpha, \delta, \nu)$ is the fluctuation in the flux density of the diffuse foreground emission, and the L distinct extragalactic radio sources are identified by their co-ordinates (α_k, δ_k) and fluxes S_k. The model visibilities $M(\mathbf{U}, \nu)$ for the non-redundant set of baselines are obtained as a pixel-by-pixel Fourier sum of the primary-beam weighted specific intensity distribution

$$\mathbf{M}(\mathbf{U}, \nu) = \sum_{\alpha,\delta} \; S(\alpha, \delta, \nu) \; \mathbf{A}(\alpha, \delta, \nu) \; e^{-i2\pi \mathbf{U}.\hat{\mathbf{n}}} \tag{5.23}$$

where

$$\hat{\mathbf{n}} = \sin(\delta)\,\hat{\mathbf{k}} + \cos(\delta)\left[\cos(\alpha - \alpha_0)\,\hat{\mathbf{i}} + \sin(\alpha - \alpha_0)\,\hat{\mathbf{j}}\right] \tag{5.24}$$

The full $\mathbf{U}$-range of the OWFA is $0 - 500\ \lambda$ approximately at $\delta_0 = 0^\circ$. However, for fields at high declinations, the range of $\mathbf{U}$ is compressed by the factor $cos\ \delta_0$, where δ_0 is the declination of the centre of the field. An equivalent but valid reinterpretation of the co-ordinate system is allowed by looking at the array from the source. At a declination 0° the baselines appear at their full physical lengths. As the declination increases, the baselines appear foreshortened and their projected lengths differ from their physical lengths by the factor $\cos \delta_0$. The shortened baselines will therefore access larger scales of emission from the sky. However, the sensitivity falls off equally by the same $\cos \delta_0$ factor due to the reduced aperture at higher declinations. The model visibilities for a single realisation of the sky that includes both the diffuse emission and extragalactic radio sources for four different declinations are shown in Figure 5.7. The higher declinations allow for a compressed range of $\mathbf{U}$ but pick up more of the extended emission at $\mathbf{U} < 100$. At those short baselines, the largest scales of emission from the diffuse foregrounds dominates the point source foregrounds. This is expected as their slopes are very different: the steep index of the diffuse foregrounds rises above the point source contribution at these very large scales of emission. The spread in $\mathbf{U}$

for a given baseline d is given by

$$\Delta \mathbf{U} = -\frac{d \cos \delta_0}{\lambda^2} \Delta \lambda \tag{5.25}$$

from which it is obvious that at higher declinations, there could be considerable overlap in **U** between physically distinct baselines, as strikingly borne out by Figure 5.8.

Figures 5.8(a) and 5.8(b) show the distinct baselines and their **U** range. The horizontal dashed lines show the range of **U** for each declination at some baseline: red is $\delta_0 = 0°$, blue is $\delta_0 = 20°$, black is $\delta_0 = 40°$ and magenta is $\delta_0 = 60°$. We see that there is no overlap between the **U** range of adjacent baselines at any declination for the short baselines. The situation changes as we move to the longer baselines. There is considerable overlap in **U** between the adjacent baselines at all declinations. The red horizontal dashed line about $d = 34$ cuts through $d = 33$ at $\delta_0 = 0°$ and $d = 35$. At higher declinations, the overlap between adjacent baselines spills to the second neighbour.

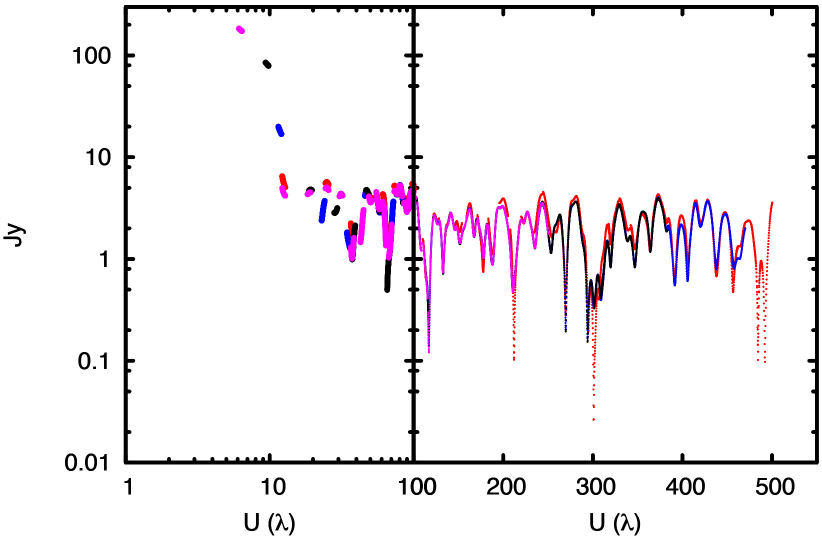

Figure 5.7: The red, blue, black and magenta colours code respectively the declinations 0°, 20°, 40° and 60°. This figure shows the model visibilities for a particular realisation of the sky, and emission from the larger scales being picked up by the shortened baselines at increasing declination.

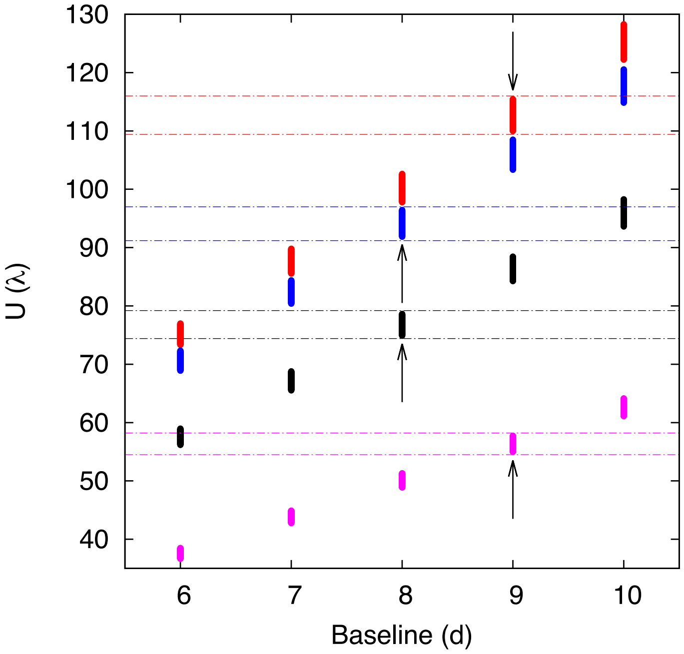

(a) Short baselines

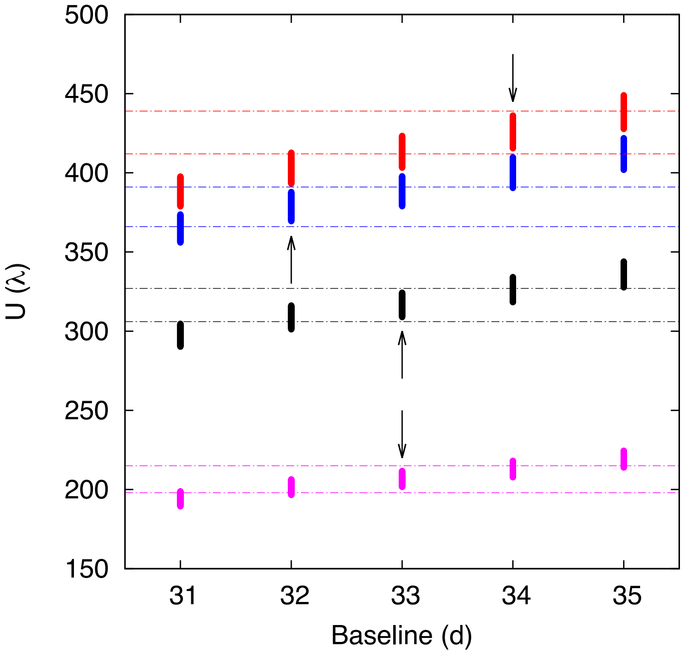

(b) Long baselines

Figure 5.8: The short and the long baselines at different declinations. The colours red, blue, black and green respectively encode the declinations $\delta_0 = 0°, 20°, 40°$ and $60°$. The overlap between the adjacent baselines is more pronounced at the longer baselines.

5.5 The redshifted HI 21-cm signal

One of the main aims of this thesis is to develop an understanding of the systematic effects introduced by the instrument through the study of simulated foregrounds. Although the simulation of the HI signal itself is out of the scope of this thesis, a very brief account follows; details can be found in Chatterjee *et al.* (2016).

The simulation uses a cosmological Particle Mesh (PM) N-body code to generate the dark matter particle distribution at $z = 3.35$. Here, the initial redshift for the simulation is $z \sim 50$. The initial linear matter power spectrum is generated by the fitting function of the ΛCDM transfer function, given by Eisenstein & Hu (1999). The cosmological parameters used are from Planck Collaboration *et al.* (2014). The simulations were run using a $N^3 = [2048]^3$ grid which corresponds to a comoving volume of $[2944 \text{ Mpc}]^3$. The grid spacing is chosen to be $L = 1.4375$ Mpc so that it exactly matches the frequency channel width, i.e. $L = r' \times \Delta\nu$; $\Delta\nu = 125$ kHz here and $r' \sim 11.5 \text{ MpcMhz}^{-1}$ (see Section 2.5). The redshift space distortion effect is incorporated from the velocity information of the dark matter particles.

Assuming a neutral fraction $x_{\rm HI} = 2.02 \times 10^{-2}$, calculated from $\Omega_{\rm HI} = 10^{-3}$ (see e.g. Lanzetta *et al.*, 1995; Storrie-Lombardi *et al.*, 1996; Rao & Turnshek, 2000; Péroux *et al.*, 2003) and that the neutral gas traces the underlying dark matter particle distribution, the dark matter halos are assigned HI with a scale independent linear bias[1] $b_{\rm HI} = 2$, following Bagla *et al.* (2010). Figure 5.9 shows the HI brightness distribution within a 1 MHz window by summing the signal in 8 125-kHz channels.

The model visibility for this brightness distribution can be obtained in exactly the same manner as for the foregrounds. The visibility of the HI signal is given by

$$\mathbf{M}_{\rm HI}(\mathbf{U}, \nu) = \int d^2\boldsymbol{\theta} A(\boldsymbol{\theta}, \nu) \delta I(\boldsymbol{\theta}, \nu) e^{-2\pi i \mathbf{U}\cdot\boldsymbol{\theta}} \tag{5.26}$$

where

$$\delta I = \bar{I}\, \frac{\delta\rho}{\bar{\rho}} \tag{5.27}$$

is the specific intensity fluctuation that traces the dark matter fluctuation. The primary beam weighted model visibility of the simulated HI distribution over 39 MHz for Mode-I of OWFA is shown in Figure 5.10.

We can square these visibilities to directly compute the power spectrum to check

---

[1] More recently, Sarkar *et al.* (2016) have modelled the bias of the post-EoR neutral Hydrogen, where they again use the fitting formula of Eisenstein & Hu (1999) for the ΛCDM transfer function to generate the matter power spectrum.

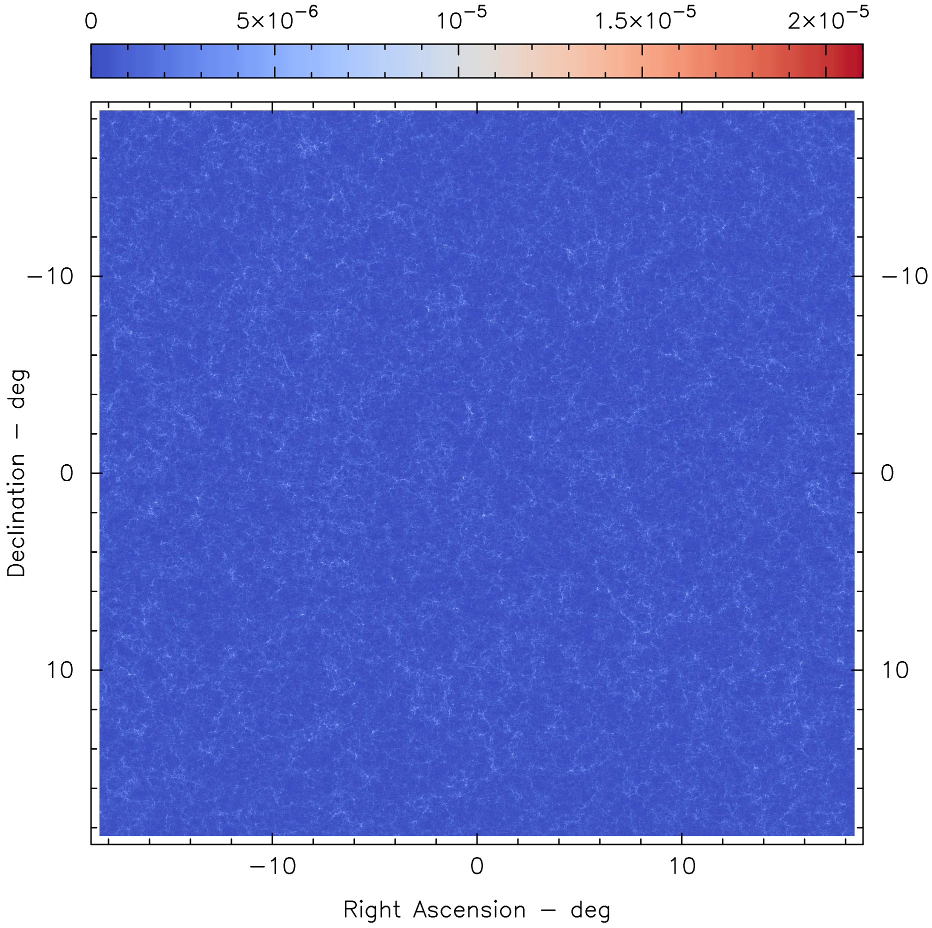

Figure 5.9: The brightness distribution of redshifted Hɪ 21 cm emission summed from 8 125-kHz channels from the simulated data, or the signal over 1 MHz. The flux scale is in Jy units. The Hɪ distribution traces the underlying dark matter particle density distribution.

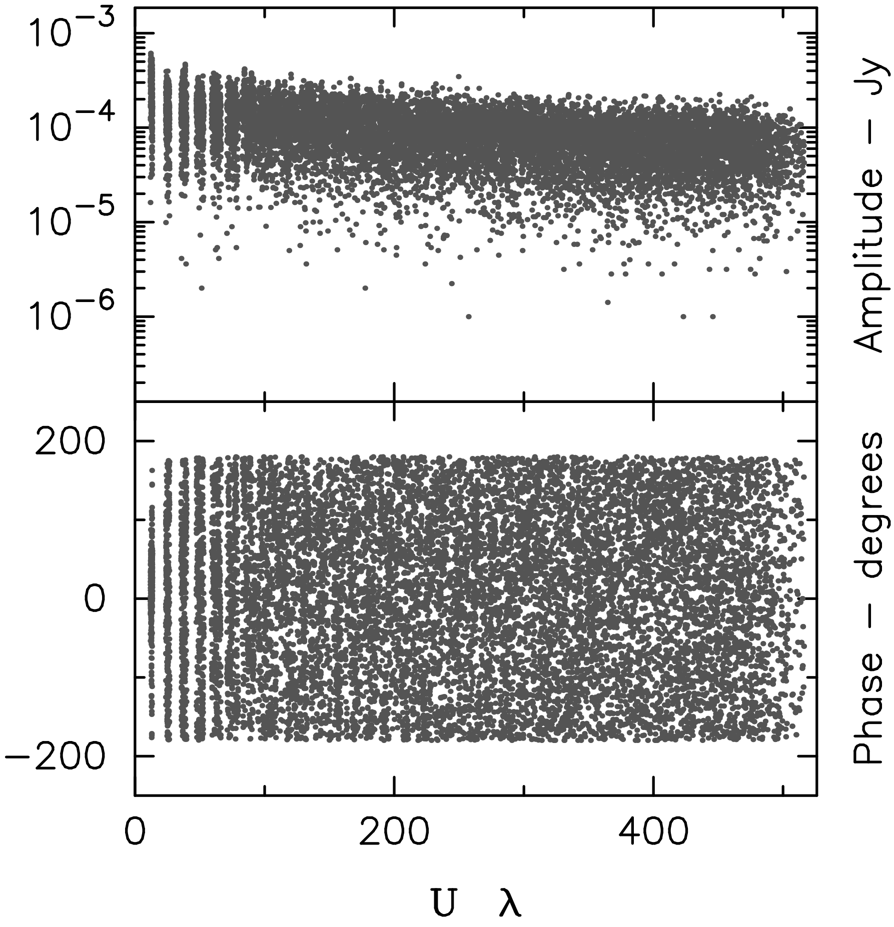

Figure 5.10: The model visibilties of the simulated redshifted HI 21 cm signal over 39 MHz is shown for Mode-I of OWFA. The input brightness distribution is shown in Figure 5.9.

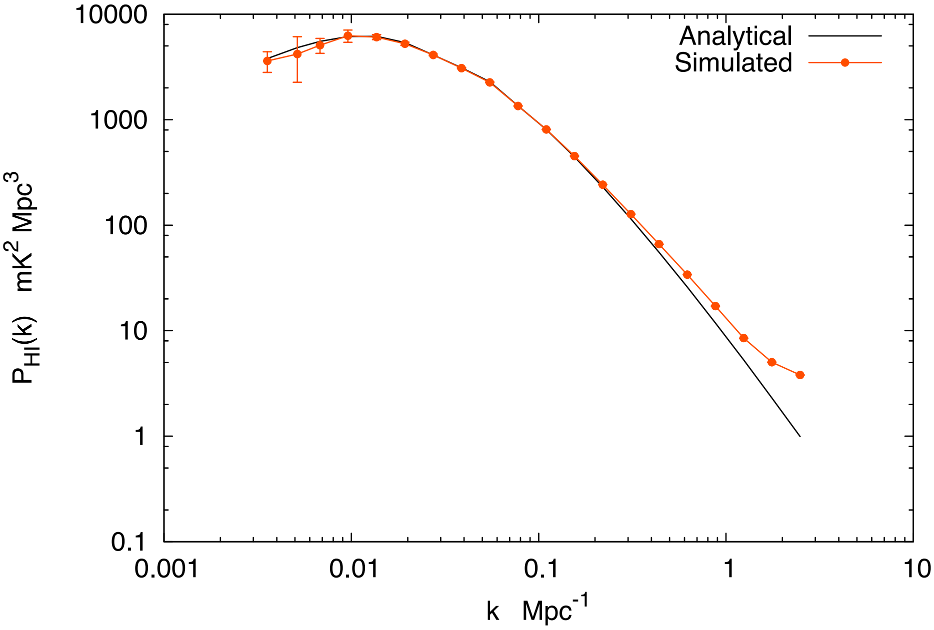

Figure 5.11: The power spectrum of the HI signal obtained after averaging over five realisations of output from the N-body code is compared with the analytically computed power spectrum. The error bars in the large scales are dominated by cosmic variance.

it against the linear dark matter power spectrum. We will separately discuss the OWFA two-visibility correlation estimator for the simulated HI signal in Section 6.8.1. Figure 5.11 compares the power spectrum $P_{\rm HI}(k)$ obtained from these simulated data with the analytically computed power spectrum predicted from linear theory. It is instructive to refer to Figure 1.4, from which it is seen that the simulated dark matter power spectrum deviates increasingly from the linear dark matter power spectrum at Fourier modes $k \geq 0.2$ Mpc^{-1}. These deviations are a consequence of the non-linear evolution of the density fluctuations. Figure 1.4 is merely the ratio of the two curves in Figure 5.11. The effects of nonlinear growth of structure on the power spectrum can be seen at large k, where smaller structures are assembling at this redshift, whereas at the larger scales the power spectrum is largely still linear. The analytically computed power spectrum is the linear power spectrum, with respect to which the departure is to be interpreted as nonlinearity.

Chapter 6

Power spectrum estimation

6.1 Introduction

One of the main goals of the cosmological HI experiments at low radio frequencies is to measure the fluctuations in the intensity of redshifted 21-cm emission, either from the EoR or from the post-reionisation epoch (Bharadwaj & Sethi, 2001; Bharadwaj & Srikant, 2004; Morales & Hewitt, 2004; Zaldarriaga *et al.*, 2004; Barkana & Loeb, 2005; Morales, 2005). The sensitivity with which the power spectrum can be measured depends on the level of thermal noise, calibration errors, systematic effects introduced by the instrument on the foregrounds and the HI signal, and residual contamination after foreground subtraction. One of the objectives of this thesis is to develop a thorough understanding of the systematic effects introduced by the instrument, and the complex ways in which the foregrounds and the instrument interact. The software model described in Chapter 3 was developed with the aim of addressing such questions, along with testing various calibration algorithms as discussed in Chapter 4.

Experiments tailored for statistical detection of the large scale structure typically aim to either: (a) determine an angular two-point correlation function of the intensity distribution, or (b) determine the power spectrum of the Fourier modes in the intensity distribution. The statistical properties of the large scale structure are generally assumed to be adequately represented by either of the two. Optical surveys typically directly measure the two point correlation function from redshift surveys. Eisenstein *et al.* (2005) measure the angular two point correlation function as well as the BAO feature in the clustering of galaxies from data taken as part of the Sloan Digital Sky Survey (SDSS; York *et al.* 2000).

Examples of the power spectrum approach abound in the literature as well. In low frequency radio experiments, the power spectrum method of detecting the signal statistically appears the most favoured method. The power spectrum can again be measured from an image of the sky, by first obtaining an angular two-point correlation function followed by a Fourier transform, or by obtaining the power spectrum from the visibilities themselves (Bharadwaj & Sethi, 2001; Bharadwaj & Pandey, 2003; Zaldarriaga *et al.*, 2004). Paciga *et al.* (2011, 2013) have set upper limits to the 21-cm HI power spectrum from $z \sim 8.6$ using the GMRT, computing it from the visibilities. Chapman *et al.* (2012), on the other hand, obtain the power spectrum by Fourier transforming a foreground-subtracted image and binning the result in the k-space for LOFAR. The advantage of working directly with the visibilities is that the noise covariance matrix of the visibilties is nearly diagonal (White *et al.*, 1999), which is of particular advantage and one which we shall exploit in computing the angular power spectrum in this chapter. The other distinct advantage of working directly with the visibilities is that the noise is well-understood in the uv plane: in the image plane, deconvolution complicates the noise properties.

The relation between the interferometric visibilities, the sky brightness distribution and the power spectrum is captured by Figure 6.1, adapted from Crovisier & Dickey (1983). A Fourier transform of the visibilities along the sky co-ordinates results in the sky brightness distribution. The autocorrelation function of the sky brightness distribution can be Fourier transformed to give the power spectrum, which can also be obtained as the visibility function modulus squared. However, the square of the modulus of the visibility is almost never used as an estimator of the power spectrum, since the self-correlated noise biases the estimate of power. Since an antenna has a finite aperture, it averages the uv measurements within the aperture. Therefore, we could use this fact to correlate visibilities arising from baselines separated by less than an antenna aperture. This fact has been employed in the context of GMRT, for example, by Begum *et al.* (2006). In the case of OWFA, visibilities from different redundant baselines can also be correlated without introducing a noise bias.

In this chapter, an estimator for the multi-frequency angular power spectrum that can operate directly on the visibility data is described. The estimator has been introduced earlier: by Bharadwaj & Ali (2005) in the context of cosmological HI experiments, by Begum *et al.* (2006) as applied to the study of HI distribution in dwarf galaxies and later by Datta *et al.* (2007) specifically in the context of EoR, all with the GMRT. However, in this chapter, the estimator is reintroduced specifically for OWFA, taking particular advantage of its geometry and redundancy. We shall see how this leads to a simple algorithm for computing the estimator. The main goal of this chapter is to not merely introduce the estimator and validate it, but to develop a rigorous understanding of the instrumental effects on the observed foregrounds. This study is possible with simulated foregrounds, which comprised the subject matter of

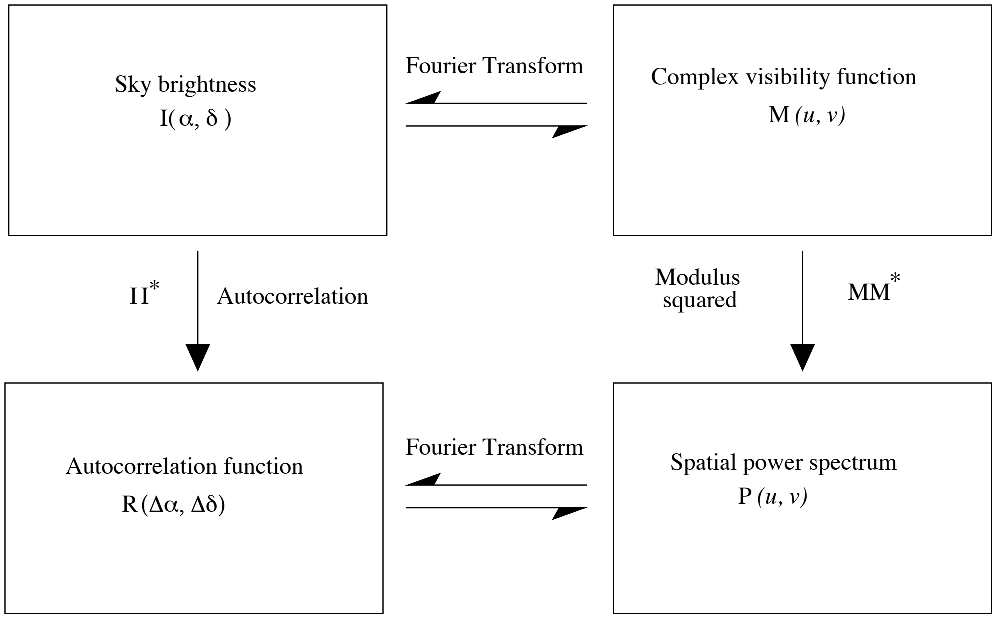

Figure 6.1: The relation between the interferometric visibilities, the sky brightness distribution and the power spectrum is brought out clearly by this schematic. Adapted from Crovisier & Dickey (1983).

the previous chapter.

6.2 The multi-frequency angular power spectrum

6.2.1 The two-visibility correlation as the MAPS estimator

From an observation of a region of the sky, we want to extract the angular power spectrum of emission $C_\ell(\Delta\nu)$. Let us denote the specific intensity of emission from the sky at a frequency ν by a fluctuation imprinted on a mean specific intensity as

$$I(\boldsymbol{\theta},\nu) = \bar{I}(\nu) + \Delta I(\boldsymbol{\theta},\nu) \tag{6.1}$$

The visibility function for a baseline $\mathbf{U} = (u, v)$ is

$$\mathbf{M}(\mathbf{U},\nu) = \int d^2\boldsymbol{\theta} A(\boldsymbol{\theta},\nu) I(\boldsymbol{\theta},\nu) e^{-i2\pi\mathbf{U}.\boldsymbol{\theta}} \tag{6.2}$$

where $A(\boldsymbol{\theta},\nu)$ is the primary beam and $I(\boldsymbol{\theta},\nu)$ is the specific intensity function of the sky as a function of sky co-ordinates $\boldsymbol{\theta}$ at the frequency ν. Its Fourier transform is

$$\tilde{A}(\mathbf{U},\nu) = \int d^2\boldsymbol{\theta} A(\boldsymbol{\theta},\nu) e^{-i2\pi\mathbf{U}.\boldsymbol{\theta}} \tag{6.3}$$

If the antenna aperture has a finite size, the Fourier transform of the primary beam power pattern $\tilde{A}(\mathbf{U},\nu)$ has compact support in $\mathbf{U}$. Further, an interferometer is sensitive only to the varying component of the specific intensity function on the sky. The visibility can hence be written as a convolution equation.

$$\mathbf{M}(\mathbf{U}_n,\nu) = \int d^2\mathbf{U}'\tilde{A}(\mathbf{U}_n-\mathbf{U}',\nu)\Delta\tilde{I}(\mathbf{U}',\nu) \tag{6.4}$$

where $\Delta\tilde{I}(\mathbf{U}',\nu)$ is Fourier transform of the fluctuation in the specific intensity function.

In practice, we estimate the model visibilities through calibration. If $\mathcal{V}(\mathbf{U}_n,\nu)$ is defined as an estimate of the true visibility $\mathbf{M}(\mathbf{U}_n,\nu)$ obtained after calibration, we can define the two-visibility correlation for a baseline, $\mathbf{S}_2$, as

$$\mathbf{S}_2(\mathbf{U}_n,\mathbf{U}_m,\nu_i,\nu_j) \ \equiv \ \langle\mathcal{V}(\mathbf{U}_n,\nu_i)\mathcal{V}^*(\mathbf{U}_m,\nu_j)\rangle \tag{6.5}$$

where the angular brackets denote averaging over the multiple copies of $\mathcal{V}(\mathbf{U}_n,\nu)$. There are three distinct cases:

1. Pairs of visibilities arising from redundant baselines correlate: $\mathbf{S}_2(\mathbf{U}_n,\nu_i,\nu_j)$
2. Baselines whose lengths differ by less than an aperture equivalent would have a non-zero correlated visibility component: $\mathbf{S}_2(\mathbf{U}_n,\mathbf{U}_{n\pm1},\nu_i,\nu_j)$
3. Visibility pairs from all other baselines are uncorrelated: $\mathbf{S}_2(\mathbf{U}_n,\mathbf{U}_{n\pm m},\nu_i,\nu_j)$; $m\geq 2$

Unless explicitly stated, we shall restrict our attention to the visibility correlation of two redundant baselines, $\mathbf{S}(\mathbf{U}_n,\nu_i,\nu_j)$. The true power spectrum that we want to estimate is

$$\langle\Delta\tilde{I}(\mathbf{U},\nu)\Delta\tilde{I}(\mathbf{U}',\nu+\Delta\nu)\rangle = P(\mathbf{U},\Delta\nu)\delta^2(\mathbf{U}-\mathbf{U}') \tag{6.6}$$

where $\delta^2(\mathbf{U}-\mathbf{U}')$ is the two-dimensional Dirac-delta function and

$$P(\mathbf{U},\Delta\nu) = \left(\frac{\partial B}{\partial T}\right)^2 C_{2\pi\mathbf{U}}(\Delta\nu) \tag{6.7}$$

The final relation between $\mathbf{S}_2$ and C_ℓ is (see e.g. Ali & Bharadwaj, 2014)

$$\mathbf{S}_2(\mathbf{U}_\mathbf{n},\Delta\nu) = \left(\frac{\partial B}{\partial T}\right)^2 \int d^2\mathbf{U}'\left|\tilde{A}(\mathbf{U}_n-\mathbf{U}')\right|^2 C_{2\pi\mathbf{U}_n}(\Delta\nu) \tag{6.8}$$

where $\mathbf{S}_2(\mathbf{U}_n,\Delta\nu)\equiv\mathbf{S}_2(\mathbf{U}_n,|\nu_i-\nu_j|)$. That is, the estimator $\mathbf{S}_2$ is equal to $P(\mathbf{U},\Delta\nu)$

convolved with the Fourier transform of the primary beam power pattern (which is equal to the convolution of the aperture illumination with itself). In essence, $\mathbf{S}_2$ estimates the multi-frequency angular power spectrum (MAPS), viz., $C_\ell(\Delta\nu)$. On large baselines, it is easy to see from equations 6.4, 6.5 and 6.6 that the estimator $\mathbf{S}_2$ is merely the power spectrum $P(\mathbf{U}, \Delta\nu)$ weighted by a number that depends only on the primary beam power pattern, or equivalently on the aperture illumination function. The convolution can be approximated as a product for longer baselines

$$\mathbf{S}_2(\mathbf{U}_n, \Delta\nu) = \left(\frac{\partial B}{\partial T}\right)^2 C_\ell(\Delta\nu) \left[\int d^2\mathbf{U}' \left|\tilde{A}(\mathbf{U}_n - \mathbf{U}')\right|^2\right] \tag{6.9}$$

where $\ell = 2\pi\mathbf{U}_n$ is the angular multipole and $\frac{\partial B}{\partial T} = \frac{2k_B}{\lambda^2}$. The discrepancy arising from approximating the convolution as a product is already illustrated by Figure 5.3, where the approximation is seen to introduce a small error at the smaller multipoles and negligible error at the larger multipoles.

6.2.2 Computing the estimator

The steps in the estimation of the multifrequency angular power spectrum are now outlined. In practice, we would calibrate the simulated observed visibilities making use of the redundant measurements (see Chapter 4). Absolute fluxes are set by scaling the gains to those set by external calibration. We could, for example, use a standard calibrator like 3C295, which is unresolved at the longest baselines of the ORT, to scale the gains and visibilities obtained through redundant spacing calibration. For a baseline $\mathbf{U_n}$, let there be N_n copies of the estimated visibility $\mathcal{V}^{(i)}(\mathbf{U}_n, \nu)$ at a channel whose central frequency is ν. The N_n copies can be added to improve the signal-to-noise ratio because, effectively, due to redundancy they measure the same Fourier mode on the sky. But the noise on each redundant copy of that baseline is independent. Therefore, the sum

$$\mathcal{V}(\mathbf{U}_n, \nu) = \sum_{i=0}^{N_n} \mathcal{V}^{(i)}(\mathbf{U}_n, \nu) \tag{6.10}$$

shows a baseline-dependent $1/\sqrt{N_n}$ noise behaviour as the number of copies N_n of the baseline goes down linearly with increasing baseline length. Let us also define the quantity

$$\mathcal{V}'(\mathbf{U}_n, \nu) = \sum_{i=0}^{N_n} |\mathcal{V}^{(i)}(\mathbf{U}_n, \nu)|^2 \tag{6.11}$$

We can now define our estimator, $\mathbf{S}_2$, as

$$\mathbf{S}_2(\mathbf{U}_n, \nu_i, \nu_j) = \frac{\mathcal{V}(\mathbf{U}_n, \nu_i)\mathcal{V}^*(\mathbf{U}_n, \nu_j) - \delta_{ij}\mathcal{V}'(\mathbf{U}_n, \nu_i)}{N_n^2 - \delta_{ij}N_n} \tag{6.12}$$

For an N-channel visibility dataset, the real-valued $\mathbf{S}_2(\mathbf{U}_n, \nu_i, \nu_j)$ is a $N \times N$ matrix. When multiplying $\mathcal{V}(\mathbf{U}_n, \nu)$ with its conjugate, the product of the sums produces a "self" term (the principal diagonal) when $\nu_i = \nu_j$, which is due to the correlated noise. This fact can be understood by writing the product $\mathcal{V}(\mathbf{U}_n, \nu_i)\mathcal{V}^*(\mathbf{U}_n, \nu_j)$ in expanded terms for a particular baseline for the same pair of channels (ν_i, ν_i):

$$\begin{aligned}\mathcal{V}(\mathbf{U}_n, \nu_i)\mathcal{V}^*(\mathbf{U}_n, \nu_i) = {} & \mathcal{V}^{(1)}(\mathbf{U}_n, \nu_i)\mathcal{V}^{*(1)}(\mathbf{U}_n, \nu_i) + \mathcal{V}^{(1)}(\mathbf{U}_n, \nu_i)\mathcal{V}^{*(2)}(\mathbf{U}_n, \nu_i) \; + \; \cdots \\ & + \mathcal{V}^{(N_n-1)}(\mathbf{U}_n, \nu_i)\mathcal{V}^{*(N_n)}(\mathbf{U}_n, \nu_i) + \mathcal{V}^{(N_n)}(\mathbf{U}_n, \nu_i)\mathcal{V}^{*(N_n)}(\mathbf{U}_n, \nu_i)\end{aligned} \tag{6.13}$$

In this equation, the product of the visibility from a baseline copy with its own conjugate contributes to the noise, whereas this contribution is absent in the product of the conjugate visibilities from two different baseline copies. This correlated noise term biases the diagonal $\nu_i = \nu_j$. The second term in the numerator of equation 6.12 offsets this noise bias on the principal diagonal. The noise covariance matrix, which is expected to be nearly diagonal, is hence effectively subtracted from the estimator. The $\mathbf{S}_2$ matrix is real-valued and symmetric. The estimator for the whole observation data set can be represented as a data cube of $N_A - 1$ matrices for OWFA, each of size $N \times N$. In the following pages, the terms "two visibility correlation matrix" and "MAPS estimator" are used interchangeably to represent $\mathbf{S}_2$.

6.3 Simulations and results

The results of the foreground power spectrum estimation through the MAPS estimator are presented in this section. As a verification step, the simulations were performed for a noise-free realisation of the sky model discussed in the earlier chapter. The diffuse Galactic synchrotron was simulated as a random realisation of a power spectrum with $C_{1000} = 10.2$ mK^2 at 326.5 MHz with $\gamma = 2.34$, and $\alpha = 2.54$ imparts a spectral shape within the band. The point sources were obtained as a single realisation drawn from the equivalent of 100 maps obtained with $C_\ell^{\mathrm{P}} = 1580$ mK^2 and $C_\ell^{\mathrm{cl}} = 444$ mK^2 according to the flux limits considered in Chapter 5.

The MAPS estimator $\mathbf{S}_2$ returns a matrix of the visibility correlation as a function of the two frequencies at which it is computed. Figure 6.2 shows an example of the

the estimator matrix for foregrounds that have contributions from both the diffuse Galactic synchrotron as well as the extragalactic point sources. Each panel in the plot is a true-sense representation of the matrix: the elements go from top left to bottom right. This observation is simulated for a declination of $\delta = 0^\circ$. For the short baselines, the spectral structures are broad and smooth in the (ν_i, ν_j) plane. As the baselines get longer, more spectral structure can be seen in the matrices. This phenomenon has to be understood well, and we shall return to a rigorous treatment shortly. But we may state at the moment that the spectral structure is caused by emission arising from large angular distances from the phase centre, and the effect is more pronounced on the longer baselines.

The angular power spectrum recovered from this simulated data individually for the diffuse Galactic foregrounds and the extragalactic point source foregrounds are shown in Figure 6.3. The left panel shows the APS recovered from 10 simulated realisations of the diffuse Galactic foregrounds. The solid red line is the input angular power spectrum and the points represent the recovered angular power spectrum. The 1σ error bars in each multipole moment bin shown here are obtained from the scatter across the 10 realisations. Similarly, the right panel of Figure 6.3 shows the recovered angular power spectrum for the extragalactic point sources, where the solid red line is the input angular power spectrum, which is the sum of the Poisson and the clustered contributions shown individually in blue.

As a brief digression, it may be useful to look at the estimator matrices for pairs of non-redundant baselines which are separated by exactly one aperture. These matrices are denoted by $\mathbf{S}_2(\mathbf{U}_n, \mathbf{U}_{n\pm1}, \nu_i, \nu_j)$, and some examples are shown in Figure 6.4. Unlike the $\mathbf{S}_2$ matrices for the same baseline pair shown in Figure 6.2, these matrices are real but not symmetric. As discussed above, these visibilities correlate because they correspond to separations less than the averaging arising due to the finite size of the antenna aperture. This is illustrated in Figure 6.5. The hatched region has contribution to the baseline under consideration from the adjacent baseline or baselines. One can exercise the choice of whether or not to include the contribution from the adjacent baselines when estimating the foregrounds or the signal. Such choice would be dictated by the fraction of the cosmological HI signal available in this contribution, and whether the returns justify the added complexity of treating asymmetric matrices.

It is important to convince ourselves that the estimator has not compromised any spectral information contained in the astrophysical signal. This check is vital if we are to model the foregrounds robustly. Unless the foreground is accurately represented, foreground subtraction is not guaranteed to work optimally. We hence test if our estimator reproduces all the input spectral behaviour in a statistical sense. The spectral

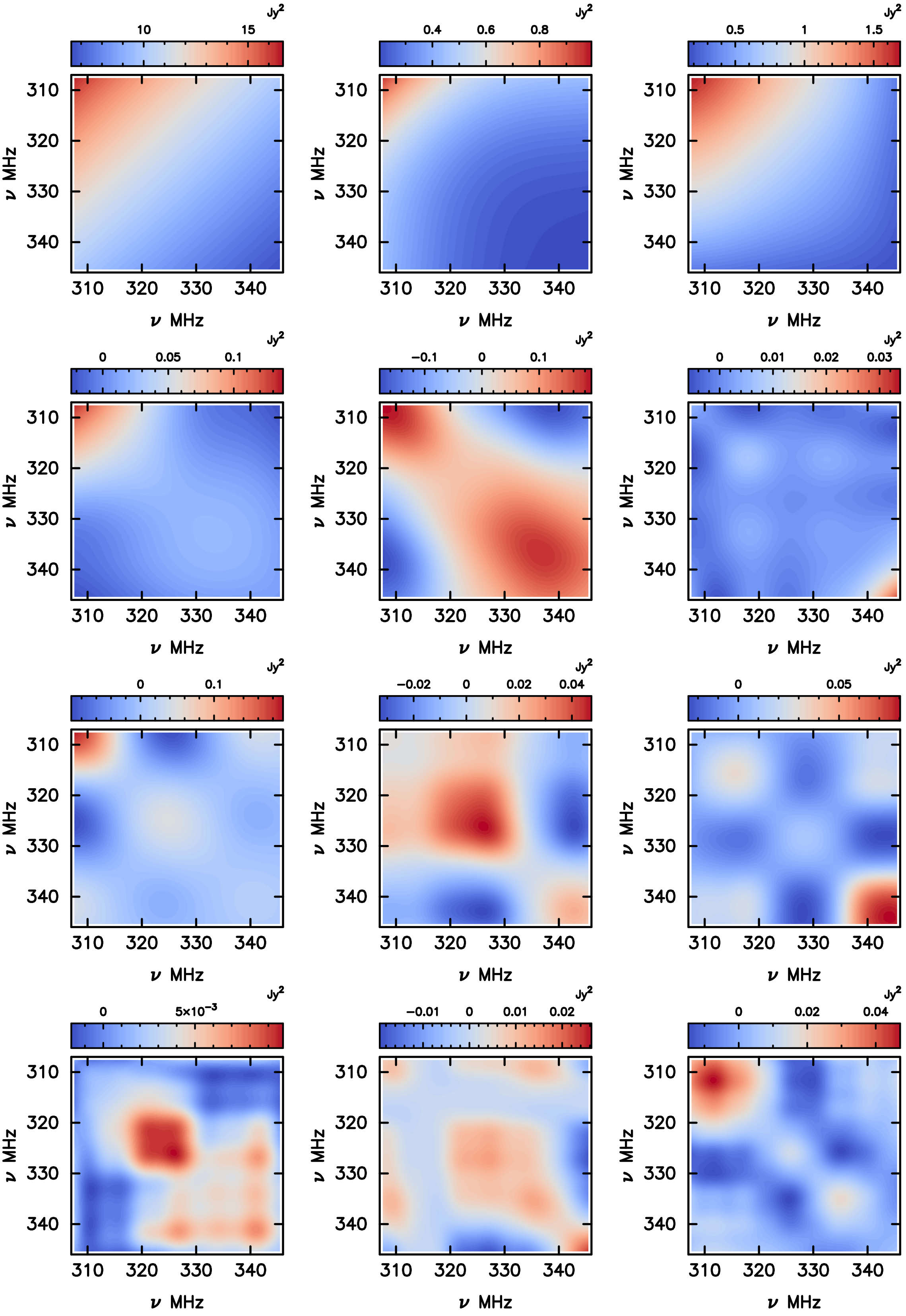

Figure 6.2: The MAPS estimator $\mathbf{S}_2(\mathbf{U}_n, \nu_j, \nu_j)$ is shown for a particular realisation of the sky, for simulated observations at $\delta = 0°$. Baselines 1, 4, 7, 10, 13, 16, 19, 22, 25, 29, 34 and 38 are shown. The longer baselines show more spectral structure than the shorter baselines. The matrices are real and symmetric. A customised divergent colour scheme is used in these plots (see Moreland, 2004).

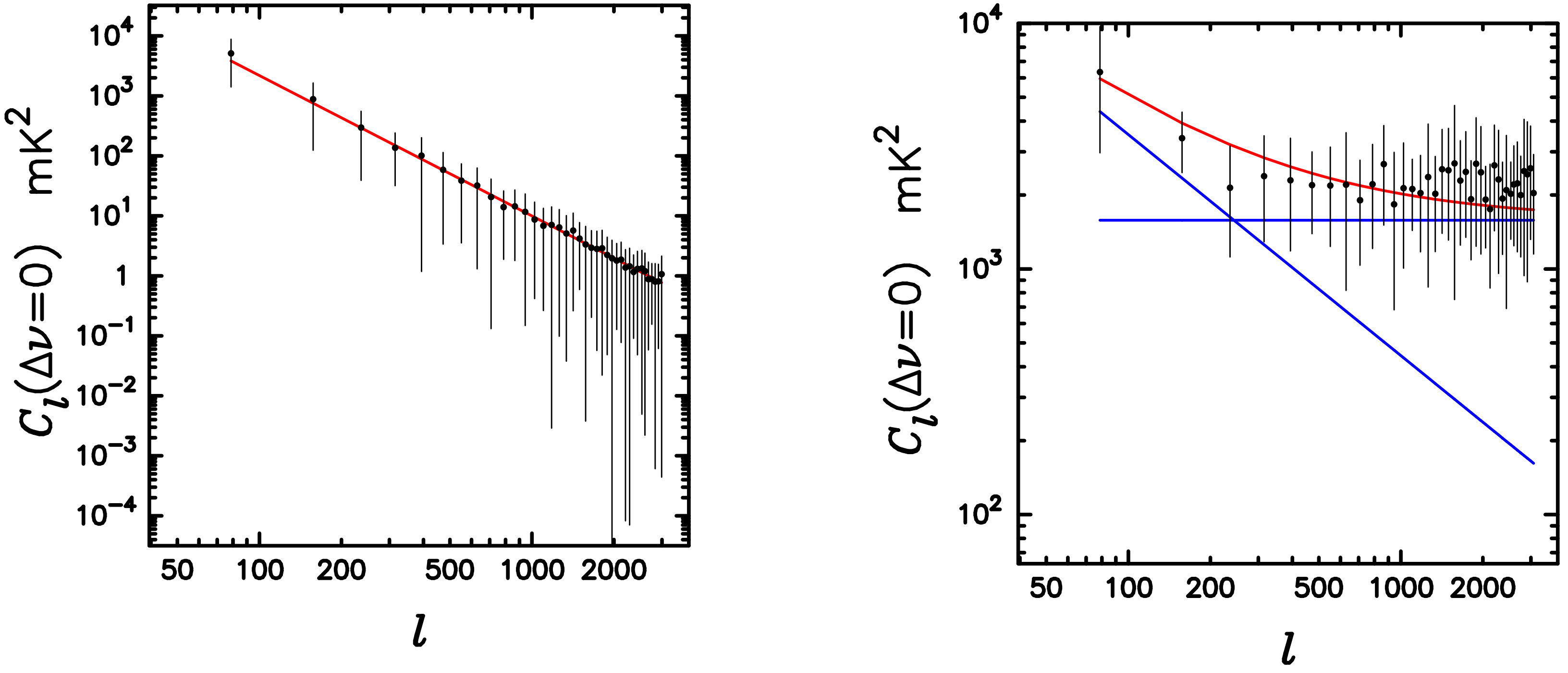

Figure 6.3: (Left)The input angular power spectrum of the diffuse power spectrum, shown in red is recovered by the MAPS estimator. The 1σ error bars correspond to averaging over 10 realisations. (Right)The input angular power spectra for the Poisson and the clustered parts of the point sources are shown in blue. Their sum is shown in red, and the angular power spectrum recovered from averaging 10 realisations, with the 1σ error bars similarly derived.

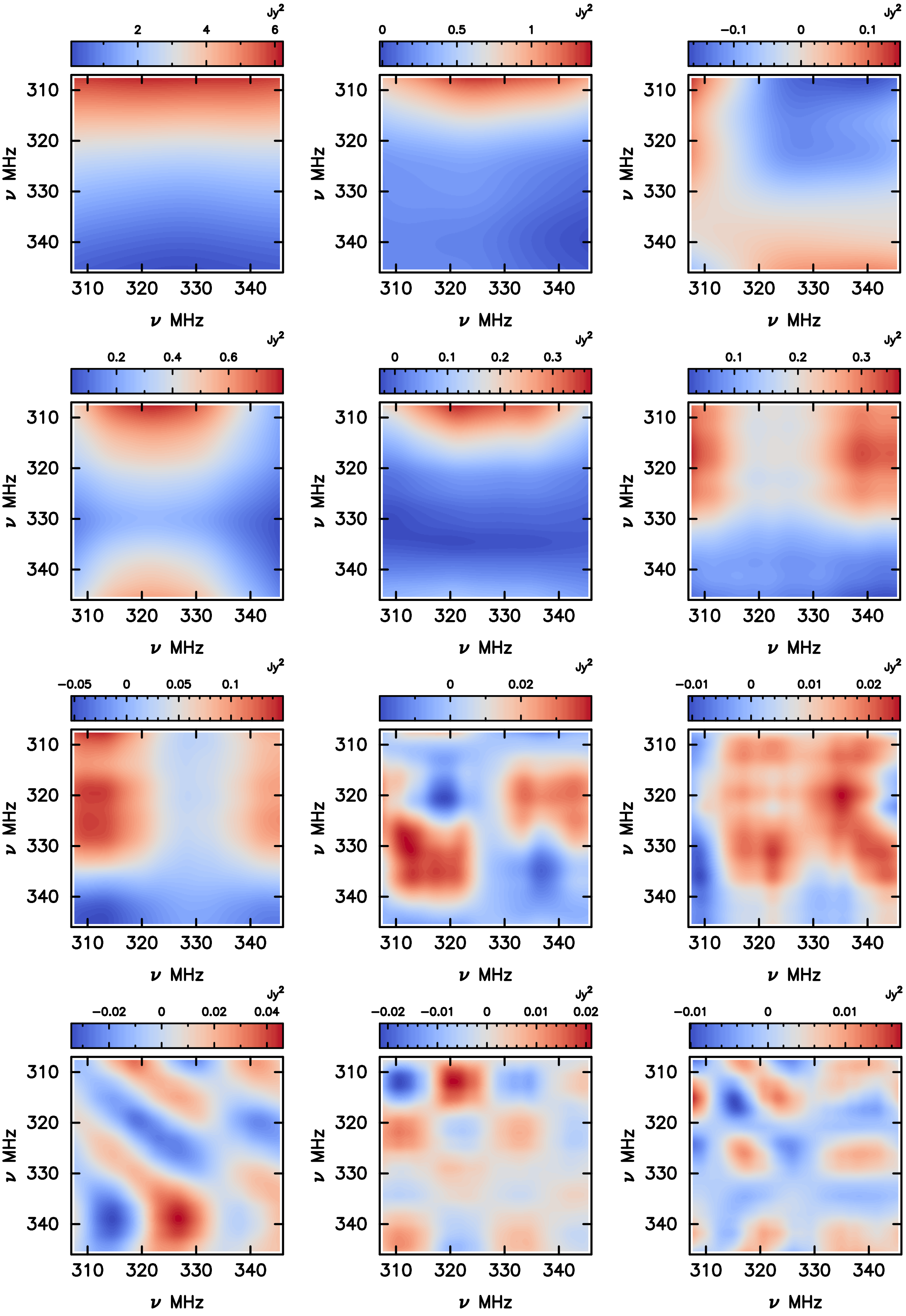

Figure 6.4: The MAPS estimator $\mathbf{S}_2(\mathbf{U}_n, \mathbf{U}_{n\pm1}, \nu_j, \nu_j)$ is shown for the same realisation of the sky used to obtain Figure 6.2. The same baselines 1, 4, 7, 10, 13, 16, 19, 22, 25, 29, 34 and 38 are shown. The matrices are real but are not symmetric.

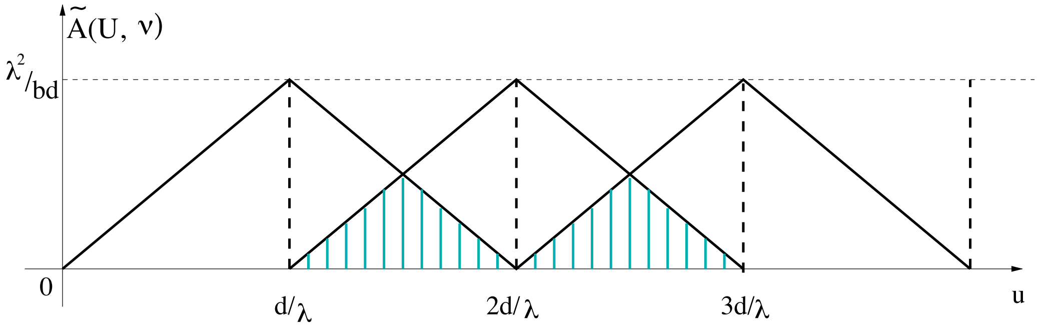

Figure 6.5: The **U** range and the respective weights contributed to each visibility from the redundant baseline pair and the adjacent baseline. The hatched region has contribution to the baseline under consideration from the adjacent baseline or baselines.

dependence in the form of the primary beam and the chromatic baseline length will introduce instrumental spectral variation in the estimator. To determine the form of the spectral dependence, we start with equation 6.9, which is repeated here so that this discussion is self-contained:

$$\mathbf{S}_2(\mathbf{U}_n, \Delta\nu) = \left(\frac{\partial B}{\partial T}\right)^2 C_\ell(\Delta\nu) \left[\int d^2\mathbf{U}' \left|\tilde{A}(\mathbf{U}_n - \mathbf{U}')\right|^2\right] \tag{6.14}$$

where

$$\left|\tilde{A}(\mathbf{U}_n - \mathbf{U}')\right|^2 = \frac{\lambda^2}{bd}\,\Lambda\left(\frac{u\lambda}{d}\right)\Lambda\left(\frac{v\lambda}{b}\right) \tag{6.15}$$

is the Fourier transform of the primary beam power pattern, or the convolution of the rectangular aperture with itself, $\mathbf{U} = (u, v)$ and $\Lambda(x)$ is the triangular function defined as

$$\Lambda(x) = 1 - |x| \text{ for } |x| < 1, \text{ and } \Lambda(x) = 0 \text{ for } |x| \geq 1. \tag{6.16}$$

$\Lambda(u)$ is periodic in u with period d/λ. Consider the Galactic diffuse foreground, described by a single power law as in equation 5.2. Given that $\ell = 2\pi\mathbf{U}$ where $\mathbf{U} = d/\lambda$, we may write

$$C_\ell \propto \left(\frac{\lambda}{d}\right)^\gamma \tag{6.17}$$

Substituting for all the terms, equation 6.14 can be rewritten as

$$\mathbf{S}_2(\mathbf{U}_n, \Delta\nu) \propto \left(\frac{2k_\mathrm{B}}{\lambda^2}\right)^2 \left(\frac{\lambda}{\lambda_0}\right)^{2\alpha} \left(\frac{1000\lambda}{2\pi d}\right)^\gamma \left(\frac{\lambda^2}{bd}\right) \tag{6.18}$$

from which it follows that

$$\mathbf{S}_2(\mathbf{U}_n, \Delta\nu) \propto \lambda^{2\alpha+\gamma-2} \tag{6.19}$$

or equivalently

$$\mathbf{S}_2(\mathbf{U}_n, \Delta\nu) \propto \nu^{2-2\alpha-\gamma} \tag{6.20}$$

Therefore, we expect the estimator to show this spectral behaviour across the band of observation centred at 326.5 MHz.

A large number of realisations of the diffuse Galactic synchrotron foreground, all with the same values of $\alpha = 2.52$ and $\gamma = 2.34$ were obtained. The model visibilities were obtained for each realisation, and the two-visibility correlation computed from each visibility set. The diagonal of the $\mathbf{S}_2(\nu_i, \nu_j)$ matrix corresponds to $\mathbf{S}_2(\nu, \Delta\nu = 0)$. The diagonal from the $\mathbf{S}_2$ matrix is obtained for 1000 independent realisations of the diffuse Galactic foregrounds and the mean of these diagonals is computed. The 1σ error bars too are computed from these 1000 independent realisations. The mean and the error bars are then individually normalised at $\nu = 326.5$ MHz; the normalised mean and error bar curves can be represented as $\|\mathbf{S}_2(\nu)\|$ and $\|\Delta\mathbf{S}_2(\nu)\|$; the argument $\Delta\nu = 0$ is implicit since it is fixed. Figure 6.6 shows the normalised mean of the diagonals as filled black circles. These have been sampled at every tenth channel so that they are seen clearly in the plot. The shaded region represents the bounds of the normalised 1σ error bars. The thin solid line in black represents the analytically computed curve $(\nu/\nu_0)^{(2-2\alpha-\gamma)}$. The two red curves correspond to two different realisations of the Galactic foregrounds: they have been normalised to $\nu = 326.5$ MHz individually to enable a consistent comparison with the estimated and the expected mean curves. As can be seen, there is excellent agreement between the normalised mean estimator and the analytical curve on the shorter baselines, where the two realisations shown here are spectrally simpler. As the baselines become longer, there is more obvious spectral structure in the estimator across the band. This increased variance has led to a small mismatch between the estimated mean and the analytical curve on the longer baselines. An even larger number of realisations need to be averaged for these to match on the longer baselines.

We conclude that the estimator, as expected, preserves the spectral information in the visibility, and therefore can be applied for foreground estimation. The $\mathbf{S}_2$ matrix is a new tool for studying the frequency structure of the foregrounds in its entirety. This is because, in principle, the signals being discussed here, viz. the foregrounds, are not stationary, i.e., $\mathbf{S}_2$ is not a function of $|\nu_i - \nu_j|$ alone. If $\langle \mathcal{V}_n(\nu_i)\mathcal{V}_n^*(\nu_j)\rangle$ were a function

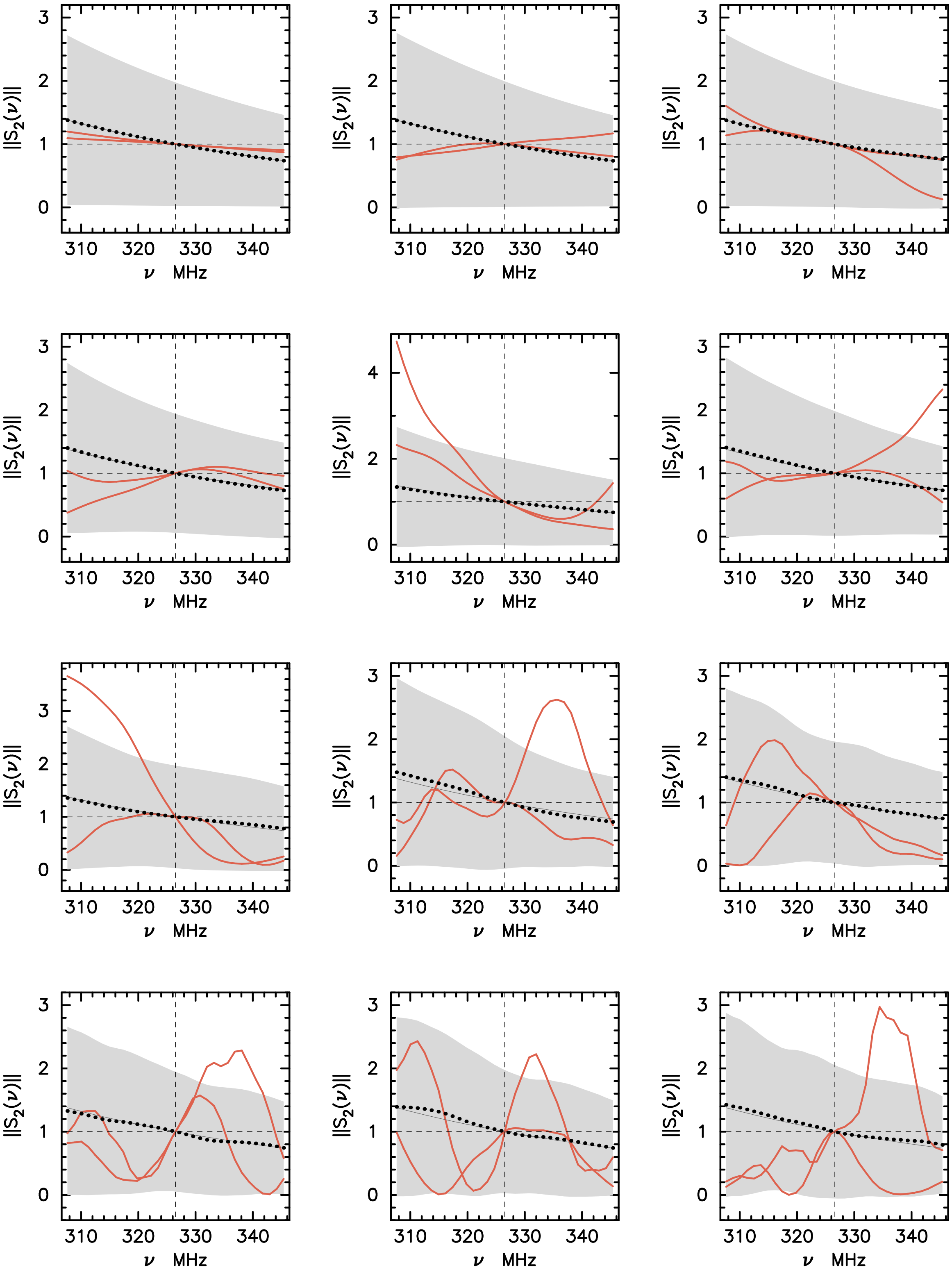

Figure 6.6: The normalised MAPS estimator $\|\mathbf{S}_2(\mathbf{U},\nu)\|$ is shown left to right, top to bottom, for baselines 1, 3, 5, 6, 7, 8, 11, 16, 21, 23, 25 and 31. The red curves relate to two different realisations of the diffuse Galactic synchrotron foreground from a total of 1000. The estimated mean is given by the filled circles and the solid black line is the analytically computed curve given by $(\nu/\nu_0)^{(2-2\alpha-\gamma)}$. The simulation is over 39 MHz split into 312 channels, but only a sampled version of the estimated mean (filled circles) is shown for clarity. The shaded region represents the 1σ error bound.

of $\Delta\nu = |\nu_i - \nu_j|$ alone, then we could have dealt only with the averages along the diagonals of $\mathbf{S}_2$. However since $\langle \mathcal{V}_n(\nu_i)\mathcal{V}_n^*(\nu_j)\rangle$ is in reality a function of both ν_i and ν_j, it is useful to retain the full information contained in the $\mathbf{S}_2$ matrix. We shall return to the usefulness of this representation later in the context of foreground subtraction.

6.4 Systematic signatures in the estimator

Having obtained the estimate for the multi-frequency angular power spectrum, let us now discuss the most important aspect of foreground estimation: the systematic instrumental effects. Numerous studies have addressed the problem of instrumental effects on the estimation of the HI signal, and the limitations posed by effects such as residual foreground contamination (see e.g. Liu & Tegmark, 2012), mode-mixing (Bowman *et al.*, 2009; Thyagarajan *et al.*, 2013) or chromatic instrumental effects (Vedantham *et al.*, 2012). Some of these studies have addressed these effects in general while others discuss them in the context of a specific instrument (e.g. Vedantham *et al.*, 2014, for LOFAR). An analysis for OWFA is carried out here. This is motivated by the need to understand the effects introduced by the specific instrument, and to devise ways and means to handle such effects in real data.

6.4.1 Sources at large angular distances

The effects of sources at large angular distances from the pointing centre coupling in through the primary beam is well-known (see e.g. Datta *et al.*, 2010; Vedantham *et al.*, 2012; Pober *et al.*, 2013a). Consider a single point source at the co-ordinates $\boldsymbol{\theta} = (l, m)$. Let us also assume that the pointing of observation is $(\alpha_0 = 0, \delta_0 = 0)$ without loss of generality. For the n^{th} baseline in the linear array, we note that at frequency $\nu = c/\lambda$,

$$\mathbf{U}_n = n\mathbf{U}_1 = n\,\frac{d}{\lambda} = n\,\frac{d}{\lambda_0}\,\frac{\lambda_0}{\lambda} \tag{6.21}$$

The visibility, obtained as a Fourier sum in the simulation and given in equation 5.23, simplifies to

$$\mathbf{M}(\mathbf{U},\nu) = \sum_{\boldsymbol{\theta}}\ \mathbf{I}(\boldsymbol{\theta},\nu)\ \mathbf{A}(\boldsymbol{\theta},\nu)\ e^{-i2\pi m \frac{nd}{\lambda_0}\frac{\lambda_0}{\lambda}} \tag{6.22}$$

Since $\mathcal{V}(\mathbf{U},\nu)$ represents an estimate of $\mathbf{M}(\mathbf{U})$, the two-visibility correlation at (ν_i, ν_j) for this baseline becomes

$$\mathbf{S}_2(\mathbf{U}_n,\nu_i,\nu_j) \sim |\mathbf{I}(\boldsymbol{\theta},\nu_0)|^2\,|\mathbf{A}(\boldsymbol{\theta},\nu_0)|^2\,e^{-i2\pi m\left(\frac{nd}{\lambda_0}\right)\left(\frac{\nu_i-\nu_j}{\nu_0}\right)} \tag{6.23}$$

assuming that the approximations

$$|\mathbf{I}(\boldsymbol{\theta}, \nu_0)|^2 = \mathbf{I}(\boldsymbol{\theta}, \nu_i)\mathbf{I}^*(\boldsymbol{\theta}, \nu_j) \tag{6.24}$$

and

$$|\mathbf{A}(\boldsymbol{\theta}, \nu_0)|^2 = \mathbf{A}(\boldsymbol{\theta}, \nu_i)\mathbf{A}^*(\boldsymbol{\theta}, \nu_j) \tag{6.25}$$

are reasonable, but in general not strictly true. A source away from the phase centre leaves oscillatory features in the MAPS estimator, and the frequency of the oscillation depends on the location of the source m as well on the baseline nd. It is interesting to note that $\Delta\nu/\nu_0$ is of the order of 12% ($\sim$40 MHz/327 MHz) for OWFA. The effective contribution to the sinusoidal feature in $\mathbf{S}_2$ from the fractional frequency separation $\Delta\nu/\nu$ is small and sub-dominant, whereas contribution from distant sources ($\propto m$) on the longer baselines is more dominant. The argument can be generalised to include many point sources, and by extension to the diffuse foregrounds as well. We must note that the sum total contribution from all emission within the field of view superimpose with a range of phases that tend to partly cancel out. But residual features remain imprinted on the innocuous-looking smooth spectra. Figure 6.7 shows the $\mathbf{S}_2$ for the same realisation of diffuse and point source foregrounds used to obtain the plots in Figure 6.2, but computed as a function of $\Delta\nu$ by averaging along the diagonals of the $\mathbf{S}_2$ matrix for two example baselines. Although the foregrounds are non-stationary as discussed in Section 6.3, it is instructive to cast the estimator in the familiar form as a function of $\Delta\nu$ for this exercise. The apparently smooth curves in the top panels can be fitted by low-order polynomials successively. The residual contamination can still be seen in the bottom panels. The frequency of the oscillatory pattern is higher as expected for longer baselines. It must be noted that the amplitude of the residual oscillatory features is about 7 orders smaller than the visibility correlation $\mathbf{S}_2$, and they are comparable to the amplitude of the expected HI visibility correlation, which is in the range of $10^{-8} - 10^{-9}$ Jy^2, shown in Figure 6.19.

We have indeed seen that these residuals remain even when excluding the point source foreground. While the contribution from point sources is significantly larger, in random realisations we have also seen that occasionally, very bright point sources ($\gtrsim$ 300 mJy) near the nulls exacerbate the problem, leaving stronger oscillatory residuals. Chapman *et al.* (2012) have discussed such effects in the context of foreground removal on simulated foregrounds for LOFAR EoR. They further point to studies (Bowman *et al.*, 2006; Liu *et al.*, 2009b) which have painted an optimistic picture: that these residuals are likely to be fainter than the HI signal. In figure 6.7, the residuals

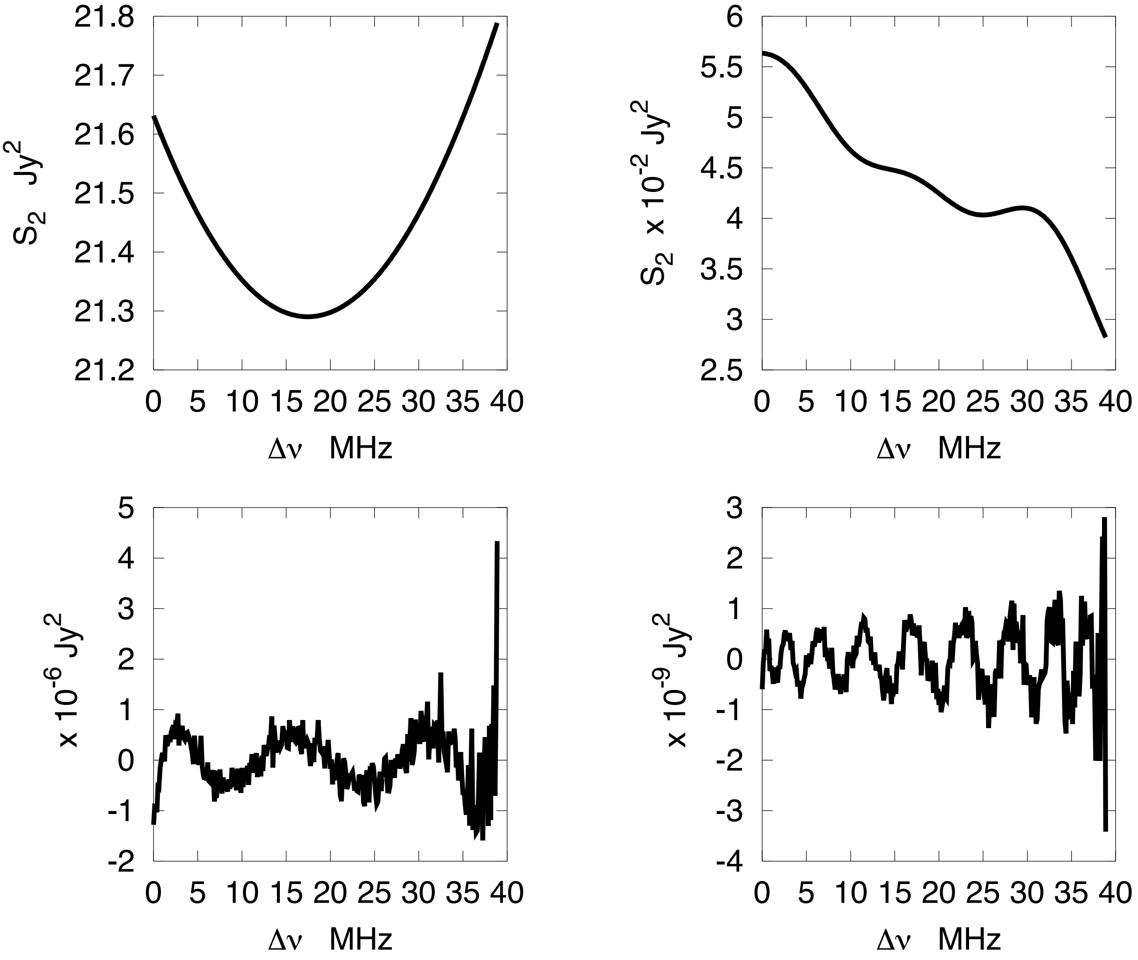

Figure 6.7: The $\mathbf{S}_2(\Delta\nu)$ curves for two baselines $\mathbf{U}_2$ and $\mathbf{U}_{17}$ are shown in the top left and right panels respectively. The residual after fitting polynomials are shown in the bottom panels, indicating the contribution from sources in the sidelobes.

are slightly brighter or at the level of the expected HI signal. We shall see results from simulated HI signal in a subsequent section. These undesirable oscillatory features can be suppressed by restricting the total FoV. This can be achieved by tapering the primary beam with a weighting function, typically a Gaussian window function. However, this is possible only in the uv-plane post-correlation, through a 2D convolution. Beam tapering in uv has been shown to be quite effective for real GMRT data (Ghosh *et al.*, 2011b). The tapered-gridded estimator has been shown to be equally effective for simulated GMRT data (Choudhuri *et al.*, 2014, 2016), but its adaptation to OWFA is proposed as an extension of this work in the near future.

6.4.2 Instrument chromatic response

As the primary beam shrinks with increasing frequency, a point source near the null produces a spectral signature in the signal. This transfer of power from angular to frequency dimension is called mode-mixing (see e.g. Bowman *et al.*, 2009). Besides, Vedantham *et al.* (2012) discuss contamination due to the point-spread function (PSF), in the context of instrument-induced limitations on imaging for EoR. Let us consider these two effects together now: (a) the chromatic primary beam response, and (b) the chromatic interferometer response. These are both the causes for mode-mixing and PSF contamination.

We shall now attempt to disentangle the intrinsic frequency dependence attributed to the emission from the sky - the spectral and spatial indices - from the chromatic instrument response. This can be achieved by varying the spectral index α and the spatial index γ over a wide range of values and observing the spectral behaviour of the MAPS estimator, but employing the same realisation of the Gaussian random field. Figure 6.8 shows the normalised MAPS estimator curves for four different baselines, in each of which cases the brightness temperature spectral index α is allowed to take three different values: 0.0, 1.0 and 2.0 (the three curves) for each γ. $\alpha = 0.0$ represents the case where the brightness temperature (in K) of the observed field is achromatic, whereas $\alpha = 2.0$ denotes an achromatic flux (in Jy) throughout the field. The principal diagonal of $\mathbf{S}_2(\mathbf{U}, \nu_i, \nu_j)$ is normalised to its value $\mathbf{S}_2(\mathbf{U}, \nu = 326.5\text{MHz})$.

Between the three values of α, the spectral trend appears to remain largely similar. The differences between the curves for the different values of α are small in comparison with the overall spectral trend seen in the plots for a given baseline. Between the three columns in the 4×3 plot, each of which takes a different value for γ, the similarity of the curves is remarkable. These different curves can also be described by a polynomial of the same order for a given baseline $\mathbf{U}_n$, with only the coefficients of the fit changing

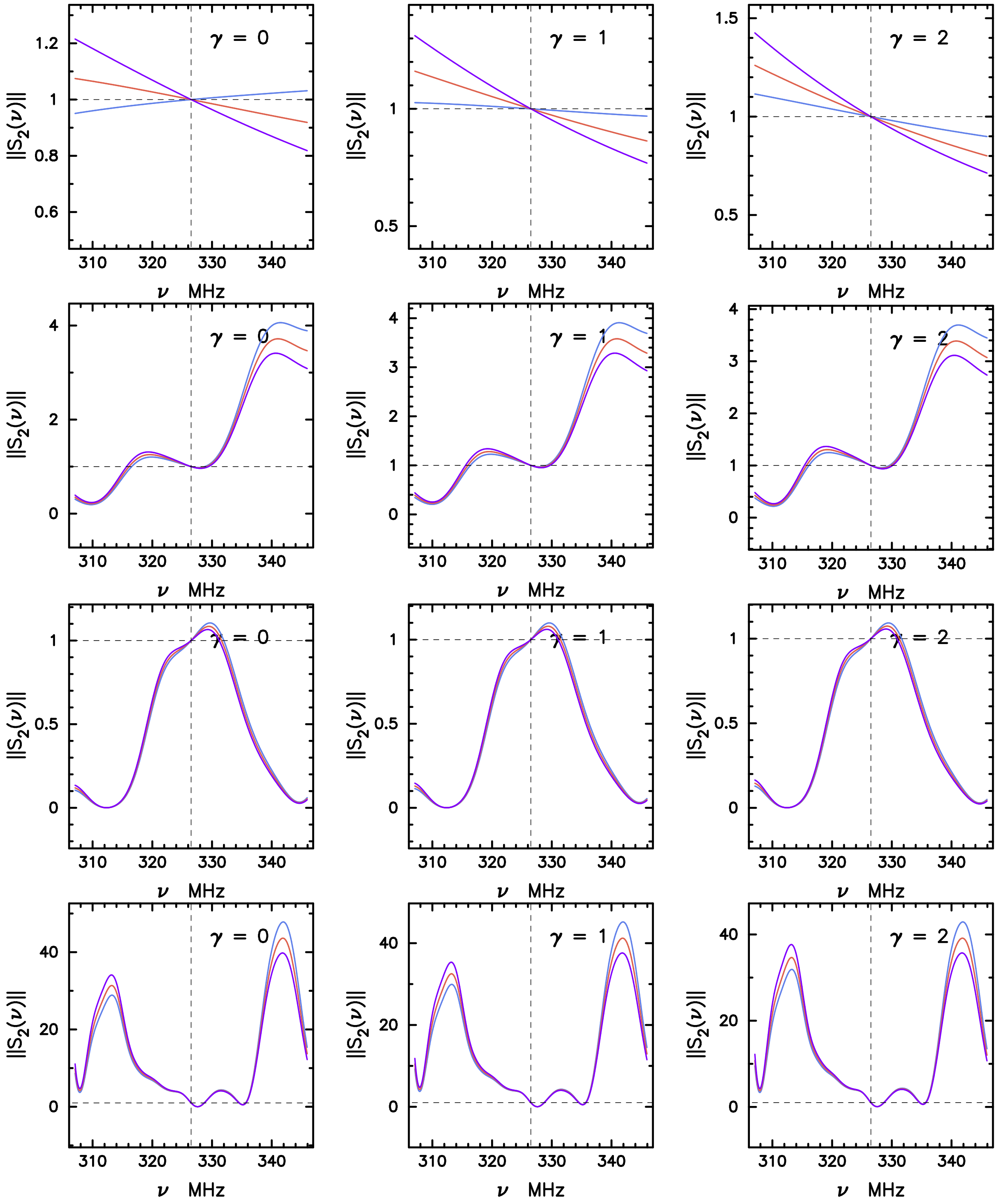

Figure 6.8: The normalised estimator $\parallel \mathbf{S}_2(\nu) \parallel$ for different values of α and γ are shown here. The first row shows the curves for the baseline $\mathbf{U}_1$ for the three values of $\gamma = 0, 1, 2$, the second for $\mathbf{U}_{15}$, the third for $\mathbf{U}_{22}$ and the fourth for $\mathbf{U}_{38}$. Each plot has three curves; one each for $\alpha = 0.0, 1.0, 2.0$, shown by the colours blue, red and purple respectively. The curves have been normalised to $\mathbf{S}_2(\nu_0)$ at $\nu_0 = 326.5$ MHz.

slightly from one γ to another. The first column represents the behaviour when $\gamma = 0$, when there is no "clustering". The spatial index γ exerts a spectral dependence through $\ell = 2\pi\mathbf{U}$, $\mathbf{U} = d\nu/c$ and $\mathbf{S}_2 \propto \ell^{-\gamma}$. α affects $\mathbf{S}_2$ through $\nu^{-2\alpha}$. By making $\gamma = 0$ and $\alpha = 2$ (achromatic flux density), we ensure that there is no contribution from the sky[1] that is likely to cause a chromatic effect in the estimator. Then, all the spectral behaviour that manifests in the $\alpha = 2$ curve in the first column is hence being caused by (a) the baselines $\mathbf{U}$ changing with frequency and (b) the primary beam shrinking with increasing frequency. Particularly striking is the fact that the different α curves for each γ follow each other closely, emphasising that the contribution to the spectral trend from the spectral index α is indeed small. We may hence conclude that the bulk of the spectral trend of the MAPS estimator $\mathbf{S}_2$ comes from the chromatic response of the primary beam and the interferometer. However, the foregrounds and these systematic effects on the foregrounds still appear smooth in frequency, a fact that is crucial to tell their spectral signatures apart from those of the HI signal.

6.5 The cylindrical power spectrum

The MAPS estimator matrix $\mathbf{S}_2$ is real and symmetric. The matrix can be reduced to the more commonly used form by summing along the diagonals in the principal direction, and retaining only one half of the sum. The diagonals are the loci of constant frequency separation, $\Delta\nu = \nu_i - \nu_j$. This one-dimensional representation of $\mathbf{S}_2$, which corresponds to the power spectrum in the case of a stationary signal, has already been shown in Figure 6.7. We now examine the cylindrical power spectrum representation. The cylindrical power spectrum can now be obtained from the two-visibility correlation MAPS estimator $\mathbf{S}_2(\Delta\nu)$ by taking a Fourier transform along the frequency separation ($\Delta\nu$) axis. The frequency separation $\Delta\nu$ is the Fourier conjugate of lag η.

The cylindrical power spectrum is an extremely useful representation of the power spectrum (see e.g. Datta *et al.* 2010; Vedantham *et al.* 2012; Thyagarajan *et al.* 2013; Liu *et al.* 2014 for more details). The brief derivation presented here draws extensively on the literature widely available on the topic (Morales & Hewitt, 2004; Datta *et al.*, 2010; Morales *et al.*, 2012; Vedantham *et al.*, 2012; Pober *et al.*, 2013a; Thyagarajan *et al.*, 2013; Seo & Hirata, 2016). The cylindrical power spectrum measures the power of the signal in different sinusoidal modes over a range of wavenumbers k on the plane of the sky and along the comoving direction. On the plane of the sky, the transverse $\mathbf{k}$-modes, called $\mathbf{k}_\perp$, are measured from the modes aligned along the imaginary x and y

---

[1] The diffuse foreground was simulated from the angular power spectrum, where α is the temperature spectral index. To convert to flux, we take $\alpha - 2$.

axes drawn on a Cartesian frame on the flat sky. The line-of-sight (LOS) wavenumber is given by $k_{\parallel}$ which is measured along the redshift or frequency axis in the visibility data. The spatial wave vectors $\mathbf{k} = (k_{\perp}, k_{\parallel})$ are related (Morales & Hewitt, 2004) to the baseline $\mathbf{U}$ and the frequency interval $\Delta\nu$ as

$$k_{\perp} = \frac{2\pi\,|\mathbf{U}|}{D(z)} \tag{6.26}$$

where

$$k_{\perp} = \sqrt{k_x^2 + k_y^2}\ , \tag{6.27}$$

$$|\mathbf{U}| = \sqrt{u^2 + v^2}\ , \tag{6.28}$$

$$D(z) = \frac{H_0\,\nu_{\mathrm{HI}}\,E(z)}{c\,(1+z)^2} \tag{6.29}$$

is the transverse comoving distance and

$$k_{\parallel} \approx \eta \frac{2\pi\,H_0\,\nu_{\mathrm{HI}}\,E(z)}{c\,(1+z)^2} \tag{6.30}$$

where

$$E(z) = \left[\Omega_{\mathrm{M}}\,(1+z)^3 + \Omega_{\mathrm{k}}\,(1+z)^2 + \Omega_{\Lambda}\right]^{1/2} \tag{6.31}$$

and

$$\eta = \frac{1}{\Delta\nu} \tag{6.32}$$

The minimum value for $k_{\parallel}$ is set by the bandwidth of the system, that is when $\eta = 1/B$, and the maximum value taken by $k_{\parallel}$ is set by the frequency resolution, or the smallest channel width, when $\eta = N/B$. These correspond respectively to the smallest and largest delays in the delay space, which is the Fourier conjugate of the frequency separation $\Delta\nu$. The minimum and maximum values taken by the transverse wavenumber $k_{\perp}$ are set by the shortest and the longest baselines respectively.

Following Parsons *et al.* (2012b), where they introduce the delay transform and delay-rate filtering for the foregrounds, we can write

$$\mathcal{V}(u, v, \eta) = \int dl dm d\nu A(l, m, \nu) I(l, m, \nu) e^{-2\pi i(ul+vm+\eta\nu)} \tag{6.33}$$

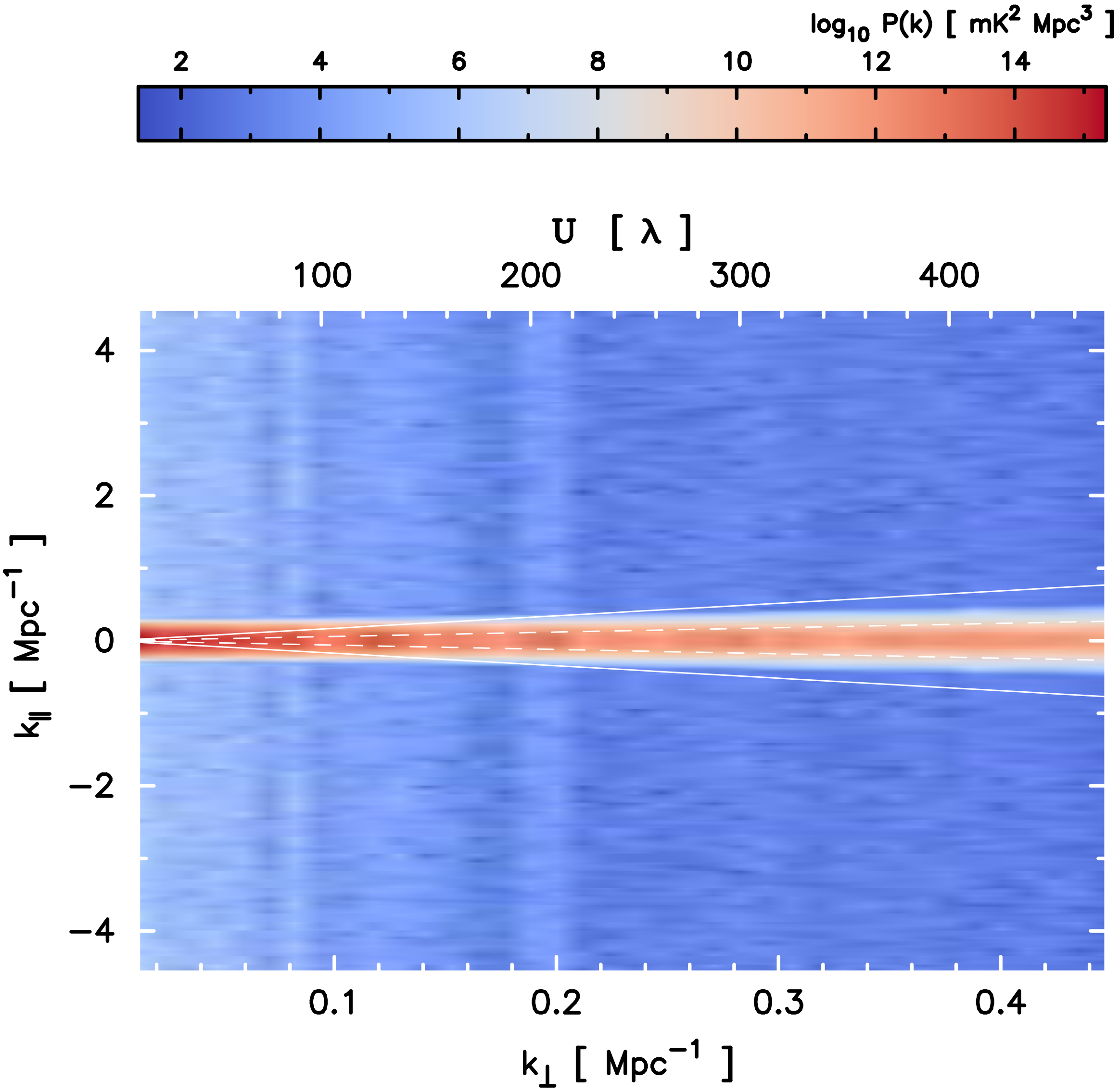

Figure 6.9: The cylindrical power spectrum for a noise-free, foreground-only sky model simulated for the Mode-I system of OWFA. The foreground wedge is clearly visible. The dashed line denotes the boundary of the wedge, which is related to the angular extent of the simulated map. In practice, its extent would depend on the FoV. The solid line denotes the horizon limit.

Since $P(\mathbf{k})$ represents the power spectrum of the temperature fluctuations, the relation between the $\mathbf{S}_2$ matrices and the power spectrum $P(\mathbf{k})$ can be derived. We can now write (see Parsons *et al.*, 2012, for a full derivation)

$$\langle \mathcal{V}(\mathbf{U},\nu_i)\mathcal{V}(\mathbf{U},\nu_j)^*\rangle = \left(\frac{\partial B}{\partial T}\right)^2 \int d^2\mathbf{U}|A(\mathbf{U})|^2 \left(\frac{B}{D(z)^2\, r'_\nu}\right) P(\mathbf{k}_\perp, k_{||}) \tag{6.34}$$

where $P(\mathbf{k}_\perp, k_{||})$ is the cylindrical power spectrum, and the left-hand side is equal to $\mathbf{S}_2(\mathbf{U},\nu_i,\nu_j)$. Since $|\mathcal{V}(\eta)|^2 = \mathcal{V}(\eta).\mathcal{V}(\eta)^*$, by the convolution theorem of Fourier transforms it follows that

$$\mathcal{V}(\eta).\mathcal{V}(\eta)^* \overset{F}{\rightleftharpoons} \mathcal{V}(\nu) * \mathcal{V}^*(\nu) \tag{6.35}$$

Therefore, equivalently we have

$$\langle |\mathcal{V}(\mathbf{U},\eta)|^2\rangle = \left(\frac{\partial B}{\partial T}\right)^2 \int d^2\mathbf{U}|A(\mathbf{U})|^2 \left(\frac{B}{D(z)^2\, r'_\nu}\right) P(\mathbf{k}_\perp, k_{||}) \tag{6.36}$$

It is easy to see that the quantity $\mathbf{S}_2(\Delta\nu)$ represents the auto-convolution of the vector $\mathcal{V}(\mathbf{U},\nu)$. The auto-convolution sum $\mathbf{S}(\Delta\nu)$ is equivalently obtained from the full $\mathbf{S}_2$ matrix by summing along the diagonals. $P(\mathbf{k})$ can now be uniquely defined by inverting equation 6.34,

$$P(\mathbf{k}_\perp, k_{||}) = \frac{\left(\frac{B}{N}\right)\int \mathbf{w}(\Delta\nu)\mathbf{S}_2(\mathbf{U},\Delta\nu)e^{-2\pi i\Delta\nu\eta}d\Delta\nu}{\left(\frac{\partial B}{\partial T}\right)^2 \int d^2\mathbf{U}|A(\mathbf{U})|^2 \left(\frac{B}{D(z)^2\, r'_\nu}\right)} \tag{6.37}$$

where $\Delta\nu$ is a variable taking the values $|\nu_i - \nu_j|$ in multiples of the channel width B/N. Writing the Fourier integral in the numerator as a Fourier sum,

$$P(\mathbf{k}_\perp, k_{||}) = \frac{\left(\frac{B}{N}\right)^2 \sum\limits_{i=0}^{N-1} \mathbf{w}(\Delta\nu)\mathbf{S}_2(\mathbf{U},\Delta\nu)e^{-2\pi i\Delta\nu\eta}}{\left(\frac{\partial B}{\partial T}\right)^2 \int d^2\mathbf{U}|A(\mathbf{U})|^2 \left(\frac{B}{D(z)^2\, r'_\nu}\right)} \tag{6.38}$$

The reduced $\mathbf{S}_2$ matrices, where the data have been summed along the diagonals in each matrix to obtain $\mathbf{S}_2(\Delta\nu)$, are weighted with a suitable window function $\mathbf{w}(\Delta\nu)$ along the frequency axis and Fourier transformed. There is some freedom in the choice of the bandpass weighting function. The weighting function suppresses the sidelobes arising from the Fourier transform, also called the “picket-fence” effect in signal processing literature. Vedantham *et al.* (2012) suggest the Blackman-Nuttall window as highly suitable for sidelobe suppression. However, the choice of the weighting function is usually a tradeoff between sidelobe suppression and loss of sensitivity and resolution (Thyagarajan *et al.*, 2013): the peak of the Fourier transform of the Blackman-Nuttall window is ~ 2.76 times lower than for a sinc function. The simulations presented here (Marthi *et al.*, 2016) have used a Blackman-Nuttall window (Nuttall, 1981), which is defined as

$$w(n) = 0.36 - 0.49\cos\frac{2\pi n}{N-1} + 0.14\cos\frac{4\pi n}{N-1} - 0.01\cos\frac{6\pi n}{N-1}\,, \quad 0 \leq n \leq M-1 \quad (6.39)$$

where M is $N/2$ for N odd and $(N+1)/2$ for N even.

In Figure 6.9 is shown the cylindrical power spectrum for a foreground-only, noise-free sky realisation for the Mode-I system of OWFA, with the 39-MHz observing band split into 312 channels of 125 kHz each. The value of $\mathbf{k}_\perp^{\rm max}$ is fixed by the longest baseline $\mathbf{U} = 487.5$, but there is some freedom in the choice of $k_\parallel^{\rm max}$ in the OWFA programmable receiver since the number of channels across the band can be chosen at the time of correlation. The values for the transverse and LOS wavenumbers are given in Table 2.4. For the Mode-I cylindrical power spectrum shown here in Figure 6.9, 1.1×10^{-2} Mpc^{-1} $< k_\perp <$ 4.6×10^{-1} Mpc^{-1} and 1.4×10^{-2} Mpc^{-1} $< k_\parallel <$ 4.6 Mpc^{-1}.

We also consider a hypothetical version of the Mode-I array with the number of antennas unchanged but their separation scaled up 6 times in the North-South direction. This is done merely to bring out clearly the features of the foreground wedge. The longest baseline in this hypothetical array is $\mathbf{U} = 2925$, and the corresponding $\mathbf{k}_\perp^{\rm max}$ is increased from 4.6×10^{-1} Mpc^{-1} to 2.76 Mpc^{-1}. This results in larger delays at the longer baselines. The power spectrum of the same foreground realisation for this scaled array is shown in Figure 6.10. A null-like feature within the wedge is apparent throughout the $\mathbf{k}_\perp$ range, but it appears particularly pronounced on the longer baselines in this figure. This corresponds to the first null of the sinc^2 primary beam in the North-South direction, as the interferometer is sensitive to delays only to the projected North-South component of an incoming wavefront. Figure 6.9 can schematically be considered to be a subset of Figure 6.10, bounded by the appropriate $k_\perp^{\rm max}$. Although the two figures show the cylindrical power spectrum for the same foreground realisation, their peak powers are slightly different. This is because the true power spectrum is not sampled in **k**-space identically, corresponding to the differences in the baseline lengths between the two interferometer modes.

The two interferometric modes of OWFA span very similar ranges of $\mathbf{k}_\perp$ since the longest baseline is ~ 500 m. There are only small differences arising from the fact that Mode-II measures a few extra $\mathbf{k}_\perp$ modes since it has a few baselines shorter than $\mathbf{U} = 12.5$ and a few slightly longer baselines than Mode-I corresponding to the extreme ends of the array. Therefore, between Mode-I and Mode-II, the cylindrical power spectrum of the sky signal is likely to appear very similar.

The wavefront from a source at a given location in the sky arrives with a delay between the two antennas of a baseline. The longer the baseline, the larger the delay. Similarly, the further away the source from the phase centre, the larger the delay. Consider a source in a given direction with a smooth spectrum across the observing band. After a Fourier transform, in the delay space this would translate into the Fourier transform of the intrinsic spectral shape of the source centred at the delay for that angular position, convolved with the Fourier transform of the instrumental bandpass. This leads to a region in the instrumental **k**-space where the power from all the smooth spectrum sources in the sky is confined to within a region bounded by a straight line that is set by the largest delay encountered by the signals at each baseline. This region then gives the appearance of a wedge. The wedge can be analytically derived from the equations given earlier. It can be seen that the delay

$$\eta = \frac{\mathbf{d}}{c} = \frac{\mathbf{U}}{\nu_0} = \frac{\mathbf{U}(1+z)}{\nu_{\rm HI}} \tag{6.40}$$

where ν_0 is the frequency of observation, given by $\nu_0 = \nu_{\rm HI}/(1+z)$. Since $\mathbf{u} = \sqrt{u^2+v^2} < L/\lambda$, where L is the largest possible separation of a pair of antennas, η, the geometric propagation delay is largest for signals arriving from the horizon. Then, from equations 6.26, 6.30 and 6.40, it follows that

$$k_\parallel = \frac{H_0\, E(z)\, D(z)}{c\,(1+z)}\, k_\perp \tag{6.41}$$

defines a straight line at the boundary of the wedge. The boundary is set by the "horizon", given by the condition $l^2 + m^2 = 1$, called the horizon limit (see e.g. Pober *et al.*, 2013a).

However, the boundary of the wedge in Figures 6.9 and 6.10 is set by the angular extent of the foreground maps and the primary beam used in the simulations here. This explains why the wedge is confined to a very small region in Figure 6.9. The effect of having longer baselines can be seen more pronounced in Figure 6.10, where the cylindrical power spectrum of the same sky realisation measured with a scaled version of the Mode-I interferometer has meant that the delays are larger at the longer baselines. For OWFA, the horizon limit, given by equation 6.41 is

$$k_\parallel \sim 1.72\, \mathbf{k}_\perp \tag{6.42}$$

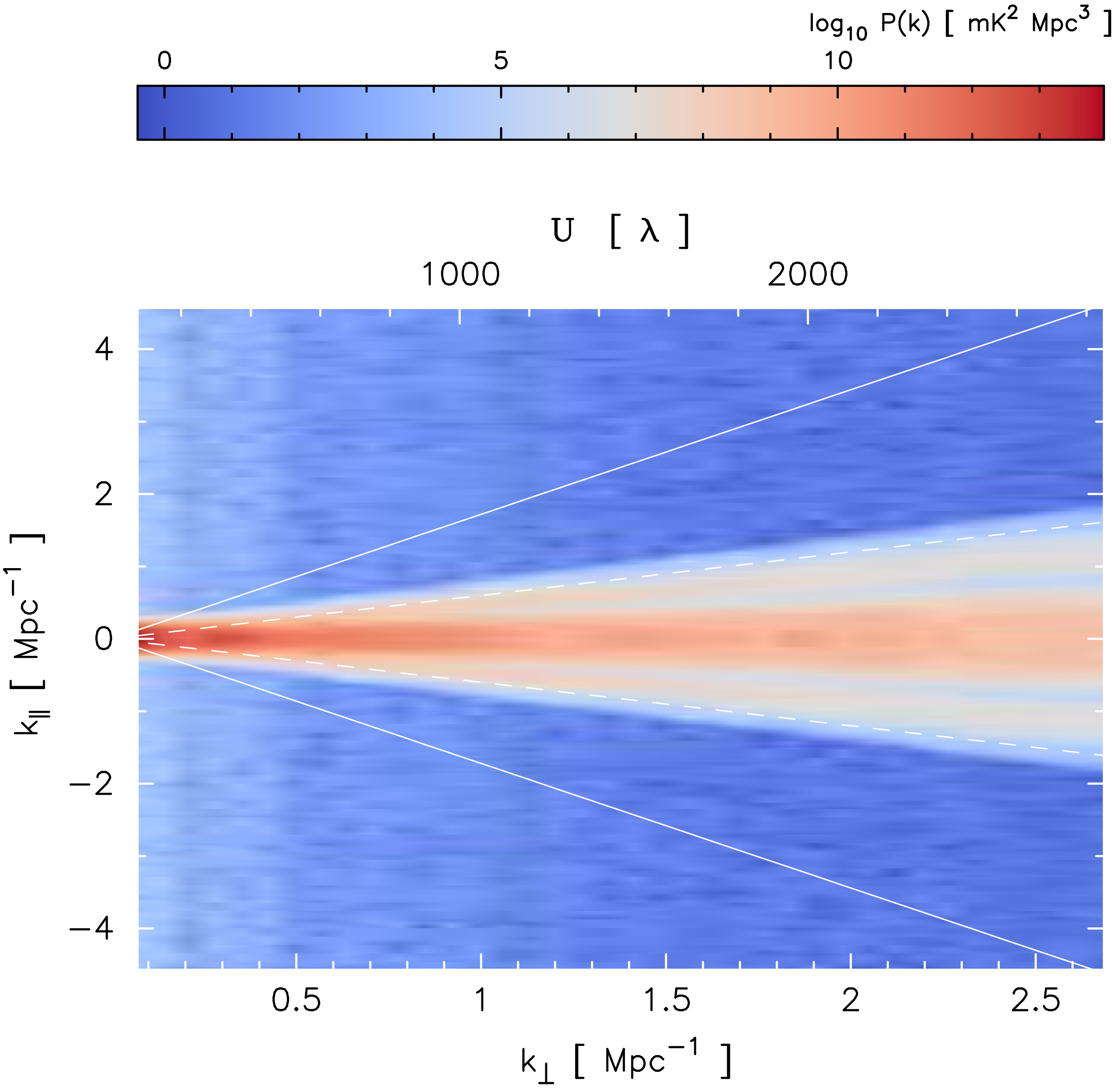

Figure 6.10: The cylindrical power spectrum for the same realisation of noise-free, foreground-only sky model simulated for a scaled version the Mode-I system of OWFA. The array has been scaled 6 imtes in length, so the baselines are all longer by the same factor. The foreground wedge is well sampled by the longer baselines of this hypothetical interferomter. Here again, the dashed line denotes the boundary of the wedge in this simulation and the solid line denotes the horizon limit.

using $D(z) = 6.67$ Gpc, computed at $z = 3.35$. It is interesting to note that the slope of the wedge depends purely on cosmological quantities and is independent of the dimensions of the instrument. The slope of the boundary of the visible wedge in these figures represents the largest delay in the simulation, caused by a source at the boundary that is approximately 20° from the phase centre of the beam. This translates into a delay of

$$\eta \sim \frac{|\mathbf{d}|}{c} \sin 20^\circ \tag{6.43}$$

that results in the relation

$$k_\parallel \sim 0.59\,\mathbf{k}_\perp \tag{6.44}$$

The edge of the foreground wedge is set by the dashed line in Figures 6.9 and 6.10, which corresponds to the extent of the FoV. The solid line sets the horizon limit, beyond which the foreground is expected to roll off very sharply, leaving a clean "foreground-free" region in the **k**-space. In reality, the primary beam of OWFA would respond to sources beyond the simulation FoV, albeit with reduced sensitivity. The wedge would therefore open with a larger angle than in these simulations, but it is expected to lie somewhere between the simulated FoV boundary and the horizon limit.

There is some power in Figures 6.9 and 6.10 beyond the extent given by the boundary of the wedge (the dashed line). This is being caused by the spectral structure of the foregrounds within the band. It can also be seen that the foregrounds beyond the FoV limit appear brighter on the shortest baselines. This can be understood as being contributed by the large scale diffuse emission which the short baselines are preferentially sensitive to (see e.g. Pober *et al.*, 2013a, for a similar discussion). The last thing one can see from Figure 6.9 is that there is a fair amount of "foreground-free" region, equivalent to the "EoR window", from which the HI signal could be estimated. One of the studies that we propose to carry out, in order to enable meaningful predictions is through a Fisher matrix formalism excluding the foreground wedge.

6.6 Error on the estimator

The estimator $\mathbf{S}_2$ has the dimensions of variance. For the error on $\mathbf{S}_2$ we are hence interested in the variance of the variance. In the simulations described above, the visibility correlation matrix $\mathbf{S}_2$ is computed at every one-second interval. For an N-second observation, therefore, N such matrices are available for each baseline, from which the mean matrix and the RMS matrix for each baseline can be computed. It has been shown in Section 6.2.2 that the error on the summed model visibility goes down as $\sqrt{1/N_n}$ when visibilities from N_n baselines are added. This means that the error on the estimator itself goes inversely as N_n for each baseline n.

A noise-only simulation was run in which noise equivalent to $T = 150$ K, the OWFA system temperature, was added to zero visibility data for each baseline, and the data were simulated for an observation of 60 seconds. The visibility correlation estimator is, of course, consistent with zero. But the error bars on the estimate can be obtained from the 60-second observation itself, as the RMS of the 60 $\mathbf{S}_2$ matrices, as outlined above. Figure 6.11 shows the RMS error drawn from the reduced data, where baselines of equal lengths have been added prior to cross-correlation, as set out by equation 6.10. The solid line through the RMS error points follows the behaviour $1/N_n$, where N_n is the number of copies of baseline n. A larger number of copies results in a smaller RMS error on the shorter baselines. The agreement between the measured errors and the expected error is not readily apparent in a single realisation. But when averaged over 1000 different realisations of 60 seconds each, which is equivalent to observing for 1000 minutes, the agreement between the measured RMS errors and the expected scaling behaviour, shown in Figure 6.12, is excellent. The error bars on the RMS errors relate to the 1σ error obtained over all the 1000 realisations.

The estimator $\mathbf{S}_2$ and the error matrix $\Delta\mathbf{S}_2$ are computed similarly for a single realisation of the Galactic diffuse foreground, with the same system temperature of 150 K and a 60-second observation. This is equivalent to deriving the error bars from as many independent realisations (60) of the noise, given a single realisation of the foreground. Figure 6.13 shows the mean estimator matrix $\mathbf{S}_2(\nu_i, \nu_j)$ on the left and the 1σ error matrix $\Delta\mathbf{S}_2$ on the right. Figure 6.14 shows the recovered power spectrum by shooting imaginary skewers through the mean and RMS cubes, $\mathbf{S}_2$ and $\Delta\mathbf{S}_2$, at the same (ν_i, ν_j) co-ordinates: the power spectrum is obtained from the mean $\mathbf{S}_2$ matrix and the error bars from the RMS $\Delta\mathbf{S}_2$ matrix. The left plot of Figure 6.14 shows the “self” power spectrum with the error bars where $\nu_i = \nu_j =$326.44 MHz, and the right plot shows the “cross” power spectrum with error bars, at $\nu_i =$342.19 MHz and $\nu_j =$326.94 MHz. The dashed straight line through the plots is not a fit, but it is the input power spectrum used for simulating the diffuse Galactic foreground. The $\mathbf{U}$ values on the x-axis are computed at the central frequency 326.5 MHz, as there is no other meaningful way to represent $\mathbf{U}$ at a pair of frequencies (ν_i, ν_j) at which these spectra have been extracted. Figure 6.14 is an important result purely from the perspective of foregrounds: a 60-second integration has resulted in a 10σ detection of the diffuse foregrounds, under the implicit assumption that the point source foregrounds have

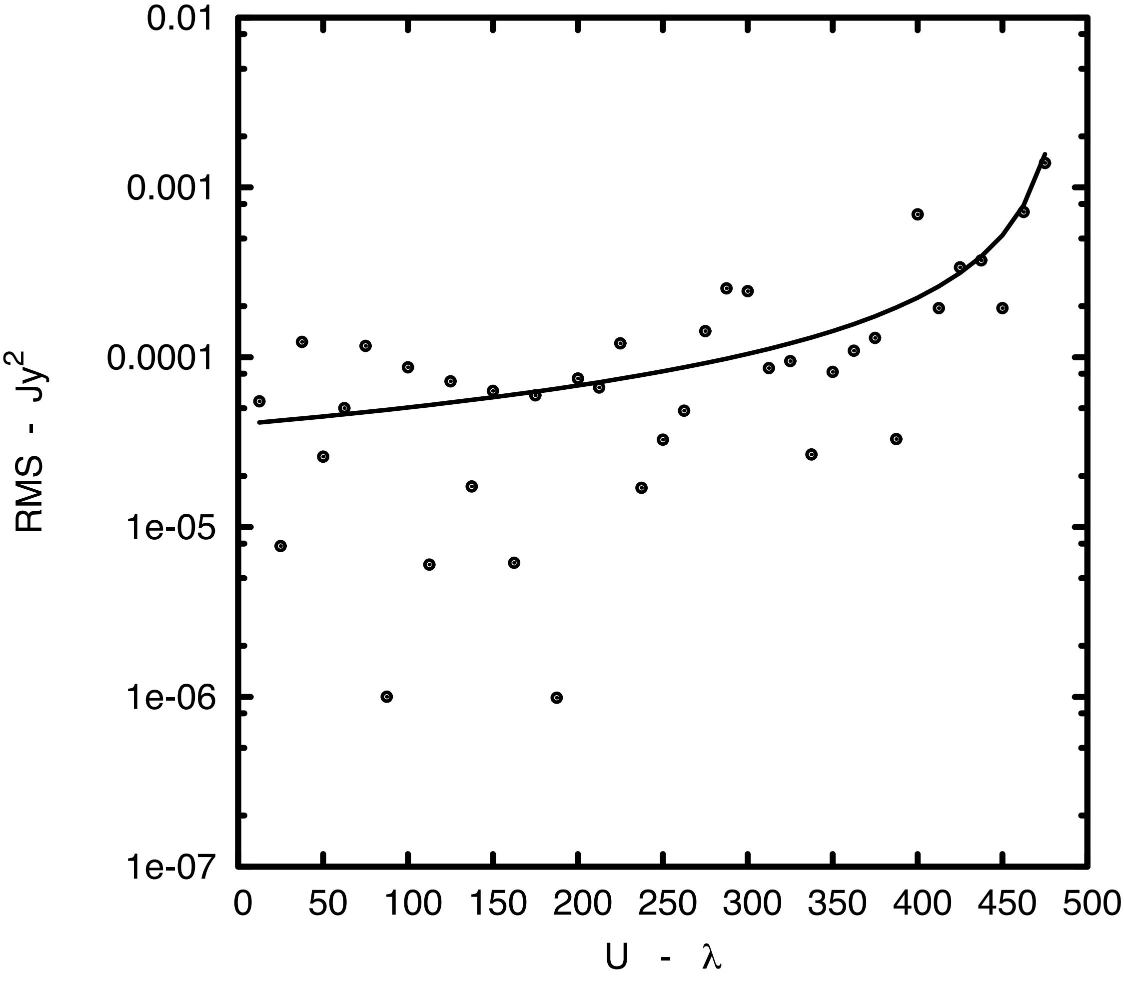

Figure 6.11: The band-averaged RMS noise in the estimator on each baseline for a simulated zero-signal, noise-only observation. The total integration time is 60 *s* with $T_{\rm sys}$ = 150K. The RMS decreases as the number of copies of the shorter baselines increases. The points represent the measured RMS and the solid line, proportional to $1/N_n$, shows the general expected RMS behaviour, and is not a fit to the points.

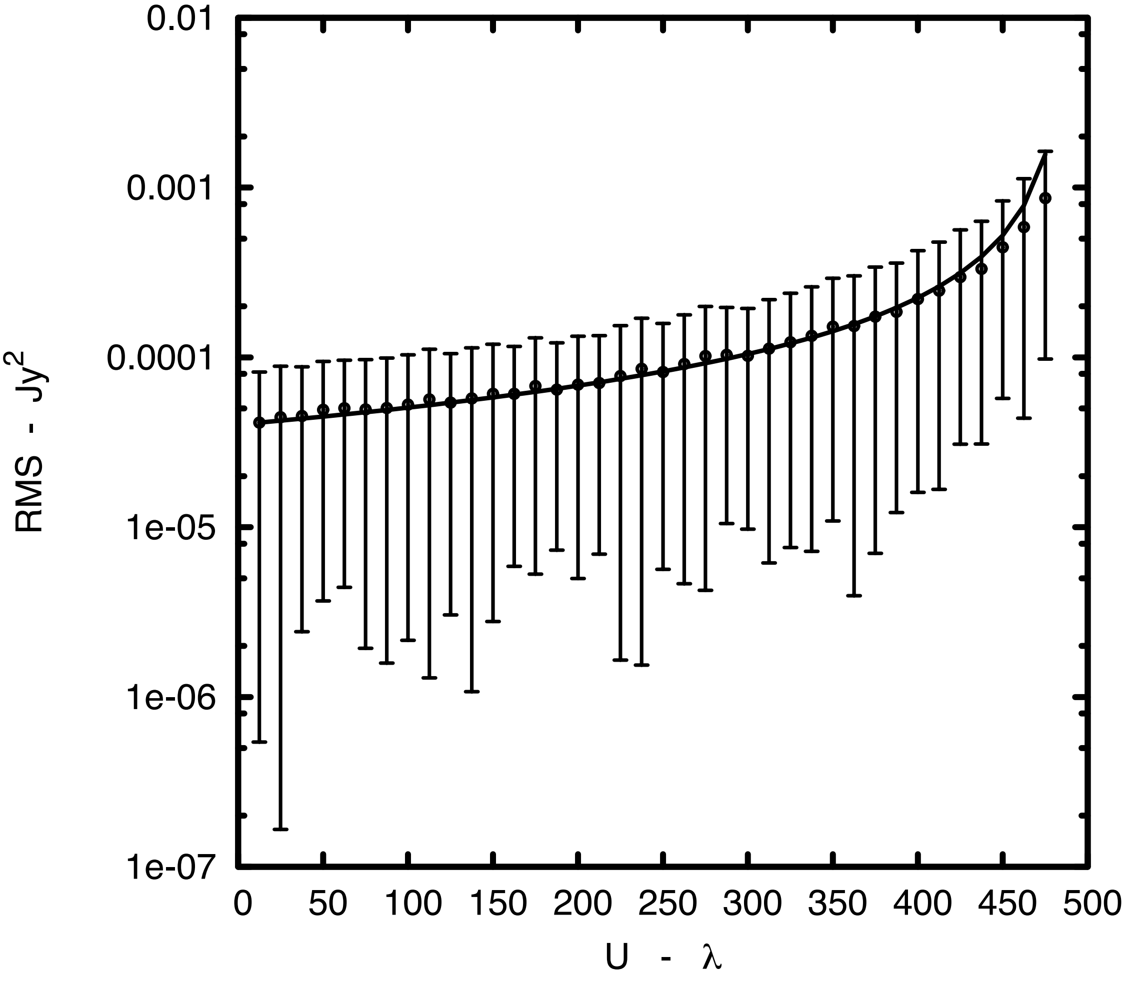

Figure 6.12: The band-averaged RMS noise in the estimator on each baseline averaged over 1000 realisations of a simulated zero-signal, noise-only observation. The total integration time for each realisation is 60 s with $T_{\rm sys} = 150$K. The RMS error measured in each baseline is in excellent agreement with the expected RMS behaviour, scaling as $1/N_n$, given by the solid line. The error bars on the RMS errors are 1σ obtained over these 1000 realisations.

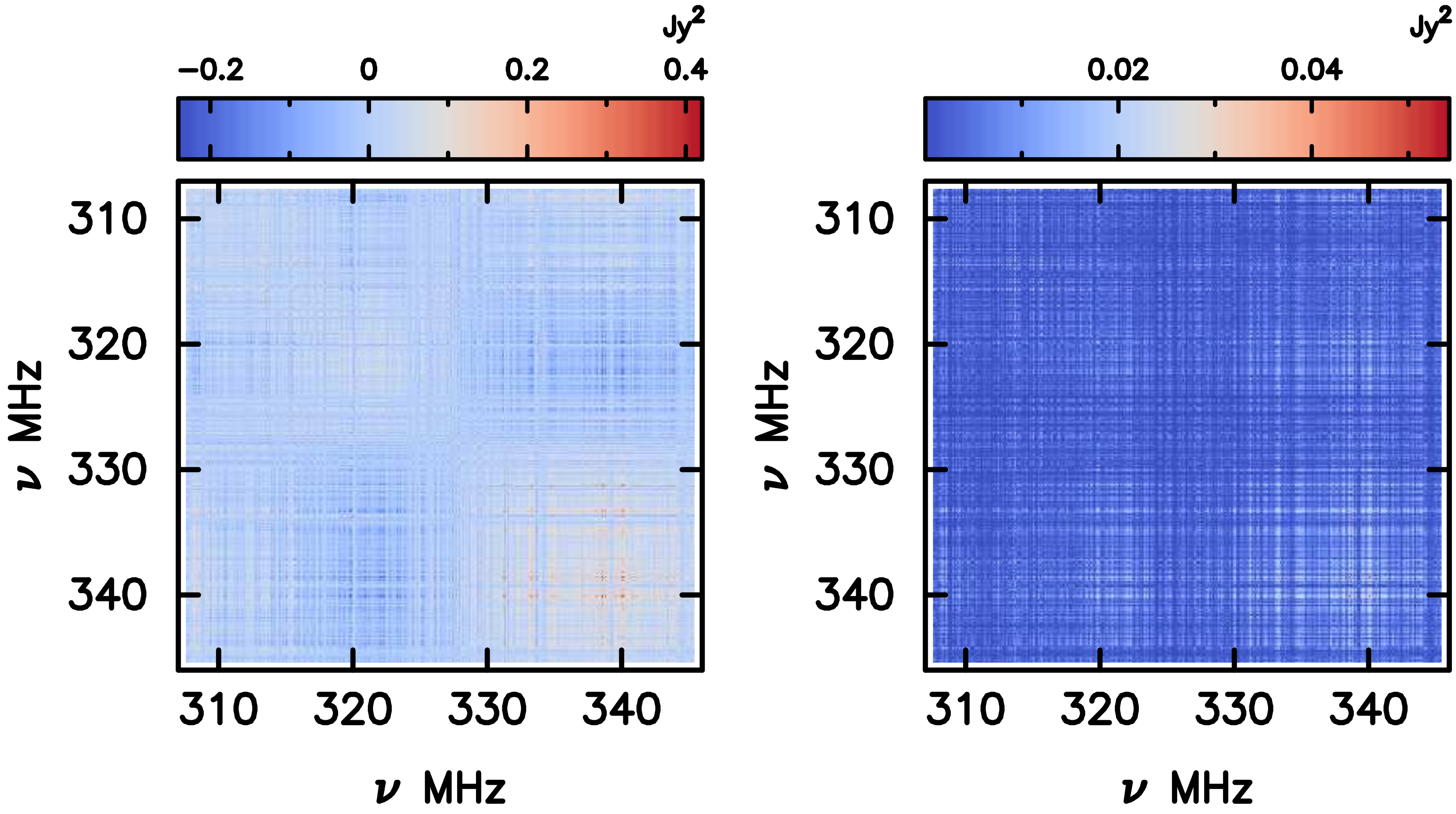

Figure 6.13: The MAPS estimator $_2$ (left) and its RMS error (right) for a realisation of the Galactic synchrotron foreground with system noise equivalent to $T_{\mathrm{sys}} = 150$ K added to the model visibilities and integrated for 60 seconds.

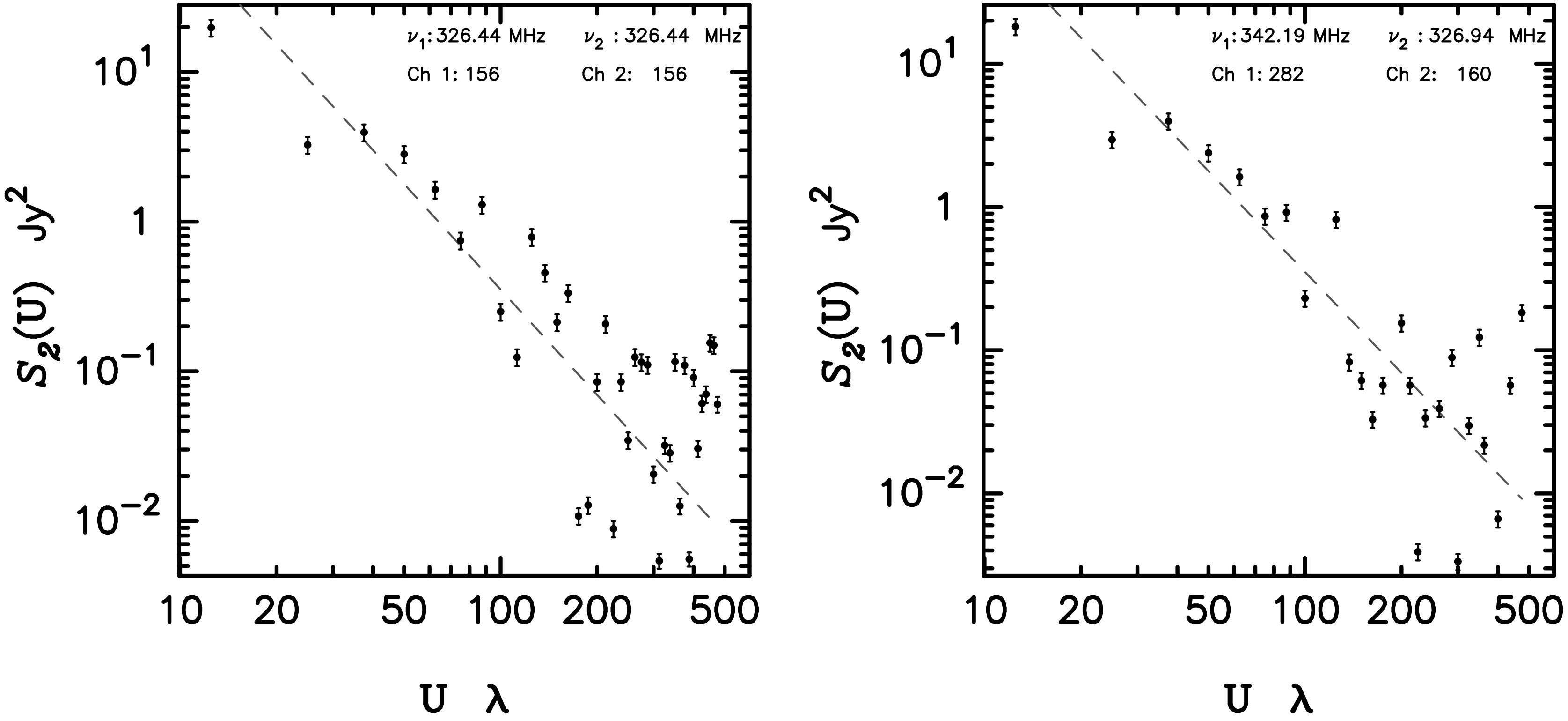

Figure 6.14: The left and right panels respectively show the “self-power spectrum” and “cross-power spectrum” at different values of (ν_1, ν_2) by shooting skewers through the $\mathbf{S}_2$ cube. The error bars, drawn from the same co-ordinates of the RMS cube, correspond to 60 seconds of integration with a system temperature of $T_{\rm sys} = 150$ K. The dashed straight line is the input angular power spectrum of the Galactic diffuse synchrotron foreground. The scatter in the estimated power spectrum arises from the stochasticity of this realisation of the foreground.

been modelled out, or are sub-dominant, as would be the case for the short baselines of OWFA (see Section 5.4). This is a very optimistic scenario if we are interested in the study of the statistics of the intensity of the diffuse foregrounds.

6.7 Estimator representation in eigenspace

We have seen that the two-visibility correlation is an estimator of the multi-frequency angular power spectrum. The power spectrum is obtained from the data in one of two ways: through a Fourier transform of the angular two-point correlation of the brightness temperature map, or through the visibility correlation directly. The MAPS estimator discussed in Section 6.2 is obtained through visibility correlations, and we have seen it in action in Section 6.3. Since we are concerned with estimation and characterisation of the foregrounds here, we have applied the MAPS estimator to a "foregrounds-only" sky signal. In reality, the cosmological signal is embedded in the estimator: we have not addressed that aspect yet. Owing to the smooth spectral nature of the foreground signal, we expect that it has a small number of degrees of freedom in ν. We now seek to characterise the foreground signal in ν on every baseline in a uniformly consistent manner.

From Section 6.2.2, we see that the MAPS estimator has the general form of the sum of two independent vectors

$$\mathbf{S}_2 \approx Re(V).Re(V) + Im(V).Im(V) \tag{6.45}$$

where V has dimensions of the visibility. We now seek an eigenspace to orthogonalise the vectors. Obviously, in the N-dimensional orthogonal space (dimension equal to the number of channels), the estimator matrix would occupy a rank of 2. The components along the subspace axes can be obtained through a Karhunen-Loève (KL) transform. The transformation

$$\mathbf{S}_2 = \mathbf{W}\boldsymbol{\Lambda}\mathbf{W}^{\dagger} \tag{6.46}$$

diagonalises the MAPS matrix: it returns the matrix of the orthonormal column eigenvectors $\mathbf{W}$ and the eigenspectrum $\boldsymbol{\Lambda}$ with rank 2. Figure 6.15 shows the eigenvectors of the foreground obtained $\mathbf{w}_{\mathrm{FG}}$ through the KL transform, and one of the foreground-free eigenvectors $\mathbf{w}_{\mathrm{n}}$, along with their estimator matrices.

The KL transform is a norm-preserving transform because the matrix of the eigen-

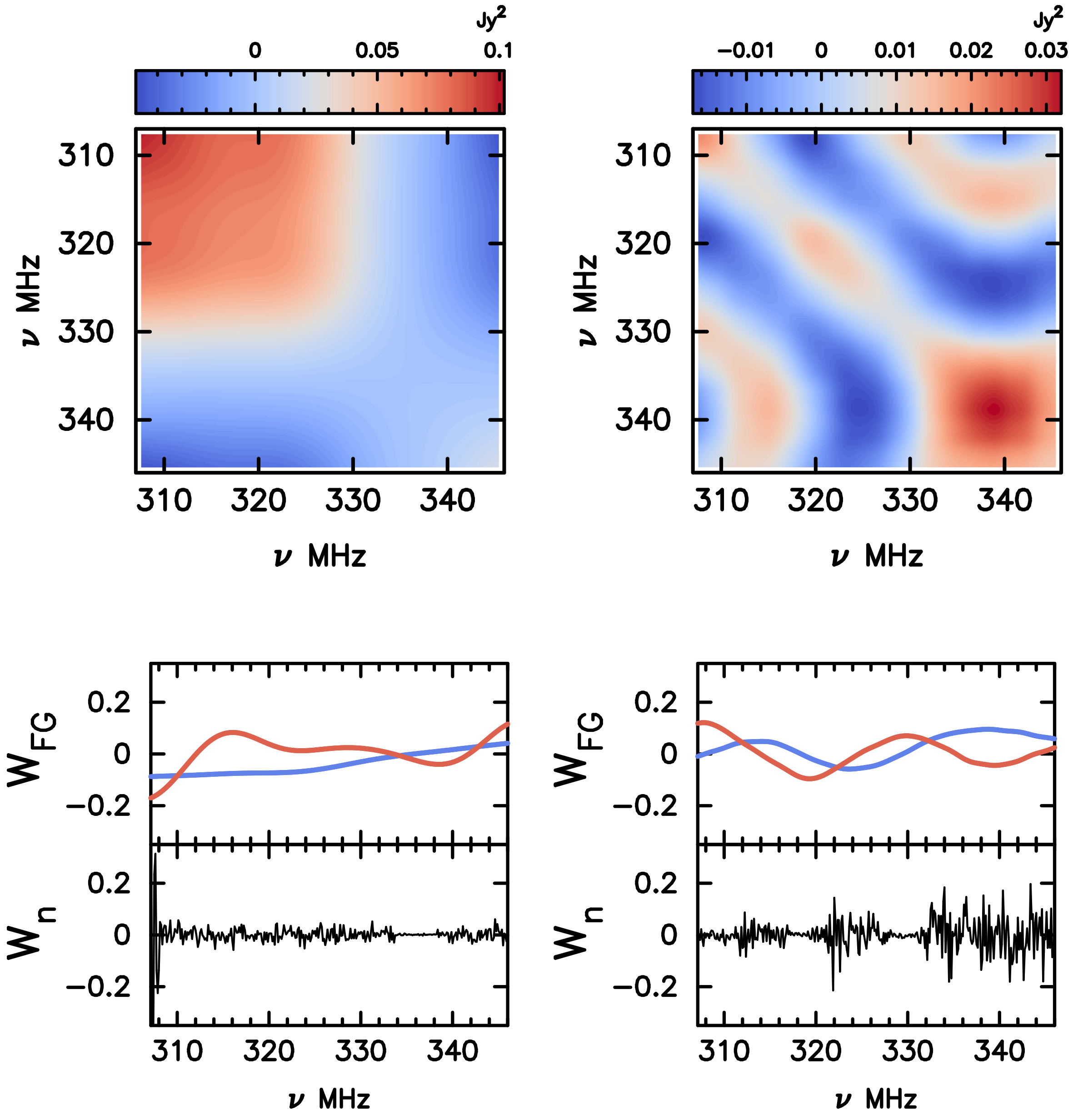

(c) Baseline 7

(d) Baseline 29

Figure 6.15: The estimator matrix $\mathbf{S}_2(\mathbf{U}, \nu_i, \nu_j)$ is shown in the top panels for the two baselines $\mathbf{U}_7$ and $\mathbf{U}_{29}$. The two foreground eigenvectors and one of the foreground-free eigenvectors are shown for each matrix in the bottom panels.

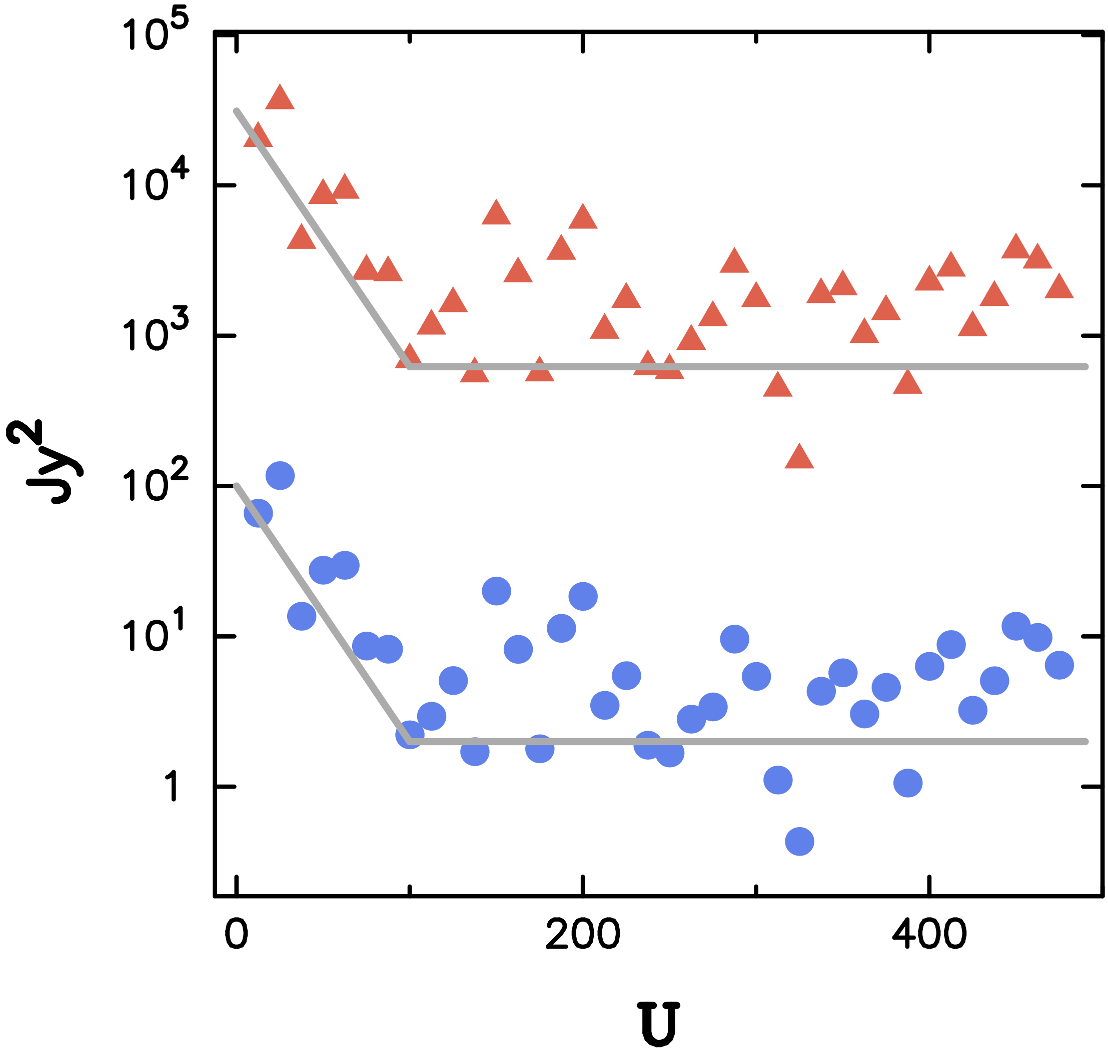

Figure 6.16: The lower set of filled circles is the square of the input model visibilities averaged across channels, equal to $\mathbf{S}_2$, and the upper set of filled triangles is a proxy for $\mathbf{S}_2$ through the sum $\sum_{k=0}^{L} \lambda_k$. If we had summed the squares of the visibilities instead of averaging them across channels, the points would lie one on top of the other. The straight lines through the two sets of points are not fits, but merely a visual aid for the factor of 312 separation as a result of averaging rather than summing across the 312 channels.

vectors is unitary by construction.

$$\|\mathbf{S}_2\| = \|\mathbf{\Theta}^{FG}\|, \quad \|\mathbf{S}_2 - \mathbf{\Theta}^{FG}\| \approx 0 \tag{6.47}$$

Equivalently,

$$tr(\mathbf{\Lambda}) - \sum_{k=0}^{L} \lambda_k \approx 0 \tag{6.48}$$

where L is the rank of the matrix under transformation, in general. Therefore, $\sum_{k=0}^{L} \lambda_k$ gives a direct estimate of the channel-summed foreground power spectrum in the observing band. For the foregrounds, because of equation 6.45, L is always 2. Therefore the sum of the two eigenvalues is thus a measure of the total angular power within the band for that baseline.

We test this against the power spectrum obtained through the square of the input model visibility function $V(\mathbf{U}_n, \nu_i)$ in our simulation. This is allowed for the OWFA since there is no rotational aperture synthesis. The visibilities are all measured at regularly spaced points on the v axis. The expected two-visibility correlation can be directly obtained from the input model visibilities against which the true estimator can be validated. Figure 6.16 shows the channel-averaged square of the input model visibilities, which is proportional to the power spectrum as we have shown in Section 6.2 and the estimate of the power spectrum through the sum of the foreground eigenvalues. The latter sum is up exactly by a factor equal to the number of channels, which is 312 here.

Three points have to be noted in the context of this exercise: (1) the per baseline foreground eigenvectors in frequency are orthonormal in this representation, giving us a consistent comparison of the normalised frequency dependence of the foreground signal in each baseline, (2) the trace of the eigenspectrum directly measures the total power in each baseline, and (3) the $d-\nu-\nu$ representation can be further compressed as we retain only the two eigenvalues and their eigenmodes. The eigenspace representation of the $\mathbf{S}_2$ matrix has led to a fast algorithm for obtaining random realisations of the HI visibilities, which shall be described in the next section.

6.8 The HI power spectrum

The two-visibility correlation estimator in action for simulated foregrounds was demonstrated in the previous section. The estimator $\mathbf{S}_2$ itself is blind to the nature of the signal it is being used to estimate, and is hence equally effective in recovering the

HI signal. This section draws largely on the work presented in Chatterjee *et al.* (2016) and Sarkar *et al.* (2016b).

6.8.1 Visibility correlation of the HI signal

The HI power spectrum was introduced in Section 1.3. To summarise, the mean brightness temperature $\bar{T}$ of HI at a post-EoR redshift z is given by

$$\bar{T}(z) = 4.0\ (1+z)^2 \left(\frac{\Omega_b h^2}{0.024}\right)\left(\frac{0.7}{h}\right)\left(\frac{H_0}{H(z)}\right)\ \mathrm{mK} \tag{6.49}$$

The HI power spectrum $P_{\mathrm{HI}}(\mathbf{k},\mu)$ traces the dark matter power spectrum $P(\mathbf{k})$, and is given by

$$P_{\mathrm{HI}}(\mathbf{k},\mu) = b_{\mathrm{HI}}^2\ \bar{x}_{\mathrm{HI}}^2\ \bar{T}^2\ [1+\beta\mu^2]^2\ P(\mathbf{k}) \tag{6.50}$$

where β is the linear redshift space distortion parameter and μ is the correction to account for the line of sight component of the peculiar velocities. The average specific intensity of the HI emission, given by

$$\bar{I} = 2.5\times 10^2\ \frac{\mathrm{Jy}}{\mathrm{sr}} \left(\frac{\Omega_{\mathrm{b}} h^2}{0.022}\right)\left(\frac{0.7}{h}\right)\frac{H_0}{H(z)} \times \bar{x}_{\mathrm{HI}} \times b_{\mathrm{HI}} \tag{6.51}$$

can be determined for any assumed values of parameters $\bar{x}_{\mathrm{HI}}$ and b_{HI}, i.e., the neutral faction and the HI bias. Further, the visibility correlation for the HI signal can be obtained analytically (Bharadwaj & Ali, 2005):

$$\mathbf{S}_2(\mathbf{U}_n,\mathbf{U}_m,\nu_i,\nu_j) = \bar{I}_\nu^2 \int \frac{d^3k}{(2\pi)^3}\tilde{\mathbf{A}}(\mathbf{U}_n - \frac{r_\nu}{2\pi}\mathbf{k}_\perp)\tilde{\mathbf{A}}^*(\mathbf{U}_m - \frac{r_\nu}{2\pi}\mathbf{k}_\perp)P_{\mathrm{HI}}(\mathbf{k})e^{ik_\parallel r'_\nu|\nu_i-\nu_j|} \tag{6.52}$$

where r'_ν is the comoving distance at the redshift corresponding to the observed HI signal frequency ν, $\tilde{\mathbf{A}}$ is the Fourier transform of the primary beam power pattern. The visibilities at $\mathbf{U}_n$ and $\mathbf{U}_m$ will be correlated only if there is a significant overlap between the terms $\tilde{\mathbf{A}}(\mathbf{U}_n - \frac{r_\nu}{2\pi}\mathbf{k}_\perp)$ and $\tilde{\mathbf{A}}^*(\mathbf{U}_m - \frac{r_\nu}{2\pi}\mathbf{k}_\perp)$, which peak around different values of $\mathbf{k}_\perp$. It is sufficient to restrict the discussion to $\mathbf{U}_n = \mathbf{U}_m$ at the moment, since we expect the correlation to fall off to zero for separation $|\mathbf{U}_n - \mathbf{U}_m|$ larger than the aperture dimension. Subfigures 6.17(a) and 6.17(b) show the expected HI visibility correlation matrices for baselines $\mathbf{U}_1$ and $\mathbf{U}_{10}$ respectively. In frequency separation, the expected HI visibility correlation is confined to $\Delta\nu < 1$ MHz (Bharadwaj & Ali, 2005), which translates to a narrow banded region about the diagonal of the $\mathbf{S}_2$ matrix. On the longer baselines, it is expected to decorrelate more rapidly, with the consequence that the $\mathbf{S}_2$ matrix is nearly diagonal. This translates into stationarity in frequency for the expected HI signal: the statistics of the expected signal in a given baseline depends only on the separation in frequency and not the absolute frequency, within the observing band.

The visibility correlation of the redshifted HI signal can be computed from the result of a dark matter N-body simulation, in which case we proceed as follows. The HI model visibilities obtained from from the N-body dark matter simulation was described in Section 5.5. One can reuse equation 6.12, but substituting the estimated visibility $\mathcal{V}(\mathbf{U}_n, \nu)$ with the computed model visibility $\mathbf{M}_{\mathrm{HI}}(\mathbf{U}_n, \nu)$. Besides, the term to offset the noise bias is redundant in a noise-free, signal-only simulation. Therefore, the expression

$$\mathbf{S}_2(\mathbf{U}_n, \nu_i, \nu_j) = \frac{\mathbf{M}_{\mathrm{HI}}(\mathbf{U}_n, \nu_i)\mathbf{M}^*_{\mathrm{HI}}(\mathbf{U}_n, \nu_j) - \delta_{ij}\mathbf{M}'_{\mathrm{HI}}(\mathbf{U}_n, \nu_i)}{N_n^2 - \delta_{ij}N_n} \tag{6.53}$$

simplifies to

$$\mathbf{S}_2(\mathbf{U}_n, \nu_i, \nu_j) = \frac{\mathbf{M}_{\mathrm{HI}}(\mathbf{U}_n, \nu_i)\mathbf{M}^*_{\mathrm{HI}}(\mathbf{U}_n, \nu_j)}{N_n^2} \tag{6.54}$$

where, by using the computed model visibility given by equation 5.26, we obtain the visibility covariance matrices of the HI signal realisation for the baselines $\mathbf{U}_n$. The results from this exercise are shown in Section 6.8.3.

6.8.2 Simulating HI visibilities from the expected covariance

We propose (Sarkar *et al.*, 2016b) a new scheme to obtain random realisations of the HI signal visibilities from the expected HI visibility correlation. We repeat the exercise of decomposing the expected HI visibility correlation into its eigenmodes, introduced for the foregrounds in Section 6.7. For the HI signal, we can write $\mathbf{S}_2$ as

$$\mathbf{S}_2 = \mathbf{E}\mathbf{\Lambda}\mathbf{E}^\dagger \tag{6.55}$$

where $\mathbf{E}$ is the matrix of the eigenvectors and $\mathbf{\Lambda}$ is the diagonal matrix of the eigenvalues. Since the expected HI signal is stationary, we can expect the eigen-decomposition to naturally result in a Fourier-like basis, and the matrix $\mathbf{\Lambda}$ to be full-rank. Figure 6.17 shows the analytically computed expectation of HI visibility correlation for baselines $\mathbf{U}_1$ and $\mathbf{U}_{10}$ in the top panels. The bottom panels show the first four eigenmodes and

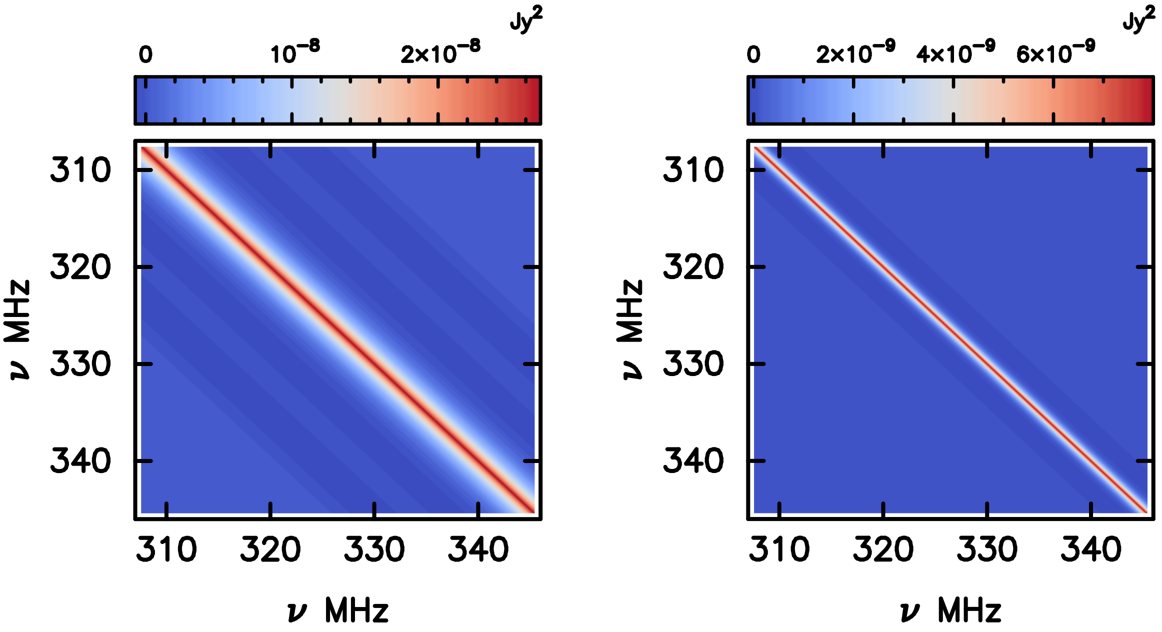

(a) $\mathbf{U}_1$: signal covariance

(b) $\mathbf{U}_{10}$: signal covariance

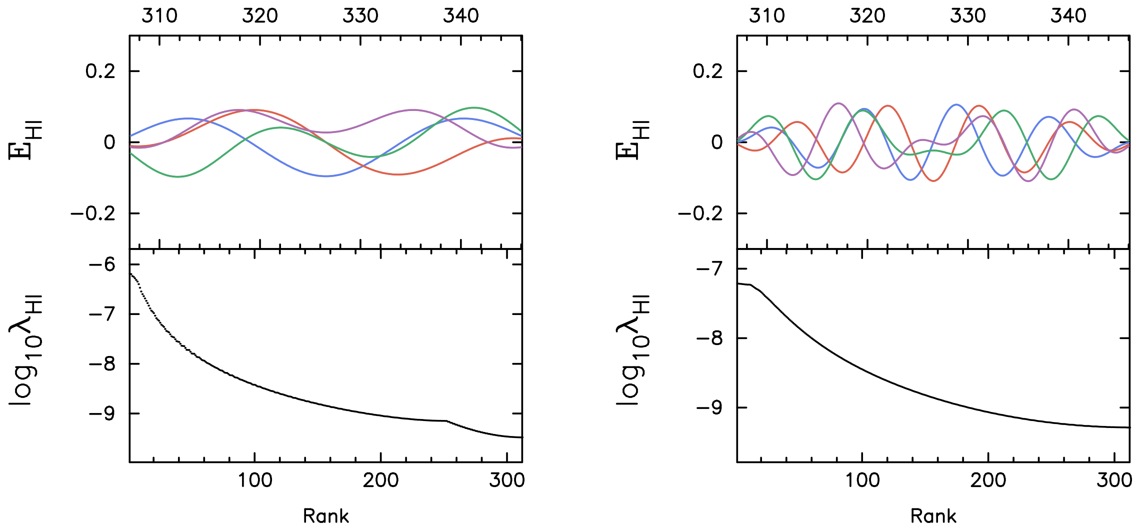

(c) $\mathbf{U}_1$: eigenmodes

(d) $\mathbf{U}_{10}$: eigenmodes

Figure 6.17: The estimator matrix $\mathbf{S}_2(\mathbf{U}, \nu_i, \nu_j)$ for the analytically computed expected HI signal is shown in the top panels for the two baselines $\mathbf{U}_1$ and $\mathbf{U}_{10}$. Their respective first four eigenvectors and the rank-ordered eigenspectrum are shown for each matrix in the bottom panels.

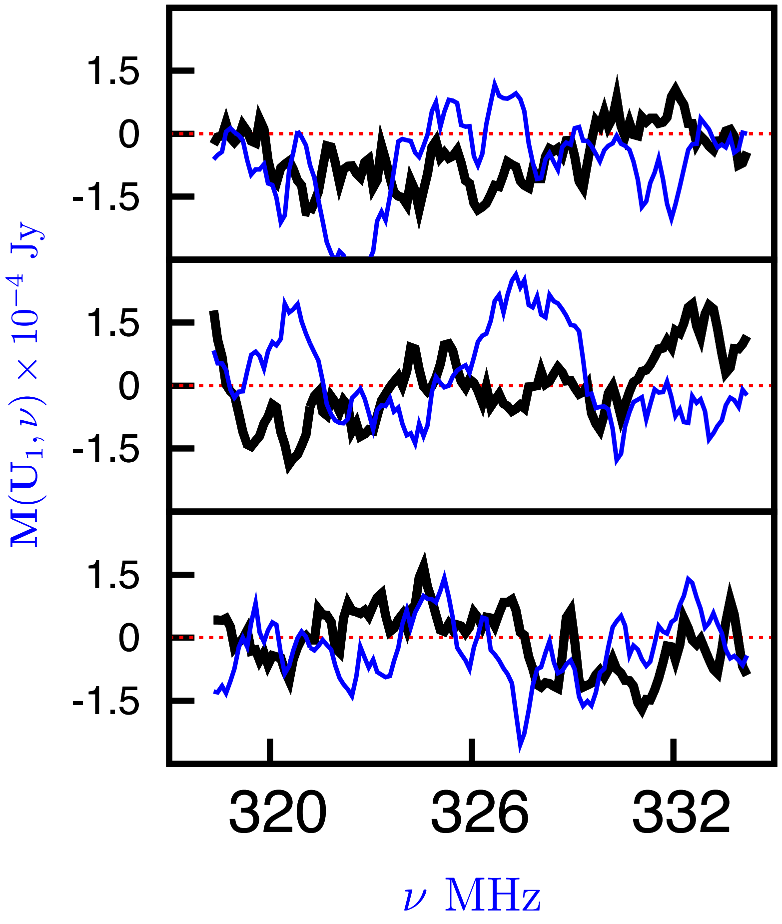

Figure 6.18: Three different realisations, from top to bottom, of the HI signal visibility for the first baseline, $\mathbf{M}_{\rm HI}(\mathbf{U}_1, \nu)$, as a function of ν for a portion of the band. The real part is shown in black and imaginary part in blue. The dotted red line in the figure represents the mean. Adapted from Sarkar *et al.* 2016b.

the rank-ordered eigenspectrum. Now, the HI visibility in channel j for baseline $\mathbf{U}_n$ can be obtained as a single random realisation of the form

$$\mathbf{M}_{\rm HI}(\mathbf{U}, \nu_j) = \sum_{k=1}^{N} \sqrt{\frac{\lambda_k}{2}}\, (x + iy)\, \hat{e}_{jk} \tag{6.56}$$

where λ_k is the $k^{\rm th}$ eigenvalue of the signal covariance matrix $\mathbf{S}_2$, $\hat{e}_{jk}$ is its corresponding eigenvector, x and y are Gaussian random numbers with zero mean and unit variance. Figure 6.18 shows the simulated visibilities for three different realisations of the HI signal for the first baseline, obtained by this method.

6.8.3 Results from simulations

The HI brightness distribution cube is available to us (see Figure 5.9), very much like the foreground signals were, and the details of simulating the HI signal have been already discussed in 5.5. Therefore, we proceed in an identical manner to obtain the model visibilities, an example of which was shown in Section 5.5 in Figure 5.10. These model visibilities can hence be used to obtained the two-visibility correlation, or the MAPS estimator. Figure 6.19 shows the $\mathbf{S}_2(\nu_i, \nu_j)$ matrices for the same baselines we showed for in Figure 6.2 for the foregrounds. These are obtained for a single realisation of the HI signal. The HI signal is confined to a narrow band around the diagonal $\nu_i = \nu_j$, and decorrelates very rapidly unlike the foregrounds. This is the chief discriminant between the HI signal and the foregrounds. It can also be seen that, as expected, the HI signal is more widepread in the $\nu_i - \nu_j$ plane on the shorter baselines. This dependence on baseline length can be quantified via the correlation coefficient $\kappa(\Delta\nu)$, which is defined as

$$\kappa(\Delta\nu) = \frac{\mathbf{S}_2(\Delta\nu)}{\mathbf{S}_2(0)} \tag{6.57}$$

Figure 6.20 shows $\kappa(\Delta\nu)$ as a function of $\Delta\nu$ as derived from the simulations described above.

The angular power spectrum can be recovered from the estimator by scaling with the Fourier transform of the primary beam and converting from flux to temperature units. The APS recovered from the estimator averaged over the five realisations of the HI signal is shown in Figure 6.21. The 1σ error bars in each bin are obtained over the five realisations.

Finally, it is worth comparing the cylindrical power spectrum of the cosmological HI signal with that of the foregrounds. Figure 6.22 shows the power of the HI signal in the **k**-space. The power spectrum shown in this figure is obtained for the same realisation of the HI visibilities shown in Figure 5.10, and the corresponding HI visibility covariance matrices shown in Figure 6.19. We observe that there is significant power from the HI emission beyond the horizon limit in the **k**-space. Although some amount of the signal is to be found within the foreground wedge region, most of it is beyond the foreground horizon on the short baselines. This presents an optimistic scenario at OWFA for isolating the HI signal in the **k**-space. In the context of the OWFA experiment, the predictions for Mode-II by Bharadwaj *et al.* (2015) and Sarkar *et al.* (2016a) present a much more optimistic outcome than for Mode-I, based on both the integration times as well as the power in the signal in the large angular scales that Mode-II will have exclusive access to. It is therefore worthwhile for us to repeat these

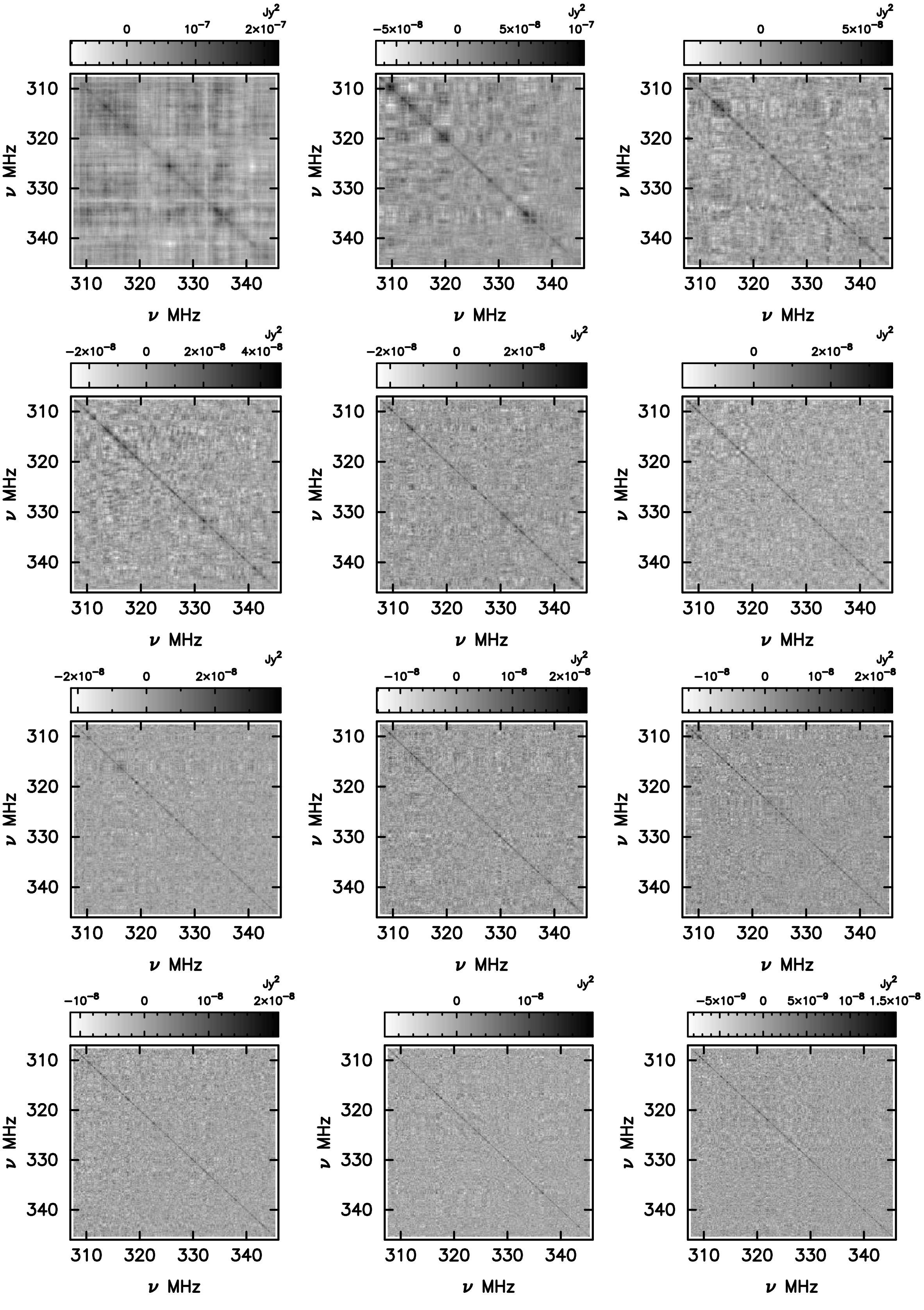

Figure 6.19: The MAPS estimator $\mathbf{S}_2(\mathbf{U}, \nu_j, \nu_j)$ is shown for the HI signal for a single realisation at $\delta_0 = 0°$. Baselines 1, 4, 7, 10, 13, 16, 19, 22, 25, 29, 34 and 38 are shown. The HI signal is confined close to the diagonal in all the baselines.

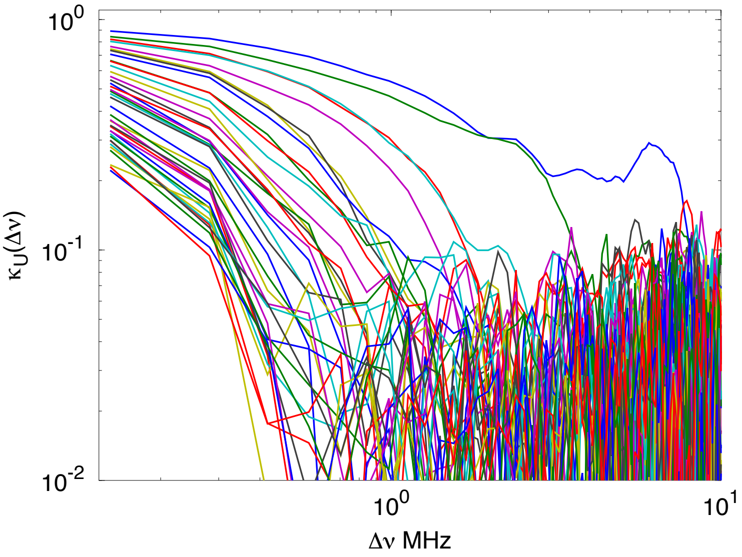

Figure 6.20: The decorrelation of the visibility correlation for the baselines of Mode-I of OWFA. The decorrelation curves have been obtained from the $\mathbf{S}_2(\Delta\nu)$ curves after averaging over five different realisations of the HI signal, equivalent to observing five different, non-overlapping direections at $\delta_0 = 0$. On most baselines, there is little signal beyond ~ 1 MHz.

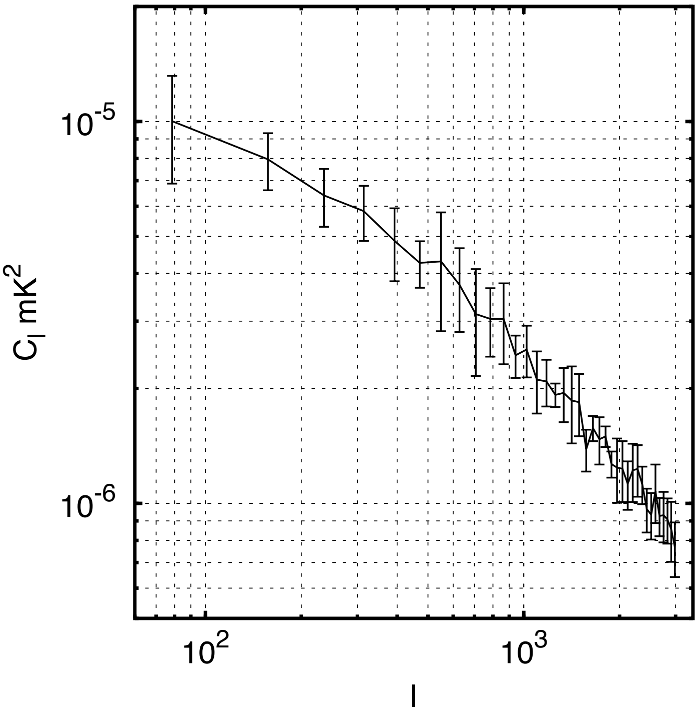

Figure 6.21: The angular power spectrum $C_\ell(\Delta\nu = 0)$ recovered from the estimator $\mathbf{S}_2(\nu_i = \nu_j)$ averaged over five realisations of the HI signal is shown here for OWFA Mode-I. The 1σ error bars have been obtained from the APS of each of the realisations.

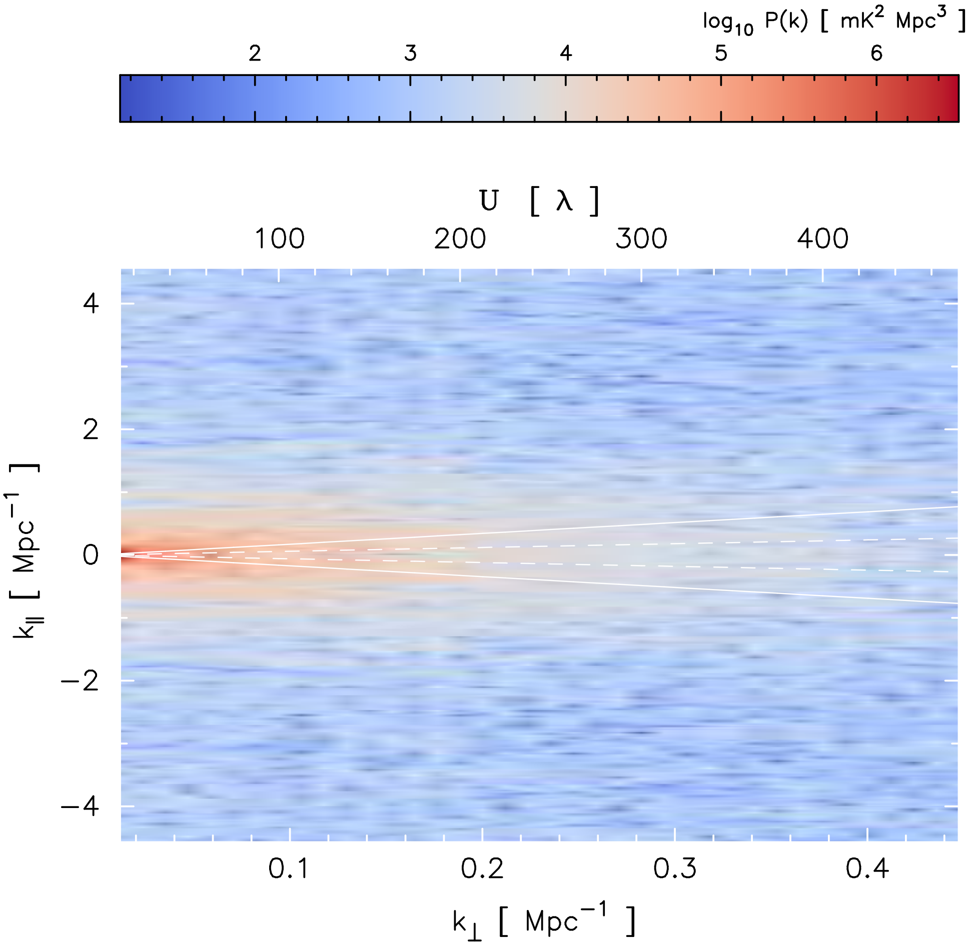

Figure 6.22: The cylindrical power spectrum for the realisation of the HI signal shown in Figure 5.10, derived from the $\mathbf{S}_2$ matrices shown in Figure 6.19. The solid line shows the horizon limit and the dashed line the boundary of the foreground wedge expected for the angular extent of the simulated maps. Most of the cosmological HI signal is expected to fall in the complementary "foreground-free" region, which can be isolated from the foreground emission in the wedge.

simulations for the foreground isolation approach for Mode-II: this is one of the possible research extensions to this thesis, which will again be pointed out in Chapter 7.

6.9 Summary and final thoughts

We have seen in this chapter that the two-visibility correlation is an estimator of the multi-frequency angular power spectrum. But it requires precise knowledge of the primary beam. The esimator matrices encode all the spectral information of the sky and the spectral response of the instrument. Although some undesirable spectral signatures result from the chromatic response of the telescope at a small level, the bulk of the foregrounds are very smooth across frequency. We also see that the decorrelation bandwidths of the foregrounds on almost all baselines are much larger, typically more than 5 MHz. In contrast, we see the HI signal to be much more confined in the $\nu - \nu$ space near the main diagonal. Physically, this translates into the HI signal decorrelating very rapidly with frequency separation. This contrasting feature is crucial for isolating the foregrounds from the signal.

Although this thesis does not discuss foreground subtraction, let us briefly note some of the earlier attempts at foreground subtraction through polynomial fitting. Many studies (see e.g. McQuinn *et al.*, 2006; Gleser *et al.*, 2008; Jelić *et al.*, 2008) have used the fact that the 21-cm signal is not smooth across frequency to fit out smooth functions to the foregrounds. Ghosh *et al.* (2011a,b) have tried fitting smooth, low-order polynomials to the foreground multi-frequency angular power spectrum at different multipoles for a post-EOR experiment with the GMRT. They assume that the HI signal is confined to $\Delta\nu < 1$ MHz in the MAPS curves for different multipole moments, $C_\ell(\Delta\nu)$, and subtract these fits from the data. However, they do find undesirable oscillatory patterns in the residuals of the fit. As discussed in Section 6.4.1, these arise due to the chromatic response of the instrument to the distant sources. They have proposed a tapering function to suppress this contribution, achieved through a convolution kernel in the uv plane. Choudhuri *et al.* (2014) and Choudhuri *et al.* (2016) have again presented a more detailed analysis of this technique and its effectiveness in suppressing oscillatory patterns. A similar exercise would have to be repeated for the OWFA experiment; however, the specifics of the convolving kernel would have to be tailored for the particular case. This is possibly a topic of research as an extension to this thesis in the near future.

The simulations here have used a limited FoV, and its effect on the cylindrical power spectrum was shown in Section 6.5. A self-consistent derivation would require accounting for the curvature of the sky for large fields of view.

At this point in time, it is not clear if the OWFA HI experiment will adopt the foreground isolation or the foreground subtraction approach to measure the cosmological HI signal. Both methods have to be explored more rigorously before an optimal strategy is identified. Nonetheless, some brief thoughts on the foreground subtraction method may be in order. Similar to the polynomial subtraction method for $C_\ell(\Delta\nu)$ of Ghosh *et al.* (2011a,b), it may be useful to try a modification of the method by fitting smooth surfaces through the $\mathbf{S}_2$ matrices by specifically excluding the region close to the diagonal in determining the surface polynomials. Similarly, the slope of the foreground wedge can be controlled to some extent by sculpting the beam to suppress emission from large angular distances by adopting the methods suggested by Choudhuri *et al.* (2014) and Choudhuri *et al.* (2016).

Chapter 7

Summary, conclusions and outlook

7.1 The cosmology experiment and OWFA

This thesis represents the research work carried out for the Ooty Wide Field Array (Subrahmanya *et al.*, 2016a) redshifted HI 21-cm experiment. The OWFA redshifted HI 21-cm experiment aims for a statistical detection of the large-scale structure around $z \sim 3.35$ (Ali & Bharadwaj, 2014). The post-reionisation HI signal is interesting because it provides both constraints on cosmological parameters as well as constraints to galaxy formation (Loeb & Wyithe, 2008; Wyithe *et al.*, 2008; Bharadwaj *et al.*, 2009; Visbal *et al.*, 2009).

OWFA is an upgrade to the legacy ORT, which is an offset parabolic reflector telescope operating at 327 MHz. The telescope is located in the Nilgiri Hills in the Indian peninsula on a hill that slopes 11°, that is equal to the geographical latitude of the place. This effectively makes the telescope equatorial mounted. This 530 m long telescope can be steered on its axis along the length of the cylinder, allowing it to track sources on the sky for 9.5 hours. The legacy receiver system works as a correlating beamformer and is used routinely for space weather studies. A statistical detection of the large-scale structure necessitates measuring either the angular correlation function of the cosmological signal or its angular power spectrum. Inorder to enable this study the ORT is being upgraded to operate as an interferometer (Prasad & Subrahmanya, 2011; Subrahmanya *et al.*, 2016a,b). The interferometer will operate in two independent but concurrent modes - Mode-I and Mode-II - which offer two different, wide fields of view and antenna configurations. In Mode-II, OWFA will have 264 antennas. Mode-I is a scaled-down version of Mode-II only in terms of the number of antennas and the field of view. Due to the smaller number of antennas and the resulting smaller number of baselines and hence data rates, Mode-I is envisaged as a test bed for data processing algorithms before proceeding to the analysis of Mode-II data. In both the modes, the bandwidth is identical at ~ 39 MHz.

7.2 The emulator and its applications

The main objectives of this thesis are three-fold: (1) to devise, test and propose optimal calibration strategies through simulations, (2) to devise and develop an efficient power spectrum estimation algorithm that can exploit the specific configuration of OWFA, and (3) to develop a thorough understanding of the various systematics arising from the chromatic response of the telescope. To address these three objectives, I have developed a software-based emulator that can produce visibility data based on a realisitc sky model (Marthi, 2016). Besides, it can run fast calibration and power spectrum estimation programs to yield "science-ready", processed data. This emulator is designed to evolve organically into the observatory data pipeline system for OWFA.

The emulator takes as its input the antenna and the array geometry, the bandwidth and the number of channels the band is to be split into. Based on the antenna description and the array configuration, the physically distinct baselines are obtained as antenna pairs, and the true baseline vectors are computed for each channel. This leads to a natural chromatic description of the interferometer. Similarly, the primary beam is defined for each channel which, again, naturally accommodates the chromatic response of the primary beam.

The foreground brightness temperature maps themselves are simulated as random realisations of the Fourier transform of the model foreground angular power spectrum (see Chapter 5). For the diffuse Galactic foregrounds, the model angular power spectrum has been measured (La Porta *et al.*, 2008) from data taken by many previous studies (Haslam *et al.*, 1982; Reich, 1982; Reich & Reich, 1986; Reich *et al.*, 2001; Testori *et al.*, 2001). Based on these we characterise the power spectrum of the diffuse foreground as a single power law in the scales of interest to OWFA (Ali & Bharadwaj, 2014). For OWFA simulations, we have used power spectrum measurements of the diffuse Galactic foreground, made with the GMRT (Ghosh *et al.*, 2012). The simulated brightness temperature maps (see Section 5.2.2) can be scaled to give specific intensity maps in every channel. This simulation of the diffuse foreground has been validated by recovering the power spectrum from the simulated data and is shown to match the input (Section 5.2.3, as well as Marthi *et al.* 2016).

Similarly, the extragalactic point source foreground can be simulated from its angular power spectrum (see Section 5.3.2). Based on previous studies of the extragalactic point source foregrounds (e.g. de Oliveira-Costa *et al.*, 2008, and all the references therein), it appears that at most of the angular scales accessible to OWFA, the extragalactic foregrounds are likely to dominate the total foreground emission (Ali & Bharadwaj, 2014). Simulating the extragalactic foreground maps is slightly more involved than simulating the diffuse foregrounds. The power spectrum of the point source distribution has two components, one with a Poisson distribution and one which is clustered (see e.g. Cress *et al.*, 1996; Condon, 2007; Owen & Morrison, 2008; Vernstrom, 2015). We simulate both the components and populate them with sources with their fluxes drawn from the observed radio source counts. Once again we validate the simulated images by computing the corresponding power spectrum and showing that it is in accord with the input (see Section 5.3.2).

7.3 Calibration

The different realisations of the simulated foreground maps (i.e. the diffuse and the point source foregrounds) are summed and weighted by the primary beam. This final map that OWFA would “see” is used to obtain the model visibilities. The model visibilities are obtained only for the small set of non-redundant baselines as a pixel-by-pixel Fourier sum (Marthi *et al.*, 2016). The instantaneously redundant copies of a baseline measure the same Fourier mode on the sky. The observed visibility on each of the baselines is simulated as a realisation of the model visibility corrupted by the complex gains of the antennas participating in the baseline.

The simulated visibilities are calibrated by exploiting the intrinsic redundancy of the baselines for which we propose a new efficient, unbiased algorithm. Redundancy calibration offers the advantage of being able to simultaneously calibrate both the complex instrument gains as well as the complex sky visibilities. Although linear least squares algorithms are available, the solutions suffer from being biased at low signal-to-noise ratios, or being computationally very intensive.

The non-linear least squares algorithm based on steepest descent that we have developed provides unbiased solutions and is also computationally very efficient (see Chapter 4). We have also established that this fast calibration algorithm is statistically optimal, in that it achieves the Cramér-Rao bound (Marthi & Chengalur, 2014). Besides simulations, we have tested and validated this calibration on real data from the historical Phase-I system. We have also validated post-correlation beamforming on the calibrated data, which can be used for studying transients at 325 MHz (see Section 4.6).

7.4 Power spectrum estimation and the expected systematics

The calibrated data is now science-ready, and we proceed to the next step that would take us closer to detecting the HI signal. The foregrounds are several orders of magnitude brighter than the cosmological signal we are interested in (Chapter 5). These foregrounds have to be either subtracted from the calibrated data, or we have to identify a strategy by which we can separate the foregrounds and the signal in a parameter space where they would occupy disjoint territories.

In this thesis, I have attempted to employ the two-visibility correlation (Bharadwaj & Ali, 2005) as a model-free foreground estimator. I have tailored the estimator to exploit the redundancy inherent in the configuration of OWFA, and apply the estimator to the simulated foregrounds (see Chapter 6). For the purpose of identifying the systematics, the simulations are noise-free. However, I have also separately addressed the noise behaviour in the estimator.

The two-visibility correlation estimator represented as a matrix for each baseline is a useful representation as it retains the complete spectral information available in the visibilities. The foregrounds appear as very smooth features in the estimator. The spectral structures are very weak on the shortest baselines. As the baseline beomes longer, the spectral structure becomes more pronounced. Much of this spectral structure can be attributed to contribution from sources at large angular distances from the beam centre. I show that from the two-visibility correlation, derivative representations such as the bandwidth decorrelation and the cylindirical power spectrum can be obtained. The systematics we are concerned about are chiefly of chromatic origin. The telescope has a slightly different response to the signal from the sky at different frequencies. We have established that these effects are much stronger than the intrinsic spectral shape of the foregrounds themselves. Most of the spectral signatures of the foregrounds visible in the estimator can conclusively be attributed to the chromatic response of the primary beam of the telescope and the interferometric baselines.

Earlier studies (such as Datta *et al.*, 2010; Vedantham *et al.*, 2012; Thyagarajan *et al.*, 2013, for example) have shown that the foregrounds are confined to a wedge in the cylindrical representation of the power spectrum. We find that for OWFA there is a significant region of the observed **k**-space that lies outside this wedge which can hence be used for estimating the HI signal. This sizeable foreground-free region arises largely because of the compact overall size of the instrument.

We apply the same two-visibility correlation estimator on simulated HI signal realisations obtained from an N-body simulation (Chatterjee *et al.*, 2016). We find that the HI signal is confined to a narrow band about the principal diagonal, in contrast with the foregrounds. This is along expected lines as the HI signal decorrelates beyond a frequency interval of 1 MHz at the redshift of $z \sim 3.35$.

7.5 Conclusions

The essential accomplishments of this thesis are the following:

- A software emulator for OWFA has been developed. It would serve as the observatory data processing pipeline for the HI experiment (Marthi *et al.*, 2016; Marthi, 2016).

- A robust and statistically optimal redundancy calibration algorithm has been devised (Marthi & Chengalur, 2014), and it is found to be fast. Our timing estimates suggest that real-time calibration of the instrument and the sky should be possible using this algorithm. The errors on the estimated solutions can be obtained at every iteration of the algorithm.

- Foreground simulations that produce realistic sky maps have been developed (Marthi *et al.*, 2016). Besides being an essential aid in devising power spectrum etimation algorithms and the study of systematics introduced by the instrument, these foreground simulation tools could be very useful in refining our predictions for the foregrounds themselves based on various statistical parameters.

- A visibility covariance based power spectrum estimator has been studied that exploits the redundancy of the baselines (Marthi *et al.*, 2016). The estimator is validated by recovering the power spectra of the foregrounds. A detailed study of the various systematics arising out of the chromatic primary beam and interferometer response of the telescope has been performed. The study suggests that the chromatic response is much stronger than the intrinsic spectral character of the emission from the sky. However, the short baselines of OWFA has also meant that the foregrounds are confined to a small region of the instrumental k-space.

- The HI signal is found to decorrelate very rapidly unlike the spectrally smooth foregrounds, and it confirms our understanding of the HI signal obtained analytically (Chatterjee *et al.*, 2016). The simulated HI signal obtained from N-body particle mesh simulations have provided us with insights into the signatures of the cosmological signal in the power spectrum representation, and how it contrasts with the foregrounds.

7.6 Limitations of OWFA

It might be useful to list the limitations within the contours of which the HI experiment is being designed.

- ORT is a single-polarised radio telescope. The most direct consequence of this fact is that it operates at a reduced sensitivity. This has consequences for the survey speed.

- Although calibration itself does not suffer severely from lack of the second polarisation, it precludes being able to calibrate polarised foregrounds. Polarised foregrounds have important consequences for the detectability of the HI signal (see e.g. Moore *et al.*, 2013; Paciga *et al.*, 2013; Shaw *et al.*, 2015). Foregrounds have a significant polarised component. Especially, the diffuse Galactic foreground has an extremely rich Faraday structure (see e.g. Jelić *et al.*, 2014). The intrinsic polarised emission from the diffuse and the extragalactic foregrounds, as well as the Faraday rotation imparted by the magneto-ionic medium of the Galaxy to the emission from the extragalactic sources would contribute to the polarisation uncertainties in the observed astrophysical signal. This can be studied in more detail using the emulator that has been developed, and discussed in this thesis.

- The lack of east-west baselines is a handicap, as it limits the number of $\mathbf{k}_\perp$ modes sampled by the telescope. With only north-south baselines, all the $\mathbf{k}_\perp$ modes we will sample are essentially pure k_y modes. A combination of k_x and k_y modes would greatly enhance the sampling density in the instrumental $\mathbf{k}$-space. Besides, the inability to make 2D images means that foreground subtraction would have to be entirely model-based, with the models having to come either from predictions or from deep high-resolution images over wide fields of view obtained through observations using other telescopes.

7.7 Outlook for the future

I now list some of the research projects that would naturally follow this thesis. These research problems have to be addressed to further our understanding of the systematics, and to make more realistic forecasts for the cosmological HI signal.

- In this thesis I have not addressed the issue of direction-dependent effects (DDE). This will be important for Mode-II more than Mode-I due to the very wide FoV.

Estimating and correcting for DDEs is challenging in the absence of imaging capabilities. However, due to the enormous redundancy of the array, the system of equations is sufficiently overdetermined to allow some simple parametrization of the direction dependence at the time of redundancy calibration itself. Although this proposition has not been tested yet, it holds the potential to nominally estimate the direction-dependent antenna gains.

- I have not addressed foreground subtraction in this thesis. The stationary nature of the HI signal, a feature borne out very clearly by the visibility covariance matrix, informs us that foreground subtraction may well be attempted on the visibility covariance matrix $\mathbf{S}_2$, but by excluding the banded region about the diagonal where the HI signal is expected. Nor have I addressed apriori point source subtraction. The inability to make images with OWFA means that point source subtraction has to be entirely model-based. Such sky models have to come from high resolution deep observations made with other telescopes, like the GMRT, for example.

- A combination of techniques such as point source subtraction and beam tapering to suppress the response from the sidelobes is required to mitigate the residual oscillatory patterns in the visibility correlation. Ghosh *et al.* (2011b, 2012), Choudhuri *et al.* (2014) and Choudhuri *et al.* (2016) propose convolving the gridded visibility data with a kernel in the *uv* plane, and have demonstrated its ability to suppress the oscillatory patterns in the residual visibility correlation. The effect of beam tapering on the foreground isolation scheme needs to be explored in detail, since the extent of the wedge can be controlled through the field of view. This has important consequences for the HI signal detection sensitivity.

- The Ooty Radio Telescope is a singly polarised radio telescope. But foregrounds in general are expected to have a small fraction of polarisation. The ORT is sensitive only to the component of polarised intensity whose electric vector is aligned with the dipole when it reaches the telescope. As a result, ORT would look at the polarised sky through a spatially distributed intensity modulation mask. So far, simulations have only treated unpolarised foregrounds in total intensity. This would underestimate as well as alter the foreground power spectra. Besides, Faraday rotation of the polarised component leads to ocillatory patterns in the polarisation basis of the telescope that could mimic the cosmological HI signal at certain Faraday depths. It appears that the polarised foregrounds are again confined to the wedge region in the instrumental **k**-space and polarisation calibration errors pose no serious threat to the isolated signal window (Kohn *et al.*, 2016).

However, a complete and rigorous study of the effects of polarised foregrounds on estimating the foregrounds and the signal with the single-polarised OWFA is therefore essential in the near future.

Appendix

Prowess - some programs and their functions

Prowess is short for "Programmable OWFA Emulator System". It was envisaged as a suite of programs capable of simulating visibilities for OWFA, based on simulated realistic sky maps. In course of time, it has organically evolved into a package that would serve as the observatory data analysis software as well. The package follows a function-rich programming philosophy: it is relatively straightforward to add more functions for a user, as well as to write a new program by calling various functions in sequence. This appendix is a very brief account of the various programs which are likely to be the most important and most frequently used. "A Project.Par" file is required by most programs as in input; an example is shown in Figure 1.

mkprbeam

Usage : *mkprbeam -o OutputFITSmap*

Given an antenna definition table Antenna.Def and the Project.Par parameter file, this program makes a channel-by-channel primary beam for as many channels requested in Project.Par. Although at the moment it produces a 2D sinc^2 beam, it can accommodate any functional form of definition for the primary beam. The output map is available as a FITS image cube.

gengalfg

Usage : *gengalfg -o OutputFITSmap*

Simulates a diffuse Galactic synchrotron map parameterized by a power law index γ and a spectral index α, both defined internally. The output map is available as a FITS image cube.

genEPS

Usage : *genEPS -n nMaps*

Simulates nMaps maps of the extragalactic radio point sources with a predefined clustering and Poisson power. The source fluxes are distributed according to the normalized

```
**********************************************************
** Project parameter inputs - edit only the par values! **
** According to the number of scans in SCANPAR, add or  **
** remove SCAN info. Do not modify the format or layout **
** of the file!                                         **
**                 -Visweshwar Ram Marthi, 09-JAN-2012 **
**********************************************************

#PROJPAR
Project Code                    : DASTEST01
Observer                        : Marthi
Obs. Mode (TRANSIT/TRACKING)    : TRACKING
Channels per sideband           : 1

#SCANPAR
No. of scans                    : 1

#SCAN
Scan number                     : 1
Source Name                     : 1330+251
Source Flux                     : 32.0
Pointing RA                     : 00h00m00.000s
Pointing Dec                    : 40d00'0.000"
Calibrator      ( Y / N )       : Y

#END
```

Figure 1: A Project.Par project definition file is required by most programs.

differential source counts. Each discrete radio source is given a spectral index drawn randomly from a Gaussian distribution with a mean spectral index of $\alpha = -0.7$ in flux density. The output map is available as a FITS image cube.

mkmodel

Usage : *mkmodel -i InputFITSmap/catalog -p [Primary Beam FITS File] -t [threshold (mJy)]*

This program computes the model visibilities, given a simulated map or a catalog of radio sources with positions (α_k, δ_k) and flux density in mJy. The primary beam file is an optional argument; by default it picks up a PRBEAM.FITS file in the same working directory. The threshold in mJy is an optional argument set by default to zero, which serves as a cutoff flux upto which to compute the model. This is equivalent to subtracting sources above the flux threshold. The model visibilities are available as an ASCII text file with the real and imaginary parts against $\mathbf{U}$ in λ units, for all baselines and all channels.

addmodel

Usage : *addmodel -i Modelfile1 -j Modelfile2 -o Outputmodelfile*
The visibilities from two input model visibility files are added and the output is written to the output model file in the same format. The two input model visibilities are expected to be at the same **U**.

submodel

Usage : *submodel -i Modelfile1 -j Modelfile2 -o Outputmodelfile -t [threshold mJy]*
The visibilities from Modelfile2 are subtracted from Modelfile1. If the threshold flux density is provided (defaults to zero), only model visibilities above that flux are subtracted.

plotmodl

Usage : *plotmodl -i InputFITSmap -m 0/1 for amp-phase / real-imag -d default x/X for Xwindow, p/P for postscript*
Plots the model visibilities against $\mathbf{u}(\lambda)$ in Jy units. Visibility data from all the frequency channels are plotted together. The -m switch chooses to plot the visibility in real/imaginary or amplitude/phase format. This switch can also be toggled dynamically when the program is running. The plotting device can be chosen to be either a PGPLOT X device or a postscript printer.

mdl2FITS

Usage : *mdl2FITS -i Inputmodelfile -o OutputFITSFile -t T*
Given a model visibility file, it produces an output UV FITS visibility file that simulates an observation of length T seconds. It requires Antenna.Def and Project.Par. The input model visibiilties are corrupted by the input antennas gains generated internally following a predefined pattern. The pattern to be followed for assigning the antenna gains is programmable.

genFITS

Usage : *genFITS -o OutputFITSFile -t T -p EPSmap -g -h HICubeFITS -b [pbeam-FITS]*
This program generates visibilities based on an input point source map EPSmap. If the -g switch is on, it also simulates the diffuse foreground map to be added to the point source map. Alternatively, the EPSmap along with the -p switch can be omitted but only the -g switch can be retained if only the diffuse foreground has to be realised. An HI data FITS cube can be supplied after the -h switch. If a primary beam FITS cube is available by the default PRBEAM.FITS name, it can be supplied by the -b

switch, otherwise it internally computes the primary beam. The -b switch is useful if the program is to be used to generate multiple realizations of visibilities repetitively, as the primary beam for a given declination is reusable. The observing duration T in seconds has to be necessarily supplied, else it produces a dummy FITS file with the headers but no data. code. The output FITS file is written to disk.

FITSinfo

Usage : *FITSinfo -i InputFITSFile [-a -b -f]*

Parses the input FITS file header and prints the information on the screen, It tells whether the FITS file is a UVFITS or FITS image file, and the relevant information like number of antennas, baselines, channels, the pointing centre of observation, or the dimensions of the FITS image file. The optional switches -a and -b allow the user to list the antennas and the baelines respectively when the file is UVFITS. They are ignored for a FITS image file. The switch -f dislpays the flag mask when used for the visibility covariance matrix cube V2CORR.FITS.

The following few visualisation programs are useful for inspecting the simulated visibility data or real data from the telescope.

imagtifr

Usage : *imagtifr -i InputFITSFile [-a=0] Ant 1 [-b=1] Ant 2 -m 0/1 [-d='X'] Plot device -f ITF: default 'l'- lin, 'g'- log, 's'- sqrt*

Plots the visibility data on a colour-coded surface in time-frequency order for the baseline (defaults to the first) comprised of antennas a and b, supplied by the options -a and -b. Real/Imaginary or Amplitude/Phase mode for the data can be toggled dynamically, or chosen at the start by the -m option. The image transfer function can be set by the -f option or can be chosen dynamically by typing 'l', 's' or 'g'. The plots can be printed to postscript by specifying the -dp option, which defaults to PGPLOT X device. The time and frequency ranges to plot can be looped dynamically at runtime.

imagtibl

Usage : *imagtibl -i InputFITSFile [-dX] Plot device [-m=0] Plot mode [-n=N/2] Channel number*

Plots the visibility data on a colour-coded surface in time-baseline order for a chosen frequency, set by the -n option. The default is the central channel. The real/imaginary or amplitude/phase mode can be chosen at the start by the -m option or toggled dynamically at runtime. Plotting defaults to the PGPLOT X device, but can be printed to postscript by choosing the -dp option.

plottibl

Usage : *plottibl -i InputFITSFile [-n=N/2] Display chan. [-r=3] plot rows [-c=5] plot cols [-d='X'] Device [m=0] mode [-s] Scale reset*

Makes line plots of the visibility data in time-baseline order for the channel given by the -n option. The number of rows and columns are set by the -r and -c options which default to 3 rows and five columns respectively. Postscript plots are obtained by choosing the -dp option. The -m option can be invoked similar to the imagtibl program either at the start or dynamically at runtime. In addition, the toggle switch -s chooses a full range or full scale for the y-axis, that can also be toggled dynamically.

imagfrbl

Usage : *imagfrbl -i InputFITSFile [-d='X'] Plot device [-m=0] Plot mode [-k=4] First k channels to blank*

Plots the visibility data on a colour-coded surface in frequency-baseline order for a chosen time instant given by the -n option. The record to plot is chosen at runtime. The real/imaginary or amplitude/phase mode can be chosen at the start by the -m option or toggled dynamically at runtime. Plotting defaults to the PGPLOT X device, but can be printed to postscript by choosing the -dp option.

plotfrbl

Usage : *plotfrbl -i InputFITSFile [-r=3] plot rows [-c=5] plot cols [-d='X'] Device [-m=0] Mode [-s] Scale reset [-k=4] First k chan to blank*

Makes line plots of the visibility data in frequency-baseline order for the record that is chosen at runtime. The number of rows and columns are set by the -r and -c options. Postscript plots are obtained by choosing the -dp option. The -m option can be invoked similar to the imagfrbl program either at the start or dynamically at runtime. In addition, the toggle switch -s chooses a full range or full scale for the y-axis, that can also be toggled dynamically. The first few number of channels to be blanked is given by the -k option, which defaults to four.

Calibration and power spectrum estimation programs are described below.

FITSbsol

Usage : *FITSbsol -i InputFITSFile -o OutputFITSFile -t T≥1 -n [Channel to calibrate 1-MAXCHAN] -k [Channels to blank for BPASS plots] -r [No. of rows per plot page] -c [No. of columns per plot page] -m [model visibility file]*

FITSbsol calibrates an input UVFITS visibility file and writes the calibrated data to an output UVFITS visibility file. Every T seconds of data can be integrated for better

SNR, and T defaults to one when it is omitted as an option. The channel which is to be considered the 0 channel for bandpass calibration can be specified after the -n switch, which defaults to the central channel. The -k option defaults to 4, which is the number of channels from the band-edge to be blanked when plotting the bandpasses of the baselines. The -r and -c switches set the number of rows and columns of the bandpass response respectively to plot in a single page. The bandpass response can be dynamically printed to a postscript file. An input model visibility file can be supplied if the model is availble, or as a calibrator model if a calibrator scan is available in the UVFITS file.

FITS2mdl

Usage : *FITS2mdl -i UVFITSfile*

This estimates the model visibilities on the set of non-redundant baselines from the input UVFITS visibility file. This is useful if the model visibilities have to be estimated on the non-redundant baselines by averaging multiple redundant baselines, after calibration.

v2corr

Usage : *v2corr -i InputFITSFile*

Computes the visibility correlation matrix $\mathbf{S}_2(\mathbf{U}, \nu_i, \nu_j)$ for a given UVFITS file. If there is more than one record, also computes the error on the covariance matrix. The outputs are V2CORR.FITS and V2ERR.FITS, which are both stored as FITS cubes, with the third axis being the baseline and the two axes of each plane being the frequency. These outputs can be viewed with FITSview.

FITSview

Usage : *FITSview -i InputFITSFile [-d='X'] Plot device [-p] to publish; default no [-c : colour map ; default monochrome] ITF: default 'l'- lin, 'g'- log, 's'- sqrt [-n : channel to show ; default N/2]*

FITSview can be used to view image cubes through three different image transfer functions that can be chosen as an input or switched dynamically at runtime. The -c option chooses a colour display, and it can be toggled at runtime using the space bar. The viewing program FITSview is interactive when it displays the V2CORR.FITS cube. Any point on the display image can be clicked to extract and plot the power spectrum through that point as a function of baseline. When using FITSview to view these outputs, the usage is

FITSview -i V2CORR.FITS -j V2ERR.FITS

The display device can be chosen through the -d option.

Bibliography

Abel, T., Bryan, G.L. & Norman, M.L. (2002). The Formation of the First Star in the Universe. *Science*, **295**, 93–98. [2]

Alexander, J.K. & Novaco, J.C. (1974). Survey of the galactic background radiation at 3.93 and 6.55 MHz. *AJ*, **79**, 777. [110]

Ali, S.S. & Bharadwaj, S. (2014). Prospects for Detecting the 326.5 MHz Redshifted 21-cm HI Signal with the Ooty Radio Telescope (ORT). *JApA*, **35**, 157–182. [vii, x, i, 8, 13, 47, 61, 110, 111, 112, 114, 117, 118, 123, 136, 179, 180, 181]

Ali, S.S., Bharadwaj, S. & Chengalur, J.N. (2008). Foregrounds for redshifted 21-cm studies of reionization: Giant Meter Wave Radio Telescope 153-MHz observations. *MNRAS*, **385**, 2166–2174. [47, 110]

Ali, Z.S., Parsons, A.R., Zheng, H., Pober, J.C., Liu, A., Aguirre, J.E., Bradley, R.F., Bernardi, G., Carilli, C.L., Cheng, C. & et al. (2015). PAPER-64 Constraints on Reionization: The 21 cm Power Spectrum at z = 8.4. *ApJ*, **809**, 61. [73]

Bagla, J.S., Khandai, N. & Datta, K.K. (2010). HI as a probe of the large-scale structure in the post-reionization universe. *MNRAS*, **407**, 567–580. [xi, 9, 128]

Bandura, K., Addison, G.E., Amiri, M., Bond, J.R., Campbell-Wilson, D., Connor, L., Cliche, J.F., Davis, G., Deng, M., Denman, N. & et al. (2014). Canadian Hydrogen Intensity Mapping Experiment (CHIME) pathfinder. In *Ground-based and Airborne Telescopes V*, vol. 9145 of *Proc. SPIE*, 914522. [vii, 10, 47, 71]

Barkana, R. & Loeb, A. (2001). In the beginning: the first sources of light and the reionization of the universe. , **349**, 125–238. [9]

Barkana, R. & Loeb, A. (2005). Probing the epoch of early baryonic infall through 21-cm fluctuations. *MNRAS*, **363**, L36–L40. [133]

BECKER, R.H., WHITE, R.L. & HELFAND, D.J. (1995). The FIRST Survey: Faint Images of the Radio Sky at Twenty Centimeters. *ApJ*, **450**, 559. [118]

BECKER, R.H., FAN, X., WHITE, R.L., STRAUSS, M.A., NARAYANAN, V.K., LUPTON, R.H., GUNN, J.E., ANNIS, J., BAHCALL, N.A., BRINKMANN, J. & ET AL. (2001). Evidence for Reionization at z˜6: Detection of a Gunn-Peterson Trough in a z=6.28 Quasar. *AJ*, **122**, 2850–2857. [2]

BEGUM, A., CHENGALUR, J.N. & BHARDWAJ, S. (2006). Power spectrum of HI intensity fluctuations in DDO 210. *MNRAS*, **372**, L33–L37. [134]

BENNETT, C.L., LARSON, D., WEILAND, J.L., JAROSIK, N., HINSHAW, G., ODEGARD, N., SMITH, K.M., HILL, R.S., GOLD, B., HALPERN, M. & ET AL. (2013). Nine-year Wilkinson Microwave Anisotropy Probe (WMAP) Observations: Final Maps and Results. *ApJS*, **208**, 20. [1, 3, 6]

BERNARDI, G., DE BRUYN, A.G., BRENTJENS, M.A., CIARDI, B., HARKER, G., JELIĆ, V., KOOPMANS, L.V.E., LABROPOULOS, P., OFFRINGA, A., PANDEY, V.N. & ET AL. (2009). Foregrounds for observations of the cosmological 21 cm line. I. First Westerbork measurements of Galactic emission at 150 MHz in a low latitude field. *A&A*, **500**, 965–979. [111]

BHARADWAJ, S. & ALI, S.S. (2004). The cosmic microwave background radiation fluctuations from HI perturbations prior to reionization. *MNRAS*, **352**, 142–146. [8]

BHARADWAJ, S. & ALI, S.S. (2005). On using visibility correlations to probe the HI distribution from the dark ages to the present epoch - I. Formalism and the expected signal. *MNRAS*, **356**, 1519–1528. [8, 33, 62, 134, 168, 182]

BHARADWAJ, S. & PANDEY, S.K. (2003). HI Fluctuations at Large Redshifts: II - the Signal Expected for the GMRT. *Journal of Astrophysics and Astronomy*, **24**, 23. [9, 134]

BHARADWAJ, S. & SETHI, S.K. (2001). HI Fluctuations at Large Redshifts: I–Visibility correlation. *Journal of Astrophysics and Astronomy*, **22**, 293–307. [8, 33, 133, 134]

BHARADWAJ, S. & SRIKANT, P.S. (2004). HI Fluctuations at Large Redshifts: III - Simulating the Signal Expected at GMRT. *Journal of Astrophysics and Astronomy*, **25**, 67. [vii, 9, 133]

Bharadwaj, S., Sethi, S.K. & Saini, T.D. (2009). Estimation of cosmological parameters from neutral hydrogen observations of the post-reionization epoch. *Ph. Rv. D*, **79**, 083538. [vii, 9, 10, 62, 179]

Bharadwaj, S., Sarkar, A.K. & Ali, S.S. (2015). Fisher Matrix Predictions for Detecting the Cosmological 21-cm Signal with the Ooty Wide Field Array (OWFA). *JApA*, **36**, 385–398. [vii, 13, 47, 172]

Bhatnagar, S., Cornwell, T.J., Golap, K. & Uson, J.M. (2008). Correcting direction-dependent gains in the deconvolution of radio interferometric images. *A&A*, **487**, 419–429. [93]

Bondi, M., Ciliegi, P., Venturi, T., Dallacasa, D., Bardelli, S., Zucca, E., Athreya, R.M., Gregorini, L., Zanichelli, A., Le Fèvre & et al.. (2007). The VVDS-VLA deep field. III. GMRT observations at 610 MHz and the radio spectral index properties of the sub-mJy population. *A&A*, **463**, 519–527. [118]

Bowman, J.D. & Rogers, A.E.E. (2010a). A lower limit of Δz0.06 for the duration of the reionization epoch. *Nature*, **468**, 796–798. [10]

Bowman, J.D. & Rogers, A.E.E. (2010b). The End of the Beginning: The Dawn of 21 cm Cosmology With EDGES. In *American Astronomical Society Meeting Abstracts #215*, vol. 42 of *Bulletin of the American Astronomical Society*, 421. [10]

Bowman, J.D., Morales, M.F. & Hewitt, J.N. (2006). The Sensitivity of First-Generation Epoch of Reionization Observatories and Their Potential for Differentiating Theoretical Power Spectra. *ApJ*, **638**, 20–26. [147]

Bowman, J.D., Rogers, A.E.E. & Hewitt, J.N. (2008). Toward Empirical Constraints on the Global Redshifted 21 cm Brightness Temperature During the Epoch of Reionization. *ApJ*, **676**, 1–9. [10]

Bowman, J.D., Morales, M.F. & Hewitt, J.N. (2009). Foreground Contamination in Interferometric Measurements of the Redshifted 21 cm Power Spectrum. *ApJ*, **695**, 183–199. [15, 146, 149]

Bowman, J.D., Cairns, I., Kaplan, D.L., Murphy, T., Oberoi, D., Staveley-Smith, L., Arcus, W., Barnes, D.G., Bernardi, G., Briggs & et al. (2013). Science with the Murchison Widefield Array. *PASA*, **30**, e031. [10]

Carilli, C.L. & Walter, F. (2013). Cool Gas in High-Redshift Galaxies. *ARAA*, **51**, 105–161. [3]

Chang, T.C., Pen, U.L., Peterson, J.B. & McDonald, P. (2008). Baryon Acoustic Oscillation Intensity Mapping of Dark Energy. *Physical Review Letters*, **100**, 091303. [8, 9, 33]

Chang, T.C., Pen, U.L., Bandura, K. & Peterson, J.B. (2010). An intensity map of hydrogen 21-cm emission at redshift z˜0.8. *Nature*, **466**, 463–465. [10, 33]

Chapman, E., Abdalla, F.B., Harker, G., Jelić, V., Labropoulos, P., Zaroubi, S., Brentjens, M.A., de Bruyn, A.G. & Koopmans, L.V.E. (2012). Foreground removal using FASTICA: a showcase of LOFAR-EoR. *MNRAS*, **423**, 2518–2532. [15, 134, 147]

Chatterjee, S., Bharadwaj, S. & Marthi, V.R. (2016). Simulating the z=3.35 HI 21-cm visibility signal for the Ooty Wide Field Array(OWFA). *JApA*, submitted. [xi, i, 12, 128, 168, 182, 183]

Chen, X. (2011). Radio detection of dark energythe Tianlai project. *Scientia Sinica Physica, Mechanica Astronomica*, **41**, 1358. [vii, 10, 47, 71]

Chen, X. (2012). The Tianlai Project: a 21CM Cosmology Experiment. *International Journal of Modern Physics Conference Series*, **12**, 256–263. [10]

Chen, X. (2015). The Tianlai 21cm intensity mapping experiment. *IAU General Assembly*, **22**, 2252187. [10]

Chen, X. & Miralda-Escudé, J. (2004). The Spin-Kinetic Temperature Coupling and the Heating Rate due to Lyα Scattering before Reionization: Predictions for 21 Centimeter Emission and Absorption. *ApJ*, **602**, 1–11. [8]

Chluba, J. & Sunyaev, R.A. (2006). Free-bound emission from cosmological hydrogen recombination. *A&A*, **458**, L29–L32. [2]

Chluba, J. & Sunyaev, R.A. (2007). Cosmological hydrogen recombination: Lyn line feedback and continuum escape. *A&A*, **475**, 109–114. [2]

Chluba, J., Rubiño-Martín, J.A. & Sunyaev, R.A. (2007). Cosmological hydrogen recombination: populations of the high-level substates. *MNRAS*, **374**, 1310–1320. [2]

Choudhuri, S., Bharadwaj, S., Ghosh, A. & Ali, S.S. (2014). Visibility-based angular power spectrum estimation in low-frequency radio interferometric observations. *MNRAS*, **445**, 4351–4365. [x, 112, 149, 176, 177, 185]

Choudhuri, S., Bharadwaj, S., Roy, N., Ghosh, A. & Ali, S.S. (2016). Tapering the sky response for angular power spectrum estimation from low-frequency radio-interferometric data. *MNRAS*, **459**, 151–156. [149, 176, 177, 185]

Condon, J.J. (1989). The 1.4 gigahertz luminosity function and its evolution. *ApJ*, **338**, 13–23. [110, 117]

Condon, J.J. (2007). Deep Radio Surveys. In J. Afonso, H.C. Ferguson, B. Mobasher & R. Norris, eds., *Deepest Astronomical Surveys*, vol. 380 of *Astronomical Society of the Pacific Conference Series*, 189. [118, 181]

Condon, J.J., Cotton, W.D., Fomalont, E.B., Kellermann, K.I., Miller, N., Perley, R.A., Scott, D., Vernstrom, T. & Wall, J.V. (2012). Resolving the Radio Source Background: Deeper Understanding through Confusion. *ApJ*, **758**, 23. [118]

Cornwell, T. & Fomalont, E.B. (1999). Self-Calibration. In G.B. Taylor, C.L. Carilli & R.A. Perley, eds., *Synthesis Imaging in Radio Astronomy II*, vol. 180 of *Astronomical Society of the Pacific Conference Series*, 187. [73]

Cress, C.M., Helfand, D.J., Becker, R.H., Gregg, M.D. & White, R.L. (1996). The Angular Two-Point Correlation Function for the FIRST Radio Survey. *ApJ*, **473**, 7. [118, 121, 181]

Crighton, N.H.M., Murphy, M.T., Prochaska, J.X., Worseck, G., Rafelski, M., Becker, G.D., Ellison, S.L., Fumagalli, M., Lopez, S., Meiksin, A. & O'Meara, J.M. (2015). The neutral hydrogen cosmological mass density at z = 5. *MNRAS*, **452**, 217–234. [3]

Crovisier, J. & Dickey, J.M. (1983). The spatial power spectrum of galactic neutral hydrogen from observations of the 21-cm emission line. *A&A*, **122**, 282–296. [vii, 134, 135]

Datta, A., Bowman, J.D. & Carilli, C.L. (2010). Bright Source Subtraction Requirements for Redshifted 21 cm Measurements. *ApJ*, **724**, 526–538. [17, 146, 151, 182]

Datta, K.K., Choudhury, T.R. & Bharadwaj, S. (2007). The multifrequency angular power spectrum of the epoch of reionization 21-cm signal. *MNRAS*, **378**, 119–128. [134]

de Oliveira-Costa, A., Tegmark, M., Gaensler, B.M., Jonas, J., Landecker, T.L. & Reich, P. (2008). A model of diffuse Galactic radio emission from 10 MHz to 100 GHz. *MNRAS*, **388**, 247–260. [110, 180]

Di Matteo, T., Perna, R., Abel, T. & Rees, M.J. (2002). Radio Foregrounds for the 21 Centimeter Tomography of the Neutral Intergalactic Medium at High Redshifts. *ApJ*, **564**, 576–580. [47]

Dillon, J.S. (2015). It's Always Darkest Before the Cosmic Dawn: Early Results from Novel Tools and Telescopes for 21 cm Cosmology. *ArXiv e-prints*. [73]

Eisenstein, D.J. & Hu, W. (1999). Power Spectra for Cold Dark Matter and Its Variants. *ApJ*, **511**, 5–15. [128]

Eisenstein, D.J. & Loeb, A. (1995). Origin of quasar progenitors from the collapse of low-spin cosmological perturbations. *ApJ*, **443**, 11–17. [2]

Eisenstein, D.J., Zehavi, I., Hogg, D.W., Scoccimarro, R., Blanton, M.R., Nichol, R.C., Scranton, R., Seo, H.J., Tegmark, M., Zheng, Z. & et al. (2005). Detection of the Baryon Acoustic Peak in the Large-Scale Correlation Function of SDSS Luminous Red Galaxies. *ApJ*, **633**, 560–574. [6, 133]

Eisenstein, D.J., Seo, H.J., Sirko, E. & Spergel, D.N. (2007). Improving Cosmological Distance Measurements by Reconstruction of the Baryon Acoustic Peak. *ApJ*, **664**, 675–679. [9]

Ewen, H.I. & Purcell, E.M. (1951). Observation of a Line in the Galactic Radio Spectrum: Radiation from Galactic Hydrogen at 1,420 Mc./sec. *Nature*, **168**, 356. [7]

Falcke, H.D.E. (2006). LOFAR- The Low Frequency Array. In *IAU Joint Discussion*, vol. 12 of *IAU Joint Discussion*. [71]

Fan, X., Strauss, M.A., Becker, R.H., White, R.L., Gunn, J.E., Knapp, G.R., Richards, G.T., Schneider, D.P., Brinkmann, J. & Fukugita, M. (2006). Constraining the Evolution of the Ionizing Background and the Epoch of Reionization with z˜6 Quasars. II. A Sample of 19 Quasars. *AJ*, **132**, 117–136. [i, 2, 4]

Field, G.B. (1958). Excitation of the Hydrogen 21-CM Line. *Proceedings of the IRE*, **46**, 240–250. [8]

Field, G.B. (1959). The Spin Temperature of Intergalactic Neutral Hydrogen. *ApJ*, **129**, 536. [8]

Franzen, T.M.O., Jackson, C.A., Offringa, A.R., Ekers, R.D., Wayth, R.B., Bernardi, G., Bowman, J.D., Briggs, F., Cappallo, R.J., Deshpande, A.A. & et al. (2016). The 154 MHz radio sky observed by the Murchison Widefield Array: noise, confusion, and first source count analyses. *MNRAS*, **459**, 3314–3325. [110]

Gardner, J.P., Mather, J.C., Clampin, M., Doyon, R., Greenhouse, M.A., Hammel, H.B., Hutchings, J.B., Jakobsen, P., Lilly, S.J., Long, K.S. & et al. (2006). The James Webb Space Telescope. *SSRv*, **123**, 485–606. [6]

Garn, T., Green, D.A., Hales, S.E.G., Riley, J.M. & Alexander, P. (2007). Deep 610-MHz Giant Metrewave Radio Telescope observations of the Spitzer extragalactic First Look Survey field - I. Observations, data analysis and source catalogue. *MNRAS*, **376**, 1251–1260. [118]

Garn, T., Green, D.A., Riley, J.M. & Alexander, P. (2008). A 610-MHz survey of the Lockman Hole with the Giant Metrewave Radio Telescope - I. Observations, data reduction and source catalogue for the central 5 deg^2. *MNRAS*, **387**, 1037–1044. [118]

Gehlot, B.K. & Bagla, J.S. (2016). Prospects of detecting HI using redshifted 21-cm radiation at $z \sim 3$. *JApA*, submitted. [13]

Ghosh, A., Bharadwaj, S., Ali, S.S. & Chengalur, J.N. (2011a). GMRT observation towards detecting the post-reionization 21-cm signal. *MNRAS*, **411**, 2426–2438. [15, 110, 176, 177]

Ghosh, A., Bharadwaj, S., Ali, S.S. & Chengalur, J.N. (2011b). Improved foreground removal in GMRT 610 MHz observations towards redshifted 21-cm tomography. *MNRAS*, **418**, 2584–2589. [15, 110, 149, 176, 177, 185]

Ghosh, A., Prasad, J., Bharadwaj, S., Ali, S.S. & Chengalur, J.N. (2012). Characterizing foreground for redshifted 21 cm radiation: 150 MHz Giant Metrewave Radio Telescope observations. *MNRAS*, **426**, 3295–3314. [ix, 15, 110, 111, 180, 185]

Giardino, G., Banday, A.J., Górski, K.M., Bennett, K., Jonas, J.L. & Tauber, J. (2002). Towards a model of full-sky Galactic synchrotron intensity and linear polarisation: A re-analysis of the Parkes data. *A&A*, **387**, 82–97. [111]

Ginzburg, V.L. & Syrovatskii, S.I. (1965). Cosmic Magnetobremsstrahlung (synchrotron Radiation). *ARAA*, **3**, 297. [109]

Ginzburg, V.L. & Syrovatskii, S.I. (1969). Developments in the Theory of Synchrotron Radiation and its Reabsorption. *ARAA*, **7**, 375. [109]

Gleser, L., Nusser, A. & Benson, A.J. (2008). Decontamination of cosmological 21-cm maps. *MNRAS*, **391**, 383–398. [15, 176]

González-Nuevo, J., Toffolatti, L. & Argüeso, F. (2005). Predictions of the Angular Power Spectrum of Clustered Extragalactic Point Sources at Cosmic Microwave Background Frequencies from Flat and All-Sky Two-dimensional Simulations. *ApJ*, **621**, 1–14. [110, 120]

Green, D.A. (2011). A colour scheme for the display of astronomical intensity images. *Bulletin of the Astronomical Society of India*, **39**, 289–295. [iv, 96]

Gunn, J.E. & Peterson, B.A. (1965). On the Density of Neutral Hydrogen in Intergalactic Space. *ApJ*, **142**, 1633–1641. [2]

Hamaker, J.P. (2000a). Self-calibration of arrays whose elements are strongly polarized. In H.R. Butcher, ed., *Radio Telescopes*, vol. 4015 of *Proc. SPIE*, 353–365. [82]

Hamaker, J.P. (2000b). Understanding radio polarimetry. IV. The full-coherency analogue of scalar self-calibration: Self-alignment, dynamic range and polarimetric fidelity. *A&AS*, **143**, 515–534. [82]

Haslam, C.G.T., Klein, U., Salter, C.J., Stoffel, H., Wilson, W.E., Cleary, M.N., Cooke, D.J. & Thomasson, P. (1981). A 408 MHz all-sky continuum survey. I - Observations at southern declinations and for the North Polar region. *A&A*, **100**, 209–219. [110]

Haslam, C.G.T., Salter, C.J., Stoffel, H. & Wilson, W.E. (1982). A 408 MHz all-sky continuum survey. II - The atlas of contour maps. *A&AS*, **47**, 1. [110, 180]

Hopkins, A.M., Mobasher, B., Cram, L. & Rowan-Robinson, M. (1998). The PHOENIX Deep Survey: 1.4-GHz source counts. *MNRAS*, **296**, 839–846. [110, 117]

Hopkins, A.M., Afonso, J., Chan, B., Cram, L.E., Georgakakis, A. & Mobasher, B. (2003). The Phoenix Deep Survey: The 1.4 GHz Microjansky Catalog. *AJ*, **125**, 465–477. [110, 117]

Hu, W. & Sugiyama, N. (1995). Toward understanding CMB anisotropies and their implications. *Ph. Rv. D*, **51**, 2599–2630. [3]

Hu, W.T. (1995). *Wandering in the Background: a Cosmic Microwave Background Explorer*. Ph.D. thesis, UNIVERSITY OF CALIFORNIA, BERKELEY. [3]

Huynh, M.T., Jackson, C.A., Norris, R.P. & Prandoni, I. (2005). Radio Observations of the Hubble Deep Field-South Region. II. The 1.4 GHz Catalog and Source Counts. *AJ*, **130**, 1373–1388. [110, 117]

Iacobelli, M., Haverkorn, M. & Katgert, P. (2013a). Rotation measure synthesis at the 2 m wavelength of the FAN region: unveiling screens and bubbles. *A&A*, **549**, A56. [48]

Iacobelli, M., Haverkorn, M., Orrú, E., Pizzo, R.F., Anderson, J., Beck, R., Bell, M.R., Bonafede, A., Chyzy, K., Dettmar, R.J. & et al. (2013b). Studying Galactic interstellar turbulence through fluctuations in synchrotron emission. First LOFAR Galactic foreground detection. *A&A*, **558**, A72. [ix, 48, 111]

Iacobelli, M., Burkhart, B., Haverkorn, M., Lazarian, A., Carretti, E., Staveley-Smith, L., Gaensler, B.M., Bernardi, G., Kesteven, M.J. & Poppi, S. (2014). Galactic interstellar turbulence across the southern sky seen through spatial gradients of the polarization vector. *A&A*, **566**, A5. [48]

International Science Development Teams & TMT Science Advisory Committee (2015). Thirty Meter Telescope Detailed Science Case: 2015. *http://www.tmt.org/documents; TMT Document Number: TMT.PMO.MGT.07.009*. []

Jarvis, M.J. & Rawlings, S. (2004). The accretion history of the universe with the SKA. , **48**, 1173–1185. [117]

Jelić, V., Zaroubi, S., Labropoulos, P., Thomas, R.M., Bernardi, G., Brentjens, M.A., de Bruyn, A.G., Ciardi, B., Harker, G., Koopmans, L.V.E. & et al. (2008). Foreground simulations for the LOFAR-epoch of reionization experiment. *MNRAS*, **389**, 1319–1335. [15, 112, 176]

Jelić, V., de Bruyn, A.G., Mevius, M., Abdalla, F.B., Asad, K.M.B., Bernardi, G., Brentjens, M.A., Bus, S., Chapman, E., Ciardi, B. & et al. (2014). Initial LOFAR observations of epoch of reionization windows. II. Diffuse polarized emission in the ELAIS-N1 field. *A&A*, **568**, A101. [ix, 110, 184]

Jelić, V., de Bruyn, A.G., Pandey, V.N., Mevius, M., Haverkorn, M., Brentjens, M.A., Koopmans, L.V.E., Zaroubi, S., Abdalla, F.B., Asad, K.M.B. & et al. (2015). Linear polarization structures in LOFAR observations of the interstellar medium in the 3C 196 field. *A&A*, **583**, A137. [110]

Joshi, M.N., Swarup, G., Bagri, D.S. & Kher, R.K. (1988). A new electronically steerable 1056 dipole array at 327 MHz for the Ooty radio telescope. *Bulletin of the Astronomical Society of India*, **16**, 111–121. [23, 38]

Kaiser, N. (1986). A sparse-sampling strategy for the estimation of large-scale clustering from redshift surveys. *MNRAS*, **219**, 785–790. [121]

Kaplinghat, M., Chu, M., Haiman, Z., Holder, G.P., Knox, L. & Skordis, C. (2003). Probing the Reionization History of the Universe using the Cosmic Microwave Background Polarization. *ApJ*, **583**, 24–32. [3]

Kemball, A.J. & Wieringa, M.H. (2000). MeasurementSet definition, ver. 2.0. [49]

Kohn, S.A., Aguirre, J.E., Nunhokee, C.D., Bernardi, G., Pober, J.C., Ali, Z.S., Bradley, R.F., Carilli, C.L., DeBoer, D.R., Gugliucci, N.E. & et al. (2016). Constraining Polarized Foregrounds for EoR Experiments I: 2D Power Spectra from the PAPER-32 Imaging Array. *ApJ*, **823**, 88. [185]

La Porta, L., Burigana, C., Reich, W. & Reich, P. (2008). The impact of Galactic synchrotron emission on CMB anisotropy measurements. I. Angular power spectrum analysis of total intensity all-sky surveys. *A&A*, **479**, 641–654. [111, 180]

Lanzetta, K.M., Wolfe, A.M. & Turnshek, D.A. (1995). The IUE Survey for Damped Lyman- alpha and Lyman-Limit Absorption Systems: Evolution of the Gaseous Content of the Universe. *ApJ*, **440**, 435. [128]

Liu, A. & Tegmark, M. (2012). How well can we measure and understand foregrounds with 21-cm experiments? *MNRAS*, **419**, 3491–3504. [146]

Liu, A., Tegmark, M., Bowman, J., Hewitt, J. & Zaldarriaga, M. (2009a). An improved method for 21-cm foreground removal. *MNRAS*, **398**, 401–406. [15]

Liu, A., Tegmark, M. & Zaldarriaga, M. (2009b). Will point sources spoil 21-cm tomography? *MNRAS*, **394**, 1575–1587. [15, 147]

Liu, A., Tegmark, M., Morrison, S., Lutomirski, A. & Zaldarriaga, M. (2010). Precision calibration of radio interferometers using redundant baselines. *MNRAS*, **408**, 1029–1050. [ix, iii, iv, 72, 73, 75, 78, 86, 89, 90, 91, 94, 104]

Liu, A., Parsons, A.R. & Trott, C.M. (2014). Epoch of reionization window. I. Mathematical formalism. *Ph. Rv. D*, **90**, 023018. [i, 16, 17, 151]

Loeb, A. & Barkana, R. (2001). The Reionization of the Universe by the First Stars and Quasars. *ARAA*, **39**, 19–66. [8]

Loeb, A. & Wyithe, J.S.B. (2008). Possibility of Precise Measurement of the Cosmological Power Spectrum with a Dedicated Survey of 21cm Emission after Reionization. *Physical Review Letters*, **100**, 161301. [9, 10, 179]

Loeb, A. & Zaldarriaga, M. (2004). Measuring the Small-Scale Power Spectrum of Cosmic Density Fluctuations through 21cm Tomography Prior to the Epoch of Structure Formation. *Physical Review Letters*, **92**, 211301. [8]

Lonsdale, C.J. (2005). Configuration Considerations for Low Frequency Arrays. In N. Kassim, M. Perez, W. Junor & P. Henning, eds., *From Clark Lake to the Long Wavelength Array: Bill Erickson's Radio Science*, vol. 345 of *Astronomical Society of the Pacific Conference Series*, 399. [93]

Lonsdale, C.J., Cappallo, R.J., Morales, M.F., Briggs, F.H., Benkevitch, L., Bowman, J.D., Bunton, J.D., Burns, S., Corey, B.E., Desouza, L. & et al. (2009). The Murchison Widefield Array: Design Overview. *IEEE Proceedings*, **97**, 1497–1506. [71]

Madau, P., Meiksin, A. & Rees, M.J. (1997). 21 Centimeter Tomography of the Intergalactic Medium at High Redshift. *ApJ*, **475**, 429–444. [8, 9]

Maiolino, R., Haehnelt, M., Murphy, M.T., Queloz, D., Origlia, L., Alcala, J., Alibert, Y., Amado, P.J., Allende Prieto, C., Ammler-von Eiff, M. & et al. (2013). A Community Science Case for E-ELT HIRES. *ArXiv e-prints*. []

Marthi, V.R. (2016). Prowess - a Programmable ORT Widefield Emulator System. *JApA*, submitted. [73, 180, 183]

Marthi, V.R. & Chengalur, J. (2014). Non-linear redundancy calibration. *MNRAS*, **437**, 524–531. [ix, 14, 72, 78, 91, 181, 183]

Marthi, V.R., Chatterjee, S., Chengalur, J. & Bharadwaj, S. (2016). Simulated foreground predictions for HI at $z \sim 3.35$. *MNRAS*, in preparation. [xi, 112, 155, 180, 181, 183]

Masui, K.W., McDonald, P. & Pen, U.L. (2010). Near-term measurements with 21 cm intensity mapping: Neutral hydrogen fraction and BAO at z2. *Ph. Rv. D*, **81**, 103527. [9]

McQuinn, M., Zahn, O., Zaldarriaga, M., Hernquist, L. & Furlanetto, S.R. (2006). Cosmological Parameter Estimation Using 21 cm Radiation from the Epoch of Reionization. *ApJ*, **653**, 815–834. [15, 176]

Miller, A.D., Caldwell, R., Devlin, M.J., Dorwart, W.B., Herbig, T., Nolta, M.R., Page, L.A., Puchalla, J., Torbet, E. & Tran, H.T. (1999). A Measurement of the Angular Power Spectrum of the Cosmic Microwave Background from L = 100 to 400. *ApJL*, **524**, L1–L4. [6]

Moore, D.F., Aguirre, J.E., Parsons, A.R., Jacobs, D.C. & Pober, J.C. (2013). The Effects of Polarized Foregrounds on 21 cm Epoch of Reionization Power Spectrum Measurements. *ApJ*, **769**, 154. [184]

Morales, M.F. (2005). Power Spectrum Sensitivity and the Design of Epoch of Reionization Observatories. *ApJ*, **619**, 678–683. [133]

Morales, M.F. & Hewitt, J. (2004). Toward Epoch of Reionization Measurements with Wide-Field Radio Observations. *ApJ*, **615**, 7–18. [133, 151, 152]

Morales, M.F., Bowman, J.D. & Hewitt, J.N. (2006). Improving Foreground Subtraction in Statistical Observations of 21 cm Emission from the Epoch of Reionization. *ApJ*, **648**, 767–773. [15]

Morales, M.F., Hazelton, B., Sullivan, I. & Beardsley, A. (2012). Four Fundamental Foreground Power Spectrum Shapes for 21 cm Cosmology Observations. *ApJ*, **752**, 137. [151]

Moreland, K.D. (2004). Ph.D. thesis, University of New Mexico, (2004). [viii, 140]

Mortlock, D.J., Warren, S.J., Venemans, B.P., Patel, M., Hewett, P.C., McMahon, R.G., Simpson, C., Theuns, T., Gonzáles-Solares, E.A., Adamson & et al. (2011). A luminous quasar at a redshift of z = 7.085. *Nature*, **474**, 616–619. [2]

Muller, C.A. & Oort, J.H. (1951). Observation of a Line in the Galactic Radio Spectrum: The Interstellar Hydrogen Line at 1,420 Mc./sec., and an Estimate of Galactic Rotation. *Nature*, **168**, 357–358. [7]

Neeleman, M., Prochaska, J.X., Ribaudo, J., Lehner, N., Howk, J.C., Rafelski, M. & Kanekar, N. (2016). The H I Content of the Universe Over the Past 10 GYRS. *ApJ*, **818**, 113. [3]

Newburgh, L.B., Addison, G.E., Amiri, M., Bandura, K., Bond, J.R., Connor, L., Cliche, J.F., Davis, G., Deng, M., Denman, N. & et al. (2014). Calibrating CHIME: a new radio interferometer to probe dark energy. In *Ground-based and Airborne Telescopes V*, vol. 9145 of *Proc. SPIE*, 91454V. [73]

Noordam, J.E. & de Bruyn, A.G. (1982). High dynamic range mapping of strong radio sources, with application to 3C84. *Nature*, **299**, 597. [71, 73]

Noordam, J.E. & Smirnov, O.M. (2010). The MeqTrees software system and its use for third-generation calibration of radio interferometers. *A&A*, **524**, A61. [93]

Noorishad, P., Wijnholds, S.J., van Ardenne, A. & van der Hulst, J.M. (2012). Redundancy calibration of phased-array stations. *A&A*, **545**, A108. [ix, 71, 77, 82]

Noterdaeme, P., Petitjean, P., Carithers, W.C., Pâris, I., Font-Ribera, A., Bailey, S., Aubourg, E., Bizyaev, D., Ebelke, G., Finley, H. & et al. (2012). Column density distribution and cosmological mass density of neutral gas: Sloan Digital Sky Survey-III Data Release 9. *A&A*, **547**, L1. [3]

Nuttall, A.H. (1981). Some Windows with Very Good Sidelobe Behavior. *IEEE Transactions on Acoustics Speech and Signal Processing*, **29**, 84–91. [155]

Offringa, A.R., Trott, C.M., Hurley-Walker, N., Johnston-Hollitt, M., McKinley, B., Barry, N., Beardsley, A.P., Bowman, J.D., Briggs, F., Carroll, P. & et al. (2016). Parametrising Epoch of Reionization foregrounds: A deep survey of low-frequency point-source spectra with the MWA. *MNRAS*. [110]

Oort, M.J.A. (1987). A deep WSRT 21 CM survey down to 0.1 mJy in the Lynx area. *A&AS*, **71**, 221–243. [117]

Oort, M.J.A. & van Langevelde, H.J. (1987). A WSRT 21 CM deep survey of two fields in Hercules. *A&AS*, **71**, 25–38. [117]

Owen, F.N. & Morrison, G.E. (2008). The Deep Swire Field. I. 20 cm Continuum Radio Observations: A Crowded Sky. *AJ*, **136**, 1889–1900. [110, 117, 118, 181]

Paciga, G., Chang, T.C., Gupta, Y., Nityanada, R., Odegova, J., Pen, U.L., Peterson, J.B., Roy, J. & Sigurdson, K. (2011). The GMRT Epoch of Reionization experiment: a new upper limit on the neutral hydrogen power spectrum at z 8.6. *MNRAS*, **413**, 1174–1183. [10, 134]

Paciga, G., Albert, J.G., Bandura, K., Chang, T.C., Gupta, Y., Hirata, C., Odegova, J., Pen, U.L., Peterson, J.B., Roy, J.et al. (2013). A simulation-calibrated limit on the H I power spectrum from the GMRT Epoch of Reionization experiment. *MNRAS*, **433**, 639–647. [10, 134, 184]

Padmanabhan, H., Choudhury, T.R. & Refregier, A. (2016). Modelling the cosmic neutral hydrogen from DLAs and 21-cm observations. *MNRAS*, **458**, 781–788. [10]

Page, L., Hinshaw, G., Komatsu, E., Nolta, M.R., Spergel, D.N., Bennett, C.L., Barnes, C., Bean, R., Doré, O., Dunkley, J. & et al. (2007). Three-Year Wilkinson Microwave Anisotropy Probe (WMAP) Observations: Polarization Analysis. *ApJS*, **170**, 335–376. [i, 3, 5]

Parsons, A.R., Backer, D.C., Foster, G.S., Wright, M.C.H., Bradley, R.F., Gugliucci, N.E., Parashare, C.R., Benoit, E.E., Aguirre, J.E., Jacobs, D.C. & et al. (2010). The Precision Array for Probing the Epoch of Re-ionization: Eight Station Results. *AJ*, **139**, 1468–1480. [10, 71]

Parsons, A., Pober, J., McQuinn, M., Jacobs, D. & Aguirre, J. (2012). A Sensitivity and Array-configuration Study for Measuring the Power Spectrum of 21 cm Emission from Reionization. *ApJ*, **753**, 81. [71, 154]

Parsons, A.R., Pober, J.C., Aguirre, J.E., Carilli, C.L., Jacobs, D.C. & Moore, D.F. (2012b). A Per-baseline, Delay-spectrum Technique for Accessing the 21 cm Cosmic Reionization Signature. *ApJ*, **756**, 165. [152]

Parsons, A.R., Liu, A., Aguirre, J.E., Ali, Z.S., Bradley, R.F., Carilli, C.L., DeBoer, D.R., Dexter, M.R., Gugliucci, N.E., Jacobs & et al. (2014). New Limits on 21 cm Epoch of Reionization from PAPER-32 Consistent with an X-Ray Heated Intergalactic Medium at z = 7.7. *ApJ*, **788**, 106. [10]

Patil, A.H., Yatawatta, S., Zaroubi, S., Koopmans, L.V.E., de Bruyn, A.G., Jelić, V., Ciardi, B., Iliev, I.T., Mevius, M., Pandey, V.N. & et al. (2016). Systematic biases in low frequency radio interferometric data due to calibration: the LOFAR EoR case. *ArXiv e-prints*. [89]

Péroux, C., McMahon, R.G., Storrie-Lombardi, L.J. & Irwin, M.J. (2003). The evolution of Ω_{HI} and the epoch of formation of damped Lyman α absorbers. *MNRAS*, **346**, 1103–1115. [128]

Peterson, J.B., Bandura, K. & Pen, U.L. (2006). The Hubble Sphere Hydrogen Survey. *ArXiv Astrophysics e-prints*. [10, 71]

Petrovic, N. & Oh, S.P. (2011). Systematic effects of foreground removal in 21-cm surveys of reionization. *MNRAS*, **413**, 2103–2120. [15]

Planck Collaboration, Ade, P.A.R., Aghanim, N., Alves, M.I.R., Armitage-Caplan, C., Arnaud, M., Ashdown, M., Atrio-Barandela, F., Aumont, J., Aussel, H. & et al. (2014). Planck 2013 results. I. Overview of products and scientific results. *A&A*, **571**, A1. [40, 41, 128]

Pober, J.C., Parsons, A.R., Aguirre, J.E., Ali, Z., Bradley, R.F., Carilli, C.L., DeBoer, D., Dexter, M., Gugliucci, N.E., Jacobs, D.C. & et al. (2013a). Opening the 21 cm Epoch of Reionization Window: Measurements of Foreground Isolation with PAPER. *ApJL*, **768**, L36. [146, 151, 156, 158]

Pober, J.C., Parsons, A.R., DeBoer, D.R., McDonald, P., McQuinn, M., Aguirre, J.E., Ali, Z., Bradley, R.F., Chang, T.C. & Morales, M.F. (2013b). The Baryon Acoustic Oscillation Broadband and Broad-beam Array: Design Overview and Sensitivity Forecasts. *AJ*, **145**, 65. [vii, 10, 47, 71]

Pober, J.C., Liu, A., Dillon, J.S., Aguirre, J.E., Bowman, J.D., Bradley, R.F., Carilli, C.L., DeBoer, D.R., Hewitt, J.N., Jacobs & et al. (2014). What Next-generation 21 cm Power Spectrum Measurements can Teach us About the Epoch of Reionization. *ApJ*, **782**, 66. [10]

Poor, H. (1994). *An Introduction to Signal Detection and Estimation*. Springer. [84]

Prasad, P. & Subrahmanya, C.R. (2011). A high speed networked signal processing platform for multi-element radio telescopes. *ExA*, **31**, 1–22. [vii, 10, 21, 34, 36, 47, 95, 179]

PRESS, W., TEUKOLSKY, A., VETTERLING, W. & FLANNERY, B. (1992). *Numerical Recipes in C: The Art of Scientific Computing*. Cambridge. [81]

PRITCHARD, J.R. & LOEB, A. (2011). Extracting The Astrophysics Of The First Sources From The 21 Cm Global Signal. In *American Astronomical Society Meeting Abstracts #217*, vol. 43 of *Bulletin of the American Astronomical Society*, 107.03. [9]

PRITCHARD, J.R. & LOEB, A. (2012). 21 cm cosmology in the 21st century. *Reports on Progress in Physics*, **75**, 086901. [vii, 7]

PUGET, J.L. & HEYVAERTS, J. (1980). Population III stars and the shape of the cosmological black body radiation. *A&A*, **83**, L10–L12. [2]

RAO, S.M. & TURNSHEK, D.A. (2000). Discovery of DampedLyα Systems at Redshifts Less than 1.65 and Results on Their Incidence and Cosmological Mass Density. *ApJS*, **130**, 1–35. [128]

REES, M.J. (1978). Origin of pregalactic microwave background. *Nature*, **275**, 35–37. [2]

REICH, P. & REICH, W. (1986). A radio continuum survey of the northern sky at 1420 MHz. II. *A&AS*, **63**, 205–288. [111, 180]

REICH, P., TESTORI, J.C. & REICH, W. (2001). A radio continuum survey of the southern sky at 1420 MHz. The atlas of contour maps. *A&A*, **376**, 861–877. [111, 180]

REICH, W. (1982). A radio continuum survey of the northern sky at 1420 MHz. I. *A&AS*, **48**, 219–297. [111, 180]

RENGELINK, R.B., TANG, Y., DE BRUYN, A.G., MILEY, G.K., BREMER, M.N., ROETTGERING, H.J.A. & BREMER, M.A.R. (1997). The Westerbork Northern Sky Survey (WENSS), I. A 570 square degree Mini-Survey around the North Ecliptic Pole. *A&AS*, **124**. [117, 119, 123]

RICHARDS, E.A. (2000). The Nature of Radio Emission from Distant Galaxies: The 1.4 GHZ Observations. *ApJ*, **533**, 611–630. [110, 117]

RIESS, A.G., FILIPPENKO, A.V., CHALLIS, P., CLOCCHIATTI, A., DIERCKS, A., GARNAVICH, P.M., GILLILAND, R.L., HOGAN, C.J., JHA, S., KIRSHNER & ET AL. (1998). Observational Evidence from Supernovae for an Accelerating Universe and a Cosmological Constant. *AJ*, **116**, 1009–1038. [1]

Rogers, A.E.E. & Bowman, J.D. (2008). Spectral Index of the Diffuse Radio Background Measured from 100 to 200 MHz. *AJ*, **136**, 641–648. [111]

Rowan-Robinson, M., Benn, C.R., Lawrence, A., McMahon, R.G. & Broadhurst, T.J. (1993). The evolution of faint radio sources. *MNRAS*, **263**, 123–130. [117]

Rubiño-Martín, J.A., Chluba, J. & Sunyaev, R.A. (2006). Lines in the cosmic microwave background spectrum from the epoch of cosmological hydrogen recombination. *MNRAS*, **371**, 1939–1952. [2]

Salvini, S. & Wijnholds, S.J. (2014). Fast gain calibration in radio astronomy using alternating direction implicit methods: Analysis and applications. *A&A*, **571**, A97. [78]

Santos, M.G., Cooray, A. & Knox, L. (2005). Multifrequency Analysis of 21 Centimeter Fluctuations from the Era of Reionization. *ApJ*, **625**, 575–587. [47, 111, 117]

Sarkar, A.K., Bharadwaj, S. & Ali, S.S. (2016a). Estimating the binned 21-cm HI power spectrum using Fisher matrix analysis for OWFA. *JApA*, submitted. [47, 172]

Sarkar, A.K., Bharadwaj, S. & Marthi, V.R. (2016b).Eigen-decomposition based visibility simulations for HI at z=3.35. *MNRAS*, in preparation. [xi, x, 168, 169, 171]

Sarkar, D., Bharadwaj, S. & Anathpindika, S. (2016). Modelling the post-reionization neutral Hydrogen HI bias. *ArXiv e-prints*. [128]

Sathyanarayana Rao, M., Subrahmanyan, R., Udaya Shankar, N. & Chluba, J. (2015). On the Detection of Spectral Ripples from the Recombination Epoch. *ApJ*, **810**, 3. [10]

Schmidt, B.P., Suntzeff, N.B., Phillips, M.M., Schommer, R.A., Clocchiatti, A., Kirshner, R.P., Garnavich, P., Challis, P., Leibundgut, B., Spyromilio, J. & et al. (1998). The High-Z Supernova Search: Measuring Cosmic Deceleration and Global Curvature of the Universe Using Type IA Supernovae. *ApJ*, **507**, 46–63. [1]

Selvanayagam, A.J., Praveenkumar, A., Nandagopal, D. & Velusamy, T. (1993). Sensitivity boost to the Ooty Radio Telescope: A new phased array of 1056 dipoles with 1056 Low Noise Amplifiers. *IETE Technical Review*, **10**, 333–339. [21, 23]

Seo, H.J. & Hirata, C.M. (2016). The foreground wedge and 21-cm BAO surveys. *MNRAS*, **456**, 3142–3156. [xi, 9, 151]

Seymour, N., McHardy, I.M. & Gunn, K.F. (2004). Radio observations of the 13^hXMM-Newton/ROSAT Deep X-ray Survey Area. *MNRAS*, **352**, 131–141. [110, 117]

Shaver, P.A., Windhorst, R.A., Madau, P. & de Bruyn, A.G. (1999). Can the reionization epoch be detected as a global signature in the cosmic background? *A&A*, **345**, 380–390. [9]

Shaw, J.R., Sigurdson, K., Sitwell, M., Stebbins, A. & Pen, U.L. (2015). Coaxing cosmic 21 cm fluctuations from the polarized sky using m -mode analysis. *Ph. Rv. D*, **91**, 083514. [184]

Simpson, C., Martínez-Sansigre, A., Rawlings, S., Ivison, R., Akiyama, M., Sekiguchi, K., Takata, T., Ueda, Y. & Watson, M. (2006). Radio imaging of the Subaru/XMM-Newton Deep Field - I. The 100-μJy catalogue, optical identifications, and the nature of the faint radio source population. *MNRAS*, **372**, 741–757. [110, 117]

Singal, J., Stawarz, Ł., Lawrence, A. & Petrosian, V. (2010). Sources of the radio background considered. *MNRAS*, **409**, 1172–1182. [117]

Singh, S., Subrahmanyan, R., Udaya Shankar, N. & Raghunathan, A. (2015). On the Detection of Global 21-cm Signal from Reionization Using Interferometers. *ApJ*, **815**, 88. [10]

Sirothia, S.K., Dennefeld, M., Saikia, D.J., Dole, H., Ricquebourg, F. & Roland, J. (2009). 325-MHz observations of the ELAIS-N1 field using the Giant Metrewave Radio Telescope. *MNRAS*, **395**, 269–281. [iv, vi, 89, 92, 117, 119, 121, 122]

Smirnov, O.M. (2011). Revisiting the radio interferometer measurement equation. II. Calibration and direction-dependent effects. *A&A*, **527**, A107. [93]

Smoot, G.F., Bennett, C.L., Kogut, A., Wright, E.L., Aymon, J., Boggess, N.W., Cheng, E.S., de Amici, G., Gulkis, S., Hauser, M.G. &

et al. (1992). Structure in the COBE differential microwave radiometer first-year maps. *ApJL*, **396**, L1–L5. [1, 6]

Storrie-Lombardi, L.J., McMahon, R.G. & Irwin, M.J. (1996). Evolution of neutral gas at high redshift: implications for the epoch of galaxy formation. *MNRAS*, **283**, L79–L83. [128]

Subrahmanya, C.R., Manoharan, P.K. & Chengalur, J.N. (2016a). The Ooty Wide-Field Array. *JApA*, submitted. [vii, 3, 10, 23, 28, 47, 51, 179]

Subrahmanya, C.R., Prasad, P., Girish, B.S., Somasekhar, R., Manoharan, P.K. & Amit Mittal, S.G. (2016b). The Ooty Wide-Field Array: Receiver System. *JApA*, submitted. [ii, 28, 29, 30, 47, 51, 179]

Swarup, G., Sarma, N.V.G., Joshi, M.N., Kapahi, V.K., Bagri, D.S., Damle, S.H., Ananthakrishnan, S., Balasubramanian, V., Bhave, S.S. & Sinha, R.P. (1971). Large Steerable Radio Telescope at Ootacamund, India. *Nature Physical Science*, **230**, 185–188. [10, 21, 28, 35]

Tegmark, M., Eisenstein, D.J., Hu, W. & de Oliveira-Costa, A. (1999). Overview of Foregrounds and their Impact. In A. de Oliveira-Costa & M. Tegmark, eds., *Microwave Foregrounds*, vol. 181 of *Astronomical Society of the Pacific Conference Series*, 3. [14]

Tegmark, M., Eisenstein, D.J., Hu, W. & de Oliveira-Costa, A. (2000). Foregrounds and Forecasts for the Cosmic Microwave Background. *ApJ*, **530**, 133–165. [111]

Testori, J.C., Reich, P., Bava, J.A., Colomb, F.R., Hurrel, E.E., Larrarte, J.J., Reich, W. & Sanz, A.J. (2001). A radio continuum survey of the southern sky at 1420 MHz. Observations and data reduction. *A&A*, **368**, 1123–1132. [111, 180]

Thompson, A., Moran, J. & Swenson, G. (2008). *Interferometry and Synthesis in Radio Astronomy*. Wiley. [73]

Thyagarajan, N., Udaya Shankar, N., Subrahmanyan, R., Arcus, W., Bernardi, G., Bowman, J.D., Briggs, F., Bunton, J.D., Cappallo, R.J., Corey, B.E. & et al. (2013). A Study of Fundamental Limitations to Statistical Detection of Redshifted H I from the Epoch of Reionization. *ApJ*, **776**, 6. [17, 146, 151, 155, 182]

Tingay, S.J., Goeke, R., Bowman, J.D., Emrich, D., Ord, S.M., Mitchell, D.A., Morales, M.F., Booler, T., Crosse, B., Wayth, R.B. & et al. (2013). The Murchison Widefield Array: The Square Kilometre Array Precursor at Low Radio Frequencies. *PASA*, **30**, e007. [10, 71]

Toffolatti, L., Argueso Gomez, F., de Zotti, G., Mazzei, P., Franceschini, A., Danese, L. & Burigana, C. (1998). Extragalactic source counts and contributions to the anisotropies of the cosmic microwave background: predictions for the Planck Surveyor mission. *MNRAS*, **297**, 117–127. [110]

Turtle, A.J. & Baldwin, J.E. (1962). A survey of galactic radiation at 178 Mc/s. *MNRAS*, **124**, 459. [109]

Turtle, A.J., Pugh, J.F., Kenderdine, S. & Pauliny-Toth, I.I.K. (1962). The spectrum of the galactic radio emission, I. Observations of low resolving power. *MNRAS*, **124**, 297. [109]

University of California, California Institute of Technology, The Association of Canadian Universities for Research in Astronomy & TMT Observatory Corporation (2007). Thirty Meter Telescope Construction Proposal. *http://www.tmt.org/documents; TMT Document Number: TMT.PMO.MGT.07.009*. []

van Haarlem, M.P., Wise, M.W., Gunst, A.W., Heald, G., McKean, J.P., Hessels, J.W.T., de Bruyn, A.G., Nijboer, R., Swinbank, J., Fallows, R. & et al. (2013). LOFAR: The LOw-Frequency ARray. *A&A*, **556**, A2. [10, 71]

Vedantham, H., Udaya Shankar, N. & Subrahmanyan, R. (2012). Imaging the Epoch of Reionization: Limitations from Foreground Confusion and Imaging Algorithms. *ApJ*, **745**, 176. [17, 146, 149, 151, 154, 182]

Vedantham, H.K., Koopmans, L.V.E., de Bruyn, A.G., Wijnholds, S.J., Ciardi, B. & Brentjens, M.A. (2014). Chromatic effects in the 21 cm global signal from the cosmic dawn. *MNRAS*, **437**, 1056–1069. [146]

Vedantham, H.K., Koopmans, L.V.E., de Bruyn, A.G., Wijnholds, S.J., Brentjens, M., Abdalla, F.B., Asad, K.M.B., Bernardi, G., Bus, S., Chapman, E. & et al. (2015). Lunar occultation of the diffuse radio sky: LOFAR measurements between 35 and 80 MHz. *MNRAS*, **450**, 2291–2305. [110]

Vernstrom, T. (2015). The Faint Extragalactic Radio Sky. Ph.D. thesis, The University of British Columbia, (2015). [118, 181]

VILLAESCUSA-NAVARRO, F., VIEL, M., ALONSO, D., DATTA, K.K., BULL, P. & SANTOS, M.G. (2015). Cross-correlating 21cm intensity maps with Lyman Break Galaxies in the post-reionization era. *JCAP*, **3**, 034. [9, 10]

VISBAL, E., LOEB, A. & WYITHE, S. (2009). Cosmological constraints from 21cm surveys after reionization. *JCAP*, **10**, 030. [9, 10, 179]

WEISTROP, D., WALL, J.V., FOMALONT, E.B. & KELLERMANN, K.I. (1987). A deep 6-centimeter radio source survey - Optical identifications. *AJ*, **93**, 805–810. [117]

WELLS, D.C., GREISEN, E.W. & HARTEN, R.H. (1981). FITS - a Flexible Image Transport System. *A&AS*, **44**, 363. [49]

WEYMANN, R.J., CARSWELL, R.F. & SMITH, M.G. (1981). Absorption lines in the spectra of quasistellar objects. *ARAA*, **19**, 41–76. [2]

WHITE, M., CARLSTROM, J.E., DRAGOVAN, M. & HOLZAPFEL, W.L. (1999). Interferometric Observation of Cosmic Microwave Background Anisotropies. *ApJ*, **514**, 12–24. [134]

WHITE, S.D.M. & REES, M.J. (1978). Core condensation in heavy halos - A two-stage theory for galaxy formation and clustering. *MNRAS*, **183**, 341–358. [2]

WIERINGA, M.H. (1991). Ph.D. thesis, Rijksuniversiteit Leiden, (1991). [iv, vi, 71, 73, 82, 89, 92, 104, 117, 119, 120, 121, 122]

WIERINGA, M.H. (1992). An investigation of the telescope based calibration methods 'redundancy' and 'self-cal'. *Experimental Astronomy*, **2**, 203–225. [ix, iii, 71, 73, 75, 82, 86, 89, 90, 91]

WIJNHOLDS, S.J. (2010). Ph.D. thesis, Technische Universiteit Delft (2010). [77]

WINDHORST, R.A. (1986). Is the upturn in the source counts caused by primeval radio galaxies? *Highlights of Astronomy*, **7**, 355–366. [118]

WINDHORST, R.A., MILEY, G.K., OWEN, F.N., KRON, R.G. & KOO, D.C. (1985). Sub-millijansky 1.4 GHz source counts and multicolor studies of weak radio galaxy populations. *ApJ*, **289**, 494–513. [118]

WINDHORST, R.A., FOMALONT, E.B., PARTRIDGE, R.B. & LOWENTHAL, J.D. (1993). Microjansky source counts and spectral indices at 8.44 GHz. *ApJ*, **405**, 498–517. [118]

Wouthuysen, S.A. (1952). On the excitation mechanism of the 21-cm (radio-frequency) interstellar hydrogen emission line. *AJ*, **57**, 31–32. [8]

Wyithe, J.S.B. & Loeb, A. (2009). The 21-cm power spectrum after reionization. *MNRAS*, **397**, 1926–1934. [8]

Wyithe, J.S.B., Loeb, A. & Geil, P.M. (2008). Baryonic acoustic oscillations in 21-cm emission: a probe of dark energy out to high redshifts. *MNRAS*, **383**, 1195–1209. [10, 179]

Xu, Y., Wang, X. & Chen, X. (2015). Forecasts on the Dark Energy and Primordial Non-Gaussianity Observations with the Tianlai Cylinder Array. *ApJ*, **798**, 40. [10, 47, 71]

Yatawatta, S., de Bruyn, A.G., Brentjens, M.A., Labropoulos, P., Pandey, V.N., Kazemi, S., Zaroubi, S., Koopmans, L.V.E., Offringa, A.R., Jelić, V. & et al. (2013). Initial deep LOFAR observations of epoch of reionization windows. I. The north celestial pole. *A&A*, **550**, A136. [10, 110]

York, D.G., Adelman, J., Anderson, J.E., Jr., Anderson, S.F., Annis, J., Bahcall, N.A., Bakken, J.A., Barkhouser, R., Bastian, S., Berman, E. & SDSS Collaboration (2000). The Sloan Digital Sky Survey: Technical Summary. *AJ*, **120**, 1579–1587. [133]

Zaldarriaga, M. (1997). Polarization of the microwave background in reionized models. *Ph. Rv. D*, **55**, 1822–1829. [3]

Zaldarriaga, M., Furlanetto, S.R. & Hernquist, L. (2004). 21 Centimeter Fluctuations from Cosmic Gas at High Redshifts. *ApJ*, **608**, 622–635. [33, 133, 134]

Zaroubi, S., de Bruyn, A.G., Harker, G., Thomas, R.M., Labropolous, P., Jelić, V., Koopmans, L.V.E., Brentjens, M.A., Bernardi, G., Ciardi, B. & et al. (2012). Imaging neutral hydrogen on large scales during the Epoch of Reionization with LOFAR. *MNRAS*, **425**, 2964–2973. [9, 33]

Zheng, H., Tegmark, M., Buza, V., Dillon, J.S., Gharibyan, H., Hickish, J., Kunz, E., Liu, A., Losh, J., Lutomirski, A. & et al. (2014). MITEoR: a scalable interferometer for precision 21 cm cosmology. *MNRAS*, **445**, 1084–1103. [73]